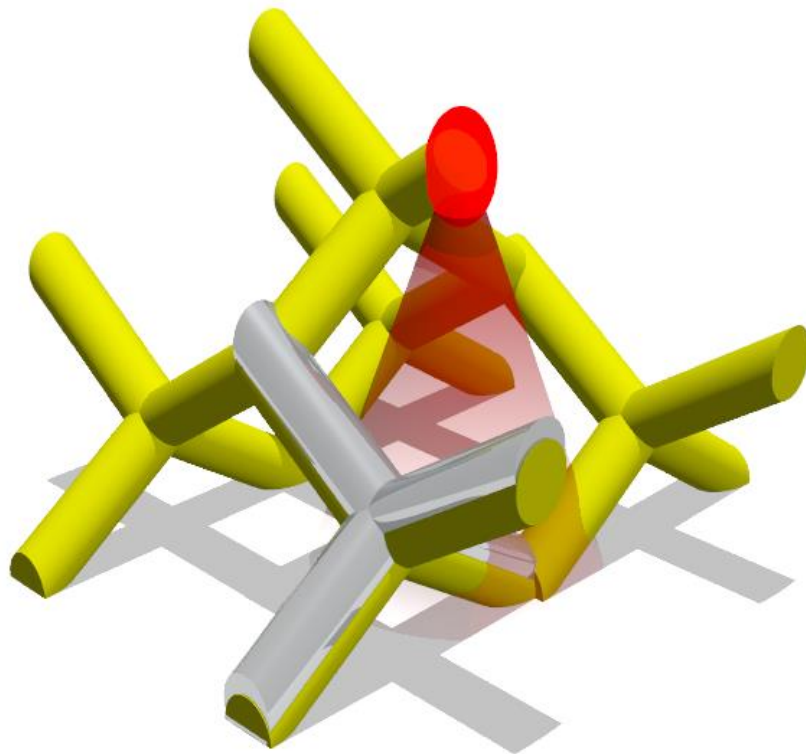

REALISING 3D ARTIFICIAL SPIN-ICE SYSTEMS
USING
TWO-PHOTON LITHOGRAPHY
AND
LINE-OF-SIGHT DEPOSITION



by

Andrew Stephen May

A THESIS SUBMITTED TO CARDIFF UNIVERSITY
FOR THE DEGREE OF DOCTOR OF PHILOSOPHY

DECEMBER 2020

Author: Andrew Stephen May

Title: Realising 3D Artificial Spin-Ice Systems using Two-Photon lithography and Line-of-Sight Deposition

Date of submission: December 2020

Significant Contributions

‘Don’t be afraid to ask questions. Don’t be afraid to ask for help when you need it. I do that every day. Asking for help isn’t a sign of weakness, it’s a sign of strength. It shows you have the courage to admit when you don’t know something, and to learn something new’

BARACK OBAMA

I would like to start by giving special thanks go to the exceptionally talented people who have trained me in numerous techniques during my PhD. Within Ladak Lab, Gwilym Williams and Lucas Chapuis taught me two-photon lithography, Matthew Hunt trained me to conduct MOKE and MFM measurements, and Arjen van den Berg taught me how to perform finite-element simulations. Outside of our research group, Angela Sobiesierski, Robert Lang, and Tyrone Jones trained me in various exoerimental techniques in the ICS cleanroom. Duncan Muir assisted in performing EDX and many of the SEM measurements taken during my PhD.

Many thanks to those who have performed simiulations and/or experimental measurements that have contributed to this thesis. Matthew Hunt performed finite difference simulations herein and captured the MOKE data presented in fig. 3.27. Arjen van den Berg performed the finite-element simulations given in chapter 3. Michael Saccone performed all Monte-Carlo simulations presented in

this thesis. Rolf Allenspach's group at IBM, Zurich performed spin-SEM measurements on several samples, which I am confident will contribute to future publications.

All finite-element simulations in this thesis have been performed using the Raven and Hawk supercomputing clusters at ARCCA, Cardiff University.

Dedication

‘It takes a village to raise a child’

OLD AFRICAN PROVERB

I don't tend to be one for emotional outpouring, although as I find myself hurtling towards the end of seven incredible years in Cardiff, I feel it's time to indulge in a little self-reflection. Firstly, I would like to thank my supervisor, Sam, who's invaluable help and support has guided me through my PhD. I want to thank everyone who I've worked alongside in Ladak Lab over the years, first and foremost is our resident postdoc, Matt, who has been an arbiter of knowledge and patience whenever anything went wrong, despite my frequent basic questions. Next are the students I've worked alongside, namely Arjen, Joe, and Alaa, thank you for all of your help, I've hugely enjoyed the laughs we've shared! My time in this group simply wouldn't have been the same without our annual summer interns, thank you to Lucas who first trained me, Mylène, Jacquelyn, Felix, Eloise, and David. You guys always livened things up! A particular trip to London springs to mind, you know who you are...

Outside of our group there are far too many students to name, who have helped me along the way. So I'll just say this, to the portakabin crew, the regular coffee goers, and my friends over in 53, thank you for all of our chats over the years. The importance of a kind word, a little piece of advice, or a large piece of cake can never be overstated. Of course, this thesis is not just the culmination of my PhD in Cardiff, but also my unforgettable undergraduate days beforehand. All of which stemmed from my first day in the Trevithick, when I happened to sit next to my friend, Mike. A seemingly minor, random act which lead to me also meeting Ben,

Lewys , Rory, and Sammy, all of whom changed my time in Cardiff for the better, which I will always be grateful for.

Now, anyone close to me will know I can't possible ramble on this long without mentioning korfball (look it up if you don't know it!). Throughout my PhD, this sport and the exceptional people who I've met through it, have given me a much needed escape from the research related anxieties I was likely having on any given week. Again, there a far too many people to name who have had a positive influence on me here, so I'll just thank everyone who's known me, first at Cardiff University Korfball Club, then at Cardiff Raptors, and more recently in the Wales squad.

I can't possibly acknowledge those who have helped me get to where I am today without thanking my parents and brother. From a young age I have always been supported, not only to achieve as highly as possible, but also to be inquisitive, to both wonder and investigate why something is the way it is. Doubtlessly, this is the reason I opted to study physics seven years ago, and had the opportunity to do so. Finally I thank my partner, Hannah, who has always listened to my ramblings, encouraged me, and stood up for me. Without you I doubt that I would currently be nearing completion of a PhD, and I simply would not be the person that I am today.

Publications

*‘If we knew what it was we were doing,
it would not be called research, would
it?’*

ALBERT EINSTEIN

FIRST AUTHOR

Andrew May, Matthew Hunt, Arjen van den Berg, Alaa Hejazi, and Sam Ladak, *Realisation of a frustrated 3D magnetic nanowire lattice*, Commun. Phys, 2.1, 2019.

CO-AUTHOR

Matthew Hunt, Mike Taverne, Joseph Askey, Andrew May, et al., *Harnessing Multi-Photon Absorption to Produce Three-Dimensional Magnetic Structures at the Nanoscale*, Materials, 13.3, 2020.

Gwilym Williams, Matthew Hunt, Benedikt Boehm, Andrew May, et al., *Two-photon lithography for 3D magnetic nanostructure fabrication*, Nano Research, 11.2, 2018.

Sourav Sahoo, Sucheta Mondal, Gwilym Williams, Andrew May, et al., *Ultra-fast magnetization dynamics in a nanoscale three-dimensional cobalt tetrapod structure*, Nanoscale, 10.21, 2018.

List of Symbols and Acronyms

Symbol	Definition
a	Lattice parameter
A	Area
A_{ex}	Exchange stiffness
\mathbf{B}, B	Magnetic induction
\mathbf{d}_{ij}	Dzyalashinskii-Moriya interaction vector between atoms i and j
d_{vox}	Voxel diameter
D	Coupling constant
e	Electron charge
\hat{e}_{ij}	Ising axis unit vector
\mathbf{E}	Optical field vector
E_A	Effective anisotropy energy density
E_{DM}	Dzyalashinskii-Moriya interaction energy density
E_{EDM}	Effective Dzyalashinskii-Moriya interaction energy density
E_{ex}	Exchange energy density
E_F	Fermi energy
E_{inter}	Sample-tip interaction energy
E_{ms}	Magnetostatic energy density
E_{mc}	Magnetocrystalline anisotropy energy density
E_{zee}	Zeeman energy density
f_γ	Laser repetition frequency
F	Force
\mathbf{F}_L	Lorentz Force
$g(E)$	Density of states
g_l	Orbital angular momentum g-factor
g_s	Spin g-factor
h	Planck constant

\hbar	Reduced Planck constant
\mathbf{H}, H	Magnetic field strength
H_C	Coercive field
\mathbf{H}_d	Demagnetising field
H_D	Depinning field
H_{eff}	Effective magnetic field
I	Current
I_γ	Photon flux intensity
$I_{\gamma focus}$	Photon flux intensity in the focus plane
\mathbf{J}	Effective electron angular momentum
J_1, J_2	Interaction strength between neighbouring nanowires
J_{ij}	Exchange integral
k	Spring constant
k_B	Boltzmann constant
K_n	n th order magnetocrystalline anisotropy constant
K_S	Shape anisotropy constant
l	Length
l_q	Orbital angular momentum quantum number
l_{vox}	Voxel length
\mathbf{L}	Orbital angular momentum vector
\mathbf{m}	Magnetic moment
m_B	Bohr Magneton
m_e	Electron mass
m_l	Spatial quantisation number
\mathbf{m}_L	Magnetic moment associated with orbital angular momentum
m_s	Electron spin quantum number
\mathbf{m}_S	Magnetic moment associated with electron spin
\mathbf{M}	Magnetisation
M_c	Madelung Constant
M_R	Remanent magnetisation
M_S	Saturation magnetisation
n	Refractive index
n_0	Electron density
n_{pulse}	Number of pulses
n_q	Principal quantum number
n_t	Number of turns per unit length
n_\downarrow	Number of spin-down electrons per unit volume

n_{\uparrow}	Number of spin-up electrons per unit volume
\mathcal{N}	Demagnetising tensor
N_D	Demagnetising factor
NA	Numerical aperture
p	Magnetic pole
\mathbf{P}	Polarisation vector
P_{γ}	Laser power
Q, q	Charge
\mathbf{Q}	Voigt vector
\mathbf{r}, r	Position vector, distance/radius
s_q	Electron spin quantum number
\mathbf{S}	Electron spin vector
S_R	Residual entropy
t	Time
t_0	Attempt time
t_m	Measurement time
T_B	Blocking temperature
u_{ij}	Dipolar interaction energy between two spins, i and j
u_{system}	Total dipolar interaction energy for a system of n spins
U_{ice}	Total energy of adjoining, ice-rule obeying vertices
U_{MAP}	Total energy of a system harbouring a monopole anti-monopole pair
v_{γ}	Laser wave frequency
V	Volume
W	Number of possible states
z_R	Rayleigh length
α_D	Damping constant
α_{ij}	Factor to modify the strength of interaction between spins i and j
α_n	Directional cosines of the magnetisation vector
δ_i	Disorder parameter
δ_t	Domain wall thickness
δ_W	Domain wall width
ϵ_0	Permittivity of free space
ϵ_{ex}	Exchange energy
ϵ_{ms}	Magnetostatic energy
ϵ_{mc}	Magnetocrystalline anisotropy energy
γ_L	Orbital angular momentum gyromagnetic ratio
γ_P	Precession term

γ_S	Electron spin gyromagnetic ratio
\mathcal{H}	Hamiltonian
λ	Wavelength
μ	Permeability
μ_{pot}	Chemical potential
μ_{pot}^*	Effective chemical potential
μ_0	Permeability of free space
ρ_{init}	Primary initiator particle density
ρ_{rad}	Density of radicals
σ	Variance of a Gaussian peak
σ_2	Two-photon absorption cross-section
σ^-, σ^+	Left and right handed portions of a circularly polarised optical beam
θ	Angle
τ	Torque
τ_γ	Laser pulse width
ω_e	Electron angular velocity
ω_0	Optical beam waist
$\omega(z)$	Optical beam radius at a distance z
χ	Magnetic susceptibility
χ_m	Linear susceptibility of a medium

Acronym	Definition
2D	Two dimensional
3D	Three dimensional
3DNL	Three dimensional nanowire lattice
AFM	Atomic force microscopy
AOM	Acousto optic modulator
AR	Aspect ratio
ARCCA	Advanced research computing at Cardiff
ASI	Artificial spin-ice
BCC	Body centred cubic
CAD	Computer aided design
DMI	Dzyaloshinskii-Moriya interaction
DW	Domain wall
EDX	Energy dispersive x-ray
FCC	Face centred cubic

FD	Finite difference
FE	Finite element
GWL	General writing language
HDD	Hard disk drive
HH	Head-to-head
IPA	Isopropyl alcohol
LLG	Landau-Lifshitz-Gilbert
MAP	Monopole anti-monopole pair
MFM	Magnetic force microscopy
MOKE	Magneto-optical Kerr effect
PGMEA	Propylene glycol methyl ether acetate
PEEM	Photoemission electron microscopy
QCM	Quartz crystal monitor
RMS	Root mean square
SEM	Scanning electron microscopy
SNR	Signal-to-noise ratio
Spin-SEM	Spin-polarised scanning electron microscopy
TPL	Two-photon lithography
TPP	Two-photon polymerisation
TT	Tail-to-tail
UV	Ultra-violet
VDW	Vortex domain wall
XMCD	X-ray magnetic circular dichroism

Contents

Significant Contributions	v
Dedication	vii
Publications	ix
List of Symbols and Acronyms	xi
List of Tables	xxi
List of Figures	xxiii
Abstract	1
1 Background Theory	5
1.1 Magnetic Moments - Dipoles and Current Loops	5
1.1.1 Magnetic Dipoles	6
1.1.2 Current Loops	8
1.2 The Atomic Magnetic Moment	10
1.2.1 Spin-orbit Interaction	14
1.3 Diamagnetism and Paramagnetism	15
1.3.1 Diamagnetism	15
1.3.2 Paramagnetism	16
1.4 Ferromagnetism	16
1.4.1 Direct Exchange Interaction	17
1.4.2 Magnetostatic Energy	19
1.4.3 Magnetocrystalline Anisotropy Energy	21
1.4.4 Transition Metals	23
1.4.5 Domains and Domain Walls in Bulk Ferromagnets	26

1.4.6	Hysteresis	30
1.5	Domain Walls in Magnetic Nanowires	32
1.6	Domain Wall Pinning	36
1.7	Curvature	40
1.8	Frustrated Systems	42
1.8.1	Bulk Frustrated Materials	43
1.8.2	Artificial Spin-ice	46
1.9	Two-Photon Polymerisation	54
2	Experimental Techniques	63
2.1	Two-Photon Lithography	63
2.2	Thermal Evaporation	74
2.3	Scanning Electron Microscopy and Energy Dispersive X-ray Spectroscopy	78
2.4	Atomic Force Microscopy	80
2.5	Magnetic Force Microscopy	84
2.6	Optical Magnetometry	89
2.7	Simulations	94
2.7.1	Finite Element Techniques	95
2.7.2	Finite Difference	98
3	Exploring Two-Photon Lithography for 3D Magnetic Nanostructure	
	Fabrication	101
3.1	Introduction	101
3.2	Permalloy films and planar microwires	104
3.3	Raised Permalloy Nanowires and Micro Pads	108
3.4	Realising a 3D Ferromagnetic Nanowire Lattice	113
3.5	Isolating the 3D Ferromagnetic Nanowire Lattice	120
3.5.1	Physical Characterisation	121
3.5.2	Micro-magnetic Simulations	130
3.5.3	Magnetic Characterisation	139
3.6	Summary	150
4	Imaging Magnetic Monopole Excitations on a 3D Frustrated Magnetic Lattice	153
4.1	Direct observation and manipulation of a 3D spin texture	154

4.2	Modelling switching in 3D Artificial spin-ice.	177
4.3	The implications of broken symmetry	195
4.4	Summary	208
5	Conclusions and Future Work	209
5.1	Realising a 3D Artificial Spin-Ice	209
5.2	Magnetic Characterisation	211
5.3	Simulations and Modeling	213
5.4	Future Work	215
6	Appendices	219
6.1	Unmasked MFM Data	219
6.2	Dipolar Framework Calculations	226
6.3	Monte-Carlo Simulations	227
	Bibliography	249

List of Tables

1.1	Typical χ values for diamagnets, paramagnets and ferromagnets. . . .	15
1.2	Anisotropy coefficients of Fe and Ni.	22
1.3	DW structure for each vertex type, in a connected artificial spin-ice .	53
1.4	Chemical reactions during two-photon polymerisation.	57
2.1	Summary of Nanowrite commands.	72
2.2	Details of MFM probes used in this study.	87
3.1	Lateral and z-axial features sizes on different wire layers.	126
3.2	Energy density values of various tetrapod remanent states	138
4.1	A survey of commercial MFM probes	160
4.2	Total energy density for each simulated remanent state of a bipod and tetrapod.	179
4.3	Domain wall characteristics within micromagnetic simulations of 2-in bipods and type 3 tetrapods.	184
4.4	Results of effective chemical potential calculations	207

List of Figures

1.1	Dipole model of a magnetic moment.	6
1.2	Magnetic field lines associated with a dipole moment.	7
1.3	Magnetic moment associated with a one-turn current loop.	8
1.4	A single-turn current loop under an applied magnetic field.	9
1.5	Magnetic moment associated with a hydrogen atom.	11
1.6	Illustrations of electron orbitals.	12
1.7	Classical picture of the Bohr model.	14
1.8	Magnetic moments aligning to an external field in a paramagnet. . . .	16
1.9	Illustration of neighbouring hydrogen atoms.	18
1.10	Demagnetisation field associated with a ferromagnet.	20
1.11	Crystallographic axes in BCC and FCC lattices.	22
1.12	Illustration of the electron structure in nitrogen and oxygen.	23
1.13	Electron occupancy in the 3d bands of Fe, Co, Ni, and Cu.	25
1.14	Slater-Pauling curve for transition metals.	26
1.15	Flux-closure domain structure in a ferromagnet.	27
1.16	How shape anisotropy can affect domain structure.	28
1.17	Structure of Bloch and Néel domain walls.	28
1.18	Magnetic poles associated with Bloch and Néel domain walls.	29
1.19	Typical example of a ferromagnetic hysteresis loop.	30
1.20	Reversal mechanism of a single-domain ferromagnet.	31
1.21	Types of domain walls in nanostrips.	33
1.22	Permutations of vortex domain wall structure.	34
1.23	Typical domain wall structures in 2D and 3D magnetic nanowires. . .	35
1.24	Reversal of a single-domain, notched nanowire.	37
1.25	Spin canting in a curved ferromagnet.	41

1.26 Spin texture in a curved nanowire.	42
1.27 Example of frustration in a triangular lattice.	42
1.28 Schematic of the molecular structure in water-ice.	43
1.29 Illustrating the dumbbell model in bulk spin-ice.	45
1.30 Monopole interactions in bulk spin-ice.	46
1.31 Vertex types in artificial spin-ice.	47
1.32 Monopole excitations in artificial spin-ice.	49
1.33 A 2.5D artificial spin-ice.	51
1.34 Illustration of a connected artificial spin-ice.	52
1.35 Electron excitation for one-photon and two-photon absorption.	55
1.36 Laser intensity profile for three photolithography setups.	56
1.37 Intensity distribution of photoinitiator excitation.	58
2.1 Illustration of TPL process.	65
2.2 Schematic of the TPL setup.	66
2.3 Defining a geometry in DeScribe for fabrication via TPL.	67
2.4 Illustrations of TPL scanning modes.	68
2.5 Manually defining the GWL code for a tetrapod in Nanowrite.	69
2.6 Visualising a 3×3 array of tetrapod structures in Nanowrite.	70
2.7 Spin curve for AZ9260 photoresist.	74
2.8 Schematic of the main components in a thermal evaporator.	75
2.9 Illustration of a tetrapod scaffold after a line-of-sight metal deposition.	77
2.10 Illustration of four angled gold depositions via thermal evaporation.	77
2.11 Typical SEM setup	78
2.12 Schematic of a typical AFM setup.	80
2.13 Illustration of an AFM probe scanning in tapping mode.	81
2.14 MFM measurement of magnetic tape.	85
2.15 Illustration of the two-pass scanning method used during MFM.	86
2.16 Diagram of a bespoke electromagnet.	88
2.17 Schematic of the optical setup for MOKE measurements.	90
2.18 Illustrating the magneto-optical Kerr effect.	93
2.19 The three configurations for MOKE measurements.	94
2.20 Finite-element mesh for a sphere.	96
2.21 Consequences of the Landau-Lifshitz-Gilbert equation	97

2.22	Finite-difference cell grid for a sphere.	98
2.23	How a cell grid relates to a desired geometry.	99
3.1	Optical images of cuboidal trenches in positive-tone photoresist. . . .	104
3.2	AFM/MFM of planar $Ni_{81}Fe_{19}$ microwires.	105
3.3	Line profiles showing the thickness of a $Ni_{81}Fe_{19}$ deposition.	106
3.4	Hysteresis loop of a $Ni_{81}Fe_{19}$ film.	107
3.5	SEM images of $Ni_{81}Fe_{19}$ nano/micro wires and pads on a polymer scaffold.	109
3.6	AFM/MFM data and MuMax simulations of $Ni_{81}Fe_{19}$ nano/micro wires and pads.	110
3.7	CAD renderings of a diamond-bond lattice geometry.	114
3.8	SEM images of 3D nanowire lattice, produced with the piezo scan mode.	114
3.9	GWL co-ordinates for a diamond-bond lattice unit cell.	116
3.10	Dose array of diamond-bond lattice scaffolds.	117
3.11	SEM images of a diamond-bond lattice, 1 unit cell in height.	118
3.12	AFM scan of a diamond-bond lattice structure.	119
3.13	Properties of $Ni_{81}Fe_{19}$ nanopads.	121
3.14	SEM images of a diamond-bond lattice, 5 unit cells in height.	123
3.15	Illustrating the crescent shaped cross-section of a $Ni_{81}Fe_{19}$ nanowire.	124
3.16	Schematic of the 3D nanowire lattice geometry.	125
3.17	Measuring the tetrahedral angle upon the lattice surface.	125
3.18	Characterising the lateral and axial feature sizes as a function of height.	127
3.19	Measuring the nanowire surface roughness.	128
3.20	EDX mapping of the sample composition.	130
3.21	Designing a $Ni_{81}Fe_{19}$ nanowire for micro-magnetic simulations.	131
3.22	Finite-element simulation of a single domain $Ni_{81}Fe_{19}$ nanowire.	132
3.23	Simulating the domain wall structure in a $Ni_{81}Fe_{19}$ nanowire.	133
3.24	Simulated hysteresis loops of diamond-bond lattice building blocks.	134
3.25	Simulating a bipod surface termination at remanence.	137
3.26	Simulated MFM contrast for various tetrapod remanent states.	138
3.27	Hysteresis loops measured from a diamond-bond lattice structure.	140
3.28	Illustrating a possible reversal mechanism for a bipod.	141
3.29	SEM images of a deformed diamond-bond lattice structure.	143

3.30	SEM images of a diamond-bond lattice with an underlying gold layer.	145
3.31	Hysteresis loops measured from a diamond-bond lattice structure with an underlying gold layer.	146
3.32	MFM scans of a diamond-bond lattice following in-plane external fields applied along the two principle lattice directions.	147
3.33	AFM/MFM scans taken before and after inverting the tip magnetisation.	148
3.34	Multiplying the AFM and MFM data to highlight the surface contrast.	149
3.35	Quantitative analysis of the MFM data before and after the tip reversal.	151
4.1	MFM scans of opposing saturation states for the upper two sub-lattices	156
4.2	MFM scans with masks covering the voidal regions.	157
4.3	MFM data captured from a non-saturated state.	158
4.4	Successive MFM scans with opposing slow scan directions.	159
4.5	MFM scans of a non-saturated state, using a SSS-MFMR probe. . . .	161
4.6	AFM/MFM scans with opposing slow scan directions, using a SSS-MFMR probe.	162
4.7	Illustrating the nanowire cross-sectional area calculation.	163
4.8	Identifying different states for an individual L1-L2 junction.	164
4.9	Two intermediate states with associated vector maps.	165
4.10	MFM dataset observing an incremental reversal of the L1 sub-lattice.	167
4.11	MFM dataset observing an incremental reversal of the L2 sub-lattice.	169
4.12	Analysis of the L1 and L2 incremental reversals.	172
4.13	AFM scans using probes with a varying degree of degradation.	173
4.14	MFM data observing monopole propagation on the L3 sub-lattice. . . .	176
4.15	Finite-element simulations of three bipod remanent states.	178
4.16	Diagrams of the initial conditions defined for finite-element simulations.	180
4.17	Simulating a domain wall depinning from a bipod vertex.	181
4.18	Simulating the four vortex domain wall permutations in a bipod. . . .	182
4.19	Structure of a vortex domain wall with upwards polarity in a bipod. . .	185
4.20	Structure of a vortex domain wall with downwards polarity in a bipod.	187
4.21	Vortex domain wall permutations in type 3 tetrapods with opposing upper wires	189
4.22	Structure of a vortex domain wall pinned at a tetrapod vertex.	190
4.23	Simulating a depinning event in the L1 sub-lattice reversal.	191

4.24	Domain wall position in a tetrapod for opposing chiralities.	192
4.25	Vortex domain wall permutations in type 3 tetrapods with opposing lower wires.	193
4.26	Simulating a depinning event in the L2 sub-lattice reversal.	194
4.27	Monte-carlo simulation of the L1 sub-lattice reversal.	198
4.28	Monte-carlo simulation of the L2 sub-lattice reversal.	200
4.29	Diagrams of a sub-surface monopole nucleation event.	202
4.30	Schematic of a tetrapod geometry in a dipolar approximation.	203
4.31	Diagrams of monopole nucleation on the lattice surface.	205
4.32	A monopole-antimonopole pair at adjacent L1-L2 junctions.	206

Abstract

‘If you wish to make an apple pie from scratch, you must first invent the universe.’

CARL SAGAN

The core purpose of this thesis is to examine if two-photon lithography (TPL), coupled with a line-of-sight deposition, can facilitate the production of ferromagnetic nanowire arrays in three dimensional (3D) frustrated geometries, and to characterise the fabricated structures. Specifically, nanowire arrays possessing a diamond-bond lattice geometry are of interest herein, as this emulates the arrangement of rare-earth magnetic moments in bulk spin-ice. Simple, planar structures are first studied to form an understanding of the fabrication and characterisation processes, before progressing to investigate frustrated 3D nanowire lattices (3DNLs), fabricated upon polymer scaffolds. These complex structures extend $50 \times 50 \times 10 \mu\text{m}^3$ whilst individual nanowires are 1000 nm in length, 200 nm in lateral width, and have a peak thickness of 50 nm . Here, $\text{Ni}_{81}\text{Fe}_{19}$ wires exhibit a crescent shaped cross-section, due to the ellipsoidal geometry of the voxel during TPL. Shadowing effects during the line-of-sight $\text{Ni}_{81}\text{Fe}_{19}$ deposition limit the 3DNL to one unit cell in height, although scaffolds are defined as 5 unit cells high to isolate the 3DNL from the surrounding sheet film. Atomic force microscopy (AFM) measurements indicate that the upper two sub-lattices (L1 and L2) exhibit RMS surface roughness of $(10.8 \pm 4.3)\text{nm}$ and $(16.1 \pm 3.2)\text{nm}$ respectively.

Micromagnetic simulations of a single wire, bipod, and tetrapod, representing a system of 1, 2, and 4 spins respectively, indicated the wires to be single domain

at remanence and reverse via the propagation of vortex domain walls (DWs). A near-degenerate ice rule manifold is seen by considering the energetics of the possible tetrapod configurations, where the energy minimum is type 2. MOKE magnetometry, in a longitudinal configuration, is sensitive to the upper two sub-lattices of the 3DNL, these measurements indicate a coercive field of 8.0 mT. However, the intense laser beam used in this technique can cause significant deformation due to the poor conductivity of the polymer scaffold. Coating the polymer sidewalls with gold prior to the $Ni_{81}Fe_{19}$ deposition is found to be one solution to this concern. Wires in the 3DNL are experimentally confirmed to be Ising-like via Magnetic force microscopy (MFM) images captured after applying an external field parallel and perpendicular to the uppermost sub-lattice. MFM signal associated with the 3DNL topography is then proven to be magnetic in origin by inverting the tip magnetisation, as this process yields an inversion in the observed MFM contrast.

Field-driven MFM experiments facilitate the identification of various vertex states. Furthermore, monopole excitations on the upper-most sub-lattice are seen to propagate via long cascades of reversing wires and are only seen as isolated charges, which are never observed upon two-wire surface terminations (bipods). In contrast, sub-surface monopole excitations propagate via short chains of wire reversals and frequently appear in closely correlated, charge neutral pairs. Field-driven micromagnetic simulations demonstrate the energy difference between the low energy and excited states to be a factor of 3.23 greater for a bipod, compared with a tetrapod. This indicates that enhanced surface energetics are present, due to the broken lattice symmetry at the upper-boundary. In addition, the vertex spin texture significantly impacts the pinning of monopole excitations, which is studied as a function of applied field, where the precise domain wall structure plays a key role. Monte-Carlo simulations are used to recreate the field-driven experiments, both with and without enhanced surface energetics. Simulations bear a far closer resemblance to experimental observations when surface energetics are considered. These results can be understood in the context of an effective chemical potential (μ_{pot}^*). Sub-surface charge pairs nucleate across one, sub-surface wire, leading to $\mu_{pot}^* = 1.18$. Whereas the enhanced energy barrier for the reversal of a surface wire, originating from the broken lattice symmetry at the upper boundary, yields an

enhanced effective chemical potential upon the surface. This is calculated to be within the range of $\mu_{pot}^* = 2.50 - 4.39$, where the exact value depends upon the method that is used to define the surface energetics factor. It is therefore determined that the broken lattice symmetry induces an enhanced μ_{pot}^* at the surface which is responsible for the striking differences in monopole dynamics observed on different sub-lattices.

Chapter 1

Background Theory

‘Any fool can know. The point is to understand.’

ALBERT EINSTEIN

This chapter presents a summary of significant concepts and fundamental theory, required to provide context for the research conducted herein. Particular attention is given to the origin of ferromagnetism, two-dimensional (2D) ferromagnetic nanowires, frustrated materials, and the phenomenon of two-photon polymerisation (TPP). Relevant literature is also discussed, concerning domain wall (DW) pinning within 2D nanowires, and past examples of artificial spin-ice systems, providing a brief background for the current state of each of these fields.

1.1 MAGNETIC MOMENTS - DIPOLES AND CURRENT LOOPS

To begin to comprehend the origin and consequences of magnetism, we must first consider the most fundamental quantity within magnetic materials. This is the magnetic moment, which exists on an atomic scale within all magnetic materials. It is the response of these moments to an external magnetic field, and the manner of coupling between nearby neighbours that ultimately determines much of the bulk magnetic characteristics. Two models can be used for the basic understanding of these moments, a magnetic dipole and a one turn current loop, which are

mathematically seen to have equivalent ramifications.

1.1.1 MAGNETIC DIPOLES

Firstly, we examine the magnetic dipole model, which shows a strong analogy with the field of electrostatics. Here, a magnetic moment (\mathbf{m}) is imagined to consist of two poles, possessing equal yet opposite pole strength, $+p$ and $-p$, as seen in fig. 1.1.

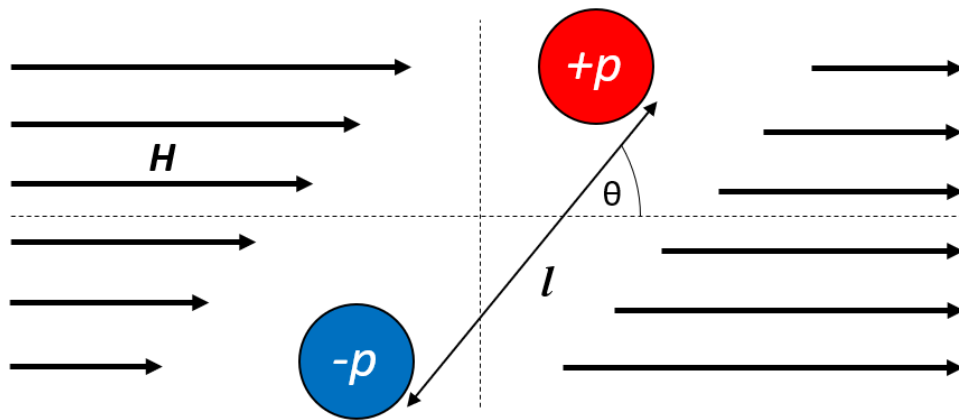


Figure 1.1: A magnetic dipole consisting of two poles, separated by a fixed distance, in an external magnetic field \mathbf{H} at an angle θ to the dipole axis. Adapted from¹.

For this dipole model, the magnetic moment is dependent on the pole strength and the separation between poles (l), this has a magnitude of¹

$$|\mathbf{m}| = pl \quad (1.1)$$

where pole strength has units $[Am]$, and hence magnetic moment has $[Am^2]$. Upon interacting with an external magnetic field (\mathbf{H}), a torque (τ) is experienced by the dipole moment. If sufficient in magnitude, this torque induces a rotation in the dipole axis towards the applied field direction, where¹

$$\tau = \mu_0 m H \sin\theta \quad (1.2)$$

where μ_0 is the permeability of free space. Equation (1.2) can also be written as

$$\boldsymbol{\tau} = \mu_0 \mathbf{m} \otimes \mathbf{H} = \mathbf{m} \otimes \mathbf{B} \quad (1.3)$$

where \mathbf{B} denotes magnetic induction with units of Tesla, which describes the response of a medium to a magnetic field, given by

$$\mathbf{B} = \mu_0(\mathbf{H} + \mathbf{M}) \quad (1.4)$$

here, \mathbf{M} is the material magnetisation. In order for this dipole rotation to occur, work (W) must be done upon the dipole moment by the external field

$$W = \mu_0 m H \int_0^\theta \sin\theta d\theta = -mH \cos\theta. \quad (1.5)$$

Prior to this taking place, the energy associated with rotating the moment is stored as potential energy, this introduces our first energy term known as Zeeman energy (E_{zee})¹. Rewriting eq. (1.5), Zeeman energy can be determined using

$$E_{zee} = -\mu_0 \mathbf{m} \cdot \mathbf{H} = -\mathbf{m} \cdot \mathbf{B}. \quad (1.6)$$

E_{zee} , is found to be at a minimum in the case of the moment aligning with the external field ($\theta = 0^\circ$) as $E_{zee} = -mB$. Conversely, E_{zee} is maximised when the moment and external field orientate antiparallel ($\theta = 180^\circ$) to one another ($E_{zee} = mB$), whilst the intermediate state ($0^\circ < \theta < 180^\circ$) yields $E_{zee} = -mB \cos\theta$.

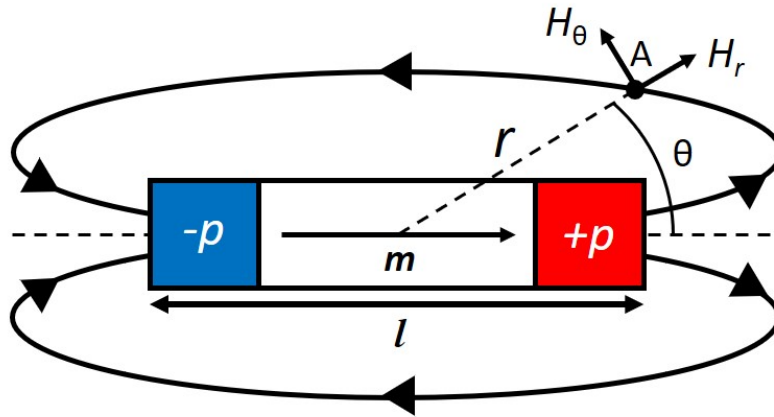


Figure 1.2: Magnetic field lines associated with a magnetic dipole moment, \mathbf{m} , of length, l . Orthogonal components H_r and H_θ of the dipole field are indicated for an arbitrary position, A , at a distance, r , where $r \gg l$. Adapted from¹

In magnetic dipoles, the moment orientates from -p to +p, as seen in fig. 1.2, therefore determining the direction of the associated magnetic stray field lines. Considering the stray field at an arbitrary position A, which is produced by a magnetic dipole moment, this can be resolved into components $H_r = 2mr^{-3}\cos\theta$ and $H_\theta = mr^{-3}\sin\theta$. Combining these components yields a resultant magnitude of

$$H = \frac{m}{4\pi r^3}(3\cos^2\theta + 1)^{\frac{1}{2}} \quad (1.7)$$

which can be used to build up a field distribution of $\mathbf{H}(\mathbf{r}, \theta)$ by allowing this resultant H to vary across all physical values of r and θ .

1.1.2 CURRENT LOOPS

Dipoles consisting of two magnetic poles with equal but opposite pole strength (fig. 1.1) help introduce the concept of a magnetic moment, and offer an insightful analogy to electrostatics. However a model with much greater similarities to reality is that of the single-turn current loop (see fig. 1.3).

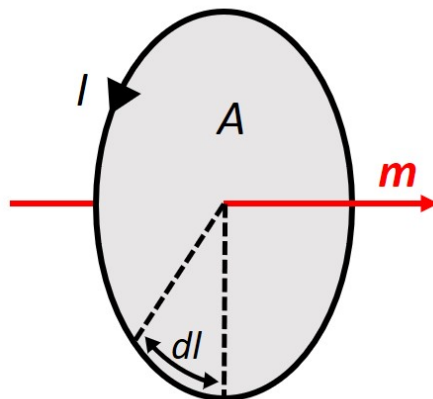


Figure 1.3: A circular, one-turn current loop, with a magnetic moment, \mathbf{m} , generated perpendicular to the current flow.

Here, a magnetic field is generated due to a current (I) circulating about an enclosed area A . This field is defined as the magnetic moment, equivalent to that which was described within a magnetic dipole, given by¹

$$|\mathbf{m}| = IA \quad (1.8)$$

this moment acts perpendicular to the charge motion and possesses an orientation described by the right hand rule. To demonstrate the equivalence of

a dipole and current loop, consider the region dl upon a current loop under the influence of an external field (fig. 1.4).

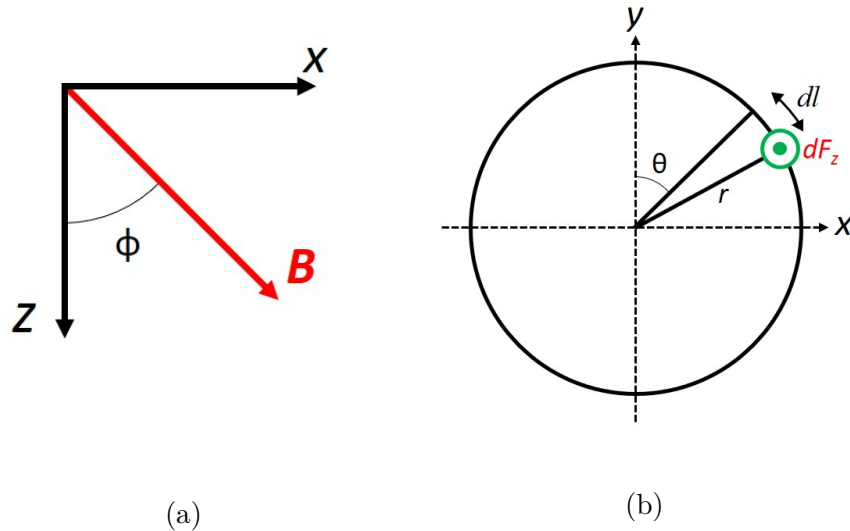


Figure 1.4: A single-turn current loop under an applied magnetic field. **a**, Geometry of applied field in x-z plane. **b**, Current loop of radius, r , extending along the x-y plane. A length, dl , is indicated, this experiences a Lorentz force, dF_z acting along the z-axis.

Electrons within the segment $dl = r d\theta$ experience a Lorentz force dF_z , leading to a torque $d\tau_y$, where¹

$$\tau_y = \mu_0 I r^2 H \int_0^{2\pi} \sin^2 \theta \sin \phi d\theta = \mu_0 I A H \sin \phi \quad (1.9)$$

substituting in eq. (1.8) and $\mathbf{B} = \mu_0 \mathbf{H}$, leads to the general form

$$\boldsymbol{\tau} = \mathbf{m} \otimes \mathbf{B} \quad (1.10)$$

which is identical to the result achieved in eq. (1.3) for a magnetic dipole moment, showing the two definitions of a magnetic moment to be equivalent. Next, we shall postulate that the circulating current portrayed in fig. 1.3 and 1.4 resembles a classical picture of orbiting electrons within individual atoms, meaning that all atoms possess a magnetic moment as a result of this orbiting charge.

Finally, we recall eq. (1.7), rewritten for the field with components parallel to \mathbf{m} and \mathbf{r} as¹

$$\mathbf{H}(\mathbf{m}, \mathbf{r}) = \frac{1}{4\pi} \left(3 \frac{(\mathbf{m} \cdot \mathbf{r})\mathbf{r}}{r^5} - \frac{\mathbf{m}}{r^3} \right) \quad (1.11)$$

this can be combined with eq. (1.6), to deduce the dipolar interaction energy (u_{ij}) between two magnetic moments \mathbf{m}_i and \mathbf{m}_j which have separation defined by \mathbf{r}_{ij} .

$$u_{ij}(\mathbf{m}_i, \mathbf{m}_j, \mathbf{r}_{ij}) = \frac{\mu_0}{4\pi} \left(\frac{\mathbf{m}_i \cdot \mathbf{m}_j}{r_{ij}^3} - 3 \frac{(\mathbf{m}_i \cdot \mathbf{r}_{ij})(\mathbf{m}_j \cdot \mathbf{r}_{ij})}{r_{ij}^5} \right). \quad (1.12)$$

A common approximation within the nanomagnetism and spin-ice communities is to model a complex, many-body system as a network of magnetic dipoles^{2,3,4}. This is known as a dipolar framework, whereby Ising-like magnetic nanowires can each be modeled as an individual dipole which interacts with neighbouring dipoles in a manner governed by eq. (1.12). When modeling each nanowire as a dipole, the finer micromagnetic detail of the system is not considered, however this approximation greatly simplifies calculations and simulations which allows extended systems to be evaluated.

1.2 THE ATOMIC MAGNETIC MOMENT

Here we shall introduce aspects of quantum mechanics to further discuss the origin of an atomic magnetic moment. Following on from section 1.1.2, we note that the magnetic moment generated by an atom is predominantly due to the atomic angular momentum. This has two primary components, the angular momentum associated with the electron orbit, and an intrinsic angular momentum known as electron spin. Beginning with the simplest possible scenario, the Bohr model⁵, we consider a classical picture of a single electron orbiting a proton (fig. 1.5).

Recalling eq. (1.8), we substitute $A = \pi r^2$ and define current as being the electron charge (e) divided by the orbit period, to derive the expression⁵

$$|\mathbf{m}_L| = -\frac{e\omega_e}{2\pi r} \pi r^2 = -\frac{1}{2} e\omega_e r \quad (1.13)$$

where m_L is the moment attributed to orbital angular momentum (L) and ω_e is the electron angular velocity. L can be related to the moment by introducing $L = m_e \omega_e r$ to eq. (1.13), yielding

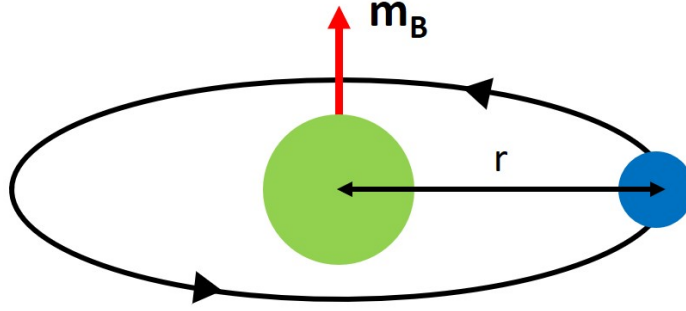


Figure 1.5: An electron (blue) orbiting a proton (green), producing a magnetic moment (m_B).

$$\mathbf{m}_L = -\frac{e}{2m_e}\mathbf{L} = \gamma_L\mathbf{L} \quad (1.14)$$

where $\gamma_L = -e/(2m_e)$ is the gyromagnetic ratio for \mathbf{L} , and m_e is the electron mass. For this elementary example of a single electron, the atomic moment is often referred to as the Bohr magneton (m_B). As further electrons are added to the atom, they methodically fill into sub-groups, known as electron shells. Additionally, quantum mechanics dictates that one cannot resolve the electron momentum and position with absolute precision (Heisenberg uncertainty principle⁵), so electrons can be considered as clouds of charge density which have a unique structure in each shell (see fig. 1.6).

Here we see the individual orbitals which comprise the first 3 electron shells, where orbitals within a particular shell are found to be degenerate. Each electron can be described using a set of quantum numbers, to be introduced throughout this section. The first of these is the principal quantum number (n_q), this allocates a unique index for every electron shell. Each orbital can hold a total of 2 electrons, resulting in a maximum occupancy of 2, 6, and 10 electrons in the s, p and d shells respectively. This discrete set of orbitals leads to a quantisation in the angular momentum with only distinct values of \mathbf{L} permitted, moreover the component of \mathbf{L} along any given direction (eg. along the z-axis) is also quantised⁵.

$$\begin{aligned} |\mathbf{L}|^2 &= \hbar^2 l_q(l_q + 1) \\ L_z &= \hbar m_l \end{aligned} \quad (1.15)$$

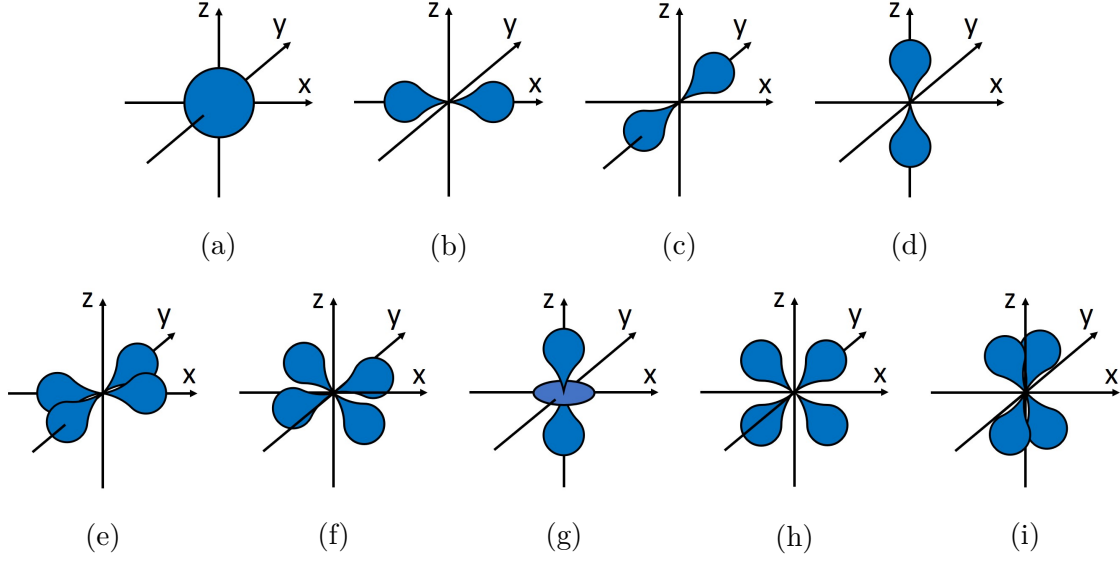


Figure 1.6: Illustrations of the electron orbitals within the **a**, s shell, $n_q = 1$. **b - d**, p shell, $n_q = 2$. **e - i**, d shell, $n_q = 3$. Adapted from¹.

where \hbar is the reduced Planck constant, l_q is the orbital angular momentum quantum number, and m_l is the spatial quantisation number. Both l_q and m_l take integer values depending on the number of orbitals within an electron shell, where $m_l = -l_q, -(l_q + 1), \dots, +(l_q - 1), +l_q$, and $l_q = 0, 1$, and 2 for the s, p and d orbitals respectively. For each shell, the number of possible orientations is therefore given by⁵

$$Degeneracy = 2l_q + 1 \quad (1.16)$$

using eq. (1.15), we can rewrite eq. (1.14) to give the quantised magnetic moment

$$\begin{aligned} |\mathbf{m}_L| &= \gamma_L \hbar \sqrt{l_q(l_q + 1)} = m_B \sqrt{l_q(l_q + 1)} \\ m_L|_z &= \gamma_L \hbar m_l = -m_B m_l. \end{aligned} \quad (1.17)$$

Experimental studies of the Zeeman effect confirm this quantisation of L by observing the energy levels of electron in the absence and presence of an external magnetic field. The Zeeman effect describes the splitting of energy levels, due to a magnetic field, where electrons in the p-shell ($l_q = 1, m_l = -1, 0, +1$) are degenerate in zero field, but split into energy levels of $-m_B B, 0$, and $+m_B B$ in a field, due to eq. (1.6)⁵. These defined energy peaks directly contradict the classical idea of a well defined particle in a circular orbit, for which a broad distribution of

energy with a single peak would be expected upon the application of a magnetic field.

Whilst the above description of atomic angular momentum is sufficient for atoms which contain 2 electrons in every orbital, a further contribution known as electron spin is found in atoms with unpaired electrons, such as silver, where the 5s shell has only one electron. To test this, an experiment was proposed by Otto Stern and performed by Walter Gerlach in the early 1920s¹, in which silver atoms were propelled through a magnetic field gradient, causing a deflection in the atomic path. Two distinct lines were observed in the spatial distribution rather than a single wide peak, as would be expected classically. Since the unpaired electrons are in the s-shell where $l_q = 0$, this splitting is not a result of the orbital angular momentum, instead it is due to spin, a component of the angular momentum that is intrinsic to the electron. This constituent of the atomic angular momentum is expected to show strong analogy with L, and so the electron spin (\mathbf{S}) is described by⁵

$$\begin{aligned} |\mathbf{S}|^2 &= \hbar^2 s_q(s_q + 1) \\ S_z &= \hbar m_s \end{aligned} \tag{1.18}$$

where s_q and m_s are the spin quantum numbers, similar to l_q and m_l . As Gerlach observed two peaks in the silver atom spatial distribution, a two-fold degeneracy is indicated, therefore recalling eq. (1.16) and rearranging for the quantum number (s_q in this case) we find $s_q = 1/2$ and, $m_s = \pm 1/2$. The positive and negative electron spin states are often referred to as spin-up or spin-down respectively. Just as was the case in eq. (1.17), electron spin is seen to have an associated magnetic moment (m_S). Continuing the analogy with orbital angular momentum, and recalling eq. (1.14), it can be expected that

$$\mathbf{m}_S \propto -\frac{e}{2m_e} \mathbf{S} = -g_s \frac{e}{2m_e} \mathbf{S} \tag{1.19}$$

where the constant of proportionality, g_s , is known as the g-factor for spin angular momentum. Experimental studies have demonstrated that $g_s \approx 2$, and the equivalent orbital angular momentum g-factor, $g_l \approx 1$ ¹. Combining eq. (1.18) and eq. (1.19) yields the magnitude of the spin magnetic moment

$$\begin{aligned}
|\mathbf{m}_S| &= g_s \frac{e}{2m_e} \hbar \sqrt{s_q(s_q + 1)} = 2m_B \sqrt{s_q(s_q + 1)} \\
m_S|_z &= m_s g_s \frac{e}{2m_e} \hbar = m_s g_s m_B = \pm m_B.
\end{aligned}
\tag{1.20}$$

It should be noted that the nucleus also exhibits an intrinsic angular momentum, however this is very small in comparison with \mathbf{L} and \mathbf{S} , so is often disregarded.

1.2.1 SPIN-ORBIT INTERACTION

Now that the electron orbit and spin have been shown to be components of the atomic magnetic moment, we consider how these parameters couple together, producing an effective electron angular momentum (\mathbf{J})¹.

$$\mathbf{J} = \mathbf{L} + \mathbf{S}.
\tag{1.21}$$

To explain this interaction, we use the Bohr model once again, however here the electron rest frame is considered. In this frame of reference, the electron is stationary and the proton has an orbital motion. Here the circulating positive charge induces a magnetic field acting upon the electron, and since the electron has no orbital motion in this frame, the field only acts upon \mathbf{S} .

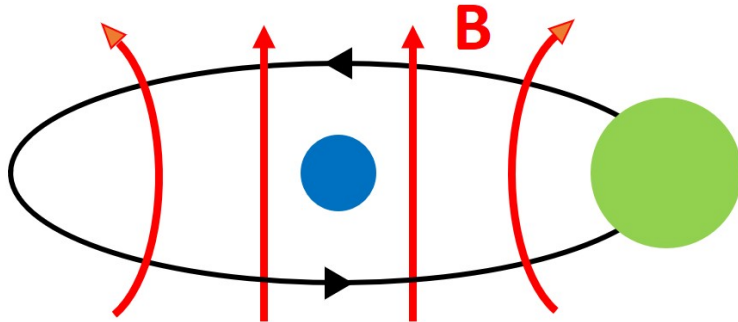


Figure 1.7: Classical picture of the Bohr model, shown from the electron (blue) rest frame, the orbiting proton (green) generates a field with magnetic induction \mathbf{B} .

Whilst simple in principle, this interaction has profound repercussions for the behaviour of magnetic materials, particularly with regard to magnetocrystalline

anisotropy, as discussed in section 1.4.3. Thus far we have only discussed the characteristics of individual magnetic moments, next we move to examine the macroscopic world of magnetic materials.

1.3 DIAMAGNETISM AND PARAMAGNETISM

Magnetic materials exist in distinct groups, dependant upon the response to an external magnetic field. Whilst only ferromagnetic materials are considered herein, first we will briefly review the areas of diamagnetism and paramagnetism to provide context. Materials are often classified by magnetic susceptibility (χ), which is the ratio of material magnetisation to the applied field

$$\chi = \frac{\mathbf{M}}{\mathbf{H}} \quad (1.22)$$

where \mathbf{M} is defined as the total magnetic moment per unit volume. Equation (1.22) only applies if \mathbf{M} and \mathbf{H} are parallel with one another. To give context for this classification of materials, typical values of χ , measured from a range of materials are given in table 1.2.

Material	Typical Susceptibility Range
Diamagnet	$-10^{-5} \leq \chi < 0$
Paramagnet	$10^{-5} < \chi \leq 10^{-3}$
Ferromagnet	$10 \leq \chi \leq 10^4$

Table 1.1: Typical χ values for diamagnetic, paramagnetic and ferromagnetic materials¹.

1.3.1 DIAMAGNETISM

Diamagnetic materials exhibit the weakest response to an applied field of any materials considered herein. All atoms display diamagnetic behaviour, however this effect is orders of magnitude weaker than the response of paramagnetic and ferromagnetic atoms, so is often considered to be negligible in these materials. The weak response of diamagnetism is due to the lack of an effective atomic magnetic moment, because atoms within diamagnetic materials only possess electron shells that are entirely filled. Under the application of an external field, electron orbits precess about

the field direction such that they oppose the applied field, producing a small, negative susceptibility¹.

1.3.2 PARAMAGNETISM

Paramagnetic atoms do exhibit an effective magnetic moment, due to these atoms possessing shells with unpaired electrons. However, neighbouring atoms have negligible interactions, and so prior to the application of an external field, the orientation of each individual magnetic moment is effectively random, leading to a net zero magnetisation across the sample. Once a magnetic field is applied, atomic moments begin to align parallel to this direction, with more moments rotating to lie along the field direction as the magnitude is increased¹. Eventually the saturation magnetisation (M_S) is reached when the field strength is great enough such that every atomic moment has orientated parallel to the field direction.

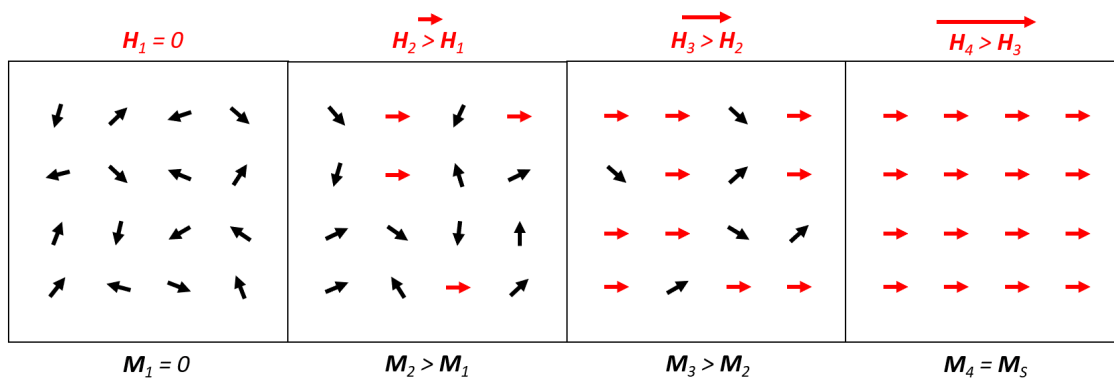


Figure 1.8: Illustration of atomic magnetic moments, in a paramagnetic material. M increases as more atomic moments rotate to align parallel with H , due to the increasing field magnitude.

1.4 FERROMAGNETISM

Ferromagnetism shares a number of common features with paramagnetism. For instance, all atoms within both materials elicit a net magnetic moment, samples may also have a net zero magnetisation prior to applying an external field, tending towards $M = M_S$ under increasing H . However, table 1.2 shows that ferromagnetic bodies exhibit χ values several orders of magnitude greater than that of paramagnetic, leading to a vast spectrum of practical applications, not accessible

to other classes of magnetic material. A key characteristic of most ferromagnetic bodies is that after an applied field is removed, the body remains at least partially magnetised in the field direction. Whereas the paramagnetic material in fig. 1.8 would simply relax back into an equivalent $M = 0$ state, upon removal of the external saturating field. Harnessing this property of ferromagnets for technological applications revolutionised the data storage industry. To understand the origins of ferromagnetism, three main energy terms must be considered, all of which play a crucial role in determining a material's spin texture. These are the exchange energy (ε_{ex}), magnetostatic energy (ε_{ms}) and magnetocrystalline anisotropy energy (ε_{mc}), each of which shall be discussed next.

1.4.1 DIRECT EXCHANGE INTERACTION

Firstly we consider the strong, short range Heisenberg exchange interaction, which is largely responsible for the great disparity in χ values of ferromagnetic and paramagnetic materials. Exchange is a key factor for the remanent magnetisation exhibited after the removal of an external field, because this interaction favours a parallel alignment of neighbouring spins in ferromagnets¹. A common example to introduce this concept is a two electron system which consists of two hydrogen atoms forming a covalent bond. In this system, two distinct states can be defined with regard to the electron spin. Firstly, the two spins can orientate antiparallel with one another, referred to as the ground or singlet state¹ with energy ε_S . Secondly, the spins can align parallel, referred to as an excited or triplet state¹ with energy ε_T . It is the energy difference between these two states which defines the exchange energy

$$\varepsilon_T - \varepsilon_S = -\varepsilon_{ex} \quad (1.23)$$

hence, if $\varepsilon_{ex} > 0$ then the triplet state is the energy minimum and so a parallel alignment is preferred, as is the case for ferromagnetic materials. An expression for the total ε_{ex} across a body of many atoms can simply be written as the sum of ε_{ex} between all atomic pairs within the body¹.

$$\varepsilon_{ex} = -2 \sum_{i,j} J_{ij} \mathbf{S}_i \cdot \mathbf{S}_j \quad (1.24)$$

where J_{ij} is the exchange integral for neighbouring spins i and j , and \mathbf{S} is the associated spin vector. The exchange integral is of great importance in determining whether ferromagnetic or antiferromagnetic behaviour shall be displayed. J_{ij} is a

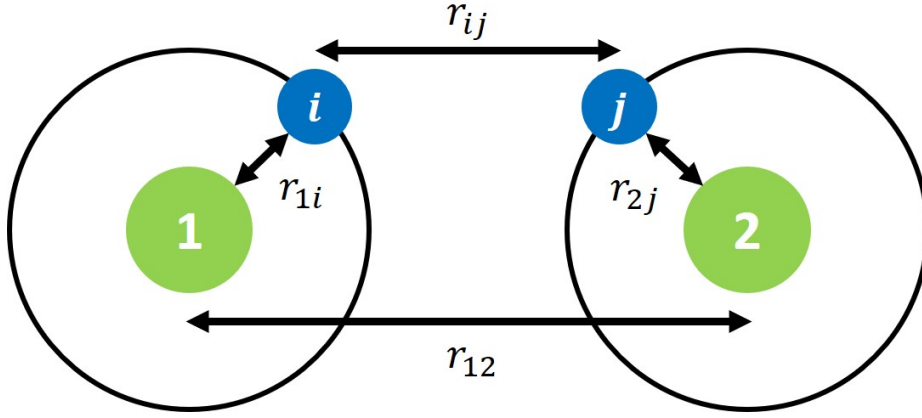


Figure 1.9: Illustration of two hydrogen atoms (1 and 2) which each possess one electron (i and j).

function of the interatomic separation and the d-orbital radius, the ratio of which determines the magnitude and sign of the exchange interaction, this is given by¹

$$J_{ij} = \int \int \Psi_1^*(r_i) \Psi_2^*(r_j) \left[\frac{1}{r_{12}} - \frac{1}{r_{1i}} - \frac{1}{r_{2j}} - \frac{1}{r_{ij}} \right] \Psi_1(r_i) \Psi_2(r_j) dv \quad (1.25)$$

where the wavefunctions and complex conjugates of atoms 1 and 2 are given by Ψ_1, Ψ_2, Ψ_1^* , and Ψ_2^* respectively, each distance parameter is defined in fig. 1.9. Using eq. (1.25), Bethe and Slater¹ demonstrated that $J_{ij} > 0$ (leading to ferromagnetic behaviour) for small r_{12} and r_{ij} , as well as for larger r_{1i} and r_{2j} . Recalling that the direct exchange interaction is typically short range, it shall now be assumed that this only occurs between nearest neighbours (nn), all of which are equal ($J_{ij} = J$), and all spins are uniform ($|\mathbf{S}_i| = S$). Hence, eq. (1.24) can be modified to

$$\varepsilon_{ex} = -2JS^2 \sum_{nn} \cos\theta_{ij} \quad (1.26)$$

where the angle between neighbouring spins is denoted by θ_{ij} . For the likely scenario that $\theta_{ij} \ll 1$, the total exchange energy can be written as

$$\varepsilon_{ex} = JS^2 \sum_{nn} \theta_{ij}^2 \quad (1.27)$$

dividing this expression by the unit cell volume (a^3), yields the exchange energy density (E_{ex}). In order to account for the material crystal structure, we must next consider the directions of the neighbouring magnetic moments \mathbf{m}_i and \mathbf{m}_j , which have

direction cosines $\alpha_1, \alpha_2, \alpha_3$. θ_{ij} can be generalised as $|\theta_{ij}| \approx |\mathbf{m}_j - \mathbf{m}_i| = (\mathbf{r}_{ij} \cdot \nabla)\mathbf{m}$. Summations can then be performed over all nearest neighbour vectors, across all lattice points, to result in

$$E_{ex} = A_{ex}[(\nabla\alpha_1)^2 + (\nabla\alpha_2)^2 + (\nabla\alpha_3)^2] \quad (1.28)$$

where the exchange stiffness (A_{ex}) is a function of J, a, S and a constant C , the exact value of which is dependant upon the crystal structure (*bcc, fcc, hcp, etc.*).

$$A_{ex} = \frac{JS^2}{a}C. \quad (1.29)$$

The exchange interaction attempts to prevent any variation in orientation between adjacent moments. E_{ex} is therefore minimised when a ferromagnetic body is fully magnetised, in which all moments are aligned parallel to the same axis.

1.4.2 MAGNETOSTATIC ENERGY

This energy term is often referred to as either the dipolar or magnetostatic energy density (E_{ms}). It is the result of the mutual Zeeman energy generated by all moments within a magnetic body through the stray field. E_{ms} is therefore minimised in bodies possessing flux-closure⁵.

When a body does not exhibit flux-closure, a divergence of \mathbf{M} occurs where the magnetisation meets the boundaries. Applying Maxwell's second equation for the divergence of \mathbf{B} , and coupling this with eq. (1.4) yields⁵

$$\nabla \cdot \mathbf{H}_d = -\nabla \cdot \mathbf{M} \quad (1.30)$$

demonstrating that this divergence of \mathbf{M} gives rise to a demagnetising field (\mathbf{H}_d) which opposes the magnetisation, as illustrated in fig. 1.10.

This demagnetising field is highly dependent on the number and separation of these magnetic poles, and hence depends heavily on the sample geometry. For example, if the magnetisation in fig. 1.10 aligned along the short-axis, the separation between positive and negative poles would be significantly reduced. Also, the magnetisation would intersect a far larger area at the boundaries, leading to the production of many more poles. This higher energy scenario would result in a far stronger \mathbf{H}_d , meaning that typically the magnetisation would preferentially align to the long-axis, also known as the easy-axis. Therefore, \mathbf{H}_d is the origin of the first

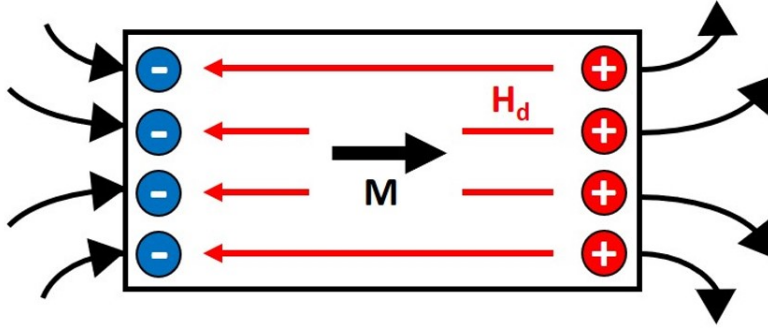


Figure 1.10: Schematic of a ferromagnetic body, with all moments aligned along the long-axis. Magnetic poles form at either end of the long-axis where the sample magnetisation encounters a boundary, a demagnetising field is generated which opposes the magnetisation. At these boundaries, stray magnetic fields emanate from the body.

anisotropy term considered herein, shape anisotropy. In essence, anisotropy results in the existence of preferential axes for the sample magnetisation to align with. In magnitude, H_d increases proportionally with increasing M , hence

$$H_d \propto -M \quad (1.31)$$

however, here the constant of proportionality strongly depends on the sample geometry. Therefore, to write a generalised expression for H_d we include a demagnetising tensor (\mathcal{N})

$$H_d = -\mathcal{N}M. \quad (1.32)$$

\mathcal{N} describes the component of flux density that is perpendicular to the surface of a body, where the components \mathcal{N}_x , \mathcal{N}_y , and \mathcal{N}_z summate to 1. Hence, an infinite sheet would possess $\mathcal{N} = 0$ or $\mathcal{N} = 1$ if magnetised in-plane or out-of-plane respectively⁵. Likewise, an infinitely extending cylinder would show $\mathcal{N} = 0$ and $\mathcal{N} = 0.5$, when magnetised parallel and perpendicular to the cylinder length respectively⁵. Typically, \mathcal{N} takes the form of a tensor function to describe the sample shape. A rudimentary example is an ellipsoid, as the internal field is uniform, leading to the diagonal tensor

$$\mathcal{N} = \begin{pmatrix} \mathcal{N}_x & 0 & 0 \\ 0 & \mathcal{N}_y & 0 \\ 0 & 0 & \mathcal{N}_z \end{pmatrix} \quad (1.33)$$

where the components \mathcal{N}_x , \mathcal{N}_y , and \mathcal{N}_z each describe one of three principal orthogonal axes. This demagnetising factor, and hence the sample geometry, is related to the magnetostatic energy density by

$$E_{ms} = \frac{\mu_0}{2} \mathcal{N} M_S^2. \quad (1.34)$$

For applications considered in this thesis, it is crucial that shape anisotropy is the dominant anisotropy factor in determining the sample spin texture. To further contemplate this notion, we shall next discuss another form of anisotropy that is inherent to the sample composition.

1.4.3 MAGNETOCRYSTALLINE ANISOTROPY ENERGY

The second form of anisotropy, and last energy term to be considered is magnetocrystalline anisotropy energy density (E_{mc}). E_{mc} is highly dependent upon the crystalline structure of the magnetic material, and is therefore intrinsic to the sample composition. Only $Ni_{81}Fe_{19}$ nanostructures are considered in this thesis, which are well known to exhibit negligible E_{mc} ¹, as such this energy term will only be considered briefly.

Within most ferromagnetic bodies, at least one crystallographic direction exists, where if the internal energy is minimised when the magnetisation aligns parallel to this direction, it is typically referred to as the easy axis. Conversely the internal energy is maximised if the magnetisation lies along crystalline directions known as hard axes, which is a state that often requires a great deal of energy to produce⁵. Qualitatively, the magnetocrystalline anisotropy energy is the difference in energy needed to orientate the magnetisation between the easy and hard axes. This phenomenon is associated with spin-orbit coupling, because electron orbits are connected to the crystal lattice through interactions with the crystalline electric field. These orbit-lattice interactions define preferential directions of electron orbit, which in turn influences the orientation of electron spin, and so it is these spin-orbit-lattice interactions which can place constraints upon the sample magnetisation¹.

Experimental measurements of magnetisation curves with an applied field parallel to different crystallographic directions, offer a simple means to decipher E_{mc} . As this is equal to the work done per unit volume required to raise the magnetisation of a sample to M_S ¹.

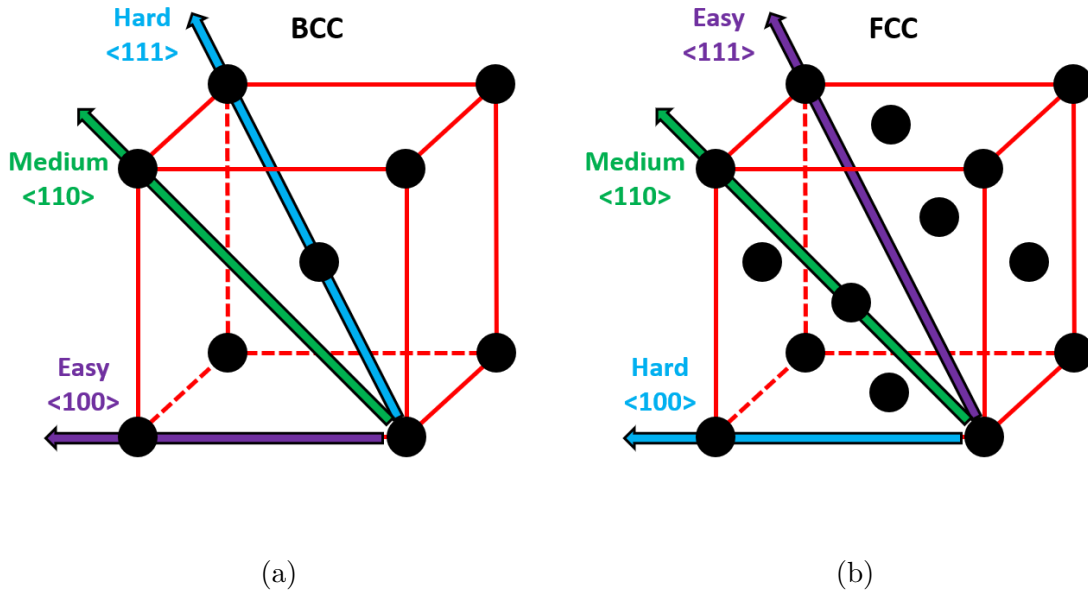


Figure 1.11: Crystal lattice unit cells denoting the easy, medium and hard crystallographic axes for **a**, Fe_{bcc} **b**, Ni_{fcc} .

$$WD = E_{mc} = \int_0^{M_S} \mu_0 \mathbf{H} \cdot d\mathbf{M}. \quad (1.35)$$

Such experimental studies have provided valuable insight into the crystallographic axes of Fe_{bcc} and Ni_{fcc} crystals, illustrated in fig. 1.11. Fe and Ni both possess cubic crystal lattices, allowing E_{mc} to be expressed as a power series, in the form

$$E_{mc} = K_0 + K_1(\alpha_1^2\alpha_2^2 + \alpha_2^2\alpha_3^2 + \alpha_3^2\alpha_1^2) + K_2(\alpha_1^2\alpha_2^2\alpha_3^2) + \dots \quad (1.36)$$

where α_n are the directional cosines of the magnetisation vector, and K_n are anisotropy coefficients, values of K tend towards zero with increasing n , so higher order coefficients can be neglected. K_0 is also often neglected as it is not dependent upon the direction of magnetisation¹.

Material	$K_1(\text{Jm}^{-3})$	$K_2(\text{Jm}^{-3})$
Fe	4.8×10^4	5.0×10^3
Ni	-4.5×10^3	-2.3×10^3

Table 1.2: Typical room temperature values for the first and second order anisotropy coefficients of Fe and Ni¹.

It is evident that K is positive in Fe, and negative in Ni, additionally the easy and hard axes of Fe lie along the $\langle 100 \rangle$ and $\langle 111 \rangle$ planes respectively, whilst the reverse is true for Ni. Experimental studies of alloys composing of Ni_xFe_{1-x} , have found that as x tends towards a critical value of 81%, the implications of magnetocrystalline anisotropy effectively vanish, as K tends towards zero. $Ni_{81}Fe_{19}$ is therefore a highly attractive material for many applications, as it provides the user with significant control over the sample spin texture, through simple consideration of shape anisotropy (discussed further in section 1.4.5).

1.4.4 TRANSITION METALS

Here we will consider the parameter which most strongly governs a material's magnetic properties, elemental composition, with emphasis placed upon the degree to which specific electron shells are filled. In particular, the 3d and 4s shells are seen to play a key role in the origin of a material's ferromagnetic behaviour. It is well documented that only Fe, Co, and Ni exhibit long-range magnetic order (i.e. behave as ferromagnets) at room temperature, which possess outer shells of $3d^64s^2$, $3d^74s^2$, and $3d^84s^2$ respectively¹. These electrons fill subsequent orbitals in accordance with Pauli's exclusion principle and Hund's rules. The former requires that no two electrons may carry an identical set of quantum numbers (l_q , m_l , s_q and m_s); in essence this means that two identical electrons cannot occupy the same quantum state simultaneously⁵.

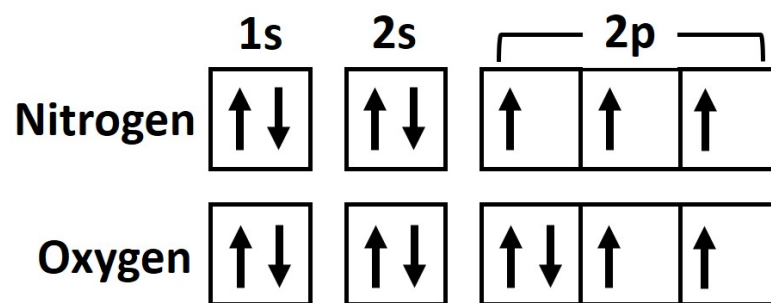


Figure 1.12: Illustration of the electron structure in nitrogen and oxygen. Each square is a quantum state or electron orbital, each arrow denotes an electron, and the orientation indicates if the electron has spin up or down.

Hund's rules⁵, dictate the order in which electrons fill their respective sub-orbitals. Figure 1.12 displays this using N and O as an example, in which O

contains one additional electron. Each square denotes a single quantum state (or electron orbital, see fig. 1.6), meaning that two electrons can only co-exist within an orbital if their spins oppose (due to Pauli's exclusion principle). However, a Coulombic repulsion also exists between the two negatively charged fermions, which increases substantially as the proximity between particles decreases. As a result, it is energetically favourable to initially fill each orbital with only one electron, in a manner which maximises the total spin (i.e. all spin-up, or all spin-down), until there are no empty sub-orbitals, as is the case for N. After this point, further electrons are added to half-filled states, such that the spins of the new electron pair oppose, as can be seen for O.

As mentioned above, the 3d and 4s shells are key to the magnetic behaviour exhibited by Fe, Co, and Ni. Whilst 4s electrons tend to be delocalised and are of less significance here in comparison with 3d electrons, the two bands have significant overlap in energy, meaning that the number of electrons in each band may not be an integer. In practice, atoms clearly do not exist independently, and when 2 atoms are in close enough proximity to produce a covalent bond, the orbitals in this bond combine to form a molecular orbital. In this new orbital, each atomic energy level splits into 2 molecular energy levels. Therefore a solid comprised of N atoms has each atomic energy level split into N levels which are so densely compacted that they may appear to be a continuous band. Here, the number of states per energy is referred to as the density of states ($g(E)$), with the definition¹

$$\int_0^{E_F} g(E)dE = n_0. \quad (1.37)$$

E_F is known as the Fermi energy, which is the energy of the highest filled levels in the system ground state, n_0 denotes the electron density, this is equal to 10 per atom in the 3d shell and 2 per atom in the 4s shell. A common approximation used when considering $g(E)$ is the rigid band model, which neglects any fine variations, and assumes that the electron bands of Fe, Co, and Ni have identical shape¹. We shall use this model to gain an insight into how the electronic configuration, and hence composition of a solid, affects its magnetic properties.

As discussed, there is substantial overlap in energy between the 3d and 4s levels, and so these will be treated together here. We shall let n equal the total number of 3d and 4s electrons, whilst setting x equal to the number of 4s electrons, hence $(n - x)$ is the number of 3d electrons. By applying Hund's rules, we can assume

that half of the 3d band (i.e. 5 sub-orbitals) is filled by spin-up electrons, to maximise the total spin, with the remaining $(n-x-5)$ electrons occupying the spin-down half of the band (see fig. 1.13a). Using this first order approximation, the magnetic moment per atom is defined by

$$m = m_B(n_\uparrow - n_\downarrow) \quad (1.38)$$

$$m = m_B(5 - (n - x - 5)) \quad (1.39)$$

$$m = m_B(10 - n + x) \quad (1.40)$$

where n_\uparrow and n_\downarrow are the number of spin-up and spin-down electrons per unit volume, respectively. Equation (1.40) can be expanded upon by considering that for Ni, $n = 10$, and experimental studies have shown it to have a moment of $0.6m_B$, and so

$$m = m_B(10.6 - n). \quad (1.41)$$

Whilst this model is relatively simplistic, it does demonstrate how the balance between Hund's rules and the Pauli exclusion principle leads to a spin-split 3d band in transition metals, which ultimately gives rise to an atomic magnetic moment that is intrinsically dependent upon the elemental composition. This model also provides reasonable estimates for the magnetic moments of Fe, Co, and Ni observed in experiments, which form part of the Slater-Pauling curve presented in fig. 1.14. The tendency towards $m = 0$ to the right-hand side of Ni is explained in fig. 1.13b,

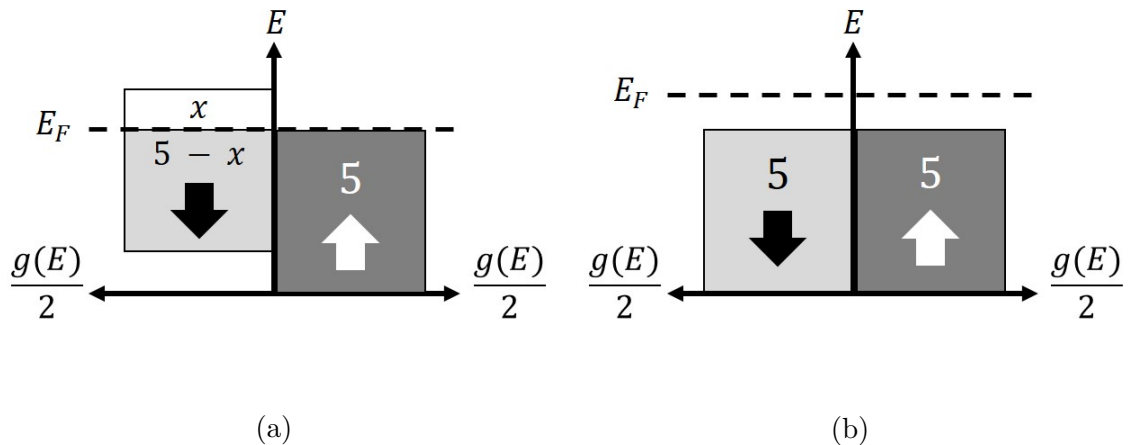


Figure 1.13: Using the rigid band approximation to visualise the electron occupancy in the up and down halves of the 3d band in **a**, Fe, Co, and Ni. **b**, Cu. Adapted from¹.

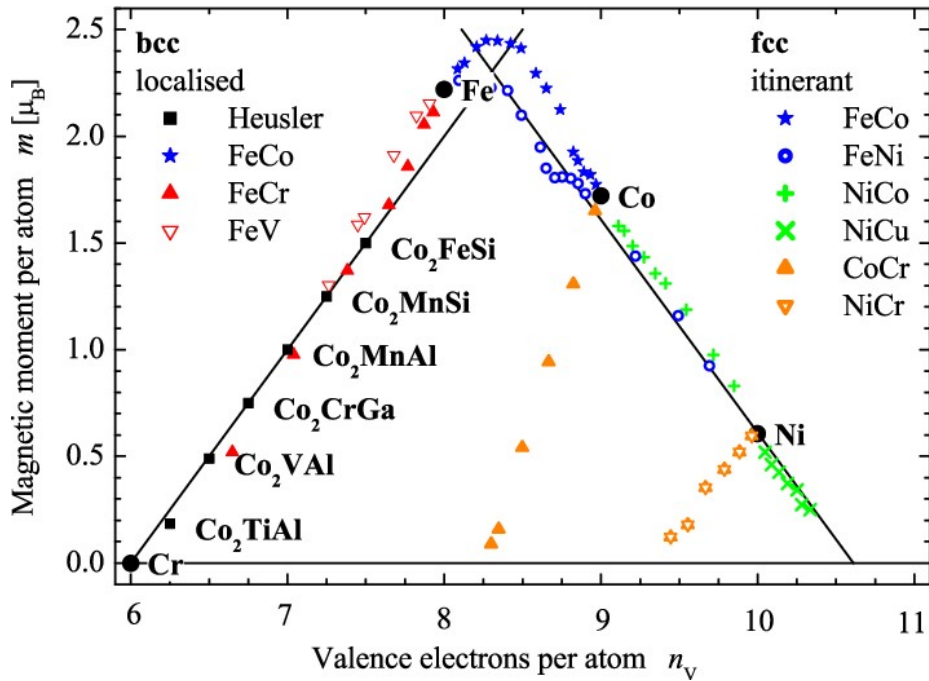


Figure 1.14: Slater-Pauling curve, showing how the elemental composition of a solid affects the atomic magnetic moment, for transition metals⁶.

where the 3d band of copper is seen to be entirely filled and so no spin-splitting can occur, resulting in copper not exhibiting any ferromagnetic behaviour.

1.4.5 DOMAINS AND DOMAIN WALLS IN BULK FERROMAGNETS

Having considered each key fundamental origin of ferromagnetism in isolation, we now examine the consequences of these interactions competing with one another in bulk ferromagnets. To reiterate, only $Ni_{81}Fe_{19}$ structures are considered in this thesis, so the effects of magnetocrystalline anisotropy are neglected. Therefore, we contemplate the competition between E_{ms} , which is minimised when the spin texture is arranged to minimise stray fields, and E_{ex} which is minimised when neighbouring spins are aligned. In order to minimise the total system energy, magnetic domains are formed to balance these components. Domains are regions in which all moments align to orientate along the same axis, domain walls (DWs) are the boundaries that separate different domains.

Figure 1.15 illustrates one possible domain configuration in a ferromagnetic body of aspect ratio 1:1. This domain pattern is the ground state, although it

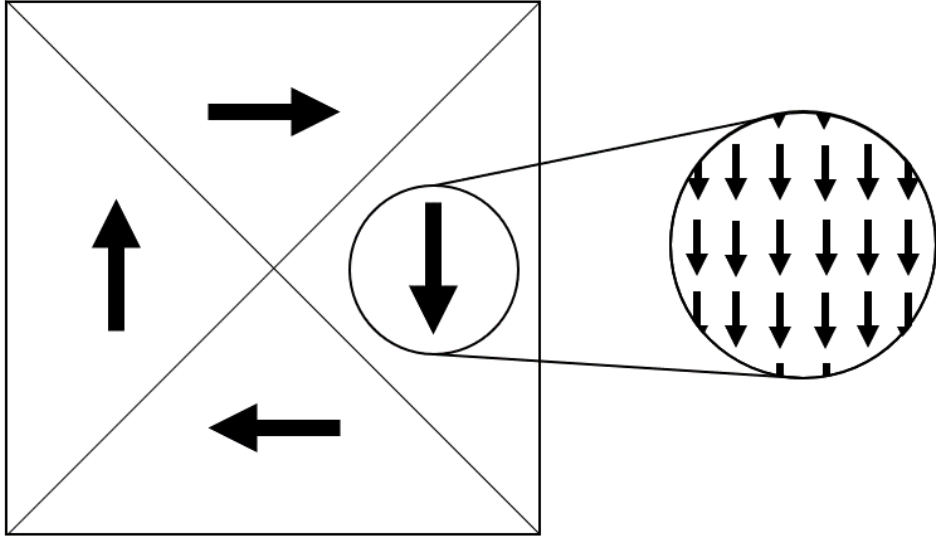


Figure 1.15: A ferromagnetic body containing four domains exhibiting flux-closure in a clockwise orientation. Individual atomic moments within the domain orientated downwards are indicated.

should be noted that an otherwise identical anti-clockwise arrangement would be energetically equivalent. It is the ground state because flux-closure is achieved using the minimum possible number of domains, as an E_{ex} cost is incurred by the formation of domains and DWs. Whilst this ground state is expected for square ferromagnets, shape anisotropy allows one to manipulate the domain structure through tuning the sample geometric parameters.

Three ferromagnets of aspect ratio 1:1, 2:1, and 4:1 are depicted in fig. 1.16a-c. Firstly, we once again see a square body, meaning that each boundary produces an equivalent \mathbf{H}_d . A low shape anisotropy allows the body to achieve flux-closure and a net zero magnetisation. For an asymmetrical aspect ratio (fig. 1.16b), the longer boundaries produce a greater \mathbf{H}_d than the short, leading to the domains preferentially aligning parallel and anti-parallel with the long axis. Here, a net zero magnetisation is still attained, however flux-closure is not. Stray fields emanate from the head of each domain, and terminate at the tail of the other, which has an associated E_{ms} cost, although the fewer number of domains gives a reduction in the E_{ex} . Increasing the aspect ratio further (fig. 1.16c) eventually generates a single domain state, where neither flux-closure nor net zero magnetisation are reached, thus maximising E_{ms} . However, the \mathbf{H}_d associated with the long boundary provides a sufficient energy barrier to prevent the formation of domain walls, thus minimising

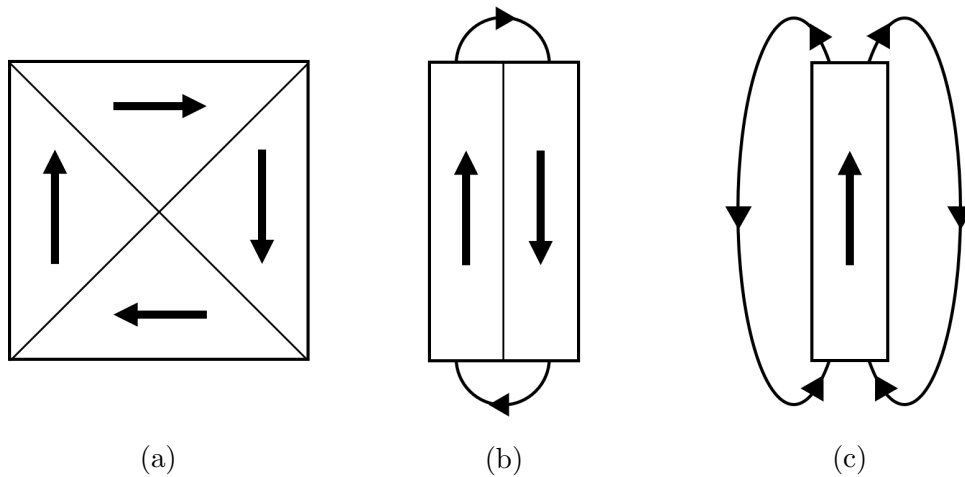


Figure 1.16: Three possible domain configurations, dependant upon the competition between E_{ex} and E_{ms} . **a**, Aspect ratio of 1:1, containing four domains exhibiting flux-closure. **b**, Aspect ratio of 2:1, containing 2 domains with stray magnetic fields extending from the head of each domain to the tail of the other. **c**, Aspect ratio of 4:1, a single domain state producing considerable stray fields.

the E_{ex} ¹.

Illustrations such as fig. 1.16 often depict DWs as sharp boundaries, abruptly transitioning between the magnetisations of the neighbouring domains. Though in reality, such a sharp transformation would be highly unfavourable for the exchange energy. Instead this rotation occurs gradually across many spins, to minimise the deviation between neighbouring moments, two possible DW configurations in thin films are presented in fig. 1.17.

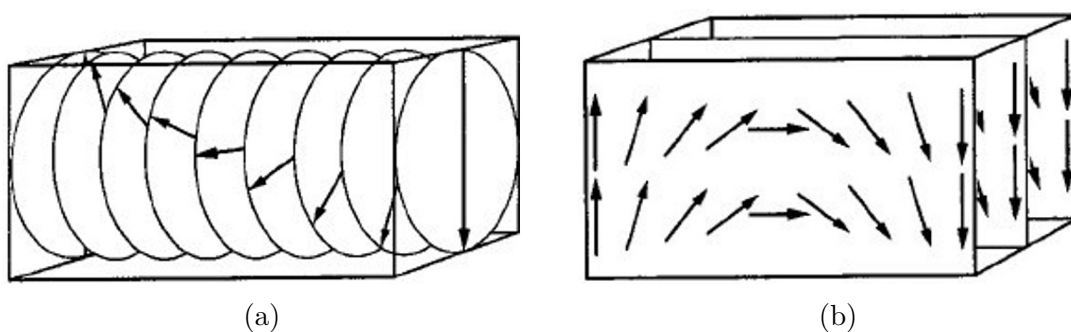


Figure 1.17: Two domain wall spin textures in bulk ferromagnets⁷. **a**, Bloch wall. **b**, Néel wall.

A Bloch wall (fig. 1.17a) mediates this 180° transformation via a gradual

out-of-plane rotation, whilst a Néel wall rotates in-plane with the axis along which the magnetisation transforms. These two DW formations are likely to exhibit comparable E_{ex} , although the differing transverse components yield opposing dependencies between the film thickness and E_{ms} . Therefore, distinct regimes exist, whereby Bloch walls are energetically favourable in thick films, and Néel walls are the preferred configuration in thin films.

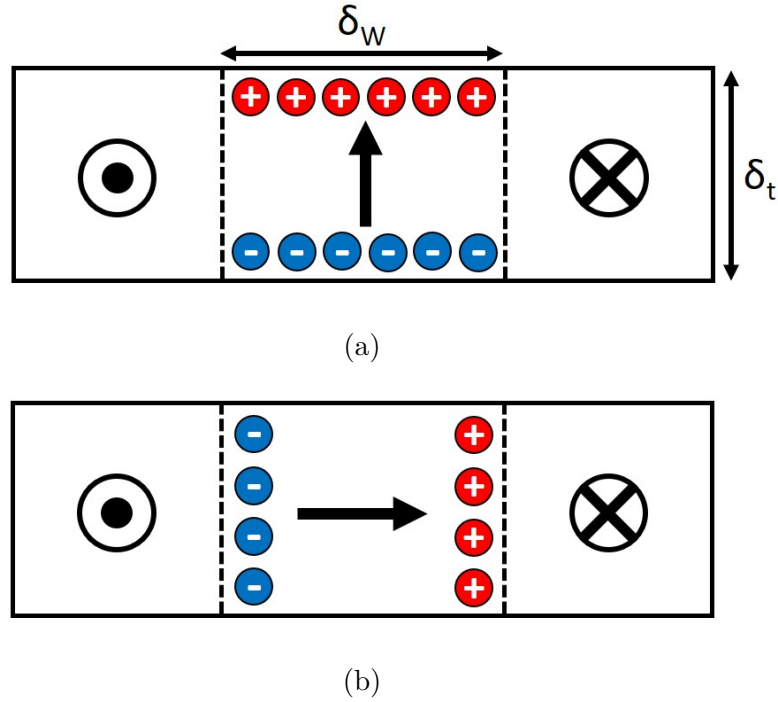


Figure 1.18: Magnetic poles generated by two types of domain wall, assuming a uniform magnetisation over the domain wall volume¹. **a**, Bloch wall. **b**, Néel wall.

To understand this geometric dependency, we consider the scenario illustrated in fig. 1.18, where DWs consist of a uniform magnetisation orientated parallel to the transverse components of Bloch walls and Néel walls respectively. Both examples produce magnetic poles on opposing boundaries due to the DW magnetisation, just as was seen in fig. 1.10. For fig. 1.18a, the number of poles remains fixed as δ_t varies, although pole separation widens with increasing δ_t . Whereas the pole separation in Néel walls is independent of δ_t , however further poles are generated at the DW boundaries as δ_t increases, thus raising E_{ms} . As a result, thinner films favour Néel walls due to the relatively large E_{ms} of Bloch walls, though in films where $\delta_t \gg \delta_W$ this E_{ms} tends towards zero, and so Bloch walls are preferred.

1.4.6 HYSTERESIS

Perhaps one of the most fundamental properties exhibited by ferromagnetic materials is hysteresis. This phenomenon dictates that the magnetic configuration of a body depends not only upon the present conditions (external fields, shape anisotropy, temperature, etc), but also upon the magnetic history of the body¹. A typical example of a hysteresis loop is presented in fig. 1.19, a commonly used method of illustrating this behaviour, which allows significant insight into the properties of magnetic materials.

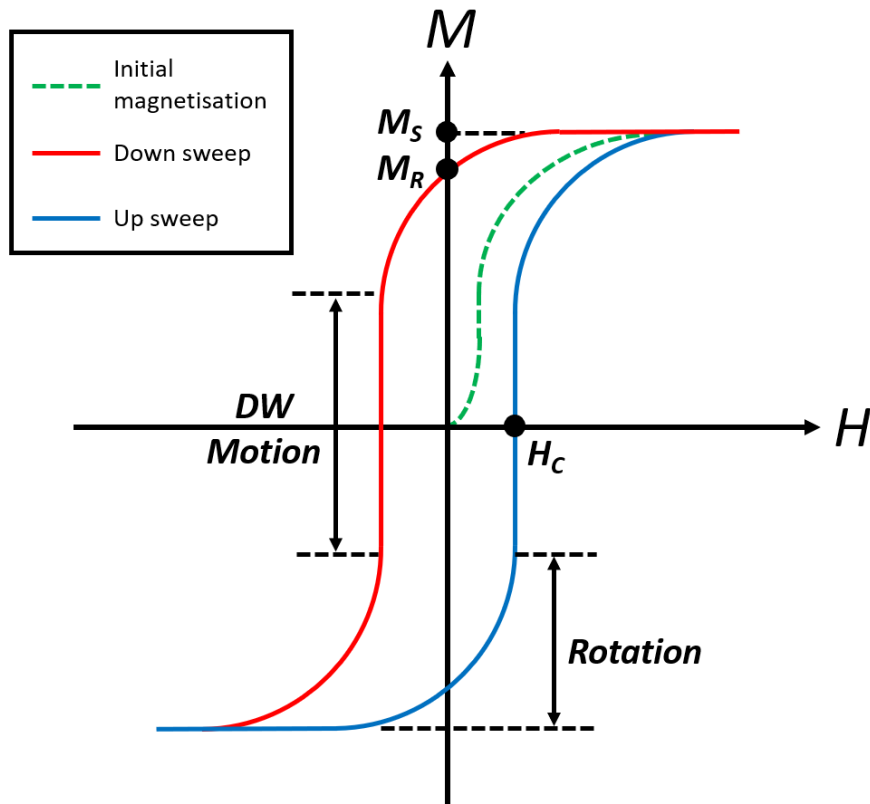


Figure 1.19: Typical example of a ferromagnetic hysteresis loop, illustrating the variation in sample magnetisation under the influence of a sweeping external magnetic field. Key features highlighted are the reversal processes of rotation and DW motion, as well as the saturation magnetisation (M_S), remanent magnetisation (M_R), and coercivity (H_C).

Prior to the body being exposed to any significant external fields, the sample magnetisation is zero, due to the internal domains forming in an arrangement which

prevents the creation of free magnetic poles, and maintains a net zero magnetisation (eg. fig. 1.15). Once an external field is applied, the internal magnetisation begins to align with the field direction until M_S is reached, as occurred in fig. 1.8, this transition is denoted by the dotted green line in fig. 1.19. A significant distinction between paramagnetic and ferromagnetic materials, is that when the external field is reduced to zero, a ferromagnet does not follow the green path back to the origin; instead it follows the red path and maintains a remanent magnetisation (M_R). It is this feature, that the magnetic configuration may not only be readily influenced but also retained upon the removal of an external field, which makes ferromagnetic materials so attractive for a wide variety of data storage applications. Now that a remanent magnetisation is present, in order to bring the sample magnetisation back to zero an opposing external field must be applied, the exact magnitude required is an intrinsic property of the sample, and is referred to as the coercive field (H_C). H_C is therefore a crucial factor in determining how readily a sample can be magnetised and demagnetised, a property which divides ferromagnetic materials into soft and hard magnets. In comparison with hard ferromagnets, soft materials typically exhibit low hysteresis and H_C , as well as high μ and χ , so are relatively easy to magnetise. Consequentially, soft ferromagnets are ideal for data storage devices, and are the only magnetic materials considered herein.

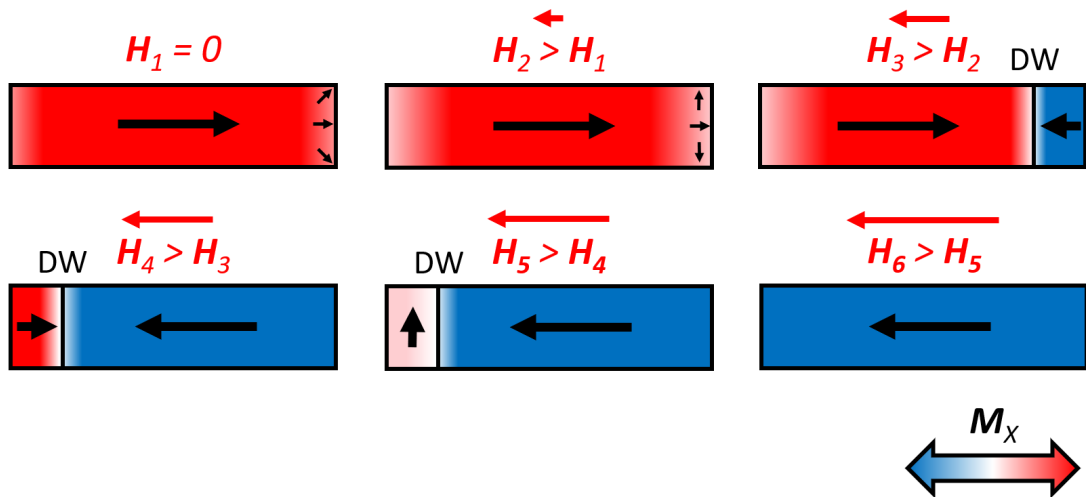


Figure 1.20: Reversal mechanism of a ferromagnetic body which has initially relaxed from positive saturation into a single domain state at $H = 0$. An external magnetic field is then applied, opposing the sample magnetisation, indicated by red arrows. Four snapshots are given during the transition from positive M_S to negative, whereby the applied field strength increases from H_1 to H_6 .

To explain the reversal mechanisms highlighted in fig. 1.19, we consider a single domain ferromagnetic body (fig. 1.20). At remanence, nearly all moments are aligned parallel to the long-axis, with only a small fraction of moments deviating due to the demagnetising field at the boundaries. At H_2 rotation has occurred, whereby moments rotate towards the direction of the applied field, this process happens gradually as the field magnitude increases, shown by the curved transition highlighted in fig. 1.19. Rotation is reversible in the sense that removing the applied field would return the body to the initial state seen at H_1 .

Once sufficient rotation takes place, an opposing domain forms and a DW is nucleated (potential DW formations are discussed in section 1.5) at H_3 . Once nucleated, a DW can move by the sequential canting of individual moments (DW motion), this process requires relatively little energy because there is minimal extra cost to E_{ex} or E_{ms} as a DW progresses along a simple wire, resulting in the sharp transition seen in fig. 1.19. As such there is typically little increase in applied field between H_3 and H_4 . Both theory and experiments have shown DW motion to be a rapid process⁸, with possible DW speeds in excess of $1\text{km}s^{-1}$.

Eventually the DW will encounter some boundary, such as a defect or the surface of the body, and DW motion can progress the wall no further. Another gradual transition (associated with rotation) ensues, causing the DW to terminate, and allowing the body to reach negative saturation.

1.5 DOMAIN WALLS IN MAGNETIC NANOWIRES

Recent decades have witnessed major advances in the ability to precisely engineer magnetic materials into devices with ever diminishing feature size. Along with these advances, new challenges have spawned which require comprehensive understanding, as even a slight alteration in the geometry, dimensions or composition of a magnetic device on the nanoscale, can drastically alter its behaviour. Unlike thin films, 2D nanowires have one dimension significantly elongated in comparison with the other two, typically referred to as the wire length. In materials of suitably low magnetocrystalline anisotropy, this elongated length leads to the shape anisotropy dominating, often resulting in only a single domain existing across the width nanowire. Depending upon the exact length and magnetic history of the wire, there may be a single domain spanning the full wire (eg. fig. 1.16c), likely to be orientated parallel to the easy/long-axis due to the high aspect ratio generating a

stronger H_d at the longer boundaries. Alternatively, a sequence of domains with alternating magnetisation may exist along the wire length, each separated by a DW.

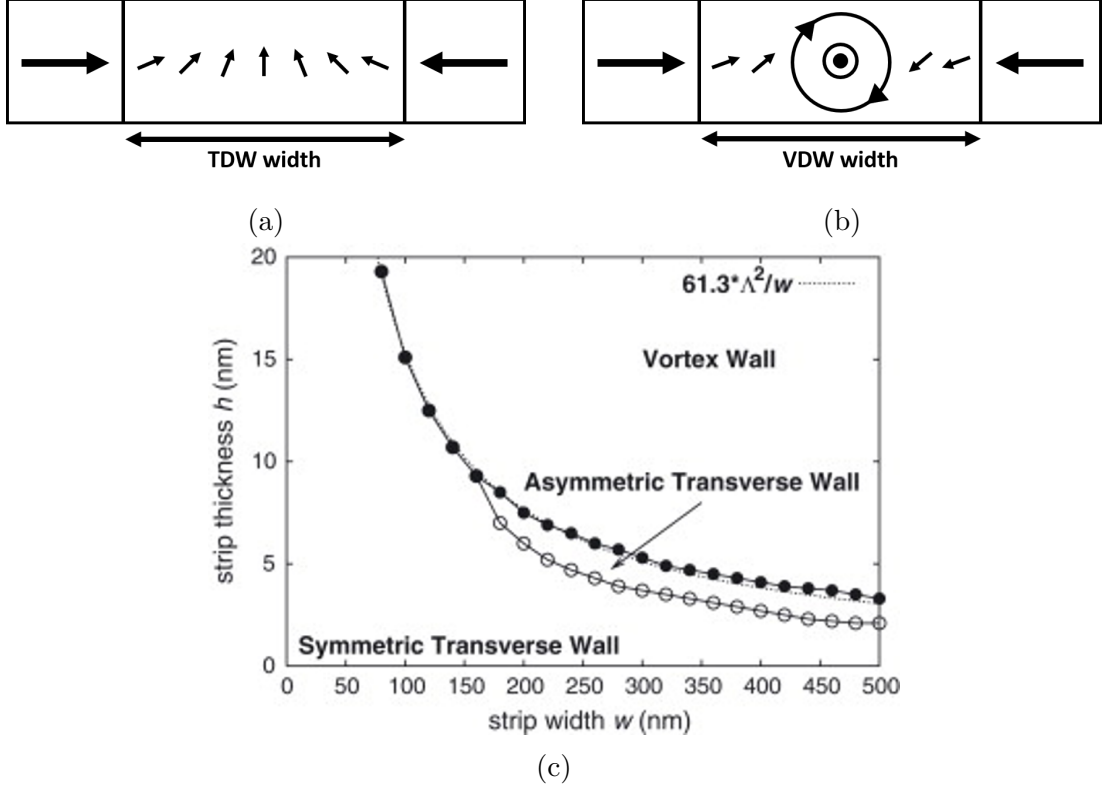


Figure 1.21: Domain walls in nanostrips. **a**, Transverse DW in the thin, narrow nanowire regime. **b**, Vortex DW in the thick, wide regime. **c**, Phase diagram of DWs in ferromagnetic nanostrips for varying width and thickness⁹.

Two main types of domain walls can typically exist in 2D nanowires¹⁰, and the dimensions of the wire play a crucial role in determining the type of domain wall which nucleates, as illustrated in fig. 1.21. Figure 1.21a displays a transverse DW, which is perhaps the most intuitive, whereby adjacent moments within the wall exhibit a slight canting, transitioning between the magnetisation in opposing domains¹. E_{ex} is favoured by this formation, since there is minimal deviation in the orientation of adjacent moments, however the transverse component of this wall leads to magnetic charges at the boundary and an associated stray magnetic field, yielding a E_{ms} cost. Transverse walls are therefore typically observed in thin, narrow wires, shown in fig. 1.21c, where the benefit of near-parallel adjacent moments, outweighs the negative of magnetic charges forming. As the wire becomes thicker and wider, further magnetic charges form at the boundaries, until a point is reached where it is energetically favourable for the wall to nucleate in a different formation

which minimises E_{ms} , known as the vortex wall (fig. 1.21b). As the name suggests, moments at the edge of the wall show a gradual canting, which enter into a vortex towards the wall centre¹. Few moments therefore orientate in such a way that produces magnetic charges at the boundary, and near flux-closure is achieved, the main exception to this being the vortex core which extends perpendicular to the circulating vortex.

Vortex domain walls are more complex structures than the transverse counterpart, with two main parameters for consideration, leading to four degrees of freedom, each possible permutation is presented in fig. 1.22. Firstly, the wall chirality defines the direction in which moments circulate about the central core, this can be either clockwise or anti-clockwise. Secondly, the vortex core polarity dictates the orientation of the moments at the very centre of the DW, which can be either up or down, describing if they have positive or negative M_Z respectively.

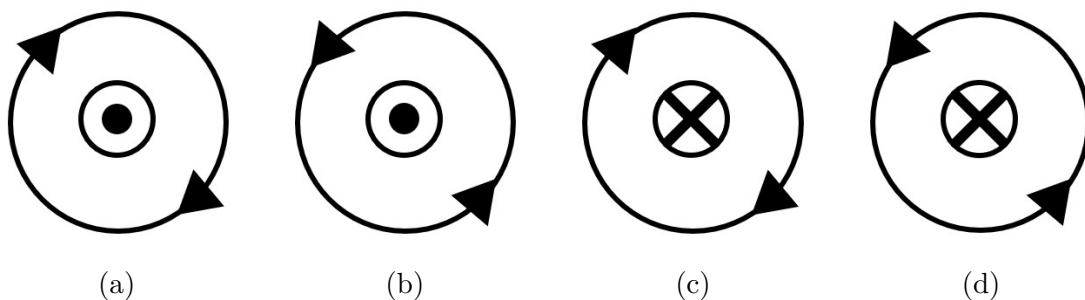


Figure 1.22: Vortex DW permutations. **a**, Clockwise chirality, up polarity. **b**, Anti-clockwise chirality, up polarity. **c**, Clockwise chirality, down polarity. **d**, Anti-clockwise chirality, down polarity.

In a typical planar nanowire with no significant features (i.e. notches, junctions, varying width), the four permutations seen in fig. 1.22 are degenerate, meaning that when a vortex DW nucleates it may possess any combination of chirality and polarity. However, more complex nanostructures have been observed to exhibit a preference towards certain DW parameters, particularly in curved wires as discussed in section 1.7. Additionally the behaviour of vortex DWs in non-trivial systems is seen to be highly dependent on these parameters, discussed further in section 1.6.

Due to the relative ease of fabrication, 2D nanowires and the associated DW properties have been studied extensively over the past few decades. Recent advances

in fabrication and simulation technologies have allowed the expansion of the field of nanomagnetism to incorporate 3D nanostructures. Specifically, studies of DW structure and dynamics within 3D cylindrical nanowires extend upon studies of 2D planar nanowires^{11,12,13}. Such 3D nanowires possess geometries that allow the formation of DWs with fascinating spin textures which have significant ramifications during DW propagation. Figure 1.23 (lower-left) illustrates one possible expected DW structure if the thickness of a planar nanowire were simply increased until a cross-section resembling a square is reached, this is known as a transverse-vortex domain wall (TVDW)¹². Here, a tube of magnetisation is present, extending along the transverse direction. Alternatively, fig. 1.23 (lower-right) depicts an expected DW structure in a cylindrical nanowire, where the spin texture follows the curvature of the rounded cross-section to minimise magnetostatic energy, known as a Bloch-point domain wall (BPDW)¹².

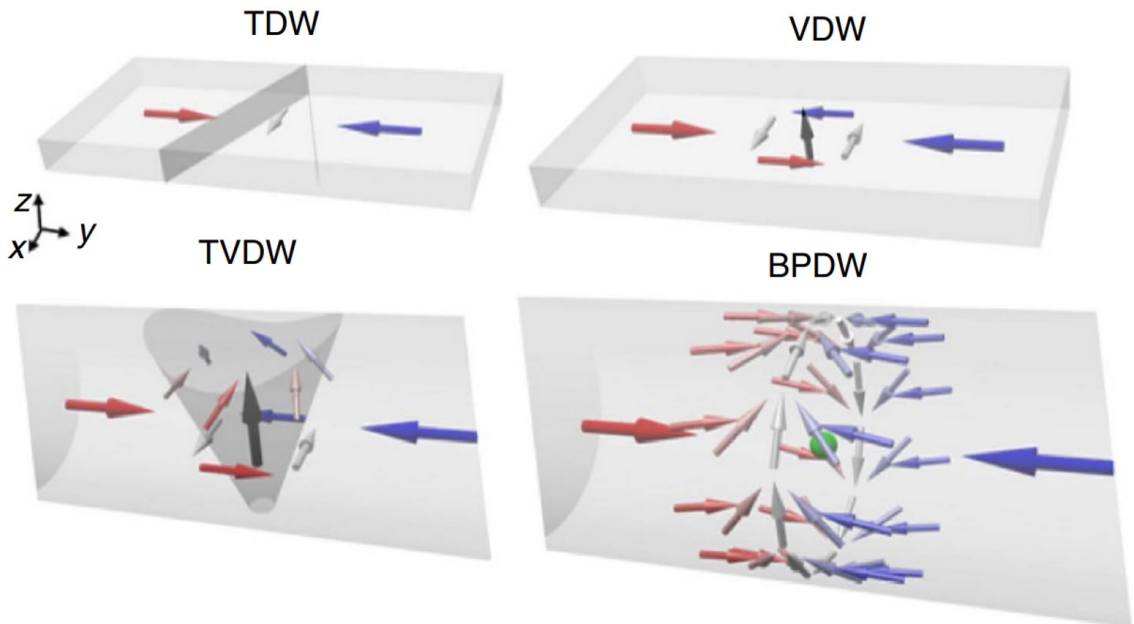


Figure 1.23: Examples of transverse and vortex domain walls in 2D nanowires, as well as transverse-vortex and Bloch-point domain walls in 3D nanowires.¹²

Curiously, both theory and simulations predict that a continuous vector field of uniform magnitude is not possible with the boundary conditions of a BPDW, leading to a singularity with no net magnetisation, referred to as a Bloch point¹¹. This singularity is not the only consequence of the axial vortex present in a BPDW. Interestingly, BPDWs can propagate smoothly at ultra-fast speed¹³, approximately 1

$km s^{-1}$, and hence do not suffer from Walker breakdown, unlike their 2D counterparts¹². This discussion of spin textures and the associated properties that can arise in 3D magnetic nanowires is far from exhaustive, although only nanowires that are effectively 2D (in the plane of the nanowire long-axis) were considered in this study, so attention is now turned towards the phenomenon of DW pinning.

1.6 DOMAIN WALL PINNING

Recent advances in our understanding of magnetic materials on the nanoscale have brought about great encouragement for potential groundbreaking applications, such as next generation data storage devices¹⁴ and nanowire logic operators¹⁵. However, for these technologies to become a reality, a comprehensive ability to control and manipulate DWs will be needed.

This requirement presents a real challenge, as many studies have proven DWs to be notoriously difficult to precisely control. In part, this is due to the immense speed at which DWs travel in nanoscale devices, therefore requiring current pulses on the order of picoseconds to move a DW partly along a wire. Also, for DW-based devices to be viable in applications like data storage, one must be able to accurately and repeatably position DWs at specific points along the wire, where they must remain in a stable state, perhaps for years in the case of archived data. One effect which can help here is DW pinning, which simply refers to the motion of a DW being impeded by some energy barrier. This barrier can take many forms, it may be due to inescapable material defects like surface roughness or grain boundaries, or it can be engineered through careful consideration of the sample design, with features such as junctions, notches, or a varied composition within the wire.

As magnetic materials continue to be structured into ever smaller devices, the surface effects of roughness and grain structure become more influential. Studies of DW pinning offer important insight into the extent of these surface effects and how they may impact potential technological applications. However, we will focus here on examples of magnetic materials being nanostructured into novel designs, which allow manipulation and tailoring of DW dynamics. We start with a simple example of a nanowire reversal containing two notches, acting as pinning sites, labeled P1 and P2 (fig. 1.24). Initially at negative saturation, the wire begins to reverse at \mathbf{H}_2 as a DW nucleates and propagates along the wire length, however the DW stops as it encounters the potential barrier imposed by P1. As \mathbf{H} increases further, the DW

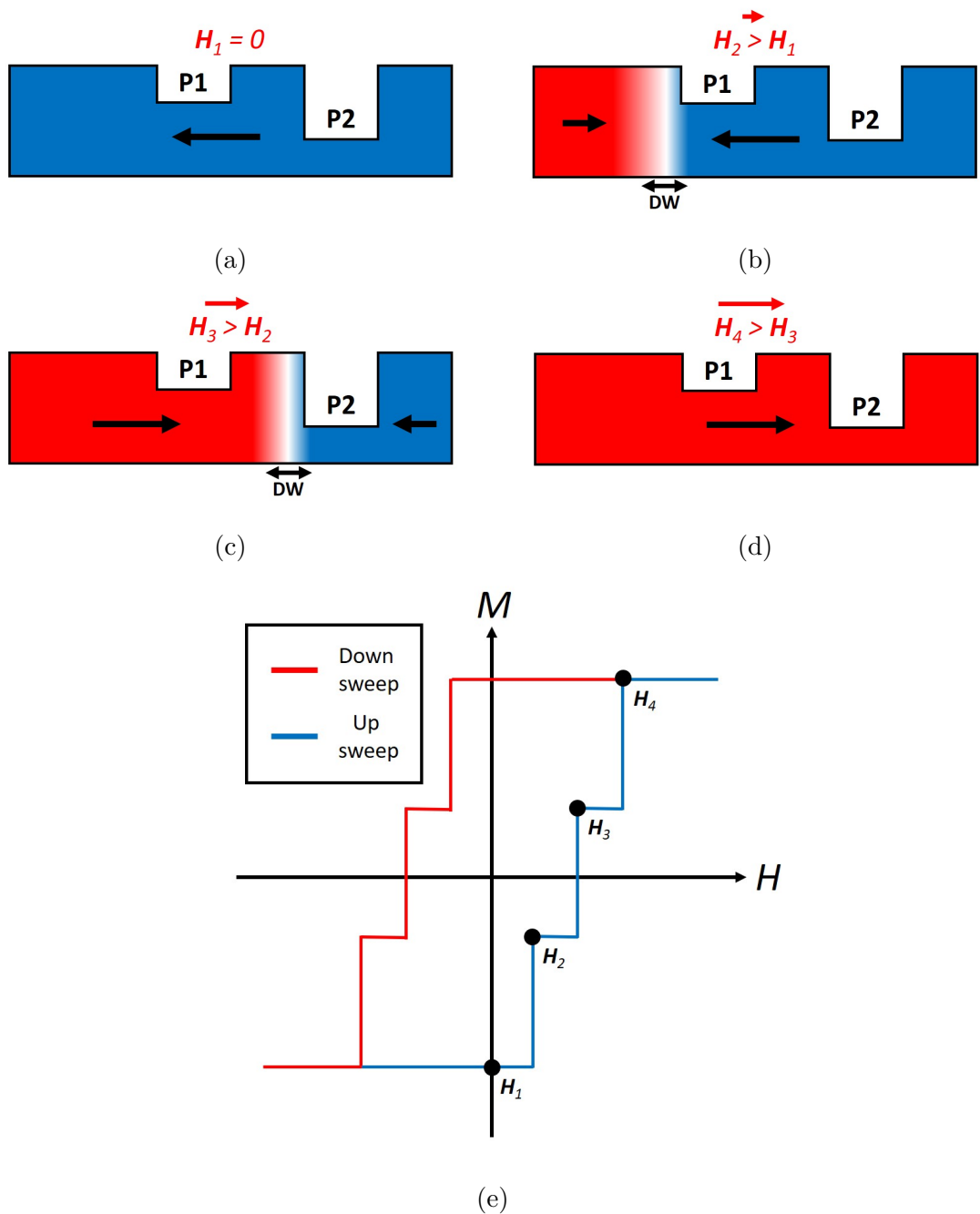


Figure 1.24: Simple schematic to demonstrate domain wall pinning at notches (P1 and P2) in a single-domain nanowire. **a**, Negative saturation in zero applied field. **b**, Partial reversal after a DW has nucleated, propagated, and pinned at P1. **c**, DW depins and propagates, but pins again at P2. **d**, Positive saturation after the DW depins from P2 and annihilates at the wire boundary. **e**, Typical hysteresis loop for the behaviour seen in a-d, associated field values are annotated, gradual reversal due to rotation is neglected here.

remains pinned in place, until it gains sufficient energy to overcome the P1 barrier, at which point it depins and continues propagating along the wire. A key point here, is that each defect has an associated pinning potential, which is highly dependent upon its geometry. Generally speaking, larger defects lead to greater potential barriers and so more energy is required for DWs to overcome these, represented here as the DW depins from P1 but is again stopped by the larger pinning potential of P2. It should be noted that in the opposite situation (reversing from positive to negative saturation) only one pinning event would be observed, as any DW which can depin from P2, will readily pass over the smaller barrier of P1.

In 2003, Atkinson et al reported one of the first experimental studies to observe the DW dynamics within a ferromagnetic nanowire¹⁶. Here, the $Ni_{80}Fe_{20}$ wire was designed with two 90° turns, so that a field applied parallel to the wire length would only propagate the wall until it encounters a corner, at which point the DW can only progress if the field is also rotated through 90° . The study also discerned that DWs propagating through nanowires can reach velocities in excess of 1km s^{-1} , an exciting realisation which prompted a wave of research, due to the potentially revolutionary applications that would be made possible if such processes could be harnessed within complex devices. Shortly afterwards, Faulkner et al demonstrated DW pinning along the length of a very similar $Ni_{81}Fe_{19}$ nanowire to fig. 1.24, though with a single, triangular notch¹⁷. Measured via optical magnetometry (similar to fig. 1.24e), the depinning field was generally seen to increase with notch depth, though this was observed to be a stochastic process.

In 2006, Parkin et al brought further attention and excitement to this field when they hypothesised a next generation data storage device, dubbed racetrack memory¹⁴. Conventional magnetic memory devices store binary data using the orientation of domains within a planar magnetic disc, whereas this suggested technology would apply spin-polarised current pulses to drive DWs through a 3D arrangement of nanowires. Key benefits of this proposal include ultra-high data density, as information could be stored across three-dimensions, and incredibly fast processing speeds, due to the high range of DW velocities already proven to be accessible in magnetic nanowires. To demonstrate the feasibility of this technology, the group directly imaged (via MFM) DWs propagating through a $Ni_{81}Fe_{19}$ nanowire acting as a ratchet system comprising of a sequence of uniformly spaced, identical triangular notches, allowing DWs to be selectively pinned at precise positions along the wire.

One of the main obstacles of Parkin’s vision is the stochastic nature of DW dynamics, a feature which was directly observed by Im et al in 2009¹⁸. Using magnetic transmission soft x-ray microscopy, this study imaged the spin texture of $Ni_{80}Fe_{20}$ nanowires possessing a single, triangular notch. Statistics were gathered of the depinning field as a function of wire width, thickness, and notch depth, where each parameter was seen to have a strong influence over the depinning-field distribution. Interestingly, this result was explained as being due to the number of possible DW types within each set of wire dimensions, thus providing further confidence that the randomness of DW dynamics can be reduced through careful sample design. Most examples of DW barriers feature some geometric defect in the wire which the DW propagates through, causing deformation to the wall structure, making comparisons with models difficult. A novel solution to this issue was found by O’Brien et al in 2011, where the stray field of a nearby magnetic “stub” provided a sufficient potential barrier to pin a DW within the main wire¹⁹. This innovation allowed for excellent agreement between experimental results and an Arrhenius-Neél model of depinning.

Recently, research into vortex DWs has been on the rise, largely due to interest in the impact of chirality-based effects. Researchers have also postulated that vortex DWs could themselves act as an additional form of storing data, due to the four degrees of freedom discussed earlier²⁰. In 2014, Omari and Hayward modelled a series of logic gates, and investigated the behaviour of vortex DWs when interacting with notches or wire junctions, giving specific focus to the impact of DW chirality²⁰. Intriguingly, a vortex DW incident upon a NOT gate comprised of two opposing triangular notches, was seen to reverse its chirality upon transitioning through the gate. Chirality was also seen to be a crucial factor in the switching of Y-shaped junctions, the scenario with a single input wire and two outputs saw preferential switching of one output wire, a preference which alternated upon reversal of the input DW chirality. Analogously, in the opposite scenario with two input wires and one output, the output DW chirality was determined by the order in which the input wires switched, and was independent of input DW chirality. This study suggested that a combination of DW logic gates could be employed to manipulate the structure of vortex DWs within nanowire devices, potentially offering an extra method of storing information in a stable, topologically protected format.

A promising study focusing on controlled DW propagation and pinning was

reported by Bahri et al in 2019²¹. Rather than introducing notches, they have produced staggered wires which periodically offset the long axis, to act as a ratchet system. Here the pinning potential can be tailored by adjusting the stagger offset. If each pinning site is designed to be identical (just as was discussed regarding fig. 1.24), it was found that a DW pins at the first offset, but once a depinning field is reached and the DW can escape its potential well, it will propagate the length of the wire without halting at further pinning sites. However, carefully designing the wire such that each staggered offset has a greater pinning potential than the previous allowed a ratchet-like behaviour, whereby a DW was seen to periodically progress along the wire, and halt at well-defined positions.

1.7 CURVATURE

All examples of DW dynamics discussed thus far have considered planar nanowire systems. Though recent theory has suggested that structures with curved geometries, such as 2D bent wires, 3D helices, or shells, exhibit additional energy terms which give rise to novel exchange-driven behaviour²². In the mid-20th century, an extra contribution to the exchange energy was discovered known as the Dzyaloshinskii-Moriya interaction (DMI), which favours canting between adjacent spins that would otherwise be parallel, hence this is also often referred to as anti-symmetric exchange. Moriya found that this effect occurs in materials lacking inversion symmetry, which also exhibit a strong spin-orbit coupling, where the DMI associated energy density (E_{DM}) is given by²³

$$E_{DM} = \sum_{i,j} \mathbf{d}_{ij} \cdot (\mathbf{S}_i \times \mathbf{S}_j) \quad (1.42)$$

here \mathbf{d}_{ij} is the vector for DMI between atoms i and j , the direction of which varies for different types of system. In curved geometries we consider an effective-DMI, originating from the competition between exchange and demagnetising energies, forcing a canting of neighbouring spins even in a single domain body²². Figure 1.25 illustrates a consequence of this effect. If one were to naively only consider E_{ms} , the spins seen here would be expected to orientate along the arc of curvature to minimise any stray magnetic fields. However, E_{ex} is minimised when neighbouring spins are orientated parallel with one another. Therefore, these competing energy terms result in spins canting out-of-plane by an angle θ at high curvature, an effect not seen in equivalent planar bodies.

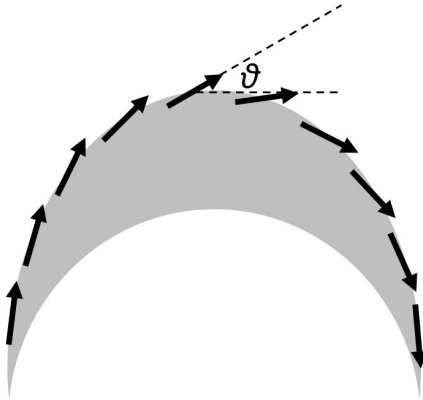


Figure 1.25: Arrows denote the orientation of spins on the upper surface of a curved ferromagnetic body.

A major assumption made here, is that shape anisotropy always causes spins to orientate parallel with the long-axis, therefore any surface roughness or defects which would act against this principle are neglected. Another curvature-induced addition to the exchange energy is effective anisotropy, acting like a scalar geometrical potential, the exact effect of which is highly dependent upon system geometry²². We can therefore rewrite our expression for exchange energy to include these two new terms

$$E_{ex} = E_{ex}^0 + E_{EDM} + E_A \quad (1.43)$$

where E_{ex}^0 is the standard isotropic exchange term discussed in section 1.4.1, E_{EDM} is the energy attributed to the effective DMI, and E_A is the effective anisotropy associated energy. These curvature-induced energy terms have a variety of real world consequences, from chirality symmetry breaking, to ultra-high DW velocities. To discuss an example, fig. 1.26 illustrates why a transverse DW pinned at a curved surface has a preference for the direction of the transverse component, not seen in planar equivalents²⁴. Both fig. 1.26b and c show a head-to-head DW with similar demagnetising energy, however there is clearly a far greater mean angle between adjacent spins in fig. 1.26c, leading to a higher exchange energy cost. As a result, it is energetically favourable for the transverse component of head-to-head DWs to orientate away from the centre of curvature, whilst the reverse is true for tail-to-tail DWs.

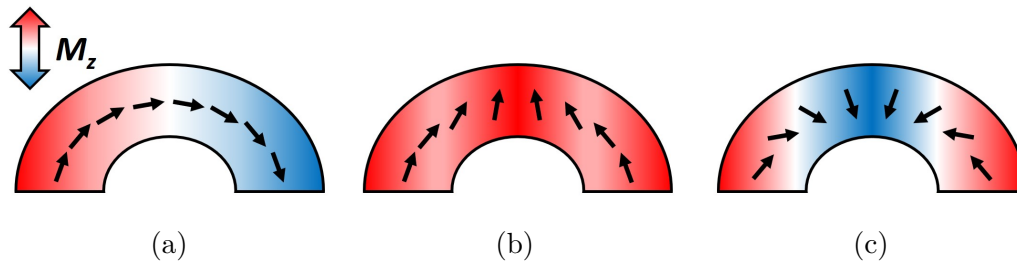


Figure 1.26: Schematic of a curved nanowire, coloured by M_z . **a**, Single-domain state. **b**, Head-to-head transverse DW, with an upwards transverse component. **c**, Head-to-head transverse DW, with a downwards transverse component.

1.8 FRUSTRATED SYSTEMS

We now turn our attention to the field of frustrated materials. In principle, the concept of frustration is a simple one: a system can be defined as frustrated if all pairwise interactions can not be met simultaneously. A common analogy is to firstly consider a system of two spins that are subject to antiferromagnetic minimisation. A minimum energy state is easily found by the two spins orientating anti-parallel. However, when a third spin is introduced to form a triangular lattice (see fig. 1.27), there is no single minimum energy state because the third spin can not simultaneously align with the other two, and so the system is frustrated. For many decades researchers have been intrigued by frustrated systems, which occur in nature across a broad range of length scales^{25,26,27}, giving rise to interesting physical phenomena.

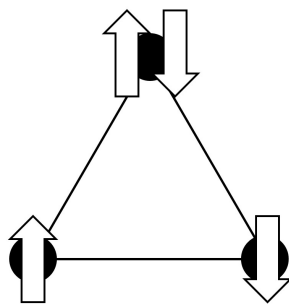


Figure 1.27: A triangular arrangement of three spins, confined to only orientate up or down. Both options are shown for the upper spin, as either will result in a minimum energy state.

1.8.1 BULK FRUSTRATED MATERIALS

It was Pauling who first noted that simple water-ice exhibits a non-zero entropy at a temperature of 0 K, a feature explained by the geometric frustration of hydrogen atoms throughout the crystalline lattice²⁵. As is illustrated in fig. 1.28, H_2O contains two hydrogen atoms for every oxygen, meaning that each oxygen atom can be considered to be adjacent to four hydrogen, whereby two are in close proximity and two are far (2-near/2-far). In this model, there exists six possible ways to arrange these four hydrogen atoms whilst maintaining a 2-near/2-far regime, each depicted in fig. 1.28.

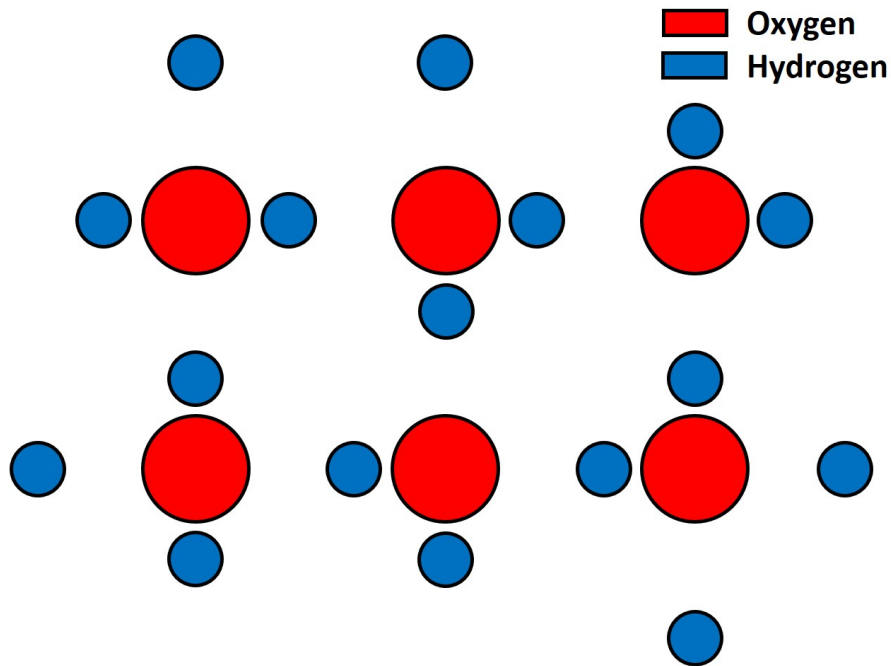


Figure 1.28: Schematic showing one possible configuration of water-ice, where all of the six available permutations of four hydrogen atoms arranged about an oxygen are present.

As these six permutations are energetically degenerate, a lattice consisting of N oxygen atoms will have 6^N possible ground states, leading to a residual entropy (S_R) at 0 K as described by Boltzmann's entropy formula²⁸

$$S_R = k_B \ln W \quad (1.44)$$

where k_B is Boltzmann's constant, and W is the number of possible configurations. With this study, Pauling uncovered an entirely new field for exploration, although in recent decades, studies of bulk geometrically frustrated materials have largely focused not on water-ice, but rather on rare earth magnetic crystals known as spin-ice. In one of the first studies of this emerging field, Harris et al reported upon the geometric frustration seen in $Ho_2Ti_2O_7$, in which Ho atoms are positioned at the corners of a pyrochlore lattice²⁹. Close analogies with water-ice exist here, although instead of these atoms alternating in position, it is the orientation of the associated magnetic moment which varies. In the low temperature regime (<10 K), these moments act as Ising spins as they are confined to only orientate directly towards or away from the centre of the associated tetrahedron. A spin pointing inwards is analogous to a close hydrogen-oxygen distance, whereas a spin pointing outwards is analogous to a far hydrogen-oxygen distance. Despite water-ice being far more readily available, many researchers have chosen to study spin-ice, partly due to the relatively large moment of Ho (or Dy in $Dy_2Ti_2O_7$), which is much easier to probe than the precise position of hydrogen atoms, but also because of the rich physics induced in these materials, such as monopole-like excitations³⁰. These complex systems are well described by the following Hamiltonian (\mathcal{H}), which considers both nearest-neighbour interactions and long range dipolar interactions.

$$\mathcal{H} = \frac{J_{ex}}{3} \sum_{\langle ij \rangle} S_i S_j + Da^3 \sum_{\langle ij \rangle} \left[\frac{\hat{e}_i \cdot \hat{e}_j}{|\mathbf{r}_{ij}|^3} - \frac{3(\hat{e}_i \cdot \mathbf{r}_{ij})(\hat{e}_j \cdot \mathbf{r}_{ij})}{|\mathbf{r}_{ij}|^5} \right] S_i S_j \quad (1.45)$$

here, the first term describes the exchange interaction between nearest neighbours, and the second term defines the long-range dipolar interactions. J_{ex} is an exchange constant, S_{ij} describes the spin orientation which can only take values of ± 1 , a is the nearest-neighbour distance, \hat{e}_{ij} is a unit vector for the Ising axis, \mathbf{r}_{ij} is the displacement between spins, whilst the coupling constant D is given by

$$D = \frac{\mu_0 |\mathbf{m}|}{4\pi a^3} \quad (1.46)$$

Figure 1.29a depicts one possible minimum energy state of two tetrahedra. Each of these has 2 spins orientated inwards and 2 outwards (2-in/2-out). This configuration is referred to as the ice rule, due to the analogy with fig. 1.28. Here, both tetrahedra have a net zero “magnetic charge” as equal fields are flowing inwards and outwards. Should the central spin be reversed (fig. 1.29b), perhaps due to thermal fluctuations, this balance is lost and a net magnetic charge at both sites is

generated.

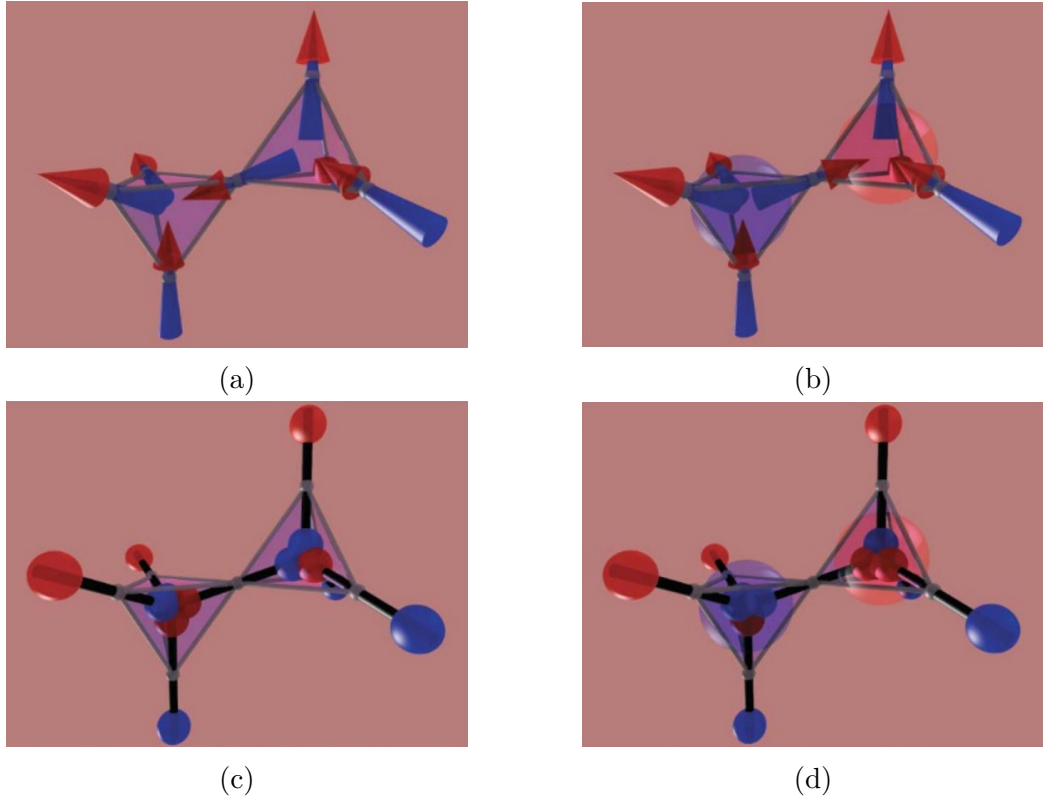


Figure 1.29: Schematic of two, corner-sharing tetrahedra in a spin-ice crystal³¹. **a**, Ice-rule-obeying 2-in/2-out configurations. **b**, Two excitations exhibiting equal and opposite magnetic charge; a 3-in/1-out state (red) and a 3-out/1-in state (blue). **c-d**, Dumbbell representations of the ice rule obeying and excited states respectively. Blue regions indicate negative magnetic charge, whilst red regions show positive.

Castelnovo et al postulated that excited sites such as these act as emergent particles, each with a net dipole moment of $\pm 2\mathbf{m}$ ³¹. It should be noted that these excitations only form due to a reversed spin, and so they are always created as part of a monopole-antimonopole pair with a total net magnetic charge of zero, as such Maxwell's laws are not violated. In order to understand the dynamics in such a lattice, and to examine if these excitations act as free particles, the group made use of the dumbbell model. This replaces each spin with a dumbbell, composed of two opposite magnetic charges ($\pm q$) extending between the centres of adjacent tetrahedra (see fig. 1.29c-d). Remarkably, this theoretical study predicted that once a monopole-antimonopole pair are formed, a chain of spins can reverse to allow these emergent particles to move apart from one another (see fig. 1.30a), whilst their interaction energy directly follows a magnetic equivalent of Coulomb's law (see fig. 1.30b). Despite

these excitations being deconfined, they are bound by the Dirac string of reversed spins which connects them. However, spin-ice crystals at low temperature contain a “soup” of such strings with arbitrary length, resulting in any one string being indistinguishable from this disordered background and displaying negligible string tension.

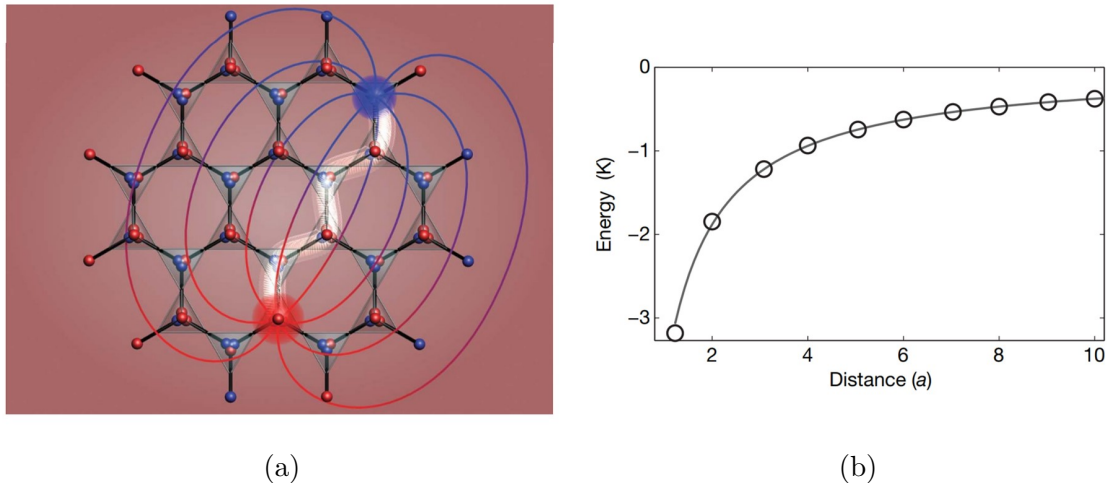


Figure 1.30: Monopole-antimonopole interactions³¹. **a**, Dumbbell model of a pyrochlore lattice, containing two oppositely charged excited states. A white path denotes the Dirac string of spins which have reversed to allow the monopoles to propagate through the lattice. **b**, Numerical evaluation of the monopole-antimonopole interaction energy (circles), overlaid on magnetic Coulomb energy (line), both are plotted as a function of monopole separation.

Shortly after this theoretical prediction, Jaubert and Holdsworth reported a new interpretation of magnetic relaxation data extracted from spin-ice crystals, in 2009³². This work demonstrated that an experimental signature appears in these measurements, allowing researchers to insinuate the existence of monopoles, and give insight into the monopole dynamics. Here, a monopole density gradient was experimentally shown to be present towards the surface of an open system.

1.8.2 ARTIFICIAL SPIN-ICE

In 2006 Wang et al³³ proposed an innovative idea, that a precisely arranged network of magnetic nanowires could serve as an artificial equivalent to the pyrochlore lattice of magnetic moments in spin-ice crystals, thereby creating the field of artificial spin-ice (ASI). Perhaps the most crucial aspect of this comparison, is that a single domain magnetic nanowire can be a suitable approximation of an

Ising spin, which may only orientate in one of two possible directions. As such, the nanowire composition must possess suitably low magnetocrystalline anisotropy, and sufficiently high shape anisotropy to ensure that only a single domain is present, the magnetisation of which must be parallel or anti-parallel with the nanowire long axis. These two possible remanent states mirror the two possible spin orientations in bulk spin-ice, and have a strong analogy with the dumbbell model.

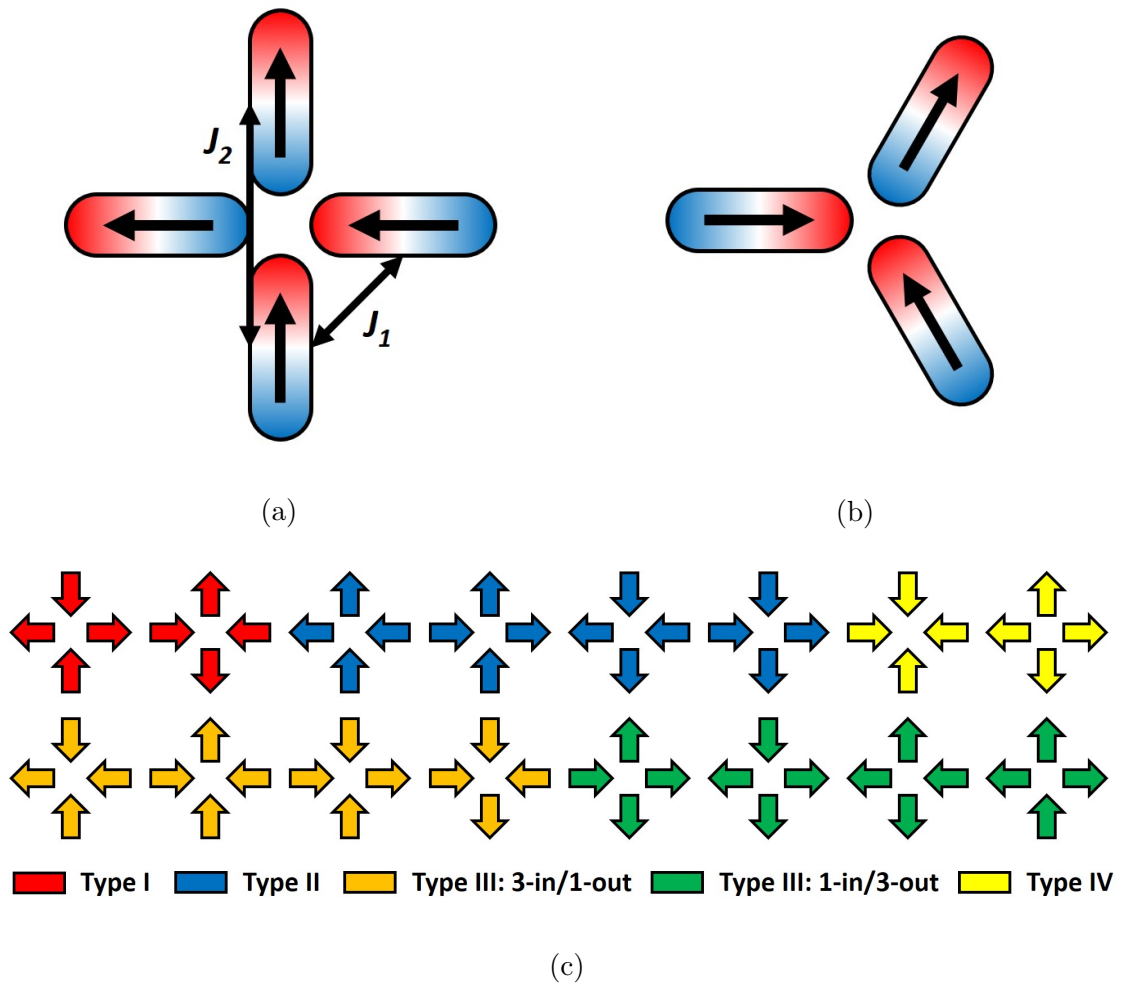


Figure 1.31: ASI vertices. **a**, A disconnected square lattice vertex, the magnetisation of each island is denoted by arrow and colour. The interaction strength of nearest neighbours (J_1) and colinear islands (J_2) are annotated. **b**, A disconnected Kagome lattice vertex. **c**, The sixteen possible square lattice vertex types, each arrow indicates the magnetisation of an island.

There are numerous advantages to ASI, which make it an exciting field for discovery and innovation. Firstly, bulk spin-ice crystals must be studied in a

low-temperature setup, which adds a level of complexity to measurements. Next, standard techniques routinely probe the magnetic configuration of nanowires through direct imaging, however visualising the orientation of individual atomic moments is far less trivial. Lastly, the exact design of ASI systems is open to a great degree of flexibility, facilitating users to explore the effect of geometry, composition, or precisely placed defects. Studies of bulk spin-ice crystals have already made great advances on research topics such as frustration, emergent magnetic monopoles, and phase transitions³⁴, as outlined in section 1.8.1. However, the discussed advantages of ASI provide further avenues for the research of these fields, with greater flexibility over the sample geometry and experimental measurements.

Individual vertices from two of the most commonly studied geometries are seen in fig. 1.31a-b, the square and Kagome lattices. Such lattices can consist of connected or disconnected nanowires, however studies of disconnected arrays are more common, as one does not need to consider the formation and propagation of DWs. It is the square lattice which most closely follows the spin configuration seen in bulk spin-ice (fig. 1.29), due to the four wires evenly spaced about each vertex. Here, all of the $N = 4$ wires can occupy one of two states, leading to $2^N = 16$ possible permutations, illustrated in fig. 1.31c, separated into four distinct vertex types which typically increase in energy from 1 to 4. Type 1 and 2 both obey the ice rule and have no net magnetic charge as they are 2-in/2-out. Type 3 vertices violate the ice rule and can be either 3-in/1-out or 3-out/1-in with a magnetic charge of $\pm 2q$. Type 4 vertices are 4-in or 4-out, therefore also violating the ice rule and possessing a magnetic charge of $\pm 4q$. The distinction between type 1 and 2 is the most subtle as it is due to nearest-neighbour wires interacting more strongly than colinear wires (i.e. $J_1 > J_2$), simply because the centres of nearest-neighbour wires are closer together when four wires are evenly spaced in 2D. This imbalance in J causes the discrepancy in the energies of type 1 and 2, where type 1 vertices possess the lowest energy because the magnetisation vectors of both nearest neighbours orientate with the preferential head-to-tail arrangement. Clearly this is not directly analogous to bulk spin-ice, in which the four spins at the corners of a 3D tetrahedron are all equidistant (i.e. $J_1 = J_2$), meaning that all ice rule obeying sites are degenerate. This discrepancy has been noted since ASI was first proposed by Wang et al³³. Notable consequences of these non-equivalent interactions include a bias towards the formation of type 1 vertices in disconnected ASI, and a finite string tension between monopoles that is distinguishable from the background spin texture³⁴. One solution to this issue with ASI is to instead arrange only three islands about each vertex

(fig. 1.31b), producing a Kagome lattice. Here, each island experiences an equal interaction strength with the other two, solving the issue of $J_1 \neq J_2$. However, this geometry ultimately offers limited insight into bulk spin-ice, as the fundamentally different spin texture of a Kagome lattice leads to only $2^N = 8$ possible vertex types, none of which obey the ice rule.

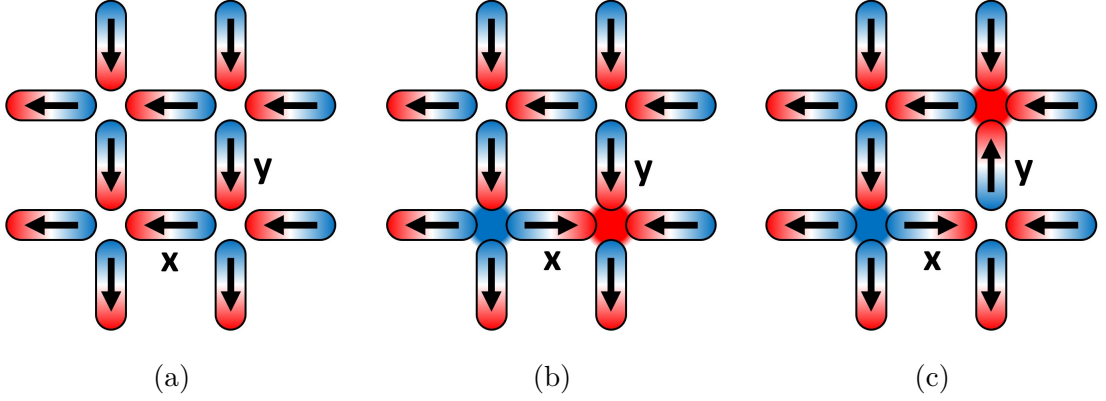


Figure 1.32: Illustration of a disconnected square lattice. **a**, All vertices obey the ice rule. **b**, Island x has reversed, generating a monopole-antimonopole pair. **c**, Island y has reversed, moving a monopole from one vertex to the next.

Similarly to bulk spin-ice, a lattice which is initially ordered and obeys the ice rule (fig. 1.32a) can experience an island reversing its magnetisation, generating a monopole-antimonopole pair (fig. 1.32b). Further switching of islands allow these monopoles to move through the lattice, whilst remaining connected by a string of switched islands³⁵ (fig. 1.32c). It is important to note that most ASI studies do not observe thermally-induced monopole dynamics, because for this to be possible, the energy barrier for an island to reverse its magnetisation would have to be smaller than the energy associated with thermal fluctuations in the surrounding medium. The threshold where this energy barrier is equal to the thermal energy is known as the blocking temperature (T_B), defining the temperature at which a ferromagnetic island becomes superparamagnetic, given by³⁶

$$T_B = \frac{K_S V}{k_B \ln(t_m/t_0)} \quad (1.47)$$

where the shape anisotropy constant (K_S) is

$$K_S = \frac{1}{2} \mu_0 M_S^2 \Delta N_D \quad (1.48)$$

and where V is the nanoisland volume, t_m is the observation time, t_0 is the attempt time ($\sim 10^{-10}s$), ΔN_D is the difference in demagnetising factors between the long and short island axes. T_B is therefore highly dependent on the volume of magnetic material, which varies over time during the nanowire growth, meaning that when the islands are very thin ($< 3nm$) their magnetisation can readily switch. This process allows monopoles to propagate through the lattice, behaviour which Farhan et al directly observed via photoemission electron microscopy (PEEM)³⁵. As the nanowire thickness continues to grow, the influence of thermal fluctuations and dipolar interactions lessens, until the lattice is frozen in a magnetic configuration dubbed the as-deposited state³⁷.

In the first study of this field, Wang et al used MFM to map out the magnetic configuration in disconnected, square $Ni_{81}Fe_{19}$ lattices of varying lattice parameter, to gather statistics of vertex populations and local-energy-minimising correlations³³. At a close lattice spacing ($\sim 300nm$), an expected excess in type 1 vertices was observed, due to the aforementioned preferential alignment between nearest neighbours. Increasing this spacing caused the excess vertex populations and correlations to tend towards zero, because the dipolar interactions between islands diminishes until they effectively become non-interacting, at which point the magnetisation of each island is random (though still constrained parallel or anti-parallel to the long-axis). Whilst this study did not fully replicate the behaviour of a spin-ice crystal, it created a whole new method for researchers to analyse frustrated systems, facilitating many others to build upon this initial effort by adding their own novel innovations.

In 2016, Perrin et al studied a disconnected, square ASI, aiming to recover a degenerate set of ice rules by offsetting one sub-lattice along the z-axis³⁸, as is illustrated in fig. 1.33a. Varying this offset modifies the nearest-neighbour interaction strength (J_1) without affecting the interaction strength between colinear neighbours (J_2), which directly influences the resulting vertex type populations observed in the ground state (see fig. 1.33b). To understand this offset dependency we consider the ground states expected when $J_1 > J_2$, $J_1 < J_2$, and $J_1 \approx J_2$ (see fig. 1.33c-e). The former is effectively the regime studied by Wang et al in the original ASI design, hence type 1 vertices are favourable and the system is populated with flux-closure loops. For $J_1 < J_2$, the two sub-lattices eventually become decoupled, and ferromagnetic ordering ensues. Between these two regimes is a threshold where $J_1 \approx J_2$. At this critical height offset (h_c) all islands will experience an equivalent interaction strength with each of the three neighbouring islands about a vertex.

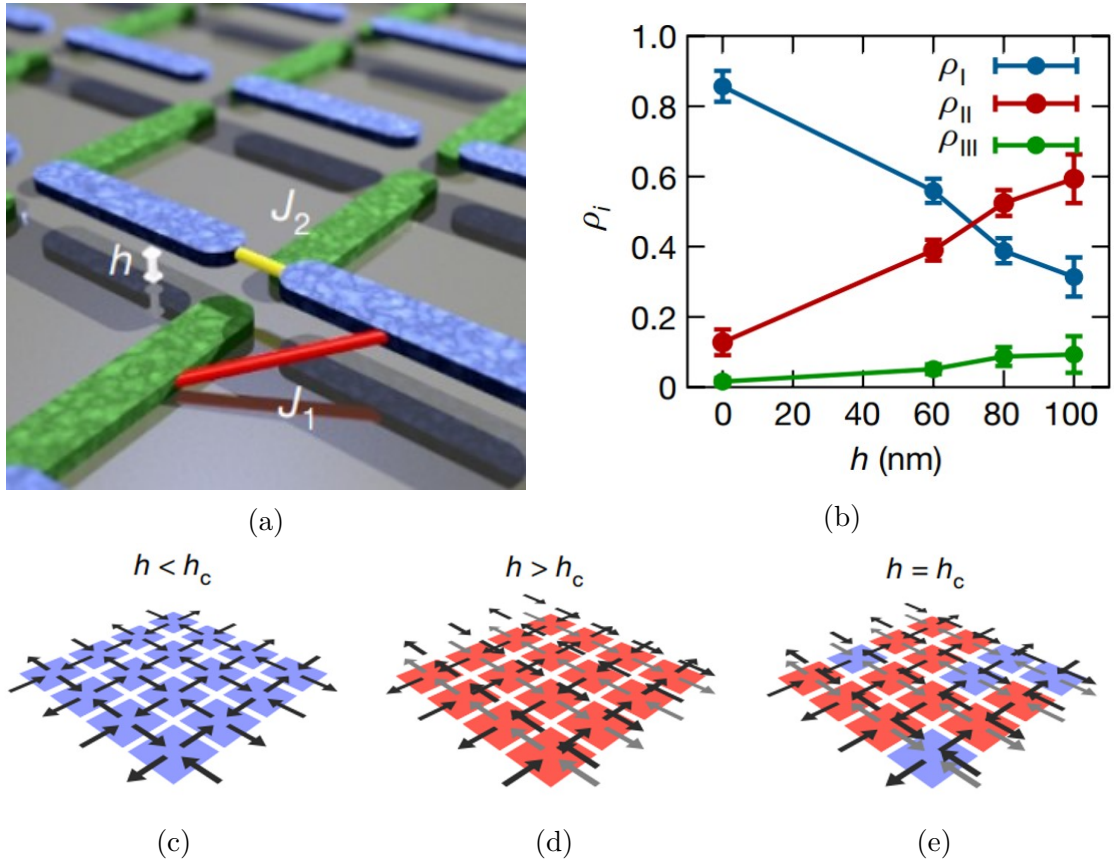


Figure 1.33: A 2.5D modified square lattice³⁸. **a**, Schematic of the nanowire array, the blue sub-lattice is offset by a height h . **b**, Normalised density of vertex type- i (ρ_i), plotted as a function of height offset. **c-e**, Typical ground states in the regimes of $J_1 > J_2$, $J_1 < J_2$, and $J_1 \approx J_2$ respectively. Blue and red tiles indicate type 1 and 2 vertices respectively.

Therefore, the degeneracy of all ice-rule obeying vertices is recovered, leading to equivalent populations of type 1 and 2 vertices. Again, MFM allowed the magnetic configuration to be mapped, but here this dataset was Fourier transformed to produce a magnetic structure factor, exhibiting pinch points in lattices near to this critical height offset. Whilst this study marked a significant step forward for ASI, the Dirac string tension did not entirely vanish at h_c , indicating that the monopoles are not fully deconfined from one another. Ribeiro et al followed a similar approach in 2017, however instead of offsetting islands in z , this study created a nanowire array in which the two sub-lattices possessed non-equal in-plane spacing, resulting in a rectangular lattice³⁹. Here, the nearest-neighbour interactions could be tailored by modifying the spacing of one sub-lattice whilst maintaining that of the other. Following a demagnetisation protocol, MFM analysis showed close agreement with theory, even observing type 4 vertices in rectangular lattices of the highest spacing aspect

ratios, not predicted by their models. Interestingly, results taken at a critical aspect ratio indicated a vanishing string tension between monopole-antimonopole pairs.

Another inventive method for tailoring the interaction energies of neighbouring islands was put forward by Östman et al in 2018⁴⁰. Magnetic discs were placed at the centre of each vertex in a disconnected, square lattice, where the magnetisation of the disc was free to rotate in-plane. By varying the disc diameter, the strength and ratio of interaction energies could be tuned, allowing the group to realise degenerate ice-rule-obeying vertices.

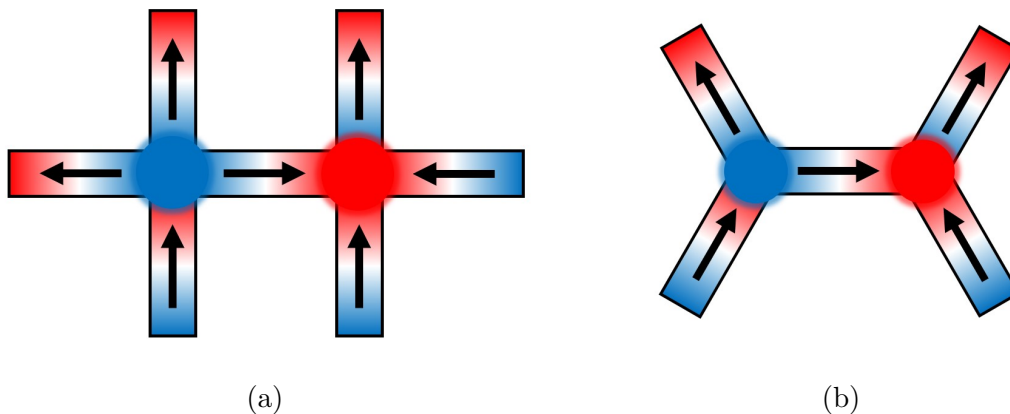


Figure 1.34: Connected ASI. **a**, Adjacent type 3 vertices forming a monopole-antimonopole pair, in a square lattice. **b**, Similar adjacent vertices in a Kagome lattice.

So far we have only considered examples of disconnected nanowire lattices, however one may also wish to produce an ASI with connected wire junctions. Figure 1.34 illustrates square and Kagome patterns in a connected nanowire system. Here, DWs are found at each vertex and can propagate through the lattice upon application of an external field or a spin-polarised current. In 2010, Ladak et al reported one of the first studies to directly image and manipulate excited states within an ASI system⁴¹. A connected Kagome lattice was fabricated, and initially saturated with a magnetic field such that no excited states are present. By reversing the field direction and applying a field much lower than M_S , MFM could then image the new magnetic configuration in an intermediate state. Successive field increments and MFM images allowed excited 3-in or 3-out states to be visualised moving across the lattice, due to DWs propagating between vertices, acting as pinning sites.

Theoretical modeling presented by Perrin et al in 2019 suggested that the square ice model, displaying a degenerate ground state manifold, could be realised in a simple connected square lattice⁴². By modeling four-wire connected junctions of varying wire thickness and width, whilst constraining the wires to remain single domain, the group found that in the regime of thick, wide wires the energy of type 1 and type 2 vertices are approximately equal. A key result of this study is that type 2 vertices were found to be the minimum energy state in connected, square ASI, contrary to the disconnected counterpart. This is a result of the DW structure which is highly dependent on the vertex type, summarised in table 1.3. A high exchange energy cost is associated with the formation of an anti-vortex DW at a type 1 vertex, whilst the gradual canting of spins seen in a type 2 vertex allows this to be the minimum energy state.

Vertex Type	Spin Texture
1	Anti-vortex DW
2	~Uniformly magnetised along the $\langle 110 \rangle$ axis
3	Transverse DW between opposing wires
4	Vortex DW

Table 1.3: Description of the DW structure for each vertex type, in a connected square lattice⁴².

Many artificial spin-ice studies have made use of a well established method for producing 2D magnetic nanostructures, where a thin ferromagnetic film is deposited upon a pre-fabricated template^{33,43,44}. A common way to do so, is to first produce a 2D template by incorporating the lattice design into a uniform layer of positive-tone photoresist. During growth, metal only deposits on to the substrate in trenches that were defined in the photoresist through subtractive manufacturing. Lastly, a lift-off procedure removes any metal that deposited upon the photoresist layer, as well as removing the photoresist itself. This technique has proved reliable over the years, however there is limited scope for expanding investigations into 3D magnetic nanostructures without radical alterations. Recent novel studies have ventured into 2.5D, by depositing a non-magnetic layers on a particular sub-lattice prior to depositing the magnetic layer, as discussed earlier^{35,38}. This raises specific magnetic structures above the substrate, providing the user with some control over features along the z-axis. Although using this methodology, one could not produce a wire extending along

the $\langle 111 \rangle$ axis, and so it falls short of providing true 3D control over the geometry. In the pursuit of 3D magnetic nanostructures, the deposition phase of this fabrication technique is unlikely to change significantly, this simply coats the upper surface of any template with a uniform metallic layer. However, the template design is open to extensive variation, as will be demonstrated in later chapters.

Excellent progress in ASI has already been made in the relatively short lifetime of this field thus far, through a wide variety of ingenious adaptations to the original design of Wang et al. Though replicating the exact 3D arrangement of atomic spins on a pyrochlore lattice has remained a severe challenge for researchers, with examples being limited to 2D or 2.5D. Primarily, this is due to the immense difficulty in nanostructuring magnetic materials in 3D, a topic which is gathering significant interest and excitement. Next we shall discuss the theory behind a phenomenon which offers significant hope towards this goal.

1.9 TWO-PHOTON POLYMERISATION

For many years now, lithographic techniques have been a primary tool for realising complex systems on the microscale, and more recently on the nanoscale as technologies have developed⁴⁵. Methods like electron beam lithography (EBL) and conventional photolithography are still widely used today across many disciplines, to produce cutting edge 2D devices with nanoscale precision. However, both of these approaches allow for little variation along the path of the incident beam, so can be referred to as line-of-sight techniques which are unsuited towards the pursuit of 3D structures featuring nanoscale resolution. Here is where advancements in laser technologies over recent decades has brought about new possibilities, particularly with the invention of femtosecond lasers allowing for pulse lengths $< 10^{-12}s$. These give access to non-linear optical processes, not available to the lower photon intensities achieved by using incoherent light. One such example is two-photon polymerisation, a third order, non-linear optical process which can be exploited to yield a sweeping variety of 3D nanostructures with arbitrary geometry.

The principle of TPP is a straightforward one, and was first hypothesized by Göppert-Mayer in 1930, long before the existence of lasers. Generally speaking, a photon will be absorbed by matter if the photon energy is equal to the energy gap between an electron ground state (E_0) and a higher energy excited state (E_*), allowing the electron to transition across this gap (see fig. 1.35a). Göppert-Mayer's prediction was that this electron excitation will also occur if multiple photons are

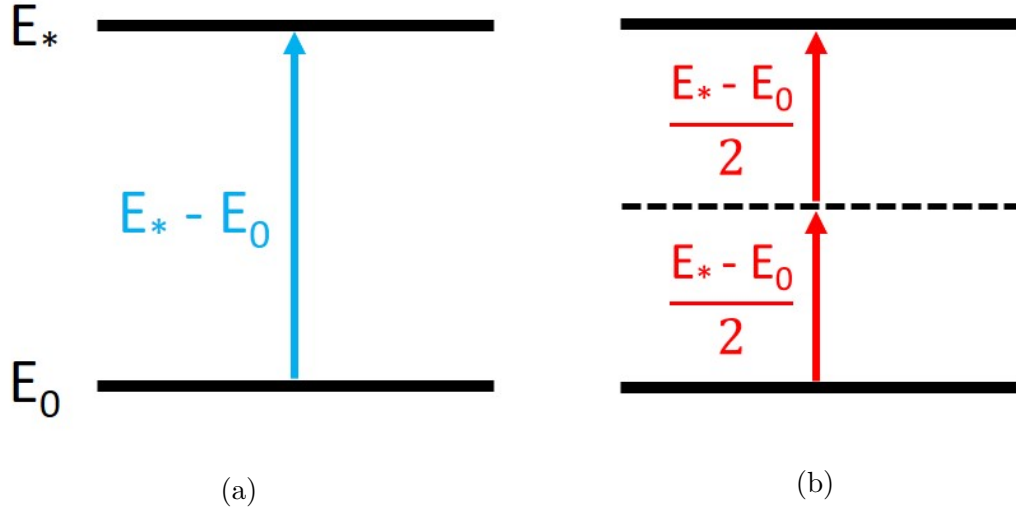


Figure 1.35: Electron excitation mechanisms. **a**, One-photon absorption. **b**, Two-photon absorption

incident upon the electron, where the total photon energy summates to be equal with the gap $E_* - E_0$ ⁴⁶ (fig. 1.35b). An essential condition of TPP is that two photons must arrive at the electron effectively at the same time, since the electron is raised to a virtual state by absorption of the first photon, although the lifetime of this state is very short ($\sim 1fs$). In conventional optical processes such as one-photon absorption, a material responds linearly to an applied electric field, as described by⁴⁶

$$P(\omega) = \epsilon_0 \chi_m(\omega) E(\omega) \quad (1.49)$$

where P is the polarisation induced by the applied field, ω and E are the frequency and magnitude of the electric field respectively, and χ_m is the linear susceptibility of the medium. For optical fields of sufficiently great intensity the material response may not be linear, and so the polarisation induced by an n^{th} order non-linear optical process can be expanded to⁴⁶

$$\mathbf{P} = \Sigma \mathbf{P}^n = \epsilon_0 (\chi_m^1 \mathbf{E} + \chi_m^2 \mathbf{E} \cdot \mathbf{E} + \chi_m^3 \mathbf{E} \cdot \mathbf{E} \cdot \mathbf{E} + \dots) \quad (1.50)$$

where the first three terms are

$$\begin{aligned} \mathbf{P}^1 &= \epsilon_0 \chi_m^1 \mathbf{E} \\ \mathbf{P}^2 &= \epsilon_0 \chi_m^2 \mathbf{E} \cdot \mathbf{E} \\ \mathbf{P}^3 &= \epsilon_0 \chi_m^3 \mathbf{E} \cdot \mathbf{E} \cdot \mathbf{E} \end{aligned} \quad (1.51)$$

Typically, the rate of absorption for a n -photon process is proportional to $\mathbf{E} \cdot \mathbf{P}^{2n-1}$, hence the rate of one-photon absorption (OPA) is proportional to $\mathbf{E} \cdot \mathbf{P}^1$ and the light intensity, whilst the rate of two-photon absorption (TPA) is proportional to $\mathbf{E} \cdot \mathbf{P}^3$ and the square of the light intensity. Figure 1.36 illustrates the laser intensity profile for both one-photon polymerisation (OPP) and TPP, which directly relates to the resolution of fabricated structures. This shows that for OPP in an optically dense medium (fig. 1.36a), the incident beam is significantly attenuated such that it can not penetrate deep into the photoresist. In a medium of low optical density (fig. 1.36b), the intensity is seen to be greatest at the focus point, and so one would expect to be able to produce a plane of polymerised photoresist by scanning the focus point along any particular x - y plane. However, in actual fact a solid block would be produced because the laser intensity is found to be effectively constant along the z -axis when the intensity in each x - y plane along the optical path is integrated. Hence, with OPP the exposure dose is independent of the z co-ordinate (z -direction is defined in fig. 1.36), making this technique unsuitable for the fabrication of 3D structures.

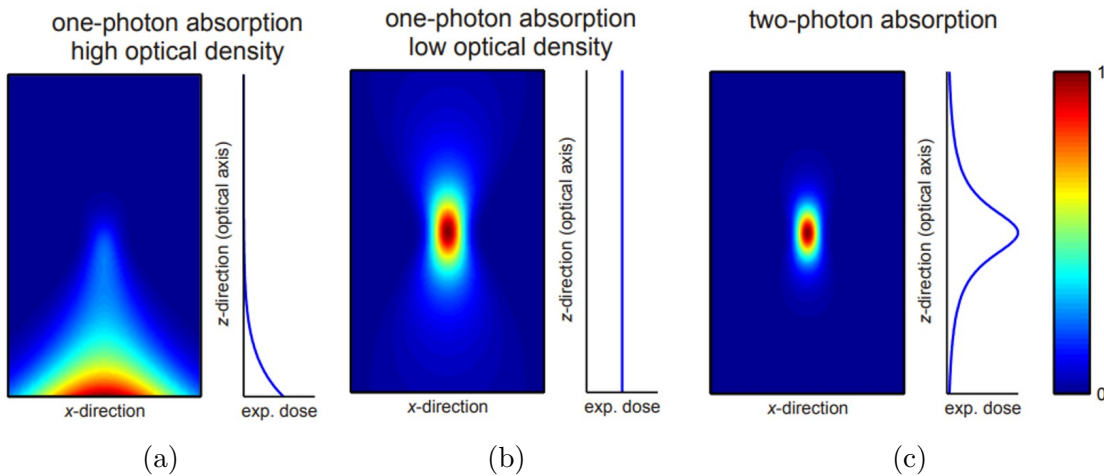


Figure 1.36: Laser intensity profile for three photolithography setups⁴⁷. **a**, OPP in a photoresist with a high photoinitiator concentration. **b**, OPP in a photoresist with a low photoinitiator concentration. **c**, TPP.

Photoresists are commonly used in conjunction with lithography techniques. These are chemicals which react when exposed to photons of specific wavelengths, by either polymerising or depolymerising depending on the type of photoresist used. A negative-tone photoresist is predominantly used herein, which is a viscous liquid containing soluble organic monomers and photoinitiator molecules. The key feature

of negative-tone photoresists is that they solidify into a hard, stable polymer upon exposure to certain wavelengths of light, a chemical chain reaction which is separated into three phases, given in table 1.4.

Phase	Chemical Process
Initiation	$PI \xrightarrow{hv+hv} PI^* \rightarrow R\cdot + R\cdot$
Propagation	$R\cdot + M \rightarrow RM\cdot \xrightarrow{M} RMM\cdot \dots \rightarrow RM_n\cdot$
Termination	$RM_n\cdot + RM_m\cdot \rightarrow RM_{n+m}R$

Table 1.4: A summary of the chemical chain reaction which ensues after a photoinitiator molecule absorbs two photons, and enters an excited state⁴⁸.

For TPP, two photons ($hv + hv$) are initially absorbed by a photoinitiator (PI), raising it to an excited state (PI^*), this subsequently decays to create free radicals ($R\cdot$). Newly formed radicals proceed to react with organic monomers (M) in the solution, generating monomer radicals ($RM\cdot$) of arbitrary length. Monomers can be added to this polymer chain until the reaction is terminated by monomer radicals combining⁴⁸. It is important to note that polymerisation of the photoresist will only occur if the density of excited photoinitiators, and hence the density of free radicals is above a certain threshold value. Therefore, this process is limited to regions of exceedingly high photon intensity, since the probability of two photons arriving at the same photoinitiator within $\sim 10^{-15}s$ is very low⁴⁶. For applications in nanotechnology, one of the primary aspects researchers desire in a fabrication technique is to have the highest possible resolution, facilitating production of structures with minimal feature size. Here is one of the benefits in moving to multi-photon absorption, as we've discussed the rate of OPA \propto photon intensity, whilst the rate of TPP \propto photon intensity squared, illustrated in fig. 1.37. The polymerised region within TPP is therefore tightly confined within a 3D voxel at the laser focal point, where the voxel geometry is directly related to the laser intensity profile illustrated in fig. 1.36c. Hence, the voxel is ellipsoidal with the elongated axis parallel to the optical plane^{47,48}. Now we arrive at the real power of TPP, because polymerisation only takes place in a well defined voxel, this can be moved with respect to a substrate, in order to create a solid 3D polymer structure of arbitrary design, a process discussed further in section 2.1.

Modern femtosecond laser systems offer a great degree of versatility concerning

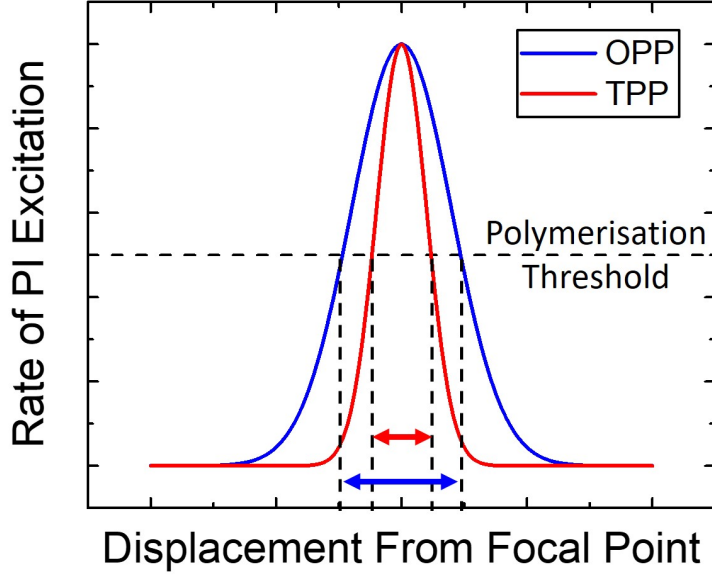


Figure 1.37: Intensity distribution of photoinitiator excitation in the plane transverse to the optical path, for one-photon (blue) and two-photon (red) polymerisation. Blue and red arrows indicate the region of photoresist which would solidify, equal to the peak width at the polymerisation threshold.

factors such as the amplitude and pulse length, meaning the TPP peak in fig. 1.37 can be readily shifted with respect to the polymerisation threshold, enabling local modification of the voxel to suit the structure design. One can theoretically determine the voxel dimensions by considering the density of radicals (ρ_{rad}) generated by laser pulses, and the photon flux intensity ($I_\gamma(r, z)$) at a point with r distance along the cross-section, and z along the optical plane⁴⁸. Beginning with an expression for the rate of radical production

$$\frac{\partial \rho_{rad}}{\partial t} = (\rho_{init} - \rho_{rad}) \sigma_2 I_\gamma^2 \quad (1.52)$$

where ρ_{init} is the primary initiator particle density and σ_2 is the two-photon absorption cross-section. Solving this for ρ_{rad} yields

$$\rho_{rad} = \rho_{init} \left[1 - \exp(-\sigma_2 I_\gamma^2 t) \right]. \quad (1.53)$$

Assuming the laser intensity exhibits a Gaussian distribution, I_γ can be written as

$$I_\gamma(r, z) = I_{\gamma 0} \left[\frac{\omega_0^2}{\omega(z)^2} \right] \exp \left[\frac{-2r^2}{\omega(z)^2} \right] \quad (1.54)$$

$I_{\gamma 0}$ is the photon flux intensity at the focal point ($r = 0, z = 0$), ω_0 is the beam waist, which defines the beam radius at the focus point, and $\omega(z)$ is the laser beam radius at a distance z . One can determine the beam waist of a laser focused through an oil immersion objective lens using

$$\omega_0 = \frac{\lambda}{\pi NA} \sqrt{n_{oil}^2 - NA^2} \quad (1.55)$$

where λ is the laser wavelength, NA is the objective lens numerical aperture, and n_{oil} is the immersion oil refractive index. Next, we express the photon flux intensity in the focus plane ($z = 0$) as

$$I_{\gamma focus} = \frac{P_\gamma}{\pi \omega_0^2 \tau_\gamma f_\gamma h v_\gamma} \quad (1.56)$$

where P_γ , τ_γ , f_γ , and v_γ denote the mean laser power, pulse width, repetition frequency, and wave frequency respectively, and h is Planck's constant. $I_{\gamma 0}$ and $I_{\gamma focus}$ are related to one another by

$$I_{\gamma 0} = \frac{2e^2}{e^2 - 1} I_{\gamma focus} \approx 2.3 I_{\gamma focus} . \quad (1.57)$$

To discern the voxel diameter ($d_{vox}(P, t)$), we examine I_γ in the focal plane by recalling eq. (1.54) and setting $z = 0$, because this plane is where photon flux intensity is at a maximum.

$$I_\gamma(r, z = 0) = I_{\gamma 0} \exp \left(\frac{-2r^2}{\omega_0^2} \right) \quad (1.58)$$

combining the above equations yields an estimate of the voxel diameter

$$d_{vox}(P, t) = \omega_0 \left(\ln \frac{\sigma_2 I_{\gamma 0}^2 n_{pulse} \tau_\gamma}{C_\rho} \right)^{1/2} \quad (1.59)$$

where the number of pulses (n_{pulse}) = ft , and C_ρ is

$$C_\rho = \ln \left[\frac{\rho_{init}}{(\rho_{init} - \rho_{th})} \right] \quad (1.60)$$

similarly, we can recall eq. (1.54) and set $r = 0$, to give the axial photon flux intensity

$$I_\gamma(r = 0, z) = \frac{I_{\gamma 0} \omega_0^2}{\omega(z)^2} \quad (1.61)$$

allowing the voxel length ($l_{vox}(P, t)$) to be approximated as

$$l_{vox}(P, t) = 2z_R \left[\left(\frac{\sigma_2 I_{\gamma 0}^2 n_{pulse} \tau_\gamma}{C_\rho} \right)^{1/2} - 1 \right]^{1/2} \quad (1.62)$$

in which the Rayleigh length (z_R) is

$$z_R = \frac{\pi \omega_0^2}{\lambda}. \quad (1.63)$$

One of the key benefits of two-photon lithography is the significant flexibility over the desired sample geometry, meaning that this fabrication technique can be applied to numerous areas of research. Examples of research fields in which two-photon lithography has been implemented to great effect include the fabrication of photonic crystals⁴⁹, micro-lenses⁵⁰, and scaffolds to support neuronal cell growth⁵¹. Herein, the use of two-photon lithography is focused only upon the nanostructuring of magnetic materials in 3D. Two fabrication methods shall be discussed in the next chapter for achieving magnetic nanostructures by combining TPL with a secondary technique, however many other techniques exist for the creation of 2D and 3D magnetic nanostructures. Each technique has associated benefits and drawbacks which must be considered when selecting the most appropriate method for fabricating the desired sample. Perhaps the most common technique for producing 2D magnetic nanostructures is the combination of electron beam lithography with a line-of-sight deposition^{52,53,54}. EBL can produce 2D templates in a photoresist layer with a resolution below 10 nm⁵⁵. There are several line-of-sight deposition methods that can be used to deposit a thin magnetic film upon templates produced by EBL and other similar techniques, such as thermal evaporation⁵⁶, electron beam evaporation⁵⁷, and sputtering⁵⁸. In addition to these uniaxial thin-film deposition techniques, there are also comparable techniques which coat all exposed surfaces of a template. Examples of this include atomic layer deposition⁵⁹ and electroless deposition⁶⁰, which hold the potential to create magnetic tube and shell-like structures.

Combining EBL and a secondary deposition technique has proved highly effective for 2D sample fabrication on the nanoscale, however the line-of-sight nature of EBL prevents this from nanostructuring magnetic materials in 3D. Two techniques for 3D fabrication on the nanoscale which have attracted significant attention in recent

years are focused electron beam induced deposition⁶¹ (FEBID) and electrochemical deposition into alumina templates⁶². The former, FEBID, directly grows magnetic materials in 3D by adsorbing a precursor gas onto a substrate and focusing an electron beam to induce a deposition of materials in the precursor gas. This powerful technique can produce 3D magnetic structures with a resolution below 10 nm⁶³, without the need for a pre-existing template. Finally, one can produce alumina templates with nanoscale cylindrical pores by anodising aluminium films⁶². By creating the alumina templates upon an electrically conductive substrate, one can use electrochemical deposition to grow 3D magnetic nanowires in the cylindrical pores. This technique can produce large yields of highly pure 3D magnetic nanowires, however one is limited to the relatively basic geometries that can be achieved using cylindrical pores.

Chapter 2

Experimental Techniques

*‘Any sufficiently advanced technology
is indistinguishable from magic.’*

ARTHUR C. CLARKE

Here, an overview of the main experimental methods used in this study is presented, predominantly focusing on the fabrication and analysis of magnetic nanostructures. This chapter is structured in line with the general workflow of this research, which includes sample design and fabrication, physical characterisation, magnetic characterisation, and lastly simulations. In this thesis, samples are created by combining two-photon lithography (TPL) with thermal evaporation. A powerful combination, seen to provide a versatile and rapid means for the production of magnetic structures on the nanoscale⁴⁵. The TPL stage of this process is discussed next.

2.1 TWO-PHOTON LITHOGRAPHY

Researchers have made use of standard photolithography techniques for decades, which allow templates for 2D devices to be engineered with nanoscale features. Typically this involves patterning a photoresist with a pre-prepared design, by first applying the photoresist onto a substrate, before exposing the sample to a UV light source. Usually, the desired pattern is realised by placing a mask in the optical path to prevent specific regions from being exposed. If a positive-tone photoresist is used, then this will typically be spin-coated onto a substrate before being heated to yield a uniform, hardened, thin film. This is a subtractive manufacturing technique, because regions that are unmasked during UV exposure

become soluble in a post-processing chemical development procedure. In contrast, negative-tone photoresists are typically used in a form of additive manufacturing, as discussed in the previous chapter. Here, UV exposure cross-links monomers to form a solid polymer structure that is insoluble during a post-processing chemical development, whilst the unexposed photoresist is washed away. In this thesis, a negative-tone photoresist is used for the vast majority of sample fabrication. Here, the excellent flexibility offered by photolithography is seen, because once a template is formed, this can be used along with a broad range of deposition techniques to form structures of tailored physical parameters, such as composition, purity, and grain size. Since the UV source in standard photolithography tends to be isotropic, and one-photon absorption is the mechanism for polymerisation, this method is unable to yield patterns with features that alter along the z-axis. Therefore this can be referred to as a line-of-sight technique which is only suited towards 2D and 2.5D devices.

As was discussed in section 1.9, replacing the isotropic UV source with a femtosecond laser facilitates TPP. Not only does this remove the necessity for a pre-designed mask, but TPP also allows the fabrication of truly 3D polymer templates, because polymerisation only takes place within the ellipsoidal voxel at the laser focal point. Firstly, a brief overview of TPL will be considered, before each stage of the process shall be discussed in detail. Illustrations of the main TPL procedural steps are given in fig. 2.1, where a negative-tone photoresist is drop cast onto a glass substrate (fig. 2.1a). Next, a femtosecond laser is focused onto the photoresist, and the desired geometry is traced out by moving the voxel with respect to the substrate, thus creating a 3D polymer scaffold (fig. 2.1b). Lastly, a development procedure washes away any unexposed photoresist to leave only the scaffold.

Now that the concept of TPL is clear, the experimental setup to facilitate such a procedure will be examined. Depending on the exact project requirements, a number of different TPL setups could be implemented, with varying capabilities⁴⁸. Here, a commercial TPL system called the Nanoscribe Photonic Professional GT is used for sample production, this is situated in a class 10000 clean room with UV filters covering the windows and lighting. A standard laboratory coat, gloves, and shoe covers are worn during operation. A schematic of the TPL setup is given in fig. 2.2. A computer provides digital control over both the laser output and the piezoelectric stage. The former allows for laser parameters (power, exposure time, pulse frequency, etc.) to be rapidly varied during exposure, whilst the latter gives

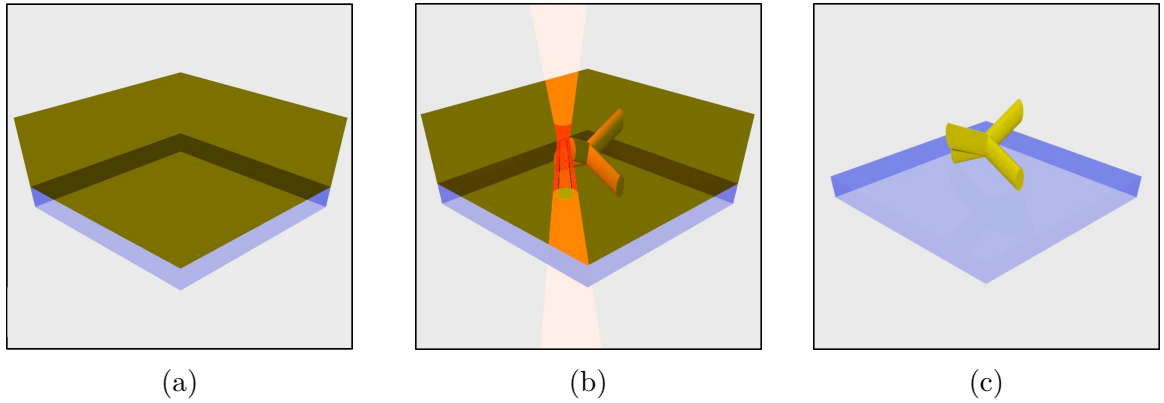


Figure 2.1: Illustration of TPL process. **a**, Negative-tone photoresist (green) drop cast on a glass substrate **b**, Arbitrary geometry is traced out by the voxel, creating a 3D polymer scaffold. **c** A development procedure washes away the unexposed photoresist.

precise control over the exposed region. Therefore, complex patterns can be digitally designed and readily modified, one could even produce a program to generate the geometry co-ordinates whilst the structure is being created, if required.

The main optical components are included in fig. 2.2, all of which are positioned upon an air cushioned table, apart from the computer which sits on a nearby desk. The generated optical beam has a wavelength of 780 nm, pulse duration of ~ 100 fs, repetition rate of 80 MHz, and a peak power of 25 kW (according to the user manual). the laser beam first passes through an acousto-optic modulator (AOM), which allows control over the laser power. Next, the laser path continues through a beam expander, before arriving at an inverted microscope. Within the microscope is a high numerical aperture objective lens ($NA = 1.4$), which tightly focuses the laser onto the photoresist. Recalling eq. (1.55), and inputting $\lambda = 780nm$, $NA = 1.4$, and $n_{oil} = 1.518$, the beam waist is calculated as 104 nm, leading to a spot size diameter of 208 nm at focus. During exposure, the lens upper surface is raised into an immersion oil droplet on the substrate lower surface. This oil is designed to match the refractive indices of the objective lens and glass coverslip as closely as possible, to prevent any significant change in refractive index along the laser path until the substrate-photoresist interface is reached. Index matching these materials helps to reduce reflections at the interface, which in turn minimises any aberrations in the optical beam. This also yields an increase in signal-to-noise when locating the substrate-photoresist interface, which is required before initiating the write procedure.

When attempting to fabricate a new structure, the first step is to digitally

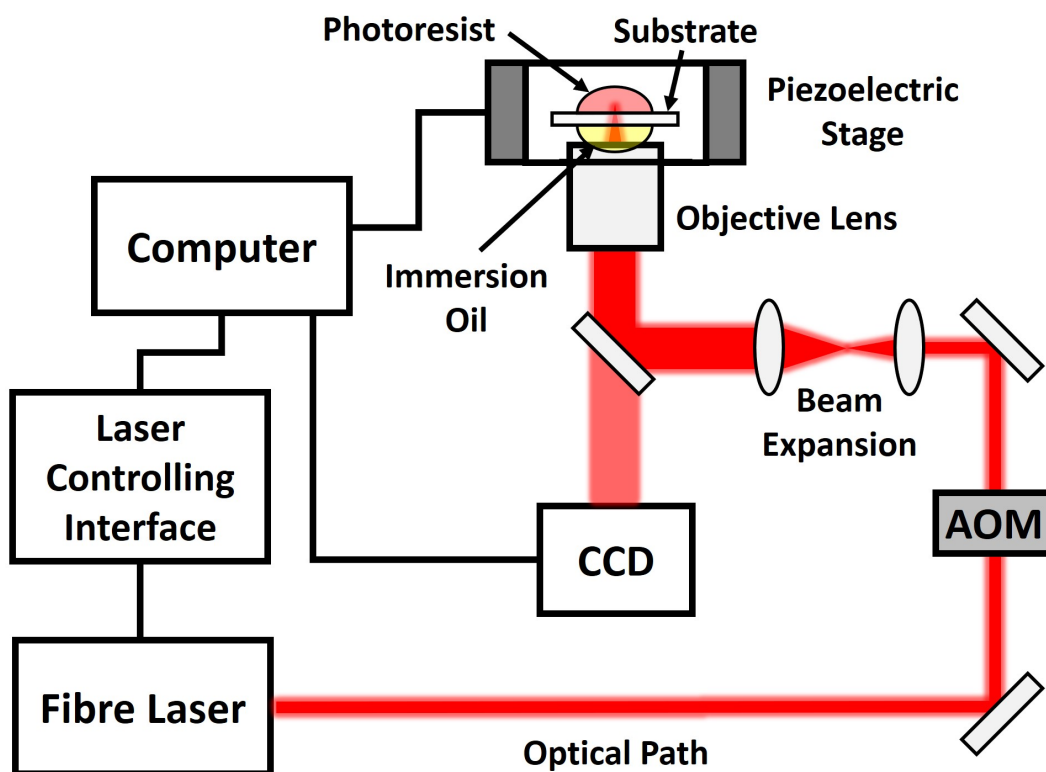


Figure 2.2: Schematic of the TPL setup, for a computer controlled laser and piezoelectric stage. Adapted from the Nanoscribe GmbH manual.

design the geometry and convert this into a format which can be traced out by the voxel, Nanoscribe TPL systems come equipped with a powerful software called DeScribe for exactly this purpose. Firstly, a computer aided design (CAD) file is constructed in an external software package, such as OpenSCAD, and is imported into DeScribe. Here, a tetrapod composed of 4 identical cylinders connected by a central vertex is given as an example (fig. 2.3a). Once imported, the geometry is ‘sliced’ into a stack of 2D layers with a user-defined thickness (fig. 2.3b), each of which is then divided into a series of individual lines in a hatching operation (fig. 2.3c-d). During the writing procedure, the voxel centre will trace along each of these lines. Therefore, to produce a structure resembling the initial design the user must carefully select the slicing and hatching distances, which define the separation between adjacent lines. To yield a solid 3D structure, the slicing and hatching distances have upper limits of the voxel height and width respectively, above which one would simply generate a series of individual polymer lines. Generally speaking,

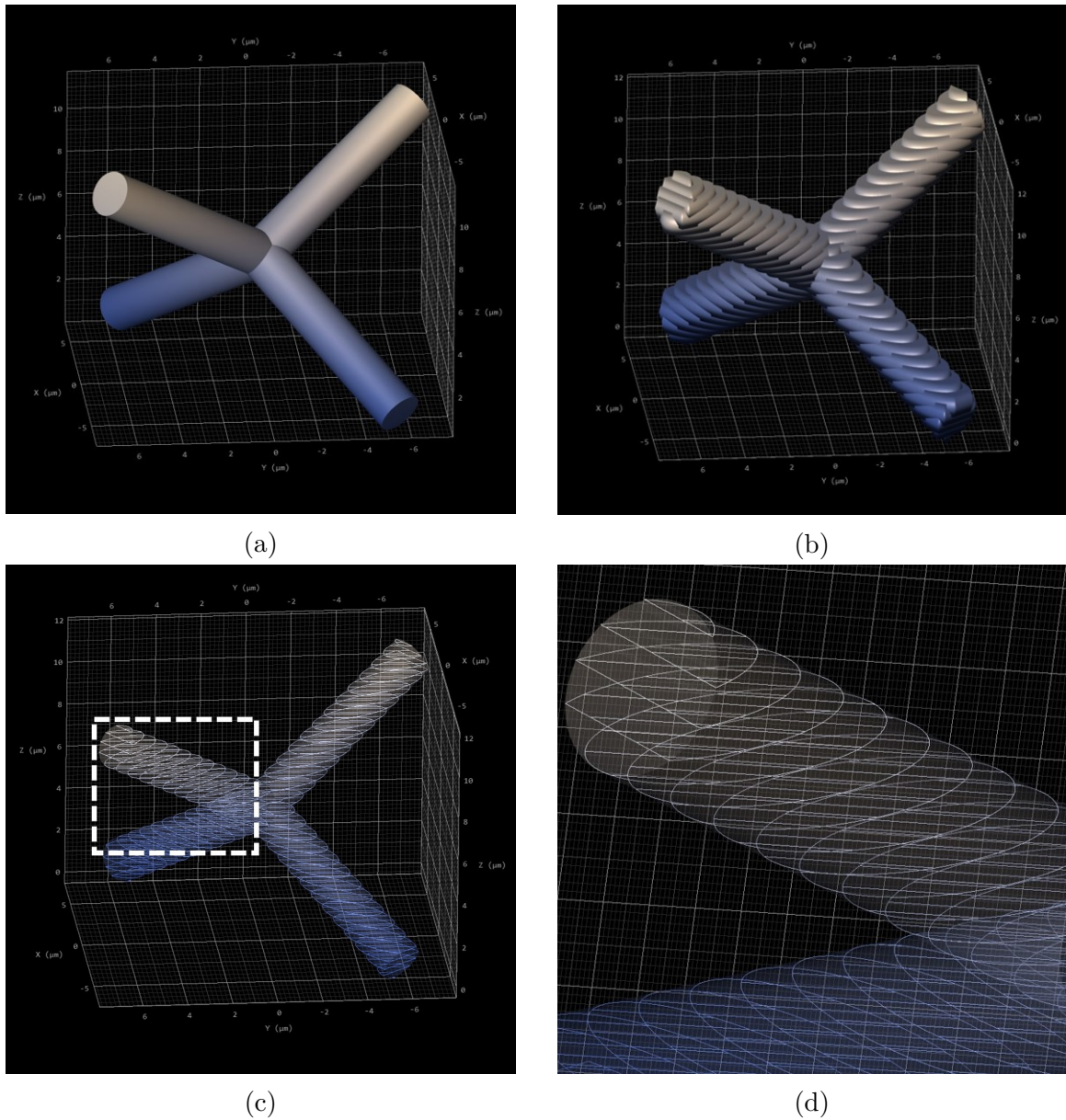
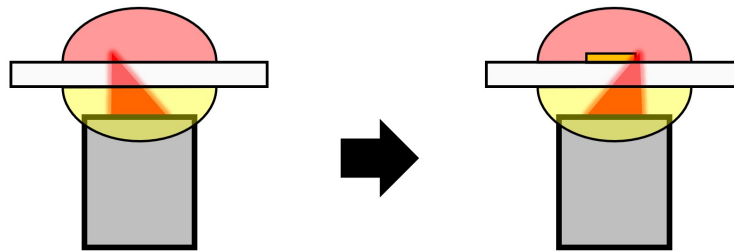


Figure 2.3: Defining a geometry in DeScribe for fabrication via TPL. **a**, CAD file of the desired geometry, imported from an external software package. **b**, A slicing procedure reduces the CAD file into a stack of 2D layers with variable thickness. **c**, A hatching operation divides each layer into individual lines. **d**, Magnified region, indicated by the dotted white box in c.

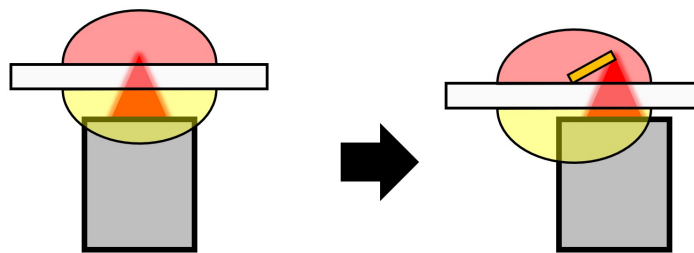
smaller slicing and hatching distances lead to higher resolution structures, as a greater density of voxel lines means allows more detail in the original design to be captured. Zhou et al give a more extensive discussion of this topic⁴⁸

Once a geometry is defined, the user has two options of scanning mode,

piezo or galvo. Galvo scanning mode (fig. 2.4a) is the most widely used, largely because it scans significantly faster (1-2 orders of magnitude), with the user manual recommending scan speeds of 1000-20000 $\mu m s^{-1}$. The manual also states a minimum lateral feature size of ~ 200 nm is expected, measured from Nanoscribe's fabrication of woodpile structures. This is a fixed stage, moving beam approach, where mirrors along the optical path maneuver to rapidly move the voxel across a 2D area whilst the stage remains fixed. The in-plane galvo scan region is ~ 200 μm in diameter, with a height of 300 μm . Once a layer is complete, the stage shifts along the z-axis before the next layer begins, thereby stacking 2D layers to build up a 3D structure. Here, voxel scanning routinely reaches speeds on the order of tens of $cm s^{-1}$, which is mostly limited by the response time and speed of automated mirror adjustments. The main drawback of the galvo mode is that it cannot scan along a direction which



(a)



(b)

Figure 2.4: TPL scanning modes. Initially the objective lens (grey) is raised into an immersion oil droplet (yellow), to focus a laser beam into a photoresist droplet (pink). **a**, Galvo scanning mode, the voxel moves with respect to the substrate to rapidly expose a 2D layer (orange), after each layer is complete the stage shifts in z, allowing 2D layers to be 'stacked' up. **b**, Piezo scanning mode, the stage moves with respect to the voxel, producing a scaffold in 3-dimensions.

has components in x , y , and z (i.e. $\langle 111 \rangle$ axis), unlike the piezo scan mode (fig. 2.4b) which can freely scan in 3D. The piezo mode makes use of a fixed beam, moving stage approach, where the laser remains focused upon a single point, and the piezoelectric stage moves around the voxel to generate a path of polymerised material. Here, recommended scan speeds are $25\text{-}300 \mu\text{m}\text{s}^{-1}$ and the available scan region is $300 \mu\text{m} \times 300 \mu\text{m} \times 300 \mu\text{m}$. The user manual also claims this scan mode to achieve marginally reduced feature sizes, likely due to reduced aberrations because the laser remains focussed on a single point, though the exact feature size reduction is not specified. Whilst this technique offers greater freedom to scan in 3D, and achieves slightly reduced feature sizes, the stage response time and speed, limits the piezo scan speed to 1-2 orders of magnitude below that of the galvo mode. Hence, this technique is more suited to smaller structures, which may require greater precision. Therefore, galvo scan mode was enabled during the fabrication of all samples presented in this thesis.

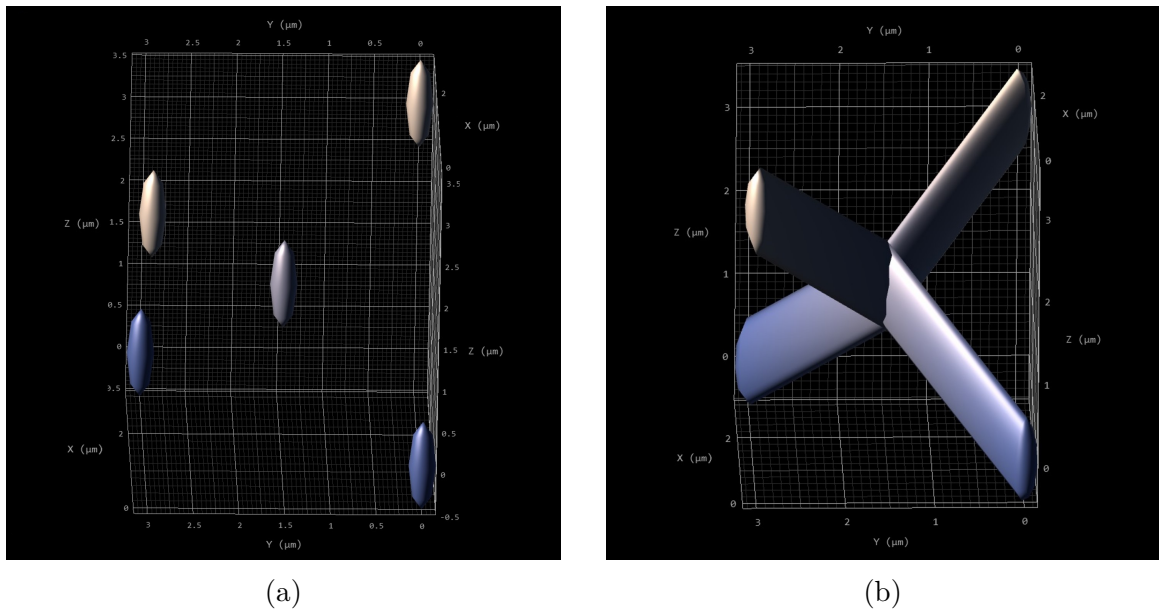
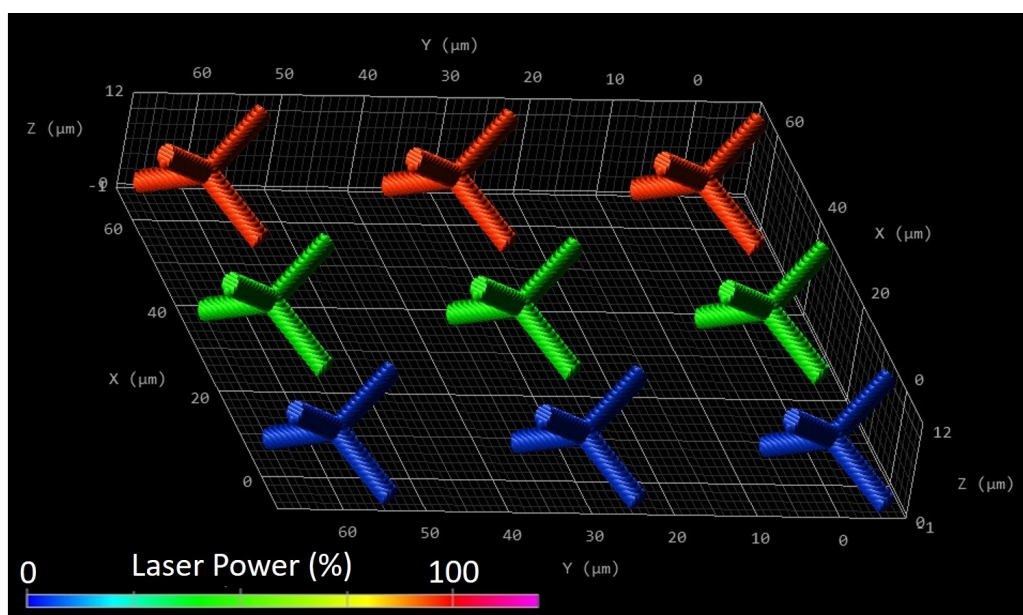


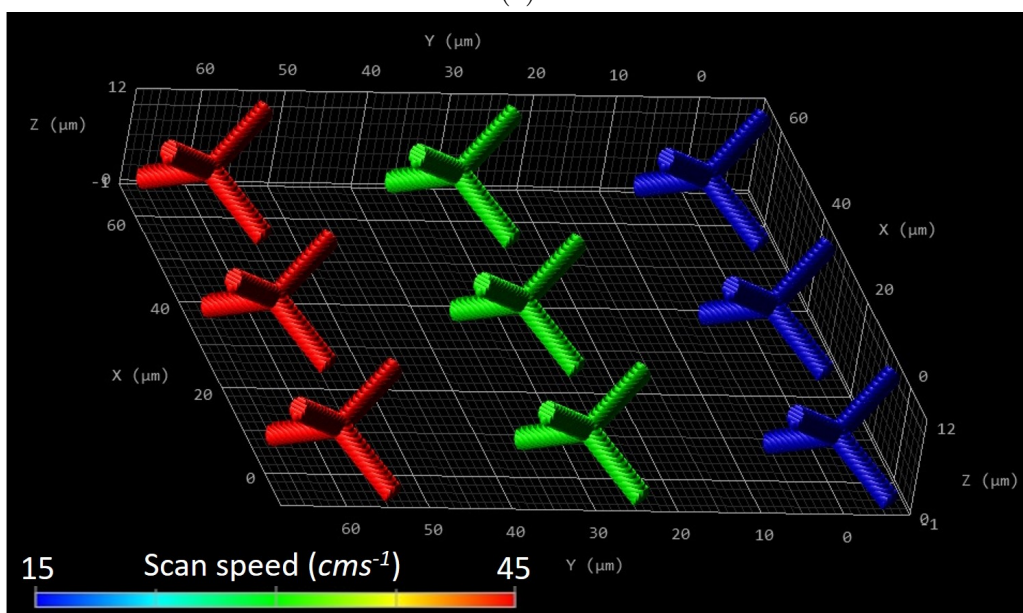
Figure 2.5: Manually defining the GWL code for a tetrapod. **a**, ConnectPointsOff, only individual points at either end of each wire are produced. **b**, ConnectPointsOn, each pair of co-ordinates is joined by a single line.

This standard technique for designing structures by importing CAD files automatically generates a general writing language (GWL) script, which is simply a list of co-ordinates that make up the desired geometry, however, an alternative method of design is to manually write out the GWL script. To do this, one must

create a script to specify the x, y, and z co-ordinates of each point that is to be exposed, as an example fig. 2.5 shows a tetrapod generated with this method, where the co-ordinates for either end of each wire is declared. Figure 2.5a is produced if the setting ConnectPointsOff is enabled, as only individual points are placed at the specified co-ordinates, see table 2.1 for a summary of Nanowrite commands. In this



(a)



(b)

Figure 2.6: A 3×3 array of tetrapod structures. **a**, Laser power increases along the x-axis. **b**, Scan speed increases along the y-axis.

scenario the laser parameters of interest are power and exposure time, the former is self-explanatory whilst the latter defines the time which the voxel lingers at each position, this geometry could be fabricated by either galvo or piezo scan mode. Figure 2.5b uses the same co-ordinate list, except here the setting ConnectPointsOn is enabled, meaning that a single line connects each pair of co-ordinates. For this situation exposure time is replaced with scan speed, denoting the speed at which the voxel scans along each line, this example displays wires orientated along the $\langle 111 \rangle$ axis, so could only be produced using the piezo scan mode. When designing structures which possess feature sizes approaching the theoretical minimum of TPL, this manual method is advantageous. This is because geometries that are designed by the method shown in fig. 2.3c-d require the voxel to scan through the wire cross-section several times, therefore increasing the exposure and hence the wire diameter. Whereas the alternative method in fig. 2.5 only scans a single line for each wire, allowing the theoretical minimum feature size to be attainable.

So far, fabrication has only been considered in terms of a single structure, however the automated nature of this TPL setup facilitates the creation of extended arrays of scaffolds, with localised control over geometry, dimensions, and fabrication parameters. Figure 2.6 presents graphical previews (rendered in DeScribe) of a 3×3 dose array of tetrapods. A dose array is a series of structures which each have an individual set of fabrication parameters, this is a standard initial approach when engineering a new geometry, because the parameters required to obtain a scaffold resembling the initial design are highly dependent on the desired geometry. By varying laser power along the x-axis (Figure 2.6a) and scan speed along the y-axis (Figure 2.6b) each tetrapod was assigned a unique combination of the two, with the lowest dose in the lower-left corner, and highest dose in the upper-right.

Once a suitable GWL program was written, the substrate(s) were prepared for loading into the TPL system. The fabrication process is different when using different photoresists and since the vast majority of sample fabrication in this thesis used a negative-tone photoresist (IPL-780), this process will be discussed first. Herein, glass coverslips ($22mm \times 22mm \times 0.2mm$) served as substrates, silicon wafers could not be used as they are opaque, so would prevent the laser from reaching the photoresist (see fig. 2.4). Glass coverslips were wiped coarsely with a cloth to remove any debris, next they were washed by submersion in acetone followed by isopropyl alcohol (IPA), for approximately one minute each. A compressed air gun was used to dry the substrates, before they were fixed to a sample mount with adhesive

Command	Description
GalvoScanMode	Initiates the galvo scan mode.
PiezoScanMode	Initiates the piezo scan mode.
LaserPower	Sets the laser power as a percentage of its maximum.
PowerScaling	A factor to scale the laser power.
ScanSpeed	Sets the speed at which the voxel scans (μms^{-1}).
ExposureTime	Sets the time which a single point is exposed for (ms).
FindInterfaceAt	Sets an offset to anchor the structure into the substrate.
Include file.gwl	Specifies the file that contains the geometry to be fabricated.
ConnectPointsOff	Co-ordinates will be exposed as individual points only.
ConnectPointsOn	Co-ordinates will be connected by straight lines.
PulsedMode	Used in conjunction with ConnectPointsOff.
ContinuousMode	Used in conjunction with ConnectPointsOn.
MoveStage	Relative stage positioning.
StageGoTo	Absolute stage positioning.
WriteText "Text"	Fabricates user-defined text.
SamplePosition	Moves the objective lens to a designated sample.

Table 2.1: Summary of the main Nanowrite commands that were used for sample fabrication during this study.

tape. The Nanoscribe sample stage contains positions for ten substrates, meaning that an automated program can produce up to 10 samples (which need not be identical) without the need for user intervention. Once mounted and fixed in place, a droplet of immersion oil (Immersionol 518F), with a refractive index of 1.518, was applied in the center of the lower substrate surface, and a droplet of negative-tone photoresist was placed in the centre of the upper surface, small plastic spatulas were used to apply both chemicals. Nanoscribe manufactures several photoresists, each tailored towards specific applications. Throughout this study IPL-780 was used, as this provides the highest resolution offered by a Nanoscribe photoresist, leading to structures possessing the smallest possible feature sizes. The sample mount could then be slotted into the TPL system, and the objective lens raised up until it was in contact with the immersion oil, as illustrated in fig. 2.2. Next, the desired GWL file was loaded on the computer, and the automated exposure protocol initiates.

Once the program had finished, the objective lens was lowered to avoid any damage, the sample mount was removed, and the samples were carefully detached from the mount before being submerged in a beaker of propylene glycol methyl ether acetate (PGMEA) for 20 minutes. Any remaining unexposed photoresist and oil was removed from the substrate by this development process. However, PGMEA leaves a residue, so the substrates were then transferred into a beaker of IPA for a further 2 minutes, which heavily dilutes any PGMEA left on the coverslips. Finally, the samples were dried once again with a compressed air gun to complete the TPL process.

Next, the fabrication process shall be considered for a positive-tone photoresist. This does not require any adjustments to the GWL program, aside from the fact that the fabrication parameters will likely need to be altered to achieve a satisfactory result. Identical glass coverslips are used as substrates here. For cleaning, the substrates were submerged in acetone within a glass beaker which was then placed in an ultrasonic bath for 30 minutes. After this, the substrates were transferred into a beaker of IPA which was placed in the ultrasonic bath for a further 5 minutes to remove the acetone, the substrates were then dried using a compressed air gun. Next, a uniform film of standard positive-tone photoresist (AZ9260) was applied on to the substrate using a spin coater. Figure 2.7 presents a spin curve for AZ9260, this assumes a 30s spin using a silicon wafer, using this curve a photoresist film approximately $10\ \mu\text{m}$ in thickness was applied to the substrate. For the application required in this thesis, it was not necessary to accurately measure the resulting film thickness. A baking procedure is performed next, whereby a hot plate was heated to $120\ ^\circ\text{C}$, the substrates were placed centrally upon the hot plate for 3 minutes with the photoresist on the upper substrate surface. This process forms a uniform, hardened film of photoresist. The samples were then mounted upon the same sample mount used for the negative-tone photoresist process, with the photoresist on the upper surface and an oil droplet on the lower surface. An identical TPL process was then performed, before the samples were removed from the TPL system and unmounted. Here, it was crucial to remove any oil from the slide, this was done by carefully wiping the lower substrate surface with IPA, ensuring that no IPA came into contact with the photoresist. Lastly, a chemical development procedure was performed to wash away any photoresist that was exposed during TPL. For this, the substrates were submerged in a solution which is composed of 25 ml developer that was diluted in 100 ml of deionised water. Depending upon the exposed surface area of the defined geometry, development time can vary between < 1 minute and several hours. Herein, the development time for positive-tone photoresist samples was in the range of 2 - 10 minutes. The samples were then transferred into

a beaker of deionised water for 2 minutes to remove any developer solution, before they could be removed and dried once again using a compressed air gun to complete the process.

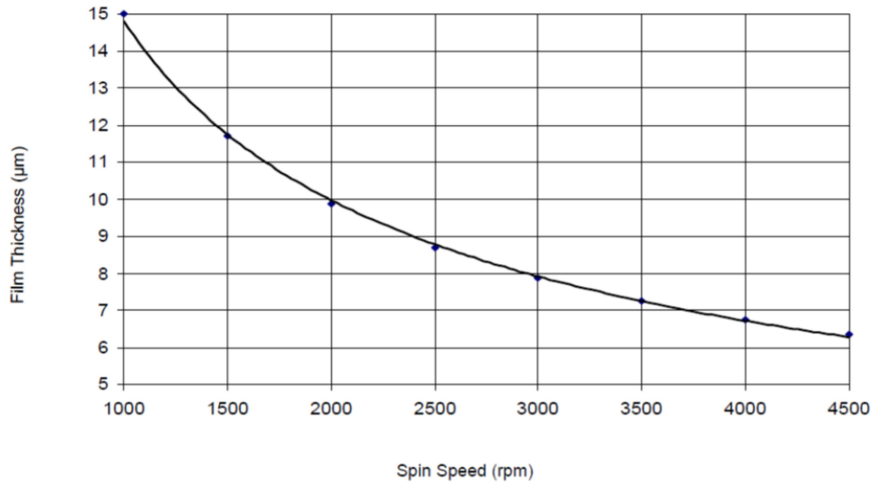


Figure 2.7: A spin curve for the AZ9260 photoresist, relating the user-defined spin speed to the resulting film thickness, reproduced from the photoresist technical sheet. This assumes a 30s spin time and a silicon wafer as the substrate.

2.2 THERMAL EVAPORATION

After a suitable sample had been produced via TPL, a secondary technique was required to generate a magnetic nanostructure, using the polymer scaffold as a template. Throughout this study, a thermal evaporator (see fig. 2.9) situated in a class 1000 cleanroom facilitated the application of a uniform metallic film through line-of-sight deposition.

To begin this process, a small solid piece of the metal which was to be deposited (evaporant) was weighed, before being submerged in a beaker of IPA, that was placed on an ultrasonic cleaner for five minutes. Afterwards the metal was transferred into an empty beaker, and a compressed air gun was gently applied to dry any remaining liquid. The cleaned metal was placed in the centre of an alumina-coated molybdenum evaporation boat, which was tightly fastened between two electrodes. Next, the samples were secured to an aluminium sample mount using small clips covering the corners of each slide, the sample mount can hold a maximum of 6 samples. The mount was placed at the top of the chamber, supported by a

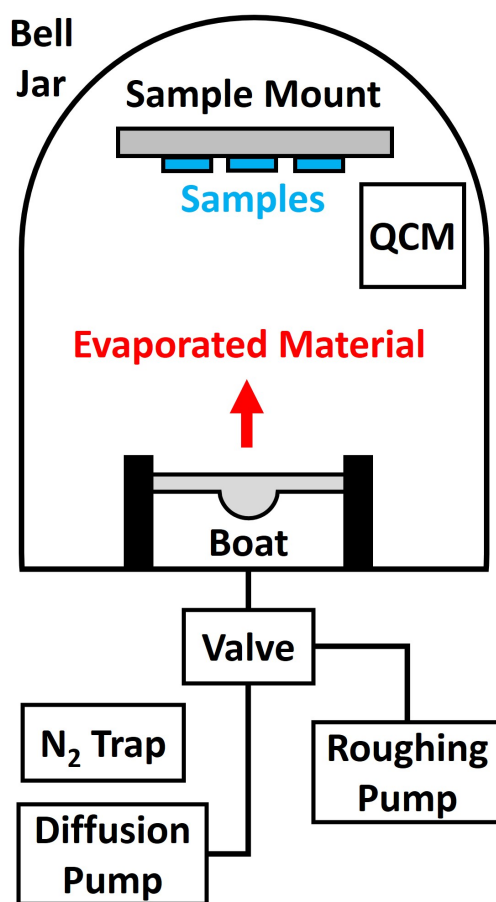


Figure 2.8: Schematic of the main components in a thermal evaporator. An evaporation boat containing the evaporant was connected to electrodes at either end, the sample mount was placed directly overhead, and a QCM was positioned towards the edge of the region confined by a glass bell jar. Below the chamber were two pumping systems and a liquid nitrogen trap.

metallic doughnut-shaped platform, with a boat-sample distance of approximately 28.5 cm. A glass bell jar was then mounted and firmly pressed downwards, ensuring no debris was present under the seal. The first of two pumping stages was initiated next, known as the roughing pump, this evacuated the chamber down to a pressure of approximately 2×10^{-2} mbar, typically occurring over several minutes. To achieve a pressure significantly below this, a second pumping method was required. During the roughing phase, a liquid nitrogen trap below the chamber was filled. Once a sufficiently low pressure was reached, the valve was switched to the diffusion pump which contained hot oil. Lower chamber pressures were then reached by projecting oil onto the nitrogen trap, the ensuing sudden temperature reduction

caused the oil to condense rapidly, a process which sucked air from the chamber, therefore lowering the pressure. This second pumping phase typically takes 30 - 60 minutes to achieve 1×10^{-6} mbar, a typical pressure for high quality film growth⁶⁴.

To reach the relatively high evaporating temperatures of metals, a large current was passed through the evaporation boat, ranging between 60 – 90 A in this study, depending on the evaporant. A gradual approach to increasing this current was required to avoid a significant sudden temperature shift, which can rupture the boat. During this current ramp, a shutter was positioned closely above the boat to avoid any evaporated material depositing on the samples, as this can lead to sample defects. Filtered goggles were worn to visually inspect the evaporant, allowing observation of the point at which this melts and begins evaporating. Shortly after this point, the shutter was opened and an isotropic evaporation deposited the metal across the chamber. A quartz crystal monitor (QCM) detected the rate of deposition. This device vibrated throughout the process, and the deposited metal dampened these vibrations. By inputting the evaporant density, acoustic impedance, and chamber tooling factor (a calibration parameter), one can measure the deposition rate and resulting film thickness. In this thesis, films were typically deposited at a rate of $0.1 - 0.2 \text{ nms}^{-1}$, hence a 50 nm deposition would typically occur over approximately 7.5 minutes. Following this, the shutter was once again positioned to closely cover the evaporation boat, and the current was reduced to zero in a gradual manner similar to the ascent. At least 30 minutes were allowed to pass before the chamber was vented and the samples could be removed.

Figure 2.9 illustrates the result, where a uniform metallic film coats the substrate, but also a 3D arrangement of nanowires sits upon the polymer template, precisely emulating the topography of the upper scaffold surface. Here, the line-of-sight nature of the deposition is seen, because any surface directly below the scaffold is shadowed from the evaporated material, therefore no metal is deposited in this region. Figure 2.9 also shows that any metal deposited upon the polymer scaffold is disconnected from the surrounding sheet film. Whilst this is useful when attempting to study isolated nanowires, some measurement techniques make use of intense electron or optical beams, for which it is highly beneficial if the sample is conductive to prevent significant heating and potential deformation. Since the polymer resist exhibits relatively poor electrical and thermal conductivity, hence this acts as an insulator and is susceptible to deformation when exposed to intense electron or laser

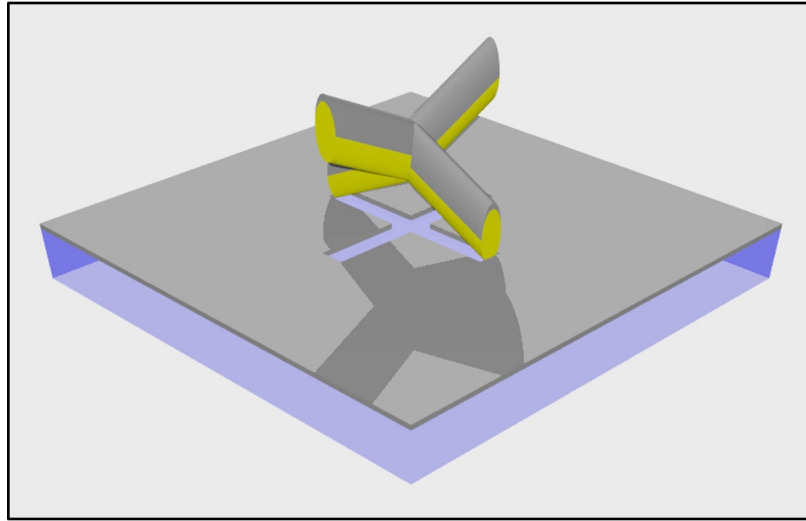


Figure 2.9: Illustration of a tetrapod scaffold (yellow) after a line-of-sight metal (grey) deposition.

beams, such as those present during scanning electron microscopy (SEM) or magneto-optical Kerr effect (MOKE) measurements. One solution to this potential concern is to coat the side walls of the polymer scaffold with a conductive material, prior to the deposition of magnetic material. Figure 2.10 illustrates an experimental procedure for this, whereby the samples are mounted at a 30° angle to the horizontal in an otherwise identical setup to the schematic shown in fig. 2.8. Gold is a convenient and highly conductive material for this purpose, and so four gold depositions can be performed whereby the sample holder is rotated 90° about the z-axis between each deposition. This process allows magnetic nanowires to be produced upon a polymer scaffold whilst remaining thermally and electrically connected to the sheet film on

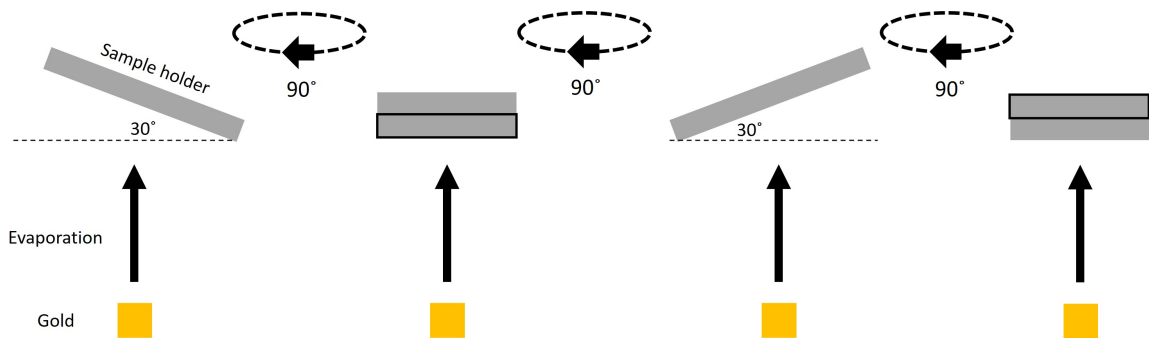


Figure 2.10: Illustration of four gold depositions with the sample holder rotated by 90° about the z-axis between each deposition. Throughout, the sample holder was mounted at a 30° from the horizontal.

the substrate.

2.3 SCANNING ELECTRON MICROSCOPY AND ENERGY DISPERSIVE X-RAY SPECTROSCOPY

Once a satisfactory sample is produced, the next step is to move into the realms of physical characterisation. For structures possessing features in 3D, fully characterising the physical properties is not always a straightforward task, because standard optical microscopy can only observe the upper-surface of a structure. Also the nanoscale features are regularly on a similar length scale to the wavelength of visible light. Researchers therefore often turn to scanning electron microscopy, a technique for imaging samples with sub-nanometre resolution. SEM exhibits a

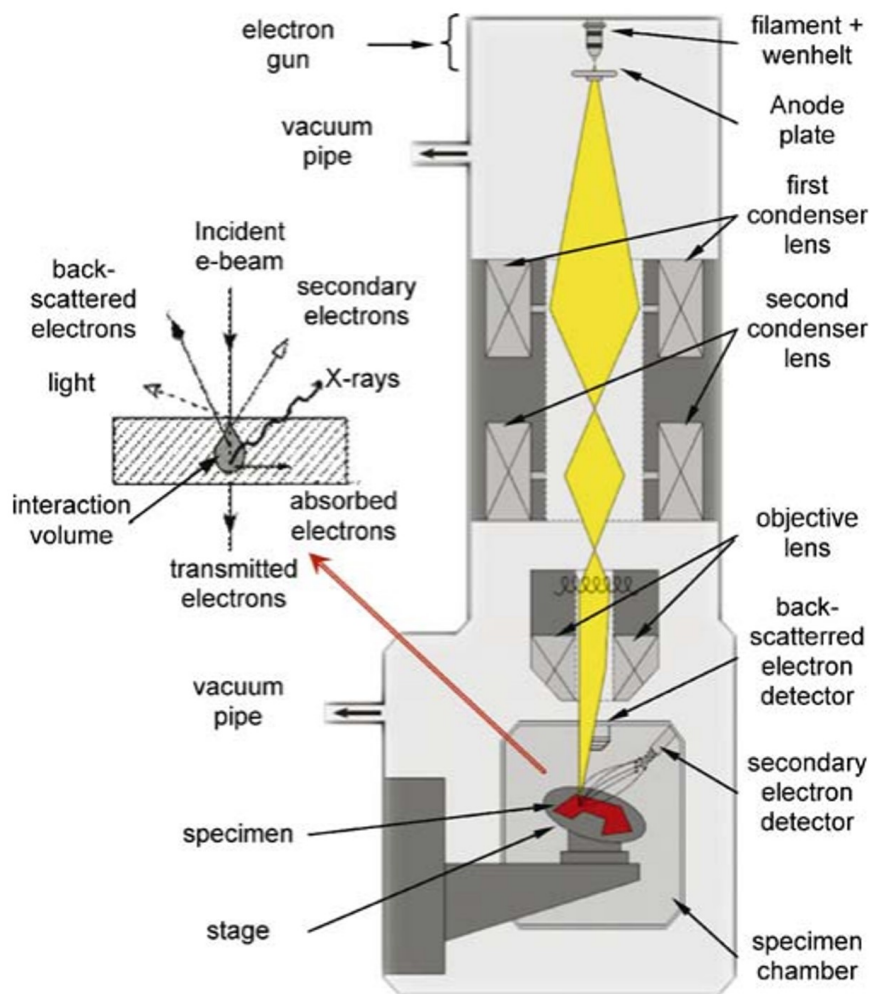


Figure 2.11: Typical SEM setup⁶⁵.

relatively large depth of field and allows significant out-of-plane sample rotation, each of which make SEM ideal for imaging 3D nanostructures.

Two SEM systems were used within this study, a Hitachi SU8230 and a Zeiss Sigma HD, both setups use a field emission gun as the electron source. Prior to entering the specimen chamber, samples were mounted on an SEM stub and fixed in place by an adhesive pad, a small clip, or several drops of carbon paint. The stub could then be mounted in the SEM, and the chamber was evacuated to a pressure below 1×10^{-4} mbar before imaging. Both systems allowed samples to be tilted beyond 45° . During imaging, primary electrons are emitted from a field emission gun, these are accelerated towards the specimen chamber by a potential difference across the anode plate. Condenser lenses deflect the electron path, allowing it to be focussed and scanned across the sample stage. Whilst some systems make use of electrostatic plates for this electron deflection, electromagnetic coils tend to be preferred due to a reduction of aberrations and scan distortion⁶⁶. Applying a current through these coils generates a magnetic field to deflect the electron path, focusing the electron beam onto the stage. Varying the applied current can move the focus point, allowing it to scan across the sample. Primary electrons penetrate the sample and undergo inelastic scattering, hence energy is transferred to the sample and lower energy secondary electrons are ejected. It is these secondary electrons which are measured by a detector within the chamber, producing a signal which a connected computer interprets, to form an image of the sample.

Due to the substantial number of incident electrons during SEM imaging, samples should be grounded throughout, and therefore must be conductive. If this is not the case then the observed region can become charged, leading to the image blurring and containing artifacts. Charging can also cause damage to the observed structure, for example a non-conducting polymer scaffold could be considerably deformed if a high energy electron beam were to closely focus on it for an extended period of time.

Energy dispersive x-ray (EDX) spectroscopy was also performed using the Zeiss Sigma HD SEM, as this possessed additional detectors to characterise x-ray photons. EDX analysis allows spatial mapping of elemental composition, using x-rays produced alongside the secondary electrons (see fig. 2.11). As an electron is ejected from the sample, a higher energy electron transitions down to the vacant energy level by releasing an x-ray with photon energy equal to the transition. A crucial aspect of EDX analysis is that the exact energy associated with this transition, and hence

the emitted x-ray, is unique to each element. Therefore an emission spectrum can be compiled, in which peaks occur at the energy levels associated with the elements present in the measured region. EDX mapping allows the user to frame an image of the desired region via SEM, then initiate a procedure which scans across the measured area taking spectra at set intervals, constructing intensity maps for each element of interest.

2.4 ATOMIC FORCE MICROSCOPY

A rather different method of physical characterisation is atomic force microscopy (AFM). This is a scanning probe technique which is typically used to measure the surface topography of 2D samples. Throughout this thesis, a Dimension 3100 AFM mounted on an air-cushioned table was used for these measurements. The AFM probe itself is a very small (approx. $3 \times 1 \times 1 \text{ mm}^3$) rectangular silicon device, from which a microscale cantilever (approx. $200 \times 30 \times 3 \text{ }\mu\text{m}^3$) extrudes from one of the short boundaries. At the very end of this cantilever, a sharp tip emerges on the lower surface (see fig. 2.13). To mount a probe on the AFM, it first had to be positioned on a cantilever holder (approx. $2 \times 2 \times 0.5 \text{ cm}^3$) and held in place by a spring-loaded clip. This cantilever holder could then be secured at the bottom of the piezotube, ready for measurements (see fig. 2.12).

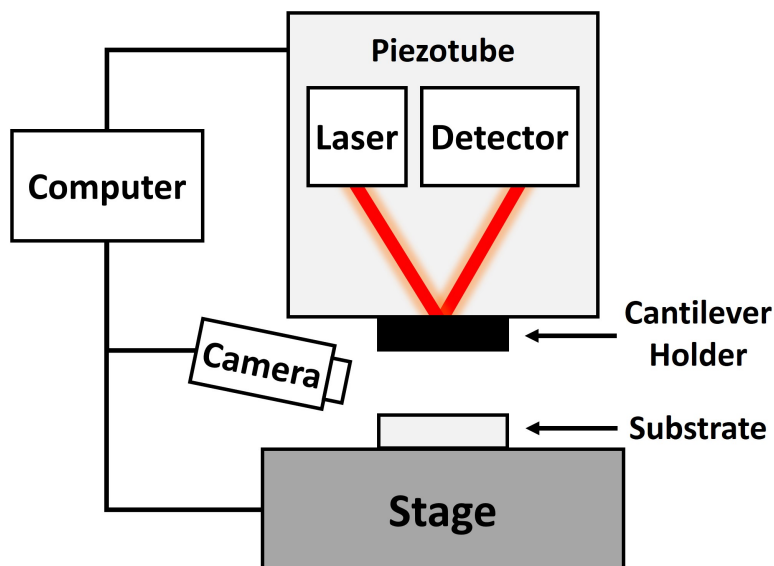


Figure 2.12: Schematic of a typical AFM setup.

An AFM detects nanoscale variations in topography by tracking the deflection

of a laser. This laser was projected down through the piezotube, and once a user has performed a manual alignment, the beam reflected from the upper cantilever surface, onto a photodiode (see fig. 2.12). To achieve good quality AFM images, this laser alignment must be done precisely, such that the laser amplitude detected by the photodiode was maximised. As the probe scans, cantilever motion results in deflections of the laser path which are tracked through the voltage produced from the photodiode. Minor deflections from the initial alignment alter this voltage, allowing the topography to be tracked by calibrating the extent of these deflections with the resulting output voltage. After the alignment, an automated tuning procedure was initiated, this applied a voltage to drive cantilever oscillations, sweeping through a frequency range until a resonant frequency was found. This was measured by monitoring the detected laser signal, which fluctuated as the cantilever oscillated.

There are three main AFM modes of operation, known as contact mode, non-contact mode, and tapping mode^{67,68}. To decide which mode is most suitable, one must consider the sample robustness and the desired data resolution. As the name suggests, contact mode involves scanning the AFM probe across a sample

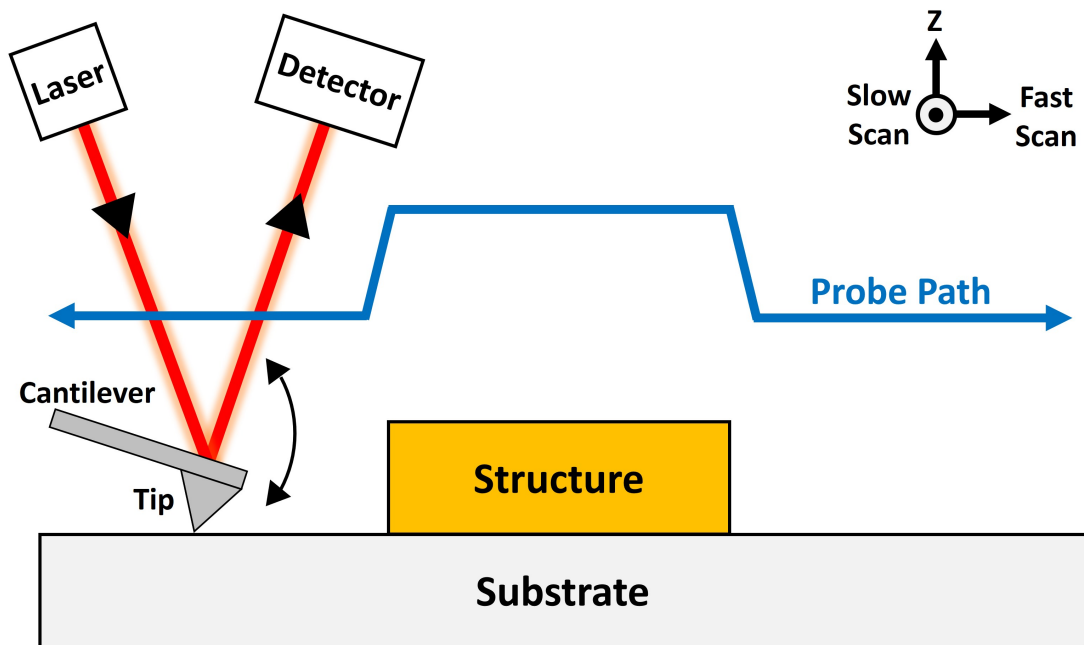


Figure 2.13: Illustration of an oscillating AFM probe scanning over a sample in tapping mode. A laser beam is incident upon the upper cantilever surface, such that the reflected beam is projected onto a detector.

in very close proximity, such that the probe-sample interactions are dominated by repulsive electrostatic forces between electrons. Contact scanning is most commonly used in constant force mode, where a feedback circuit monitors the probe and applies a voltage to maintain a constant cantilever deflection, this voltage is a measure of the surface topography. This operation mode incurs a significant degree of probe-sample contact which can severely damage softer materials. This mode is therefore most well suited to highly robust materials. For very soft materials, non-contact mode may be a more suitable option as the probe is raised by approximately 50 - 150 Å, to avoid any probe-sample contact. As the probe-sample separation is increased, the repulsive electrostatic forces diminish and so the probe-sample interactions are dominated by the attractive van der Waals force. However, such interactions are weak and the resulting cantilever deflections are very small. Therefore, the cantilever is oscillated at its resonant frequency to allow these weak interactions to be detected through variations in the amplitude, phase, and frequency of the cantilever and hence the measured signal. This non-destructive method is useful for soft materials, although the probe-sample separation limits the attainable resolution. Tapping mode (see fig. 2.13) is a compromise between the two afore mentioned operating modes, to achieve high resolution scanning with minimal sample damage. In this mode, the probe oscillates at its resonant frequency during scanning just as occurs in non-contact mode. Here however, the probe-sample separation is reduced, such that the probe briefly contacts the sample at its lowest point of each oscillation. This causes a reduction in oscillation amplitude when the probe passes over a sample peak or, conversely, a sample trough yields an increased amplitude. Throughout scanning, a feedback loop monitors the oscillations and maintains a constant amplitude by shifting the probe in the z-direction (as defined in fig. 2.13) when a deflection is detected. The magnitude of this probe shift is recorded, allowing the surface topography to be mapped out. Herein, AFM data has been acquired in tapping mode.

Once the initial calibration steps were complete, a sample was mounted on the stage directly beneath the piezotube, and the probe was lowered until it was in close proximity (< 1 mm) with the substrate. A camera connected to the computer monitored the probe position with respect to the substrate. Once the substrate was brought into focus, this coarse movement stopped and an automated engage procedure started. The piezotube then lowered itself until van der Waals forces from the sample were detected to have disturbed the cantilever oscillations. AFM images cover a pre-defined area by scanning along individual lines (fast-scan axis), each line was scanned over twice (trace and retrace) such that the probe returned to

it's initial position before shifting a set distance perpendicular to the fast-scan axis (slow-scan axis) and began another line. To control the captured image quality many parameters are open to tailoring, however the settings which were most commonly explored here are the amplitude setpoint, drive amplitude, number of lines, and scan speed. The amplitude setpoint defines the oscillation amplitude maintained by the feedback loop, and hence is a measure of the height at which the probe scanned above the sample. The drive amplitude dictates the voltage applied to drive cantilever oscillations. Increasing the number of lines decreases the slow-scan axis line spacing and increases image resolution. Scan speed dictates the speed at which the probe moves along the fast-scan axis, where faster speeds reduce image acquisition time, but can also reduce image quality. Two further feedback controls which affect the image quality are the proportional gain and integral gain⁶⁹. These parameters determine the feedback on the piezo height, whereby high gains result in the piezo position altering during scanning to maintain an approximately constant cantilever deflection. Conversely, low gains cause the cantilever to deflect from its nominal position upon interactions with a sample. Proportional gain gives a high frequency response to the feedback loop, as this value is multiplied by the values read from the analog-to-digital (A/D) converter as the probe scans. Integral gain is the low frequency response to the feedback loop, as this value is multiplied by the average of the data read by the A/D converter. To optimise these values, one should increase the integral gain until oscillations appear in the measured data, before reducing this value by several increments until there are no oscillations observed. This should then be repeated for the proportional gain.

Like many techniques, refining the feedback controls for AFM is an art of compromise. Here, these settings must be optimised with consideration of image quality, measurement time, and damage to the probe or sample. For example, one may naively think that high quality data could be rapidly obtained by setting a very low amplitude setpoint, with a very high drive amplitude and scan speed. However in many instances this combination would lead to the tip contacting the sample, known as tip strike. This leads to a bright line across the image instead of the line topography, and potentially damages both the probe and sample. The likelihood of tip strike occurring also strongly depends on the measured topography. More pronounced features along the z-axis increases the risk of this, which explains why AFM is typically used to probe the characteristics of 2D samples. Another effect resulting from tall features is illustrated in the vertical section of the probe path in fig. 2.13, where the probe continues to progress in-plane as it moves along the z-axis. This slanted path

produces blurring at the edges of features with large z-component, meaning that the resulting image may show these features to have a wider in-plane component than is true. Despite these drawbacks, many studies have proven AFM to be a powerful technique, particularly when coupled with an in situ secondary technique, such as electric force microscopy or magnetic force microscopy (MFM), the latter of which is discussed next.

2.5 MAGNETIC FORCE MICROSCOPY

MFM is a complementary technique to AFM, but is used to image the magnetic configuration of a sample. This magnetic information is acquired in parallel with the topography scan, resulting in the AFM and MFM data of a particularly region being collected and displayed side-by-side. Figure 2.14 shows data from a region of magnetic tape. The surface topography in fig. 2.14a shows no significant features, whereas the MFM image in fig. 2.14b reveals a systematic sequence of long, narrow domains with alternating magnetisation, indicated as the colour contrast varies between bright and dark. This illustrates the method in which a hard disc drive (HDD) stores data, where the two out-of-plane orientations are assigned values of 0 or 1, to record an extensive series of information in binary format.

Initial setup for MFM measurements was a very similar process to that which was described for AFM in section 2.4, the main exception being the probe. MFM probes used for this thesis are similar in size and shape to the AFM equivalent. However, MFM probes possess a hard magnetic coating on the upper-surface and a soft magnetic coating on the lower-surface. Prior to mounting the cantilever holder on the piezotube, the probe had to be magnetised parallel or anti-parallel with the tip-axis, here a 1 T permanent magnet was used for this. Remaining initiation steps were identical to those discussed in section 2.4. MFM measures the sample magnetic configuration through analysis of subtle variations in the cantilever oscillations. Deflections are caused by interactions between stray magnetic fields emanating from the sample, and the probe tip which acts as a magnetic dipole. These sample-tip interactions have energy E_{inter} , given by¹

$$E_{inter} = - \int_{V_{tip}} \mu_0 \mathbf{M}_{tip} \cdot \mathbf{H}_{sample} dV = - \int_{V_{sample}} \mu_0 \mathbf{M}_{sample} \cdot \mathbf{H}_{tip} dV \quad (2.1)$$

where \mathbf{M}_{tip} and \mathbf{M}_{sample} are the tip and sample magnetisation respectively,

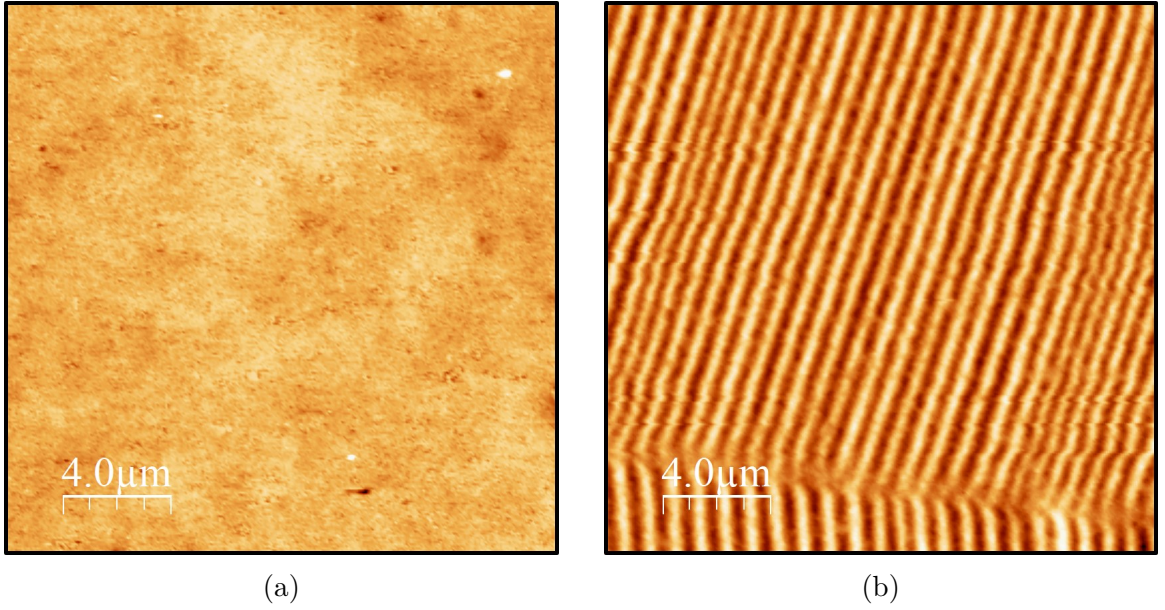


Figure 2.14: Example of MFM measurement, extracted from a $20 \times 20 \mu\text{m}^2$ region of magnetic tape. **a**, AFM scan of the surface topography. **b**, MFM scan, showing magnetic contrast.

\mathbf{H}_{tip} and \mathbf{H}_{sample} are the stray magnetic field associated with the tip and sample respectively, and V_{tip} and V_{sample} are the tip and sample volume. During MFM scanning, the probe resonant characteristics, such as the frequency and phase of the vibration, are continuously monitored through the detected laser signal discussed earlier. These properties exhibit slight changes resulting from modifications to the cantilever spring constant (k), due to a force gradient ($\delta F/\delta z$) felt by the tip, shown by¹

$$k = k_0 + \frac{\delta F}{\delta z} \quad (2.2)$$

where k_0 is the cantilever spring constant when no forces act upon it. In the event of the probe experiencing an attractive force, k would soften, causing a reduction in the resonant frequency, detected as alterations in the afore mentioned resonant characteristics¹. MFM images are generally presented as phase shift colour maps. Here, a \mathbf{H}_{sample} region yielding a positive phase shift appears as bright MFM contrast, whilst an opposing \mathbf{H}_{sample} region would generate dark contrast (see fig. 2.14 and illustrated contrast in fig. 2.15). The two-pass scanning path taken by MFM probes during data acquisition is depicted in fig. 2.15. For each line of an image, the probe performs a trace and retrace of the topography with a close sample-tip proximity (approx. 10 – 20 nm), before raising by a user-defined height (typically 80 – 120 nm) and following an identical path in the MFM pass.

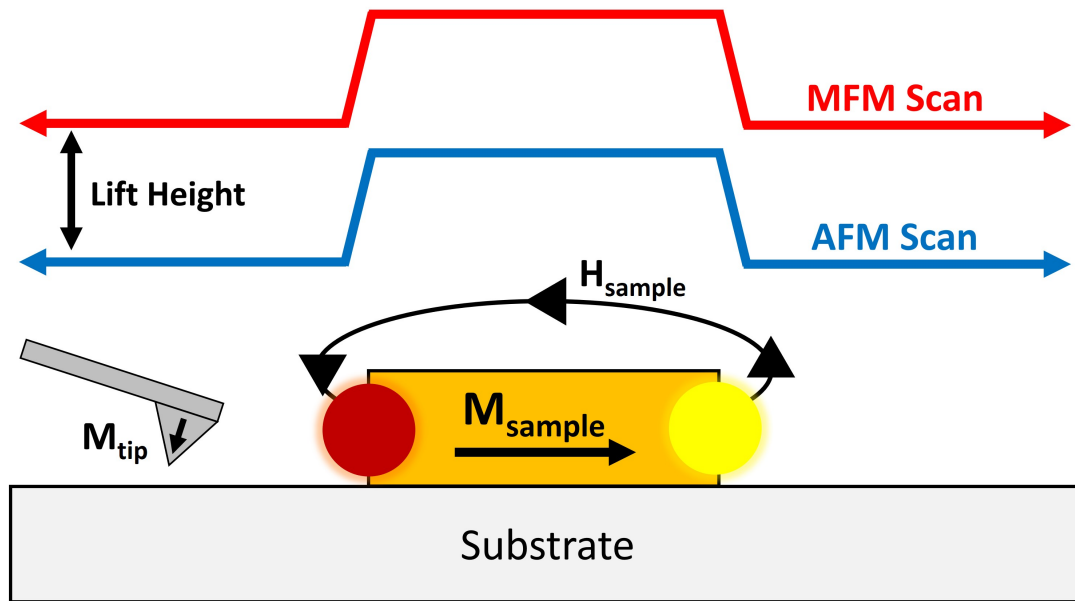


Figure 2.15: Illustration of the two-pass scanning method used for MFM measurements, here the lower probe surface is coated with a soft magnetic layer. The AFM path is scanned first, before the probe lifts by a set height and performs a second scan. Bright and dark lobes are placed at either end of the magnetic structure, to simulate the MFM contrast measured at opposing poles of a single domain magnet.

This raised scan was necessary because good quality MFM images require negligible non-magnetic interactions between the sample and tip, during this second pass, such as the atomic forces felt whilst scanning the AFM path. However throughout MFM scanning, the sample topography also had to be accurately accounted for, in order to isolate the small signal associated with cantilever deflections due to the sample stray magnetic fields. At a typical lift height of ~ 100 nm one should expect to pick up the long-range magnetic interactions with negligible short-range interactions. Although when measuring samples with large features along the z -axis, tip strike may be encountered, which diminishes with increasing lift height. Once again, this requires compromise. A higher lift height reduces the risk of data loss through tip strike, but also reduces the MFM resolution. Since a greater separation will weaken the sample-tip magnetic interactions and hence reduce the change in cantilever resonant properties. During MFM, it is crucial that \mathbf{H}_{tip} and \mathbf{H}_{sample} can not modify the magnetic configuration of one another. To this end, one must carefully select the MFM probe, ensuring the associated magnetic moment is great enough to prevent \mathbf{M}_{tip} being reversed by \mathbf{H}_{sample} , and low enough that \mathbf{H}_{tip} does

not influence M_{sample} . Herein, commercial low moment MFM probes were used, due to the relatively low coercive field typically displayed by $Ni_{81}Fe_{19}$ nanostructures. Table 2.2 gives details of the two MFM probes that have been used in this study.

Make	Model	m (10^{-13} emu)	H_c (Oe)	Tip Radius (nm)
Bruker	MESP-LM-V2	0.30	< 400	25
Nanosensor	SSS-MFMR	0.25	125	< 15

Table 2.2: Details of the two MFM probes used for measurements in this thesis, including magnetic moment, coercivity, and nominal tip radius of curvature. These data were taken from the specifications given on the web page for each probe.

Standard MFM systems are often not readily designed for the study of magnetic switching. Therefore, a custom-made electromagnet (see fig. 2.16a-b) was engineered by Dr Sam Ladak and Dr Matthew Hunt for the MFM system used in this thesis, which could be mounted on top of the sample stage, beneath the piezotube. This allowed in-plane magnetic fields to be applied to a sample, without the need for loading and unloading the sample. Aside from the obvious time saved by this, the electromagnet vastly benefits studies of magnetic switching, as one must align every image within a dataset to the same section of the sample. This process would have been extensively difficult and time consuming if the sample had to be moved in between every image. As seen in fig. 2.16a-b, four magnetic poles and coils surrounded a sample mounted on a SEM stub. During acquisition of MFM data presented in thesis, the electromagnet was configured to only generate fields along the A-C axis, although in the latter stages of this PhD, the electromagnet was reconfigured to allow users to apply fields along either the A-C or B-D axes. The electromagnet was connected to a power supply that was manually operated to adjust the supplied current, which in turn altered the generated magnetic field. Prior to conducting any experiments with a sample, it was crucial to calibrate the electromagnet. This involved suspending the Hall probe of a Gaussmeter directly between the two active poles, whilst varying the current supplied to the electromagnet. Figure 2.16c presents this field-current dependency for the positive and negative field directions, which shows a residual magnetisation of $\sim \pm 1$ mT. For both directions, a linear relationship is observed after the first data point, hence the $I = 0$ data points were neglected when calculating the gradient of either dataset. With this in mind, the positive and negative slopes yield gradients of (10.36 ± 0.04)

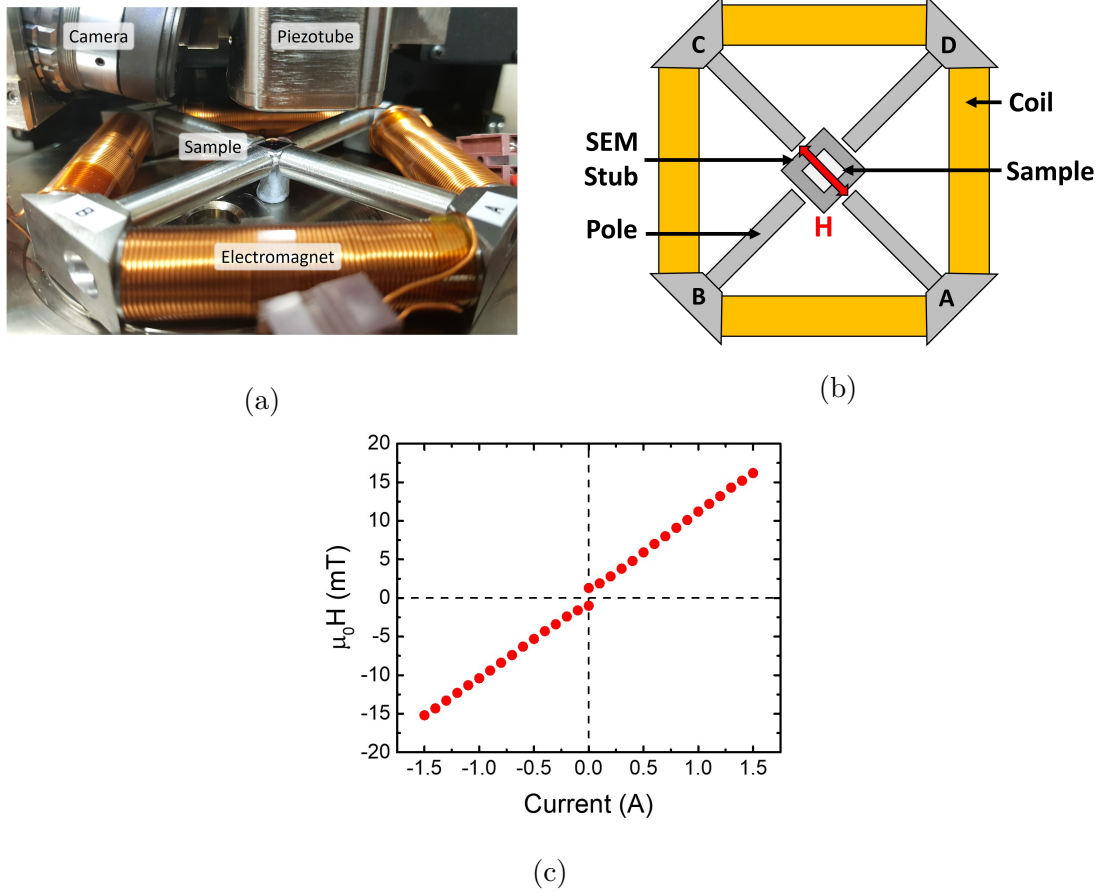


Figure 2.16: Bespoke electromagnet for the in-plane application of magnetic fields. **a**, Annotated photograph of the electromagnet seated on the AFM stage. A sample ($7\text{mm} \times 7\text{mm}$) was mounted on an SEM stub between the magnet poles. The coils were connected to a power supply in parallel. **b**, Diagram of the electromagnet, a red arrow annotates the applied field direction (H). **c**, Relationship between the applied current and the magnetic field produced by the electromagnet along the A-C axis, measured using a Gaussmeter.

mTA^{-1} and $(9.87 \pm 0.04) mTA^{-1}$, therefore this electromagnet was adjudged to show a current-field relationship of $\sim 10 mTA^{-1}$. Whilst some researchers wish to apply magnetic fields during MFM scanning, this was not necessary here. Therefore in this study, the probe was lifted by several cm prior to applying a field, such that M_{tip} was not influenced. Once the field was reduced to zero, the probe could be lowered for the next scan. When initially mounting the electromagnet, the SEM stub supported by Blu Tack, was pressed down until it appeared fixed in place. At least one hour was allowed to pass before any measurements were performed, giving time for the Blu Tack to settle, thus minimising any slight sample movements during scanning.

After capturing MFM images, the data often required processing to aid visual observations, this was typically performed using WSxM 4.0, a software package that allows AFM and MFM data to be viewed, processed, and analysed. Firstly, there were often a number of tip strike lines to remove, particularly when topography with significant features along the z-axis had been measured. This involved selecting the line/lines which needed to be removed, these were then replaced by an average of the data that was directly above and below the removed lines. Next, there was often some finite sample tilt during measurement. To correct for this, an automated flattening procedure was executed to flatten the data. This fitted a plane to each line in the raw data, which was then subtracted to eliminate any slopes or bows in the image⁷⁰. Lastly, the precise magnitude of the measured phase can vary from image to image, and so a manual adjustment of the contrast/brightness was typically performed in order to aid comparisons between images. This standard processing was performed for the majority of MFM data presented herein, any further processing for specific images will be outlined in the associated text.

When studying complex systems via MFM, the acquired signal can be difficult to interpret in some cases. To aid this, researchers have developed a method to simulate an approximation of the expected MFM signal for different magnetic configurations. This approximated MFM signal can be calculated as the divergence of the magnetisation ($\nabla \cdot M$)^{71,72}. This offers a reasonable approximation of MFM contrast because MFM is sensitive to the second derivative of H_z , which is related to $\nabla \cdot M$ by

$$\nabla \cdot M = -\nabla \cdot H = -\left(\frac{\partial H_x}{\partial x} + \frac{\partial H_y}{\partial y} + \frac{\partial H_z}{\partial z}\right) \quad (2.3)$$

It is noted that eq. (2.3) also incorporates H_x and H_y , which standard MFM is not sensitive to. Hence, the result may not entirely match experimental data, although this is still a useful tool to build confidence and provide insight into MFM measurements.

2.6 OPTICAL MAGNETOMETRY

Another technique for the magnetic characterisation of samples is optical magnetometry. Specifically, magneto-optical Kerr effect measurements were used in this study, a method which is well suited towards the analysis of magnetic dynamics within ferromagnets. Broadly put, MOKE magnetometry is sensitive to alterations

in the sample magnetisation. Alterations which are detected by monitoring the amplitude of a linearly polarised optical beam that is reflected from the region of interest.

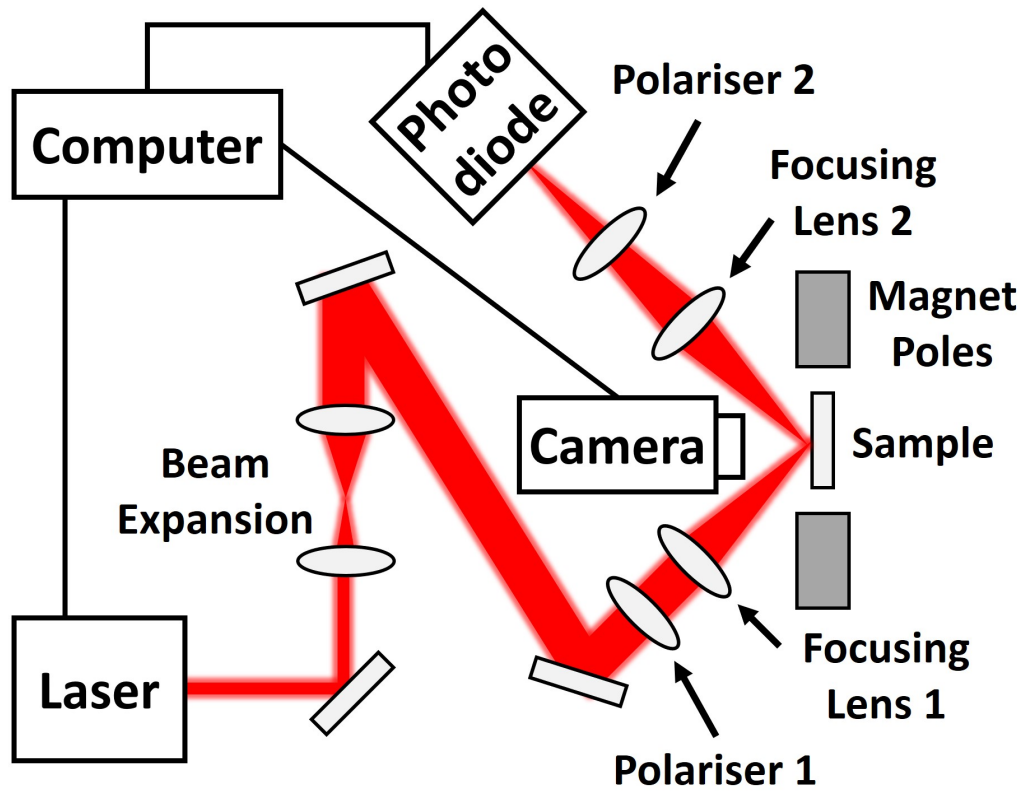


Figure 2.17: Top view of a schematic, showing the optical setup assembled for MOKE measurements in this study.

The main components of the MOKE setup used in this study are illustrated in fig. 2.17. A computer-controlled laser emitted an optical beam of user-defined power, which had a maximum power of 120 mW and a wavelength of 637 nm. The direction of the optical path was controlled by several carefully positioned mirrors. Initially the beam was expanded before being linearly polarised. A focusing lens was positioned such that the laser encounters the sample at the focus point, minimising the laser spot size, which was monitored with a camera. A minimum spot size of approximately $10 \times 10 \mu m^2$ was achieved during this study, measured using the camera. The sample was fixed to the end of an aluminium rod with vacuum grease, at it's other end this rod was connected to a motorised stage, allowing the laser spot to be scanned across the sample. This stage also allowed the sample to be rotated about it's out-of-plane axis. Movable electromagnetic poles sat either side of the

sample, typically within 1 – 2 mm of the substrate during measurements, although these were retracted for sample loading and unloading. Whilst separated by a sample (~ 2.5 cm), this electromagnet is capable of generating a 0.5 T linear magnetic field. After the laser reflects from the sample, it passed through a second focusing lens and a polariser orientated almost perpendicular to the first. The second polariser is also referred to as the analyser, both of these were Glan-Taylor polarisers. Finally, a photo-diode was positioned at the laser focus point, to detect the transmitted amplitude, and relay this information to the computer. Components which interact with the optical path prior to the sample, rarely required adjustments. However, in a real world experiment the sample is unlikely to be mounted perfectly flat, so there will be a unique, minor misalignment each time a sample is mounted. Therefore the reflected beam will propagate along a slightly different path, requiring the optics after this reflection to be realigned, this was also necessary following sample rotations.

This technique probes sample magnetisation by exploiting the MOKE, an effect which is governed by weak interactions between polarised light and magnets. If one considers a linearly polarised optical beam that is incident upon a sample, the MOKE describes a rotation in the beam's plane of polarisation, due to this laser-sample interaction. The degree of this rotation correlates with the magnetisation of the sample region which the optical beam interacts with. In the event of polariser 1 and 2 being orientated perpendicular to one another, then no signal would be detected by the photodiode if this rotation did not occur. Therefore, the magnitude of this signal detected by the photodiode is a measure of this rotation, which is directly related to the local magnetisation of the sample area that the laser interacts with. However, the detected signal tends to be of poor signal-to-noise quality when the two polarisers are orientated exactly perpendicular to one another. To aid this, polariser 2 was rotated until a minimum was found in the detected laser amplitude, before it was rotated in the reverse direction by a small margin known as the analyser angle. In a previous study using this MOKE setup, Dr Matthew Hunt determined the signal-to-noise ratio (SNR) of the data acquired by the photodiode as a function of analyser angle⁷³. This study concluded that an analyser angle of 2° maximised SNR when measuring magnetic nanostructures. Although, when measuring magnetic films, the detected signal was greatly increased and so the analyser angle is set to 1° to avoid saturating the detector.

Now, the origin for this rotation of the polarisation plane is considered, which

is analogous to the Faraday effect, where the polarisation plane rotates during transmission through a sample¹. The MOKE can be understood by considering how the electric field of the optical beam interacts with the spin-orbit coupling present in the magnetic sample. When an incident optical beam interacts with a sample, the oscillating electric field associated with the beam causes electrons in the sample to oscillate. A displacement vector (\mathbf{d}) to describe this interaction is written as

$$\mathbf{d} = \varepsilon \mathbf{E} \quad (2.4)$$

where ε is the dielectric constant of a material. Macroscopic linear response theory defines ε as a tensor, which takes a generalised form for an isotropic medium, given as¹

$$\varepsilon = \varepsilon \begin{pmatrix} 1 & -iQ_z & iQ_y \\ iQ_z & 1 & -iQ_x \\ -iQ_y & iQ_x & 1 \end{pmatrix} \quad (2.5)$$

where the Voigt vector (\mathbf{Q}) is a material constant. This describes the rotation of the plane of polarisation for an optical path, due to magneto-optical interactions, and is given by

$$\mathbf{Q} = Q_x \hat{i} + Q_y \hat{j} + Q_z \hat{k} \quad (2.6)$$

where Q_x , Q_y , and Q_z are the x , y , and z components of the Voigt vector respectively. An incident optical beam, that is circularly polarised, can be pictured as a superposition of photons with equal proportions of left (σ^-) and right (σ^+) handed circular polarisation (see fig. 2.18a). This beam interacts with a sample by rotating charges in the material, where σ^- yields anti-clockwise rotation, and σ^+ causes clockwise charge rotation. Atomic orbital angular momentum is also impacted by the incident beam, but in the opposing way to the charges. Due to spin-orbit coupling, this impact on orbital angular momentum produces energy contributions for σ^- and σ^+ with equal magnitude, but opposing sign. Effectively, this alters the refractive indices for the σ^- and σ^+ photons propagating through the sample, where the degree to which these are changed, depends on the local sample magnetisation. If the laser is incident on a region with net magnetisation, then σ^- and σ^+ will propagate with differing refractive indices, causing a phase shift, and a distinction in the reflected amplitudes of the two polarisation subsets. Now, the reflected σ^- and σ^+ lead to an elliptical superposition, with a plane of polarisation rotated by an

angle which increases with increasing sample magnetisation (see fig. 2.18b)¹.

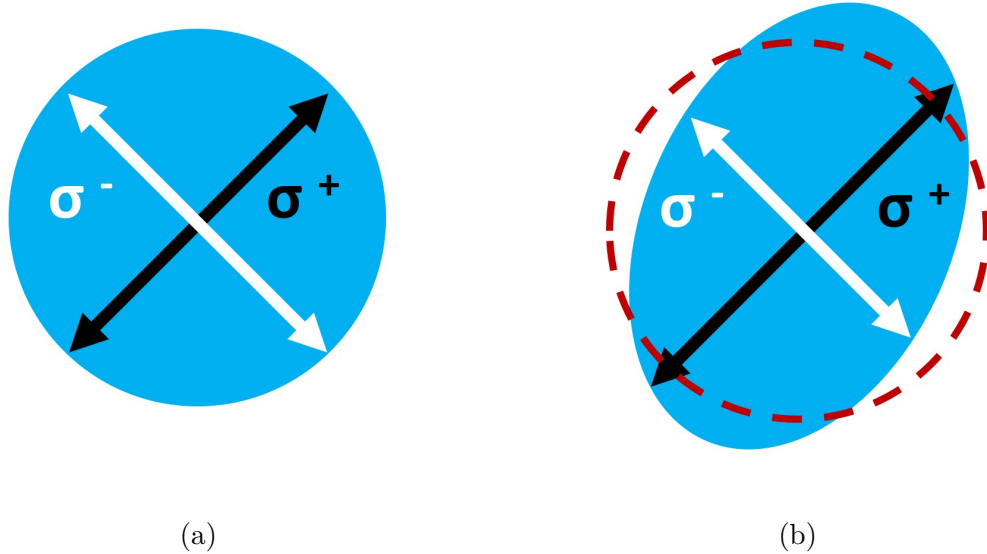


Figure 2.18: Superposition (blue) of left (white) and right (black) handed circularly polarised electric fields. **a**, Circular superposition when $\sigma^+ \approx \sigma^-$. **b**, Elliptical superposition when $\sigma^+ > \sigma^-$, dotted red outline is the perimeter of the circular superposition, for comparison. Adapted from¹.

MOKE magnetometry utilises this polarisation rotation, by recording and plotting the signal amplitude detected at the photodiode, as a function of applied magnetic field. This signal amplitude is a measure of the sample magnetisation, since a greater polarisation rotation leads to an increased number of photons passing through the analyser. One could generate a program to automatically vary the current supplied to the electromagnet. Hence, the applied field can be swept between positive and negative saturation, allowing a local hysteresis loop to be extracted from the sample area covered by the laser spot. Here, a gaussmeter directly measures the applied field magnitude, and so the local sample coercivity can be obtained. However, the signal amplitude is typically normalised between -1 and +1 in arbitrary units, meaning that the sample M_S value can not be directly probed. MOKE measurements of complex structures often exhibit poor signal-to-noise if only one field sweep is conducted. To reduce the impact of random noise, the applied field is usually swept between saturation points many times. A resulting hysteresis loop is then constructed from the mean detected signal across every field cycle.

Figure 2.19 illustrates three possible geometries, which MOKE measurements

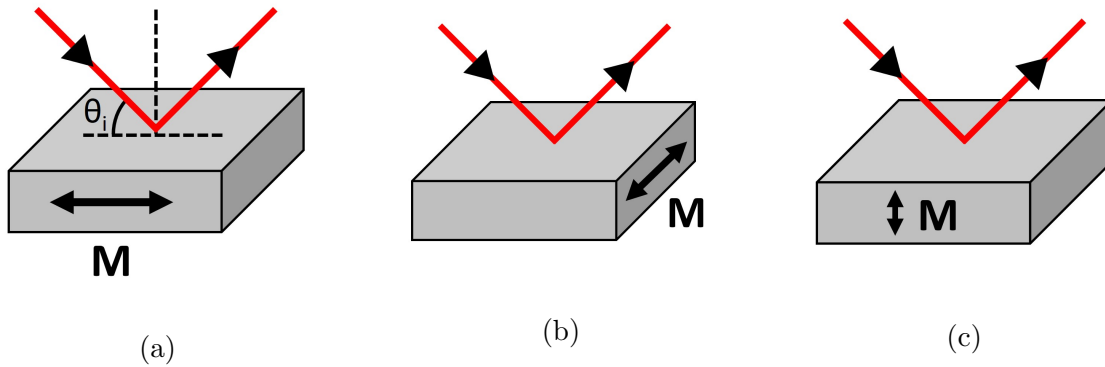


Figure 2.19: Illustrations of three geometries for MOKE measurements, adapted from¹. An optical beam (red) is incident by an angle (θ_i), upon a sample, where the direction of magnetisation reversal is annotated. **a**, Longitudinal. **b**, Transverse. **c**, Polar.

are typically performed in. Here, the key factor is the direction in which the magnetisation reverses with respect to the incident optical path. Therefore, when preparing the MOKE setup, one must first decide which magnetisation component is desired to be studied, and then arrange the apparatus into the associated geometry. These geometries correspond with the sample magnetisation orientating along the $\langle 100 \rangle$, $\langle 010 \rangle$, and $\langle 001 \rangle$ axes, though it is not always possible to measure these independently of one another. 3D structures clearly possess out-of-plane features, and so the magnetisation profile will likely possess characteristics that are both in-plane and out-of-plane. As a result, the measured signal may be a superposition of two or more of these components, which adds a level of complexity to data interpretation. Herein, only longitudinal and polar setups have been implemented for MOKE measurements.

2.7 SIMULATIONS

In the world of 3D nanomagnetism, analysis of subtle magnetic features can be very challenging, with data interpretation often being far from straight forward. To aid with this, researchers frequently turn to computational simulations, as a tool for providing additional insight. Many different methods for modeling magnetic structures are available, each of which have associated pros and cons. Therefore, one must carefully consider the geometry of interest, and the desired information, before selecting the simulation method which is most appropriate. For example, a Monte-Carlo protocol allows the modeling of extended structures, comprising of many wires. This is computationally accessible because each wire is approximated

as a single spin, possessing a magnetisation which can be tailored to emulate that of a wire. However, this technique is not suitable for studying finer details, such as the spin texture of individual wires, as well as the structure and dynamics of domain walls. For this, one can turn to micromagnetic simulations.

The principle of micromagnetic simulations is relatively straightforward, whilst the applications are limited only by one's imagination. One must first create an arbitrary geometry of a user-defined composition, then apply some protocol to this, depending on what information is desired. These simulations can be useful at any stage of the experimental sample's timeline. For instance, fabricating 3D nanoscale samples is often a complex, time consuming task, so one may wish to first conduct a variety of simulations in order to understand which geometry is worth pursuing. Simulations can be equally useful after a sample has been created and studied, as one may wish to computationally emulate the experimental analysis. This can provide a wealth of additional information, as the output data can be exported to 3D mapping software, allowing the evolution of energetics and spin texture to be visualised at pre-defined steps.

2.7.1 FINITE ELEMENT TECHNIQUES

Two techniques which are commonly used for micromagnetic simulations, are finite element (FE) and finite difference (FD). In this thesis, the former is predominantly employed, due to a greater efficiency in dealing with 3D curved surfaces. FE simulations (eg. the sphere shown in fig. 2.20) require the geometry to be defined as a tetrahedral mesh, where points on the mesh are separated by a user-defined length. This length parameter affects the influence of the exchange interaction, and so should be set below the exchange length, defined as the distance beyond which the exchange interaction rapidly decays to be negligible. Structures exhibiting curvature are considered throughout this thesis, and so simulated geometries in NMAG were defined with an adaptive mesh spacing of between 3 nm and 5 nm, allowing a finer mesh spacing to be used at the thinner regions of the geometry. The upper boundary of 5 nm in this mesh spacing range is still below the exchange length of $Ni_{81}Fe_{19}$, which is $\sqrt{2A/\mu_0 M_S^2 s} = 5.3$ nm when considering standard $Ni_{81}Fe_{19}$ values of $M_S = 8.6 \times 10^5$ Am^{-1} and $A = 1.3 \times 10^{-13}$ Jm^{-1} . Geometries were first created using an external software package, and saved as CAD files. Geometries were then converted into a usable format, by importing the CAD files into a meshing software

package, such as Netgen.

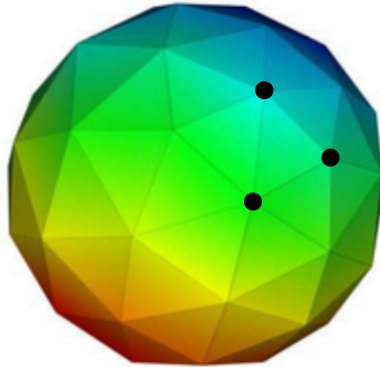


Figure 2.20: A finite element approach to creating a spherical geometry, comprised of a tetrahedral mesh⁷⁴. Three mesh points are annotated with black dots.

Herein, NMAG has been the FE package used to simulate magnetic materials⁷⁴. Like many other FE packages, NMAG is processed by CPU memory, and often requires a substantial memory allowance. To accommodate this, NMAG simulations in this study, were performed using the supercomputing unit known as Advanced Research Computing at Cardiff (ARCCA). To initiate a simulation, a directory containing at least three files was submitted to ARCCA. Firstly, a mesh file defined the geometry to be modeled, as discussed earlier. Secondly, a python script dictated what will occur within the simulation, defining material parameters, initial conditions, protocols to be executed during the simulation (eg. relaxation, field increments, hysteresis loop, etc.), and intervals at which data is saved. Lastly, a SLURM file provided technical details of the submitted job (eg. required memory, directory path, simulation to be executed, etc.).

Most NMAG simulations conducted in this study involved a relaxation from a pre-defined magnetisation, before an external field was applied with an incremented magnitude. To accurately model the behaviour of a ferromagnet, NMAG solves the Landau-Liftshitz-Gilbert (LLG) equation, integrated across all points on the mesh. This equation of motion is given by⁷⁴

$$\frac{d\mathbf{m}}{dt} = -|\gamma_P|\mathbf{m} \times \mathbf{H}_{eff} + \left(\frac{\alpha_D}{M_S}\right)(\mathbf{m} \times \frac{d\mathbf{m}}{dt}) \quad (2.7)$$

where $d\mathbf{m}/dt$ is the time-dependent response of a magnetic moment (\mathbf{m}) to an effective magnetic field (\mathbf{H}_{eff}). The effective field has several components,

which were discussed in chapter 1, these are the fields associated with the demagnetisation, exchange, Zeeman, and anisotropy energy terms. Whilst γ_P is a precessional term known as the gyromagnetic ratio, and α_D is the Gilbert damping constant. Only simulations that are effectively time-independent are considered in this thesis, which is achieved by setting the value of α_D to be much larger than the true value for $Ni_{81}Fe_{19}$. Zhou et al conducted a study of α_D in thin $Ni_{81}Fe_{19}$ films, this found α_D to vary depending on the film thickness and temperature⁷⁵. In all scenarios, this study found α_D to fall below 0.03. A value of 1 has been used for α_D throughout this study, reducing the time required to run each simulation.

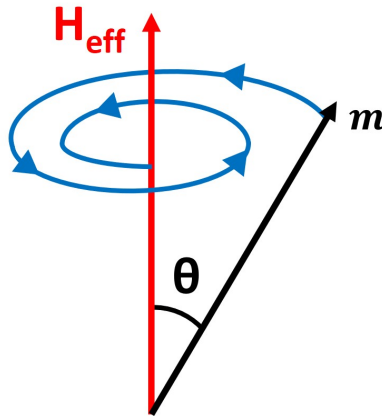


Figure 2.21: Motion of a magnetic moment (blue path), aligning to an external magnetic field, which are initially offset by an angle θ .

Each of the components in eq. (2.7) have a physical representation. The first term is $-\gamma_P |\mathbf{m} \times \mathbf{H}_{eff}|$ which describes the precessional motion of the magnetic moment. The second term is $(\frac{\alpha_D}{M_S})(\mathbf{m} \times \frac{d\mathbf{m}}{dt})$, which is associated with the damping of the precessional motion. Hence, the resultant motion precesses about the applied field direction, whilst aligning to it. During field application protocols, at every increment each moment will attempt to align with H_{eff} , such that θ exhibits the time-dependent response $d\theta/dt$. Each step is only completed when the system is settled, which occurs as $d\theta/dt$ tends towards zero, eventually falling below a user-defined threshold value. True time-dependent simulations allow users to observe the spin dynamics which occur during this settling process. Whilst this information can be very useful for analysis, these simulations can significantly increase the required processing power and memory allocation. Therefore, many researchers opt for time-independent simulations, where only the settled state is saved, after

$d\theta/dt$ falls below the threshold value. After completion, the output data required post-processing to convert each step into a VTK file, which could then be loaded into a 3D mapping software for inspection. A text file was also generated, containing values for the applied field and each component of the system energy density. One may wish to export this file, for further data analysis with an external method, such as python programming or the graphing software package, Origin.

It is a straightforward task to vary the magnetisation of the simulated material, simply by altering the magnetic properties defined in the python script. However, only $Ni_{81}Fe_{19}$ structures were experimentally studied herein, and so magnetocrystalline anisotropy was defined to be zero throughout. All simulations were also conducted without the consideration of thermal effects (i.e. $T = 0$ K). When comparing these simulations to experimental measurements at room temperature, one can expect an increased coercive field, approximately by a factor of 5, in the modeled result. Despite this difference in H_C , the spin texture itself is believed to show a strong agreement between simulations and the experimental equivalent⁷⁶.

2.7.2 FINITE DIFFERENCE

A second technique for computing micromagnetic simulations is the finite difference method. This follows a similar approach to FE, whereby a geometry is formed using a sequence of discrete points, with user-defined spacing. However here, the simulated geometry is constructed from a 3D grid of cuboidal blocks (see fig. 2.22).

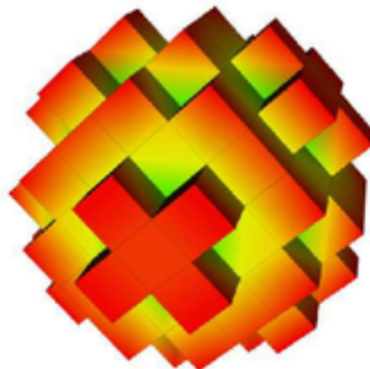


Figure 2.22: Finite difference method for simulating a spherical geometry⁷⁴. Here, the size of each cuboidal cell is exaggerated to clearly show how the sphere is produced. In reality, a far smaller cell size would be defined, leading to smoother curvature.

Comparably to the FE method, FD micromagnetic simulations solve the LLG equation at the centre of every cell on the grid, to model the behaviour of a magnetic structure. In this thesis, FD simulations were performed using MuMax3, a GPU-accelerated program for the simulation of nanoscale and microscale magnets⁷⁷. MuMax3 exhibits a greater efficiency in simulating planar magnets, when compared with the FE equivalent. This is largely due to the lower memory requirements associated with the FD method of discretisation, meaning that larger complex systems can be investigated. In addition, whilst NMAG simulations typically require a supercomputer, MuMax3 allows many systems to be modeled using only a PC. Although, when investigating larger geometries, it is significantly advantageous to run MuMax3 on a system that is well-optimised for processes requiring GPU memory.

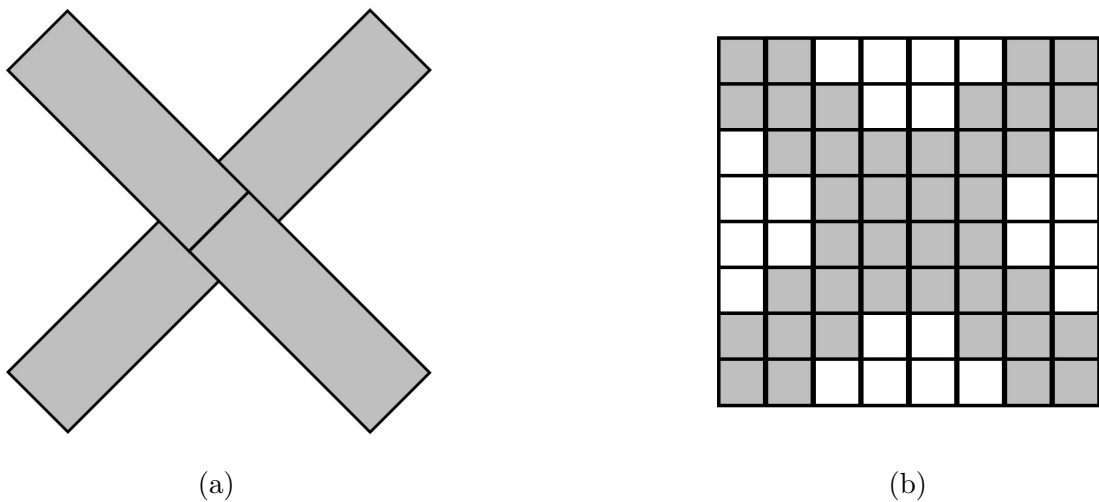


Figure 2.23: Illustration showing how a desired geometry translates to cuboidal grid of cells. **a**, Top view of an associated tetrapod geometry. **b**, Top view of FD cell grid. Grey cells simulate a user-defined magnetic material, whilst white cells are empty space. Once again, cell size is exaggerated to clearly display the FD method.

Figure 2.23 depicts one issue with the FD method when considering non-planar geometries. In fig. 2.23b, an example of a tetrapod is shown, formed from a 3D cell grid that is well-optimised for processes requiring GPU memory. However it is not possible to only define cells associated with the 3D magnetic structure. Instead, a cuboidal region must be defined, which entirely encompasses the magnetic material. Therefore, cells attributed to empty space are unavoidable in non-planar examples, thus reducing the simulation efficiency, due to these empty cells requiring a portion of the total memory allocation. Whilst this drawback is inescapable, it is still possible to study complex structures with MuMax3, providing that a processing unit with

sufficient GPU is accessible. Unfortunately for FD simulations, supercomputers tend to give a greater focus to CPU memory. Meaning that some large magnetic structures may remain either impractical or simply out of reach for now, particularly those which exhibit curved surfaces, and possess significant 3D features. It was therefore decided at an early stage of this PhD that NMAG is better optimised than MuMax3 to model the complex, 3D structures that have been studied experimentally for this thesis.

Chapter 3

Exploring Two-Photon Lithography for 3D Magnetic Nanostructure Fabrication

*‘So... physics. Physics, eh? Physics.
Physics, physics, physics!
Physics, physics, physics, physics,
physics, physics, physics.
I hope one of you is getting all this
down.’*

DOCTOR WHO

3.1 INTRODUCTION

This chapter will present and discuss the efforts which have been made towards fabricating and characterising 3D magnetic nanostructures in a frustrated geometry using a combination of TPL and thermal evaporation.

In 2018, Williams et al reported that TPL is a powerful and versatile technique for the fabrication of complex 3D structures with sub-micron feature size⁷⁸. Whilst this study touched upon the remarkable potential of TPL within the world of 3D nanomagnetism, the combination of a positive-tone photoresist

and electrochemical deposition were unable to yield small enough feature sizes to result in single-domain nanowires. Using positive-tone photoresists is a subtractive manufacturing technique that is similar to more widely used 3D magnetic nanowire fabrication, which utilises cylindrical pores in anodised alumina as templates to be filled in with a magnetic material^{79,80,81}. However, TPL boasts the significant benefit that extended, complex templates may be designed with extensive user-control over the design. Unfortunately, during a chemical development procedure dark erosion leads to an increased pore diameter compared with the user-defined specifications, which resulted in multi-domain structures. For many applications in this rapidly expanding research field, the ability to repeatably create nanostructures which constrain the magnetisation along a single axis is essential. The work presented in this thesis explores how recent advancements in TPL can push on the boundaries of nanoengineering magnetic materials in 3D, with particular focus on the topic of frustration. Using TPL with negative-tone photoresists is an additive manufacturing technique (see section 2.1), and hence does not suffer from a dark erosion induced feature size enhancement. As a result, high-resolution negative-tone photoresists are capable of sub-200 nm feature sizes, less than half of the feature size achieved using positive-tone photoresist with TPL⁴⁵.

Here is the starting point for the research conducted in this thesis, to explore the possibilities offered by TPL and negative-tone photoresists to expand ASI studies into the third dimension, to more closely capture the pyrochlore arrangement of spins in bulk spin-ice crystals. To this end, research efforts were focused upon the production of a 3D nanowire lattice (3DNL) by initially fabricating a polymer scaffold in the diamond-bond lattice geometry, before depositing a $Ni_{81}Fe_{19}$ film upon the sample from above. This approach was chosen because, in principle, it is similar to existing 2D ASI fabrication, whereby a line-of-sight deposition was used to deposit a thin magnetic film upon a pre-existing template, that was fabricated using a secondary technique. However, instead of depositing $Ni_{81}Fe_{19}$ on the substrate and removing the photoresist template, the magnetic material was deposited upon the upper surface of a 3D scaffold to capture the geometry of a diamond-bond lattice. Before embarking on any significant studies of these complex structures, it was prudent to firstly characterise $Ni_{81}Fe_{19}$ sheet films and planar wires deposited via thermal evaporation. Next, $Ni_{81}Fe_{19}$ nanowires and micropads were deposited upon cuboidal polymer scaffolds, allowing the magnetic structures to be raised above the substrate. The magnetic properties of these raised, planar structures were probed via MFM, and these are readily comparable with numerous examples in the

literature. Studying these more rudimentary geometries proved highly beneficial when attempting to understand more complex 3D nanostructured magnetic systems.

After optimising the structure design and fabrication parameters, a first example of a 3D $Ni_{81}Fe_{19}$ nanowire lattice was fabricated upon a polymer scaffold that extended by one unit cell along the z-axis. AFM measurements were found to precisely track the high-ranging 3D topography of the upper nanowire layers in these lattices. Unfortunately, a feature of this fabrication technique is that structures are surrounded by a $Ni_{81}Fe_{19}$ sheet film. A simple calculation indicated a scaffold that is one unit cell in height to be insufficient in magnetically decoupling the 3DNL from the surrounding permalloy film and intrinsic permalloy nanoislands. One solution to this issue was to simply increase the number of scaffold unit cells along the z-axis to five. Thereby increasing the separation between the substrate and 3DNL, such that any stray magnetic fields associated with the substrate film become negligible below the lowermost point on the 3DNL. Large arrays of 3DNL structures were created using systematically varied fabrication parameters in order to determine the minimal feature size which can be achieved, whilst maintaining the structural integrity of the scaffold. SEM measurements were taken to determine the 3DNL minimum feature size, defined as the lateral nanowire width.

Conventional magnetometry techniques have been employed for the magnetic characterisation of the 3DNL. MOKE measurements provide an insight into the switching mechanisms occurring in the nanowires under an applied field. Whilst MFM has allowed the direct visualisation of the magnetic configuration throughout the lattice. Reversing the MFM tip magnetisation is seen to invert the contrast originating from the $Ni_{81}Fe_{19}$ wires, demonstrating that this signal is indeed able to probe the magnetic profile of a 3DNL. Finite element simulations using NMAG were performed upon single wires, bipods, and tetrapods, each acting as 'building blocks' of the 3DNL. A number of magnetic characteristics have been modelled by this method, such as remanent states, switching mechanisms, hysteresis loops and domain wall structure.

In this chapter, finite-difference simulations were performed by Dr Matthew Hunt of Cardiff University, finite-element simulations were conducted by Mr Arjen van den Berg of Cardiff University. All sample fabrication, physical characterisation, and magnetic characterisation were performed by myself unless otherwise stated. Micromagnetic simulations presented after this chapter were conducted by myself.

3.2 PERMALLOY FILMS AND PLANAR MICROWIRES

As discussed in section 2.1, TPL allows the production of polymer scaffolds with significant user-control over the fabricated geometry in all three dimensions. It can therefore be hypothesized that a 3D network of $Ni_{81}Fe_{19}$ nanowires could be formed by engineering a suitable 3D polymer scaffold, serving as a template to be used in a line-of-sight $Ni_{81}Fe_{19}$ deposition. This deposition would coat the entire upper surface of the sample, including the scaffold, hence resulting in a 3DNL on top of the polymer structure. Exploring the potential of this proposed methodology is the main objective of this chapter.



Figure 3.1: Optical microscopy images of cuboidal trenches with four different aspect-ratios in positive-tone photoresist. **a**, A dose array, laser power increases in 5% increments (left to right) and scan speed increases in $3000 \mu m s^{-1}$ increments (bottom to top). **b**, Magnified view.

An important step of the proposed fabrication technique, is the ability to reliably deposit a uniform film of $Ni_{81}Fe_{19}$. As such, a study of $Ni_{81}Fe_{19}$ sheet films and planar microwires that were deposited using a thermal evaporator at Cardiff University was conducted. $Ni_{81}Fe_{19}$ sheet films approximately 50 nm thick were deposited upon blank glass substrates, as measured using a QCM during growth. To measure this thickness directly, a calibration sample was present during each deposition. Calibration samples were created using TPL to form an array of trenches in a uniform layer of positive-tone photoresist, very similar to the conventional 2D ASI fabrication technique. Every trench was defined with a width of $2 \mu m$, whilst the length varied with values of 2, 4, 8, and $16 \mu m$. Figure 3.1 shows optical images of a calibration sample prior to a metal deposition. As is customary, trenches

were produced in a dose array (see fig. 3.1a) to ensure a high yield of satisfactory structures. Here, the scan speed varied between $3000 \mu\text{m}\cdot\text{s}^{-1}$ and $30000 \mu\text{m}\cdot\text{s}^{-1}$ in increments of $3000 \mu\text{m}\cdot\text{s}^{-1}$ (bottom to top), the laser power varied from 30% to 75% in 5% increments (left to right). Trenches in the upper-left of the array received the lowest dose during TPL, meaning that these regions were least soluble during development, as a result they do not appear to have fully developed down to the substrate. Conversely, trenches in the lower-right received the greatest dose and were most soluble during deposition. This causes the roughness seen at the trench edges, associated with dark erosion, which occurs when photoresist that was not exposed during TPL is developed.

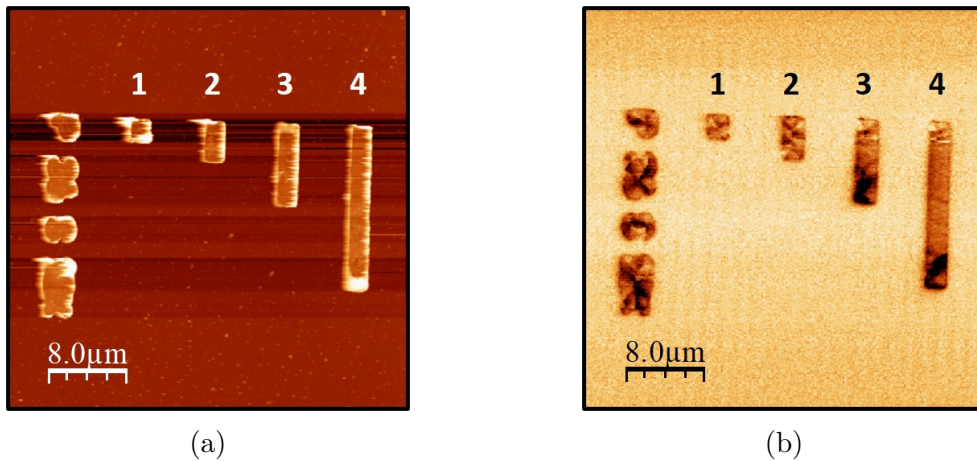


Figure 3.2: **a**, AFM and **b**, MFM scans of planar $Ni_{81}Fe_{19}$ microwires which are each annotated with a numerical index. Wire dimensions exhibit a constant thickness of 50 nm and width of $2 \mu\text{m}$, the lengths of wires 1-4 are 2, 4, 8, and $16 \mu\text{m}$ respectively.

A deposition and subsequent lift-off procedure yielded $Ni_{81}Fe_{19}$ microislands on the glass substrate. Figure 3.2a-b displays AFM and MFM measurements of a calibration sample respectively, these images show microwires with a constant width of $2 \mu\text{m}$, and lengths of 2, 4, 8, and $16 \mu\text{m}$ for wires 1-4 respectively. On each calibration sample, a dose array of trenches was fabricated to ensure a high yield. Islands that are seen on the left-hand side of each image exhibiting an unorthodox shape, are the result of text that was placed next to each set of trenches, identifying the relevant fabrication parameters. Bright regions surrounding the borders of the wires indicate an increased height of 30-100 nm, likely due to a small portion of unexposed photoresist remaining upon the deposited material. This has been documented previously in studies where metal has been deposited into positive-tone photoresists⁷⁸. Note that these edges are not seen in the associated MFM signal,

again suggesting it is only photoresist and not impacting the magnetic configuration of the wires. Figure 3.3 shows five line profiles that were measured from the AFM data in fig. 3.2a. The aforementioned peaks either side of the wire can clearly be seen, extending approximately 30-100 nm above the profile of the wire. A dotted line is plotted at 50 nm, about which the Z position associated with the deposited $Ni_{81}Fe_{19}$ fluctuates. These fluctuations result from a combination of the surface roughness associated with the glass substrate as well as roughness intrinsic to a $Ni_{81}Fe_{19}$ film associated with the grain structure.

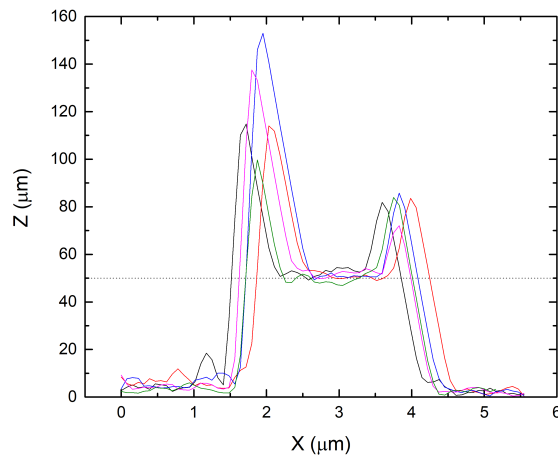


Figure 3.3: Five line profiles, measured by AFM, from the microwires shown in fig. 3.2. A dotted line indicates a thickness of 50 nm.

Figure 3.2b shows the associated MFM scan, illustrating the microwire magnetic configuration which could be measured with a low moment MFM probe. A clear magnetic domain structure is visualised in all four wires, as well as in the $Ni_{81}Fe_{19}$ islands associated with fabrication parameter text. Additionally, having four wires with constant width and thickness, whilst varying the length allows the effect of aspect ratio (of length and width) on the resulting domain structure to be investigated. Wire 1 possesses an aspect ratio of 1:1, unfortunately the domain configuration is difficult to reliably identify due to the finite resolution of the image. The expected remanent state of a planar structure with this aspect ratio and negligible magnetocrystalline anisotropy is a Landau pattern possessing flux-closure⁸². This configuration is expected, since a 1:1 aspect ratio results in each boundary producing a demagnetisation field that is equal in magnitude, meaning that shape anisotropy does not constrain the magnetisation along one single axis. Wire 2

exhibits an aspect ratio of 2:1, here a remanent domain structure can be identified. The increased length compared to wire 1 causes asymmetric demagnetisation fields at the long and short boundaries. Here, this asymmetry is not significant enough to constrain the magnetisation along the wire long-axis, and so a flux-closure domain pattern is produced. However, the increased shape anisotropy does perturb the domain structure, leading to a pattern resembling a single cross-tie state⁸². This spin texture leads to the observed signal because standard MFM is sensitive to the second derivative of M_Z , which is most prominent at DWs in planar microwires and microstrips⁵². Wire 3 displays an aspect ratio of 4:1, where regions of opposing contrast have separated to opposite ends of the wire, indicating the demagnetisation field associated with the elongated boundary is substantial enough to constrain the wire into a single domain state. This configuration yields significantly increased stray fields and hence magnetostatic energy compared with wires 1 and 2, although the exchange energy is minimised as only a single domain is present. Visual observations suggest that wire 3 exhibits an S-state⁸². Lastly, wire 4 has an aspect ratio of 8:1 which shows a similar, yet far more pronounced single domain state. Here, a C-state⁸² has formed due to the significantly enhanced shape anisotropy compared with wires 1-3.

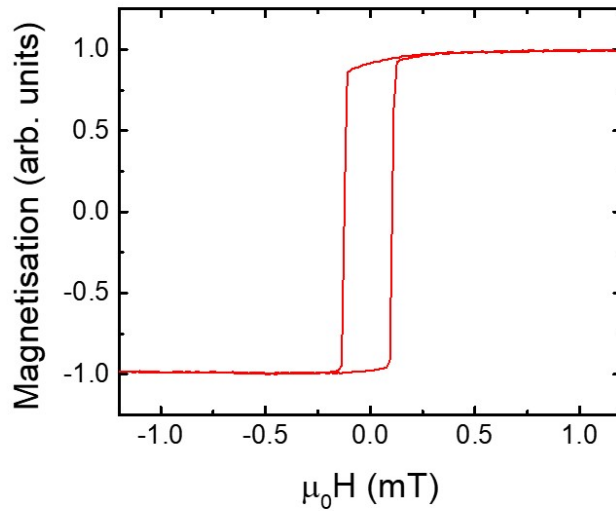


Figure 3.4: Hysteresis loop obtained via MOKE measurements of a 50 nm thick $Ni_{81}Fe_{19}$ sheet film.

One drawback of the proposed methodology for 3D nanostructure fabrication

is that the structures would be surrounded by a sheet film after deposition. Unfortunately, conventional lift-off procedures are impractical as these would remove the polymer scaffold. Therefore, a key question is to what extent does the surrounding film contribute to any signal measured from the desired nanostructure? To explore this, MOKE measurements (fig. 3.4) were taken from the sheet films that were grown alongside the calibration samples in a longitudinal setup, so that these may be compared to data obtained from $Ni_{81}Fe_{19}$ nanostructures. A single sharp transition in magnetisation is seen as the applied magnetic field sweeps between positive and negative saturation, indicating the switching is dominated by DW motion with only a small amount of rotation evident towards the end of the transition. A coercivity of $\sim 0.15mT$ is measured from the loop, in close agreement with examples in the literature^{83,84}, a direct consequence of the near zero magnetocrystalline anisotropy and magnetostriction associated with $Ni_{81}Fe_{19}$ ⁸⁵. These measurements give a very promising indication that a 50 nm $Ni_{81}Fe_{19}$ deposition is suitable for the fabrication of a nanowire lattice which can be probed via standard magnetometry techniques.

3.3 RAISED PERMALLOY NANOWIRES AND MICRO PADS

Studying $Ni_{81}Fe_{19}$ films and microwires was very beneficial in calibrating the deposited film thickness and demonstrating that low moment MFM probes can clearly determine the magnetic configuration of 50 nm thick planar microwires. This also proved that TPL can be used to make single domain wires on a planar substrate, although it is not possible to fabricate 3D structures in this way, since any pores extending along the substrate plane would not be infiltrated during deposition. Therefore, focus is now turned towards the hypothesized methodology of fabricating magnetic nanostructures upon 3D polymer scaffolds, using TPL with a negative-tone photoresist. However, there is a gulf of complexity separating the characterisation of planar microwires on the substrate, and nanowires arranged in a 3D diamond lattice geometry upon a polymer scaffold. As an intermediate step, a simple grid of nanowires and micropads lying parallel to the substrate plane, were fabricated by TPL with negative tone photoresist and thermal evaporation, seen in fig. 3.5. Here, the magnetic structures were positioned upon a polymer scaffold so that they were raised above the substrate. The polymer structures were $1.5\mu m$ in height, with widths of 0.3, 0.6, 1.1, 2.1, 3.1, 4.1 μm (left to right as viewed in fig. 3.5a), with the same values in length (bottom to top), the $Ni_{81}Fe_{19}$ layer is 50 nm thick. To aid the

structural stability of the polymer wires and pads, a large cuboidal polymer base was first fabricated upon the substrate, of dimensions $60 \times 60 \times 2 \mu\text{m}^3$. The scaffolds for the wires and micropads were then produced upon this large flat pad. To maximise the yield of usable samples, the array seen in fig. 3.5 was repeated in a 3×3 grid, the edges of adjacent arrays are visible in both SEM images. It is noticeable that dark lines can be seen on the surfaces of all structures which have an area greater than $1 \mu\text{m} \times 1 \mu\text{m}$. To understand the origin of these, one must recall that TPL produces 3D geometries by tracing an ellipsoidal voxel along individual lines to build up a structure. Therefore, these dark lines are due to slight undulations between adjacent lines of polymerised material⁸⁶. One could minimise such undulations by further optimising the hatching parameter which governs the spacing between individual lines that are adjacent along the substrate plane (see section 2.1). However, for the purposes of this study further optimisation has not been required.

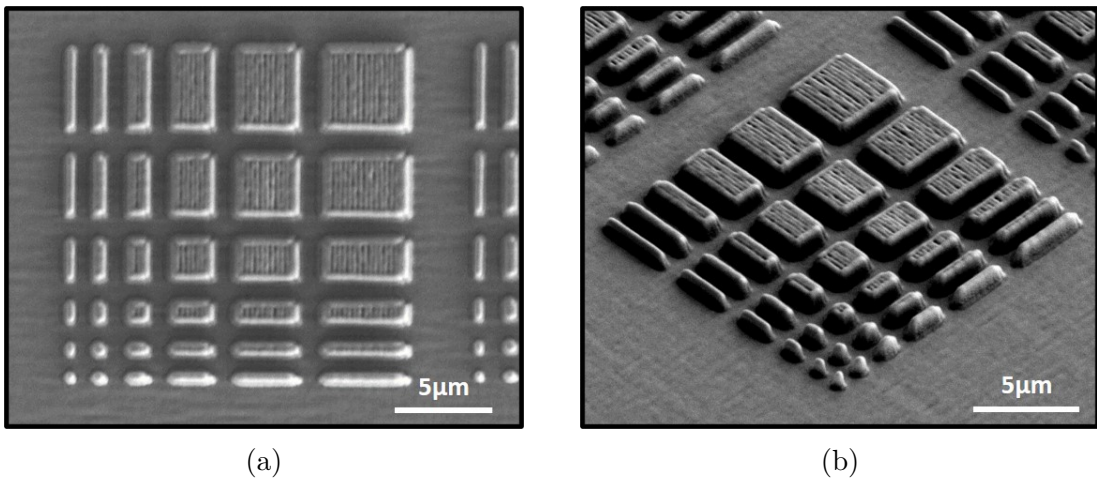


Figure 3.5: Scanning electron micrographs showing a 6×6 array of $Ni_{81}Fe_{19}$ nano/micro wires and micropads from **a**, top view and **b**, a 45° tilt.

Significant parallels can be drawn between the $Ni_{81}Fe_{19}$ wires in this system and similar $Ni_{81}Fe_{19}$ wires arranged in a diamond lattice geometry. For example, the narrowest wires here are likely to exhibit a comparable feature size and cross-sectional geometry to similar wires in a 3D ASI. Hence, these in-plane wires were expected to provide a strong indication as to whether similar wires in a 3D ASI would be Ising-like. However, those shown in fig. 3.5 can be conveniently used to examine the effect of aspect ratio upon the resulting domain structure, via AFM and MFM. In addition, these structures are far flatter than a diamond lattice, greatly simplifying the process of capturing MFM images with minimal damage to

the probe or sample. Therefore, these samples serve as a useful proof-of-principle test that suitable MFM signal can be acquired from magnetic structures situated upon scaffolds with relatively high-ranging topography, prior to studying far more time complex structures.

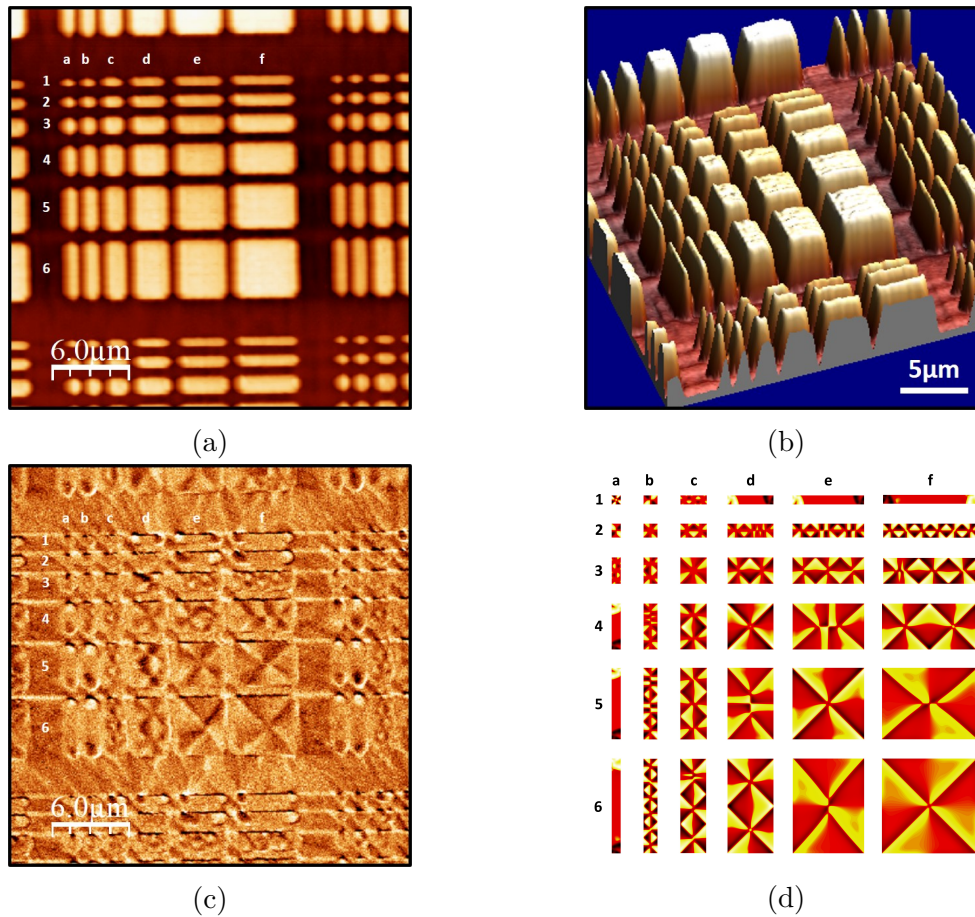


Figure 3.6: $Ni_{81}Fe_{19}$ nano/micro wires and pads. **a**, $25\ \mu m \times 25\ \mu m$ AFM scan. **b**, 3D representation of the AFM data. **c**, Associated MFM scan. Annotations assign a unique index to each structure, whereby 1-6 indicate rows and a-f indicate columns. Black arrows indicate direction of magnetisation. **d**, MuMax simulations of the MFM contrast associated with each remanent state. Each cuboid was simulated individually, the resulting states are compiled here.

Figure 3.6 presents AFM and MFM data captured from these wires and pads using a low moment MFM probe. In order to attain reliable MFM data, it is crucial that firstly the topography is closely tracked in the AFM data, allowing this to be corrected for during the second pass. Comparison between SEM (fig. 3.5) and AFM (fig. 3.6a-b) shows excellent agreement, indicating the AFM probe is closely tracking the 3D topography. Sharp, well defined edges to the nano/micro

structures are measured in fig. 3.6a indicating the feedback settings are suitably optimised, thus building confidence in the associated MFM data (fig. 3.6c). Despite this, an artefact is noted in the MFM data, intense strips including both bright and dark contrast are present immediately above each row of nanostructures. These are considered to be a result of the sudden $1.5\mu m$ increase in Z position, and not associated with the magnetic nanostructures. In fig. 3.6b, roughness can be seen on the upper-surface of pads and wires, this is predominantly associated with the afore mentioned undulations between adjacent lines of polymer which make up the scaffold. This roughness is not seen in the MFM data, indicating the feedback settings to be well optimised such that the topography is suitably accounted for.

Inspecting fig. 3.6c, a clear domain structure is observed for each magnetic island apart from 1a-c, 2a-c and 3a-b. These structures lacking strong MFM contrast each cover an area of $< 0.7\mu m^2$ of the $25\mu m \times 25\mu m$ region captured, therefore the expected contrast is likely lost due to the finite resolution of the acquired image. The islands that do exhibit distinctive MFM signal follow a similar trend to that which has been observed in fig. 3.2. Whereby islands with the lowest aspect ratio of 1:1 (4d, 5e and 6f) appear to have flux closure, whilst also possessing the fewest number of domains of any multi-domain structure. In each case, a Landau state⁸⁷ containing four domains orientated in either a clockwise or anti-clockwise state is observed, similar to the 1:1 aspect ratio micro-pad seen in fig. 3.2. This domain structure is seen for all islands of 1:1 aspect ratio regardless of physical dimensions. It is a result of the four island boundaries possessing identical dimensions, thus producing equivalent demagnetisation fields. Coupling this with the near-zero magnetocrystalline anisotropy of $Ni_{81}Fe_{19}$ leads to a minimal number of domains. This state is formed to, as far as possible, eliminate the external stray field and hence minimise the magnetostatic energy. Slightly increasing the aspect ratio to 4:3 (islands 5f and 6e) breaks the symmetry between all 4 boundaries, thus producing an offset between demagnetisation fields along X and Y. Here, this offset is insufficient to drastically alter the domain structure. Hence the result is a Landau state once again, though with the domains orientated along the island long-axis being elongated with respect to the short-axis counterparts. Further increasing the aspect ratio follows the trend seen in fig. 3.2, whereby additional domains form due to the growing offset in demagnetisation terms. This is clearly seen in 4e, 5d, and 6d which each exhibit a diamond state, as well as 4f where a single crosstie state is seen⁸⁸. Islands 3e-f, 5c, and 6c exhibit additional domains, though the exact configuration of these islands is difficult to characterise due to the

finite image resolution. To maintain flux-closure as far as possible, these islands are likely to possess a multi-diamond state, a multi-crosstie state, or a combination of the two⁸⁹. Above this aspect ratio of 4:1, a number of single domain islands are visible, indicated by regions of opposing contrast located at opposing ends of the long-axis (1d-f, 2e-f, 4a, 5a-b, 6a-b). Though in each case it can not be distinguished if the result is a C-state or an S-state, due to the finite image resolution.

To help understand if the novel fabrication technique used here affects the resulting domain structure, these observations can be compared with simulations of planar structures with equivalent dimensions. Figure 3.6d shows an array of planar structures, modeled using the finite-difference simulation package MuMax. Here, the remanent state of each structure is shown after relaxing from an initially randomised magnetisation, the result is then coloured with the associated MFM signal that is expected for the remanent spin texture. A close comparison is seen between the simulated and measured data, with a few exceptions. Notably, islands 4e and 5e are single crosstie in the simulations and diamond state in measurement whereas the opposite is true for island 4f, though this is a subtle distinction. A key difference between fig. 3.6c and d is the aspect ratio required for a single domain state, where 10 single domain wires are seen in the MFM data whilst only 6 are found in the simulations. Wires 2e-f, 5b, and 6b are the distinguishing structures, meaning that MuMax indicates planar wires which possess a width of ≥ 600 nm should be multi-domain, and so it is interesting that this is not the observed to be the case in the physical system. Two main differences exist between the measured and simulated structures which may explain this distinction. Firstly and most obviously, the measured structures do not exist in isolation and so may be magnetostatically coupled with one another as well as the surrounding sheet film. Any coupling between neighbouring islands could favour the formation of single-domain states in a head-to-tail configuration. Secondly, the geometry of the measured structures is expected to differ from planar structures at the edges, due to the ellipsoidal voxel used during the TPL stage of fabrication. This voxel geometry results in curved edges which can be seen in the SEM images in fig. 3.5, such curvature would effectively reduce the wire width, which may explain why these wires are single domain in the MFM data. The cross-sectional geometry of wires produced with this fabrication technique will be further considered later in this chapter. Lastly, simulations allow the resulting state to be viewed in significantly enhanced detail, so it can be seen that wires 1d-e, 4a, and 5a yield an S-state whilst wires 1-f and 6a exhibit a C-state, following the expected trend for single domain wires⁸².

Here it has been shown that coupling TPL and thermal evaporation to deposit a thin film of $Ni_{81}Fe_{19}$ upon a 3D polymer scaffold can lead to single-domain magnetic nanowires suspended above the substrate. Furthermore, MFM can directly image the magnetic configuration of such structures, thus providing a basis for fabricating and probing a 3DASI using this methodology.

3.4 REALISING A 3D FERROMAGNETIC NANOWIRE LATTICE

In this section the fabrication and physical characterisation of a first example of a 3DNL is discussed, here the nanowires are arranged in the diamond lattice geometry in order to precisely emulate the arrangement of atomic spins found in spin-ice.

Fabricating the scaffold for such a complex system is far less straight forward than was the case in the previous section. To simplify matters, initial fabrication efforts will focus upon a diamond lattice polymer scaffold that extends by only one unit cell along the Z direction. An essential aspect of a 3D ASI is that the wires are single domain and hence act as effective Ising spins, meaning that the desired feature size must approach the theoretical minimum of ~ 150 nm, to ensure this. With this requirement in mind, achieving wires possessing suitably small dimensions is one of the main barriers that must be overcome to realise a 3D ASI. Without this barrier the task would be simpler, as one could make use of the conventional TPL process. This would involve importing an STL file of the desired geometry into DeScribe, before an automated procedure converts this into a format which can be traced out by the voxel using the galvo scan mode (see section 2.1). Figure 3.7 shows an example of how such an STL file would appear. Unfortunately, the automated conversion process is not well suited for producing structures with feature sizes approaching the theoretical minimum, as discussed in section 2.1. Hence, using this method would not fully capitalise on the enhanced resolution that is attainable with negative-tone photoresist in comparison with positive-tone photoresists, which is one of the key aims of this study.

The most obvious solution is to use the piezo scan mode, whereby the voxel can scan along the $\langle 111 \rangle$ axis. Using this scan mode means that each wire in the scaffold can be formed by tracing the voxel along an individual line that is parallel with the wire long-axis (see section 2.1), making the minimum theoretical feature size

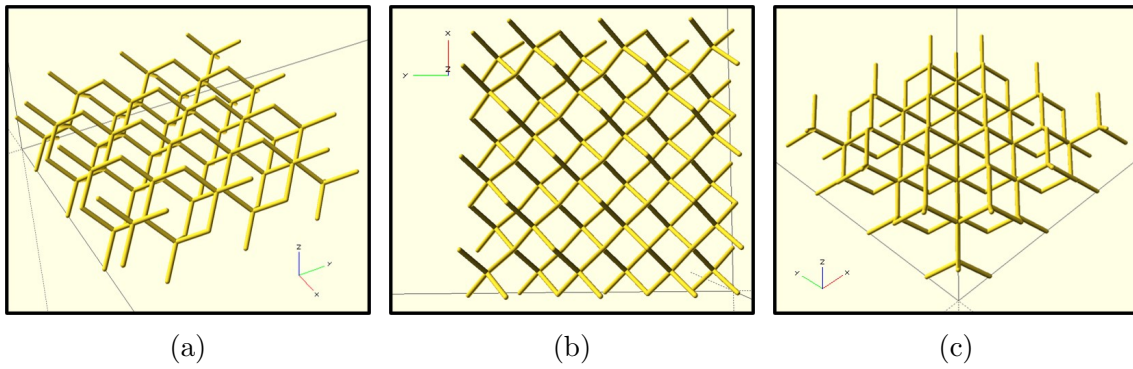


Figure 3.7: CAD renderings of a diamond lattice geometry extending $3 \times 3 \times 1$ unit cells. Viewed along **a**, an arbitrary axis, **b**, the $\langle 001 \rangle$ axis, **c**, the $\langle 111 \rangle$ axis.

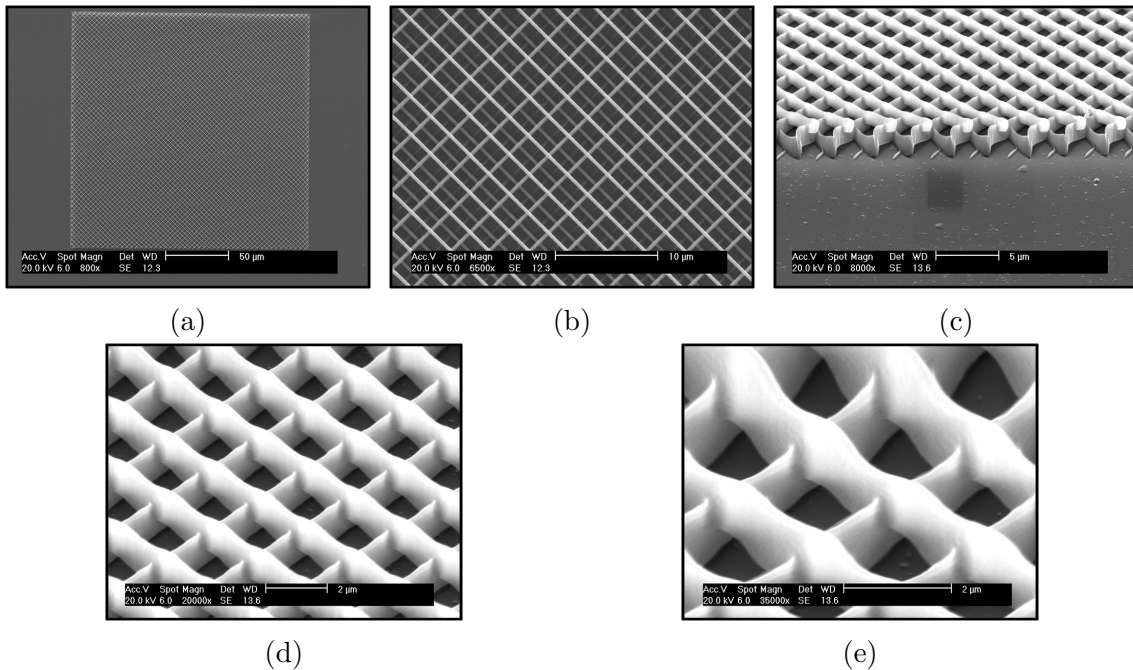


Figure 3.8: SEM images of a 3DNL, fabricated using the piezo scan mode. **a**, Full lattice, top view, 800x magnification. **b**, Top view, 6500x magnification. **c**, Angled view, 8000x magnification. **d**, Angled view, 20000x magnification. **e**, Angled view, 35000x magnification.

more achievable. As described in section 2.1, one can manually produce arbitrary geometries in DeScribe by writing a GWL script with the required co-ordinates. By defining the desired geometry in this way, it is possible to construct a diamond lattice whereby the voxel only passes through the space associated with each wire in a single straight line. Figure 3.8 shows an example of a diamond lattice which was fabricated with this method, the structure extends approximately $190 \mu m \times 190 \mu m$

$\times 2 \mu m$. This sample was fabricated by Mr Gwilym Ifan Williams whilst working at Cardiff University, all other samples studied in this thesis were fabricated by myself. A crucial aspect of a 3D ASI is that nanowire junctions are sharp and well-defined, as this allows adjacent wires on a particular wire chain to act as independent effective Ising spins. With this in mind, very slow scan speeds ($< 10 \mu m s^{-1}$) were used in an attempt to obtain sharp vertices, for context the user manual recommends typical speeds of 25-300 $\mu m s^{-1}$ for the piezo scan mode. Wires in this structure exhibit a lateral width of approximately 300 nm, a factor of 2 above the theoretical minimum. This relatively large feature size is likely due to the slow scan speeds used for fabrication. Unfortunately, even at very low scan speeds this method always produced vertices exhibiting a high degree of curvature, due to the continuous voxel movement as it scanned across each vertex. Figure 3.8c-e clearly shows this curvature, which is a significant discrepancy from the desired geometry. As such, each wire is unlikely to approximate an atomic Ising spin and so this method is not thought to be suitable for engineering a 3D ASI.

Another possible route to attaining nanowires possessing a suitably low feature size, arranged in a diamond lattice geometry with well-defined vertices is a combination of the two approaches considered so far in this section. Using the galvo scan mode is more likely to achieve sharp vertices, since the voxel does not scan along the length of wires. In addition, the approach of manually defining a GWL script gives the user significant control over the geometry design, allowing wires to be produced by individual voxel lines. Since the galvo scan mode can only scan in the x-y plane one cannot produce voxel lines along the $\langle 111 \rangle$ axis. However, one can effectively create a line along this axis by defining a sequence of closely spaced individual points. Figure 3.9 visualises the co-ordinates associated with a single unit cell of a diamond lattice, where each wire is $1 \mu m$ in length and is composed of individual points with a vertical spacing of 20 nm. Here, the voxel will expose all points on the $z = 0$ plane, before shifting upwards in the z-direction and exposing the next layer and so on. This unit cell can be divided into four sub-lattices, L1, L2, L3, and L4. To generate the GWL for an extended lattice requires two loops, these simply repeat this unit cell in the x and y directions as many times as the user desires. This geometry is defined and visualised using a python script which also outputs a text file containing the co-ordinates of every point, this text file can then be converted to a GWL file and imported into DeScribe to be created via TPL.

With a geometry defined, the next step was to to optimise the fabrication

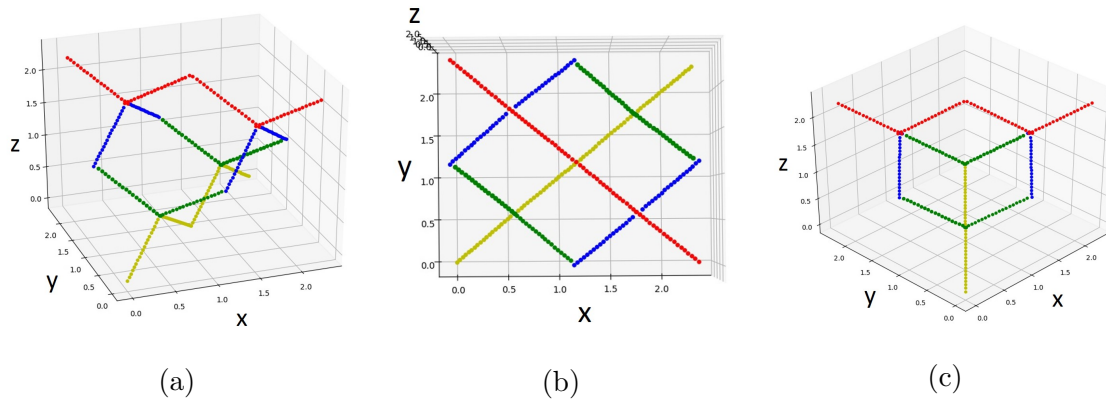


Figure 3.9: Scatter plots of the co-ordinates associated with one unit cell of a diamond lattice geometry, comprised of wires that are $1 \mu\text{m}$ in length. This can be divided into the sub-lattices L1 (red), L2 (blue), L3 (green), and L4 (yellow). Viewed along **a**, an arbitrary axis, **b**, the $\langle 001 \rangle$ axis, **c**, the $\langle 111 \rangle$ axis.

process by producing dose arrays, whereby arrays of structures were fabricated with a systematic variance in fabrication parameters. Here, it was the laser power and exposure time that were varied, exposure time was used rather than scan speed since the geometry consists of individual points instead of lines, hence `ConnectPointsOff` was enabled. When investigated a new geometry, it is good practice is to fabricate several dose arrays, where the range of parameters is narrowed down after observing each sample. This is to hone in on the parameter combination which yields the smallest feature size, without compromising the structural integrity. Figure 3.10a shows an example of a dose array of diamond lattice structures, each extending approximately $50 \mu\text{m} \times 50 \mu\text{m} \times 2 \mu\text{m}$. Here, the laser power was increased from 20% to 45% in steps of 2.5% (left to right), the exposure time was increased from 0.01ms to 0.11ms in increments of 0.01ms (bottom to top). Hence, structures in the lower-left corner received the lowest dose, explaining why some structures in this region appear faded or absent altogether, since the density of free radicals produced was either below or very close to the polymerisation threshold. In contrast, structures in the upper-right corner received the highest dose leading to micro-explosions in some cases. Micro-explosions can occur when the supplied dose is significantly above the polymerisation threshold, this induces a localised temperature increase within the photoresist causing micro-bubbles to be generated in close proximity to the voxel. Clearly, if bubbles are present whilst a structure is being fabricated, the resulting structure will be severely deformed.

After producing each dose array the sample was inspected via optical

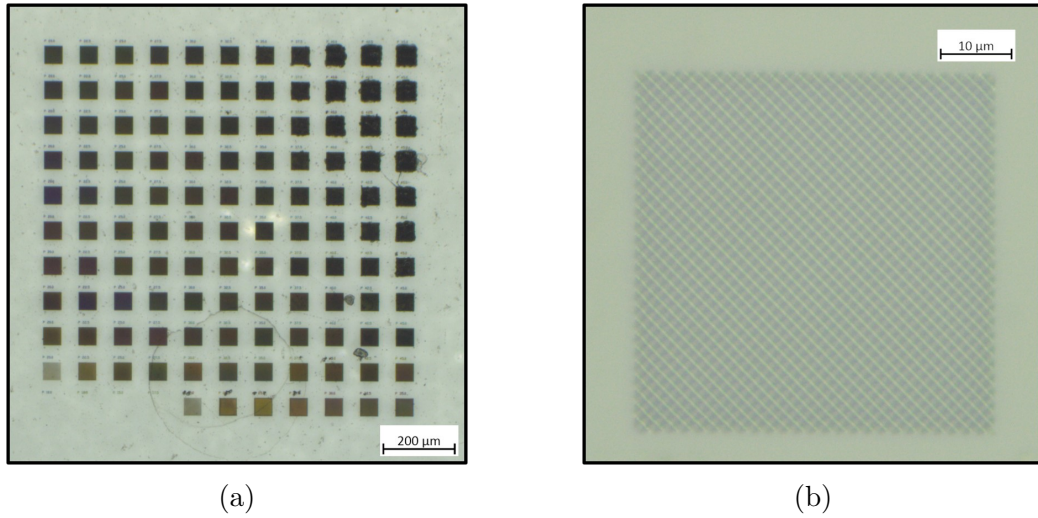


Figure 3.10: Dose array of an 11×11 grid of 3DNL polymer scaffolds, imaged via optical microscopy. **a**, Full array, laser power increases from left to right, exposure time increases from bottom to top. **b**, Individual scaffold, extending $50 \mu\text{m} \times 50 \mu\text{m} \times 10 \mu\text{m}$.

microscopy. Whilst this technique is not capable of resolving the finer details of the 3DNL (i.e. individual wire dimensions, vertex geometry, wire cross-section, etc.), it does allow one to observe if structures are severely deformed due to significant under-exposure or over-exposure. Once several dose arrays had been studied, a parameter range of 20 – 40% laser power and 0.02 – 0.10ms was determined to repeatably yield structures that did not display deformities when viewed with an optical microscope. To examine if this method proved to be more successful in capturing the diamond lattice geometry than was seen in fig. 3.8, SEM was once again used. Before SEM could be used to image the sample, a metal deposition first had to take place, since neither the polymer scaffold nor the glass substrate were conductive. Hence, a 50 nm $Ni_{81}Fe_{19}$ film was deposited on to a 3DNL sample, via thermal evaporation. This formed a 3D $Ni_{81}Fe_{19}$ nanowire lattice upon the upper surface of each polymer scaffold, as well as a $Ni_{81}Fe_{19}$ film covering the substrate. Figure 3.11a shows an SEM image of an entire 3DNL which spans $50 \mu\text{m} \times 50 \mu\text{m} \times 2 \mu\text{m}$. Covering this relatively large area provides flexibility regarding measurement methods such as MOKE and AFM/MFM. In addition, a high number of nanowire junctions is essential for the acquisition of statistically significant results in the study of vertex type populations. Figure 3.11b displays a magnified SEM image of the same structure, where the four sub-lattices that were defined in the scatter plots (fig. 3.9) are clearly identified. Individual nanowires possess approximate dimensions of 1000 nm length, 170 nm lateral width, and 50 nm peak thickness.

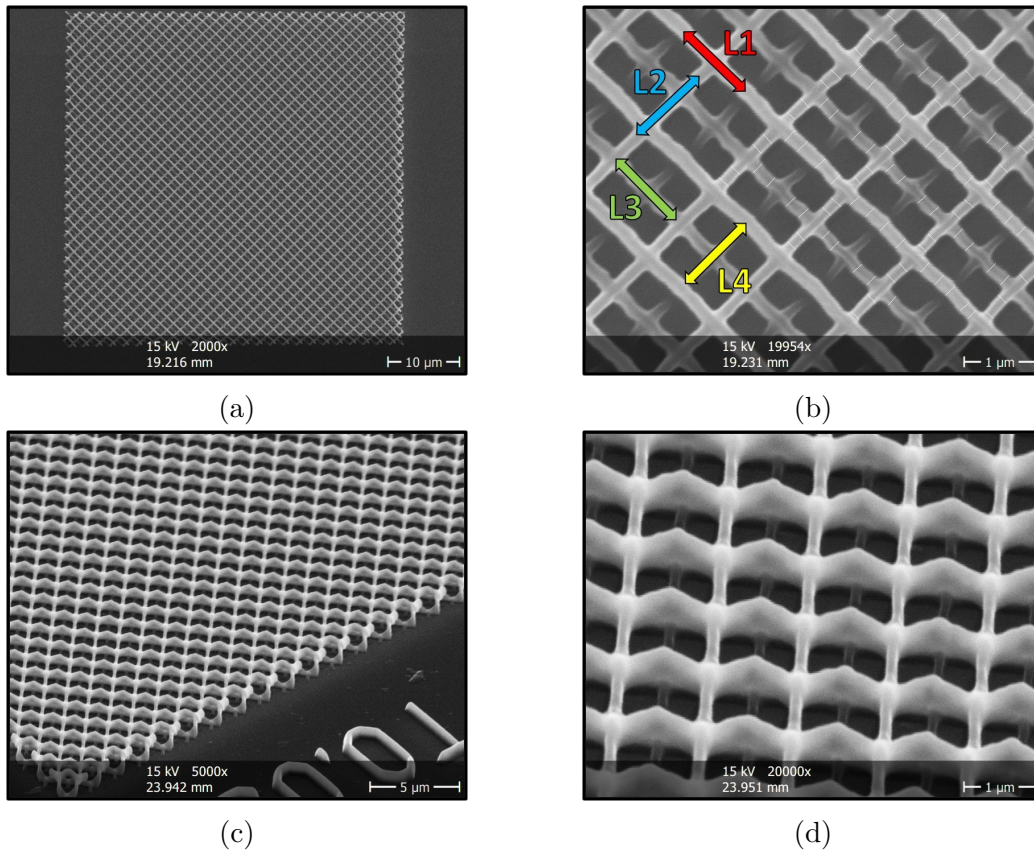


Figure 3.11: SEM images of a 3DNL as seen from **a**, top view at 2000x and **b**, 20000x magnification, **c**, a 45° angle with respect to the substrate at 5000x and **d**, 20000x magnification.

Hence, this method of defining a diamond lattice geometry has facilitated a reduction in feature size by more than 100 nm when compared with the piezo scanning method (fig. 3.8). In addition, fig. 3.11c-d views the lattice from a 45° tilt, clearly showing this structure to possess significantly sharper vertices than were seen in fig. 3.8. Therefore, all proceeding 3DNL structures presented in thesis were fabricated using this methodology.

Since evaporation is used to deposit the magnetic material, the resulting $Ni_{81}Fe_{19}$ nanowires are continuous for three complete sub-lattice layers (L1, L2, L3) in the z-direction (fig. 3.11b). A partial fourth sub-lattice layer is visible in fig. 3.11b-c, these wires are incomplete due to an offset in the z-direction during the TPL writing procedure, resulting in the base of the structure being slightly 'buried' into the substrate. Figure 3.11c-d show angled views of the nanowire network, in which the 3D geometry of the network is evident in both images. In fig. 3.11d it is

clear that the polymer nanowires do not possess a perfect cylindrical geometry, they are seen to have a greater z-axial size than lateral size. This effect is well known in two-photon lithography and it is due to the ellipsoidal point spread function of the laser at focus (see section 1.9), resulting in an elliptical cross-section of the polymer wires⁴⁸. However, since evaporation only deposits $Ni_{81}Fe_{19}$ upon the upper surface of the polymer nanowire, this asymmetry does not significantly effect the $Ni_{81}Fe_{19}$ nanowire geometry.

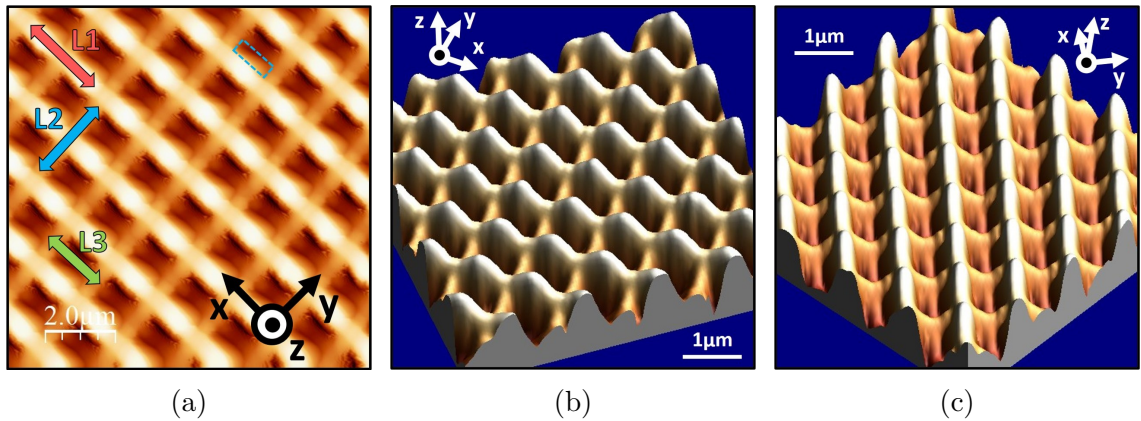


Figure 3.12: AFM data captured from a $10 \mu m \times 10 \mu m$ region of a 3DNL. **a**, AFM scan. The dotted blue box indicated an example of an artefact. **b-c**, 3D representations of the AFM data, viewed from different orientations.

It is highly preferable to be able to probe the magnetic characteristics using in-house techniques such as MFM, without the requirement of a synchrotron. To examine the possibility of this, AFM data was first collected to test if this scanning probe technique can track the 3D topography of a diamond lattice. Figure 3.12 presents AFM data that was measured from a structure that is nominally identical to the one seen via SEM in fig. 3.11. Here, it is clearly seen that topography on the L1, L2, and L3 sub-lattices can be measured using this methodology. Thus providing a strong indication that MFM can probe the magnetic magnetic properties of the upper layers in a 3DNL. The extent to which MFM can map out the magnetic configuration of a 3DNL will be considered later. One concern was that there were significant regions of vacant space throughout the lattice, which could yield problems for the tip if feedback settings were not optimised. However, the nanowires appeared to be arranged sufficiently compactly that the tip saw the 3D nanostructured sample essentially as a corrugated surface, which it could track with adequate feedback. It is noted that small artefacts are present in the AFM data due to the 3D nature

of a diamond lattice. Firstly, the area immediately to the right of each wire in L1 contains a blurred region, one example is highlighted by a dotted blue box. The origin of this artefact was outlined in section 2.4, it is due to the AFM probe continuing to scan horizontally across the 3DNL as it descended after passing over L1. This will be taken into consideration for the analysis of MFM images, although it has not affected the regions where wires are present, so is not expected to be a concern.

Here it has been shown that TPL and thermal evaporation could lead to the fabrication of a 3DNL, and that AFM had the ability to directly probe this 3D topography. However, a key issue existed within the samples presented in fig. 3.11 and fig. 3.12. The highest point in the 3DNL (as seen in fig. 3.11) extended only $2\mu\text{m}$ above the substrate, whilst the lowest point connected to the $\text{Ni}_{81}\text{Fe}_{19}$ sheet film. It is therefore not expected that this 3DNL acted as an independent array of nanowires due to both the physical connection and finite interactions between any stray magnetic fields associated with the wires and substrate film. This provided an additional layer of complexity in the application of these systems as a potential artificial spin-ice.

Two main methods could facilitate the isolation of this 3DNL. The seemingly most obvious solution would be to employ a lift-off procedure to remove any $\text{Ni}_{81}\text{Fe}_{19}$ deposited upon the substrate. However this is not trivial, primarily due to the solvent based chemical required during the development stage of TPL which would remove most materials that are commonly used as a sacrificial layer, prior to evaporation. A second solution is to increase the number of unit cells along the z-axis of the polymer scaffold, thus increasing the separation between the 3DNL and $\text{Ni}_{81}\text{Fe}_{19}$ film such that any stray field interactions become negligible in comparison with interactions between wires within the lattice. Crucially, this approach would not add a great deal of complexity to the fabrication procedure, as the superb versatility of TPL allows the production of structures with features many tens of microns along the z-axis.

3.5 ISOLATING THE 3D FERROMAGNETIC NANOWIRE LATTICE

It has so far been shown that TPL coupled with thermal evaporation could lead to the fabrication of $\text{Ni}_{81}\text{Fe}_{19}$ nanowires positioned upon a polymer

scaffold. In addition the exact scaffold geometry is highly versatile, such that nanowires can be placed into a diamond lattice geometry. The important next steps are to isolate this 3DNL from the surrounding film and to investigate the use of standard magnetometry techniques for the magnetic characterisation of these structures. The latter of which is no minor challenge, 3D magnetic nanostructures are still an emerging topic with relatively limited examples in the literature.

3.5.1 PHYSICAL CHARACTERISATION

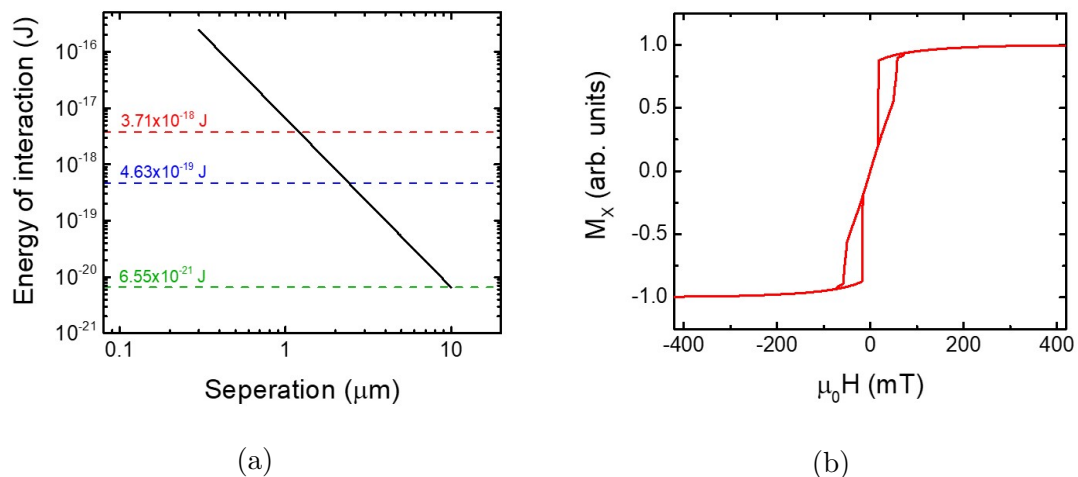


Figure 3.13: **a**, Simulated energy of interaction between a $Ni_{81}Fe_{19}$ nanowire and nanopad as a function of separation, evaluated in a dipolar approximation framework. Values are annotated for the energy of interaction between two wires at a separation of $1 \mu m$ (red) and $2 \mu m$ (blue), as well as between a wire and pad at a separation of $10 \mu m$ (green). **b**, Hysteresis loop of a $Ni_{81}Fe_{19}$ nanowire with an external field applied along the $\langle 100 \rangle$ axis, simulated using MuMax.

The simplest solution to preventing any finite interactions between stray fields from the sheet film and nanowires is to raise the $Ni_{81}Fe_{19}$ nanowire lattice above the substrate. Unfortunately, this isn't as straightforward as simply building a cuboidal polymer base beneath the 3DNL, as was done in section 3.3, since evaporated material would still infiltrate through the square voidal regions in the lattice to form $Ni_{81}Fe_{19}$ nanoislands on the base. SEM observations of these square voidal regions indicate that nanoislands on the substrate are expected to possess a volume of approximately $500 \text{ nm} \times 500 \text{ nm} \times 50 \text{ nm}$, which corresponds with a magnetic moment of $\sim 1.1 \times 10^{-14} \text{ Am}^2$. A method that can increase the separation between the $Ni_{81}Fe_{19}$ nanowires and nanoislands is to increase the number of unit

cells along the z-axis in the polymer scaffold. This approach means that any scaffold layers below the uppermost unit cell are shadowed during the $Ni_{81}Fe_{19}$ deposition. To estimate the number of unit cells required to effectively isolate the $Ni_{81}Fe_{19}$ nanowire lattice, the energy of interaction between a nanowire and a nanoisland has been evaluated as a function of separation in a dipolar approximation framework. Figure 3.13a shows this relationship, at a wire-pad separation of $10 \mu m$ the wire-pad energy of interaction is 2 orders of magnitude below that of 2 wires which are separated by $2 \mu m$, the approximate distance between L1 and L4 wires. This indicates that a scaffold consisting of 5 unit cells in the z-direction would be sufficient to effectively isolate the $Ni_{81}Fe_{19}$ nanowire lattice from any $Ni_{81}Fe_{19}$ deposited upon the substrate. Figure 3.13b presents a simulated hysteresis loop that was run in the finite difference package MuMax. This considers a $500 \text{ nm} \times 500 \text{ nm} \times 50 \text{ nm}$ $Ni_{81}Fe_{19}$ nanopad with a cell size of $5 \text{ nm} \times 5 \text{ nm} \times 10 \text{ nm}$, an in-plane external field was applied parallel to the $\langle 100 \rangle$ axis in 2 mT increments. The result is reminiscent of a vortex hysteresis loop due to the two regions exhibiting hysteresis either side of the negligible remanent magnetisation⁹⁰. This result is to be expected, because the simulated nanopad is very similar to island 2b in fig. 3.6, where at remanence a Landau state was seen which resembled a magnetic vortex. Here, the domains arrange to achieve flux closure and hence exhibit a negligible remanent magnetisation. Upon the application of an external field, DW motion occurs to mostly saturate the nanopad indicated by a sharp transition, before moments rotate to align with the field direction, shown by the gradual transition to saturation. Once the external field is removed, the flux-closure state is once again formed due to the low shape anisotropy of the 1:1 aspect ratio nanopad. This simulated hysteresis loop will prove useful when examining optical magnetometry of a 3DNL.

To produce a 3DNL scaffold which is 5 unit cells in height first required the GWL to be modified, this simply involved implementing a third loop to repeat the unit cell (shown in fig. 3.9) in the z direction. Similar dose arrays to those described previously were then produced, to optimise the fabrication parameters required for this new geometry. Figure 3.14 presents SEM images of a 3DNL which is 5 unit cells in height, the full scaffold extends over a volume of $50 \mu m \times 50 \mu m \times 10 \mu m$. Individual wires are again $1 \mu m$ in length, 50 nm in thickness, and the lateral width is dependent upon the exact fabrication parameters. For structurally sound scaffolds a minimum lateral wire width of 200 nm was found. Here, the lateral wire width is increased compared with the wires seen in fig. 3.11 because the additional nanowire layers means that a greater exposure dose is required to yield structurally

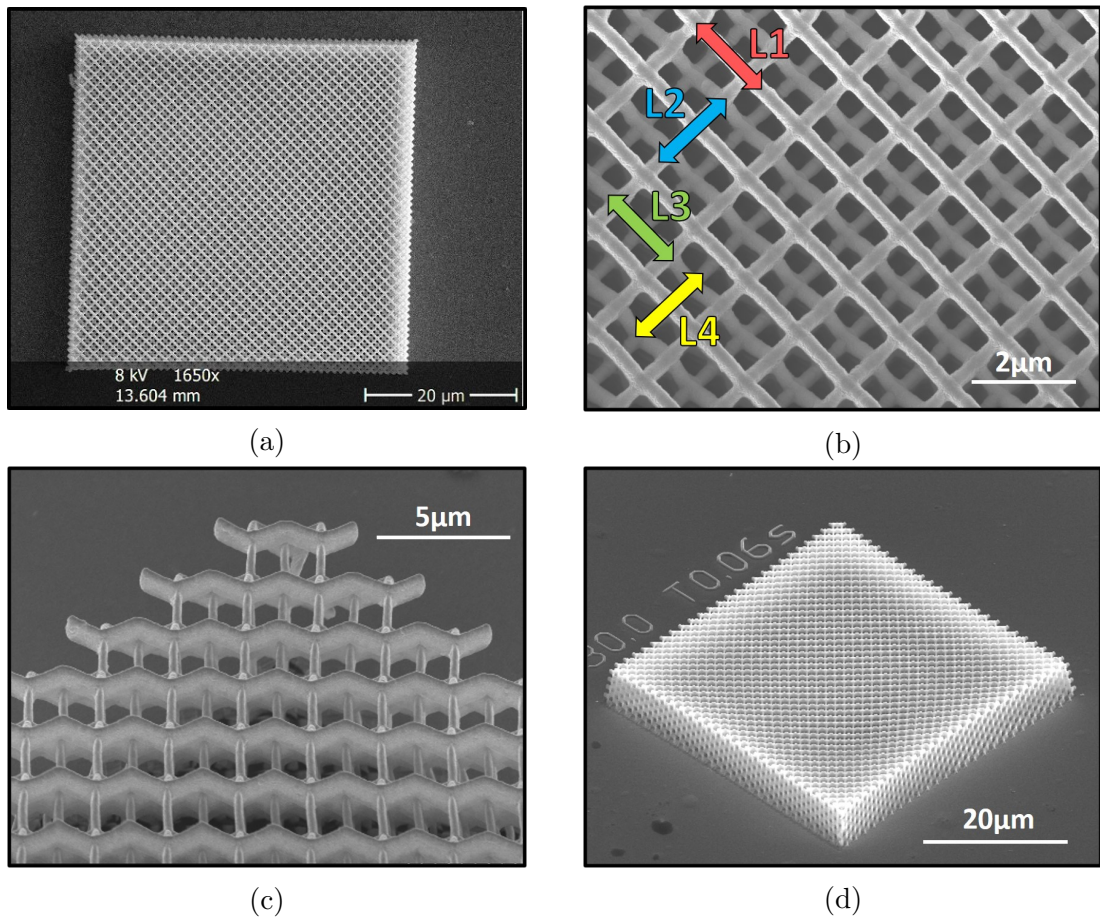


Figure 3.14: Scanning electron micrographs of a 3DNL as seen from **a**, top view at 1650x and **b**, 12000x magnification, **c**, a 45° angle with respect to the substrate at 2500x and **d**, 6000x magnification.

sound scaffolds. To understand the expected $Ni_{81}Fe_{19}$ nanowire cross-section, one must consider the TPL voxel geometry as well as the characteristics of a line-of-sight deposition. During TPL, it is clear that an asymmetric point spread function of the laser at focus leads to an ellipsoidal voxel, resulting in a polymer cross-section possessing a curved upper-surface, illustrated in fig. 3.15. Since $Ni_{81}Fe_{19}$ is deposited via thermal evaporation, the incoming metal is anisotropic and deposits in a line-of-sight format⁹¹, seen in fig. 3.15a. The expected result of this process is illustrated in fig. 3.15b, where vertical lines of constant height are annotated to show how a uniform layer being deposited on a curved surface leads to this crescent shaped cross-section. Therefore a thickness gradient exists, whereby the peak thickness at the apex of curvature is equal to the film thickness, this thickness decreases as distance from the apex increases. Annotated red lines in fig. 3.15c clearly show this thickness gradient, where the thickness is defined to extend perpendicular to the wire

surface. As the subtended angle approaches 90° from the z-axis, the wire thickness is expected to reduce below the threshold for a magnetic dead layer. Hence, for computational modeling it will be assumed that the magnetic material subtends an angle of 80° symmetrically about the z-axis. Beyond 80° , any $Ni_{81}Fe_{19}$ is likely to behave as a magnetic dead layer, since the expected thickness in this outer region is < 1 nm. Crescent shaped cross-sections that form due to a uniform film being deposited on a curved surface have been reported previously in the literature⁹².

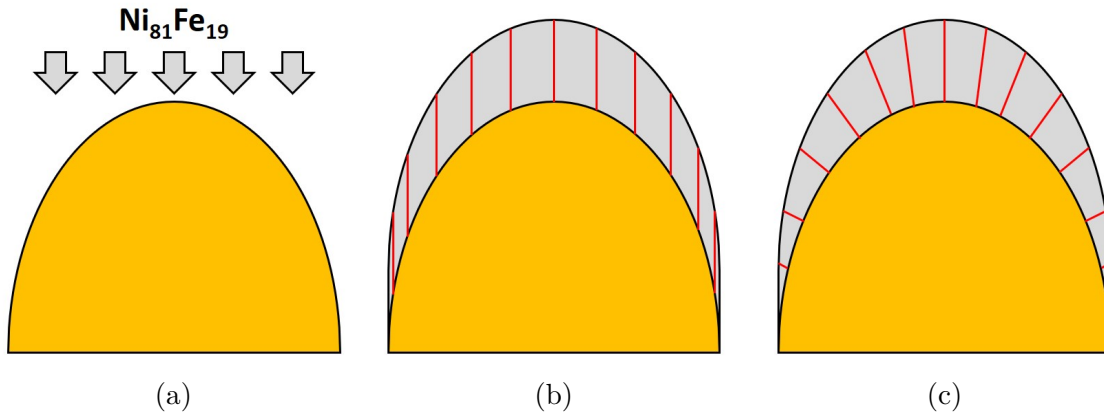


Figure 3.15: Illustrating the cross-section of a $Ni_{81}Fe_{19}$ nanowire (grey) upon a polymer scaffold (yellow). **a**, $Ni_{81}Fe_{19}$ line-of-sight deposition. **b**, After deposition, lines of constant height are annotated (red). **c**, Similar schematic in which red lines extend normal to the nanowire surface, demonstrating how the nanowire thickness varies across the cross-section.

Figure 3.16 illustrates the topography of the 3DNL. Figure 3.16a shows the full cross section of a $Ni_{81}Fe_{19}$ nanowire and the underlying scaffold. This has been designed by combining knowledge of the fabrication process (illustrated in fig. 3.15) with SEM observations. Figure 3.16b illustrates the continuous nature of the 3DNL from L1-L4, whereby wires in L1, L2, and L3 all extend from an upper to a lower junction between wire layers. Whereas wires in L4 are expected to terminate above the L4-L5 vertex due to shadowing associated with L1. Wire layers below L4 are anticipated to be shadowed to within the positional reproducibility (approximately 20 nm) of the galvanometer, used to position the stage during the TPL process. As a result, the magnetic moment of any $Ni_{81}Fe_{19}$ deposited on the scaffold below L4 is predicted to be $< 10^{-16} Am^2$, which would exhibit an interaction energy of $< 6 \times 10^{-20}$ J with L4. Hence, interactions between a $Ni_{81}Fe_{19}$ nanowire in L1-L4 and any $Ni_{81}Fe_{19}$ deposited on the scaffold below L4 would possess a dipolar energy at least two orders of magnitude below interactions between

wires on L1-L4. It is therefore reasonable to assume that any magnetic material deposited on the scaffold below L4 will have negligible dipolar interactions with L1-L4.

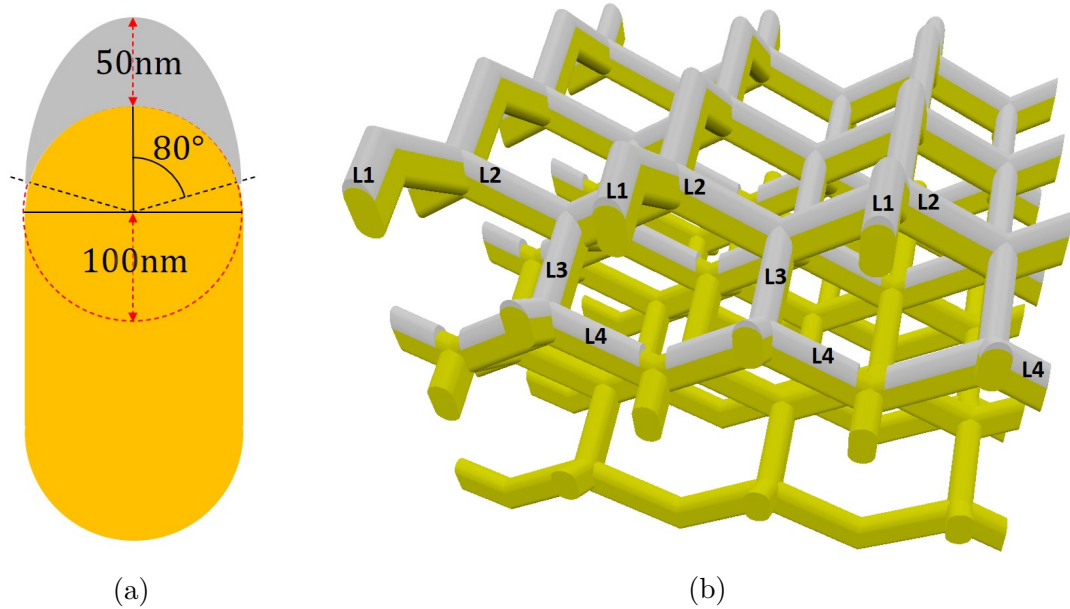


Figure 3.16: **a**, Cross-sectional geometry of the polymer (yellow) and $Ni_{81}Fe_{19}$ (grey) nanowires. **b**, A schematic of the realised 3D magnetic nanowire lattice.

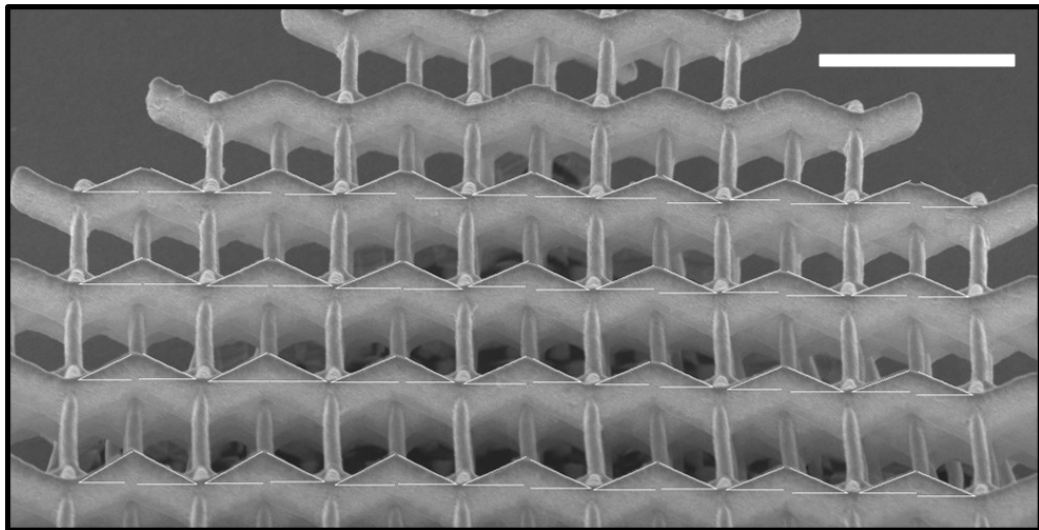


Figure 3.17: SEM image of a 3DNL viewed from a 45° tilt. 50 measurements are annotated of the angle which the L1 wire long-axis subtends from the substrate plane. A simple trigonometry calculation was used to transform the measured values, to account for the viewing angle. Scale is $4 \mu m$.

Prior to investigating any magnetic characteristics, it was crucial to form a comprehensive understanding of the 3DNL’s physical properties. The most obvious characteristic to study is the geometry of the 3DNL, and how well this compares to an idealised diamond-bond lattice (eg. fig. 3.16b). Figure 3.17 shows a magnified view of the SEM image that was presented in fig. 3.14c. Here, the 3D geometry of the L1 sub-lattice is clearly visible, allowing 50 measurements to be annotated of the angle (θ) which the L1 wire long-axis subtends from the substrate plane. Each measurement then required a simple trigonometric calculation to account for the 45° viewing angle. These measurements determine $\theta = (33.11 \pm 2.94)^\circ$ from the substrate plane, matching within error the angle of 35.25° which is expected for an idealised tetrahedral geometry⁹³.

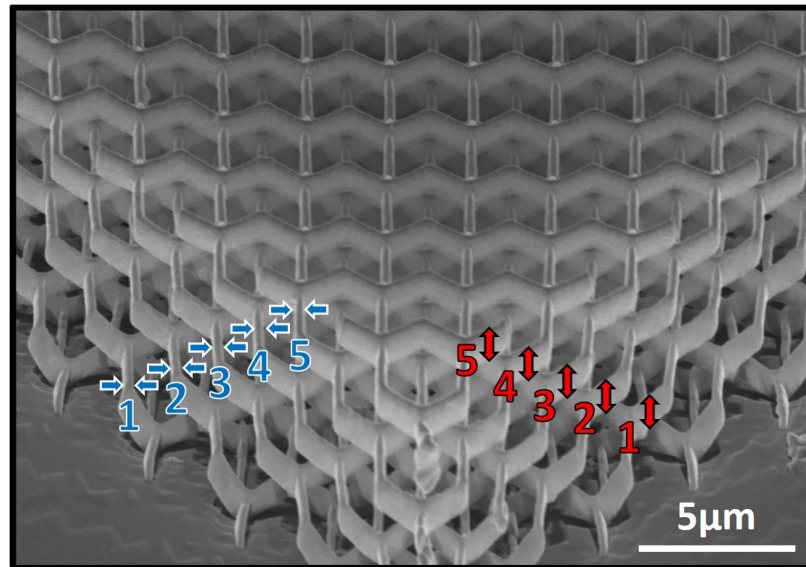
Wire layer	Lateral feature size (nm)	Z-axial feature size (nm)
1	252 ± 1	1072 ± 25
2	255 ± 7	1054 ± 33
3	264 ± 7	1044 ± 15
4	260 ± 8	1041 ± 24
5	269 ± 5	1025 ± 32

Table 3.1: Mean values of lateral and z-axial feature sizes on wire layers at different heights in a 3DNL, measured from the SEM data presented in fig. 3.18a.

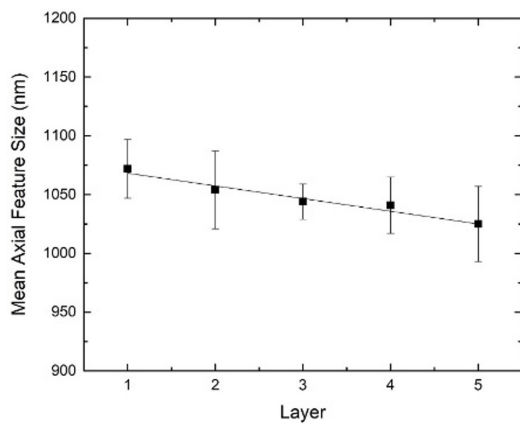
Next, it is important to consider if the nanowire quality (eg. dimensions/roughness) exhibits any variation as a function of height. Variation could be caused due to the laser travelling a greater distance through the photoresist for the fabrication of L1 when compared with that of lower sub-lattice layers, therefore resulting in different levels of attenuation. This effect is not expected to be a significant concern because the structure height considered here ($10 \mu m$) is far smaller than the maximum available Z range of $300 \mu m$. To investigate if any variation does occur between nanowires at different Z co-ordinates, the lateral and axial feature size of the polymer nanowires comprising the diamond-bond lattice presented in fig. 3.18a have been studied as a function of sub-lattice layer. Analysis of fig. 3.18a was performed using the software package ImageJ, whereby five measurements of all visible polymer wires were taken for both dimensions of interest. These data allowed the mean z-axial feature size and width for each wire to be calculated, before the mean value of both dimensions as a function of nanowire

layer could be determined. Mean values of these parameters are given in table 3.1 and are plotted in fig. 3.18b-c. No significant trend is determined between sub-lattice layers, indicating that any variation in laser attenuation which occurs is negligible within the Z range considered herein.

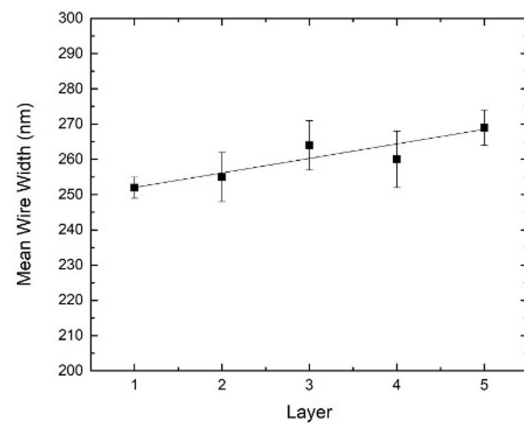
In addition to physical dimensions, the nanowire surface roughness is a useful indicator of any variation in quality between sub-lattice layers. Determining



(a)



(b)



(c)

Figure 3.18: **a**, Scanning electron micrograph of a diamond-bond lattice. Both lateral (annotated with blue arrows) and axial (red arrows) feature sizes are slightly increased from the structure presented in fig. 3.14 because 40nm of gold has been deposited prior to $Ni_{81}Fe_{19}$ in order to improve contrast. **b**, Mean axial feature size and **c**, wire width, both plotted as a function of sub-lattice layer (as annotated).

the surface roughness of all layers in the lattice is more complex. Whilst SEM can be utilised to visually inspect different layers, qualitatively showing a lack of variation in roughness, a quantitative study is a greater challenge. To address this, AFM data of the 3DNL was captured (fig. 3.19), in which L1 and L2 are clearly visible. WSxM possesses an automated protocol for quantifying the RMS roughness of AFM data by evaluating the height distribution within the specified area. This feature assumes a Gaussian height distribution and determines the RMS width of the curve. To account for the fact that this AFM data inherently possesses a significant height distribution due to the 3D nature of the lattice, a flattening procedure (detailed in section 2.5) was executed prior to analysing the surface roughness of each wire individually. After examining every wire within the observed area individually, mean RMS roughness values of (10.8 ± 4.3) nm and (16.1 ± 3.2) nm for L1 and L2 respectively were determined. The standard deviation of each dataset is given as the associated uncertainty value. The uncertainty ranges of the two sub-lattices do overlap, however the roughness values are statistically different. Unfortunately it is unclear from these data if this statistical difference is real, because it is expected that the AFM probe would have more closely tracked the topography of the uppermost sub-lattice. Hence, the increased roughness on L2 may simply be an artefact induced by this sub-lattice being less closely tracked.

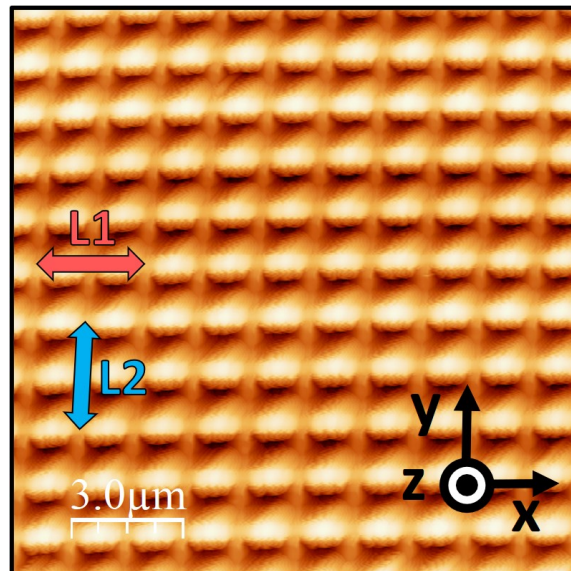


Figure 3.19: AFM scan of a 3DNL, analysis of every wire within the observed region yielded mean surface roughness values of (10.8 ± 4.3) nm and (16.1 ± 3.2) nm for L1 and L2 respectively.

Last to be examined is the elemental composition of the nanowire array. EDX is a powerful technique allowing the direct visualisation of the chemical constituents within the 3DNL, the polymer scaffold and the surrounding region. Figure 3.20 displays EDX data captured over an 8 hour period, this large capture time was necessary for the acquisition of sufficient signal required to maximise resolution. Although it is noted that this long exposure to an intense electron beam led to a slight deformation of the polymer scaffold, seen in the lower right corner of the lattice in fig. 3.20a, b and d. The IPL-780 photoresist used in this study was primarily carbon based, as the components included acrylate monomers, irgacure 369 high efficiency UV photoinitiators, and photoinhibitor molecules that reduce the voxel size. Further details of the IPL-780 composition are proprietary and so are not publicly available. Figure 3.20a maps the carbon content of the observed region, as this is only expected to be found within the polymer scaffold. The signal associated with carbon is seen to be most intense at the side walls of the scaffold, where very little $Ni_{81}Fe_{19}$ is expected to be present due to the line-of-sight nature of the $Ni_{81}Fe_{19}$ deposition. Therefore a greater proportion of carbon was exposed to incident electrons in these regions, leading to an increased signal when compared with the upper surface, where the $Ni_{81}Fe_{19}$ lattice masked the polymer.

Visualising the nickel content (fig. 3.20b-c) demonstrates that the deposited $Ni_{81}Fe_{19}$ closely emulates the 3D diamond-bond lattice topography of the polymer template and is continuous throughout the 3DNL. Conversely to carbon, the nickel signal is seen to be significantly stronger on the upper surface, in comparison to the side walls, lending further confidence that the magnetic material was deposited in a line-of-sight nature. A darkened area directly above the nanowire array is apparent in both fig. 3.20b and d, this was a result of the 3D structure shadowing this region of the substrate from the detector. Lastly fig. 3.20d maps the iron content where it is noted that the signal-to-noise ratio is lowered in comparison with fig. 3.20f-h, this is due to the reduced iron content (19%) in permalloy compared with the nickel content (81%). A low accelerating voltage was required because the $Ni_{81}Fe_{19}$ wires and film are very thin, as such higher energy electrons could have penetrated through the magnetic material, yielding a lower signal from the chemical constituents of interest. By comparing the signal obtained from iron and nickel, an estimate of the magnetic nanowire composition can be determined. Spectra from 10 different locations across the image were analysed to determine a nickel to iron ratio of 4.26, in close agreement with the expected $Ni_{81}Fe_{19}$ composition.

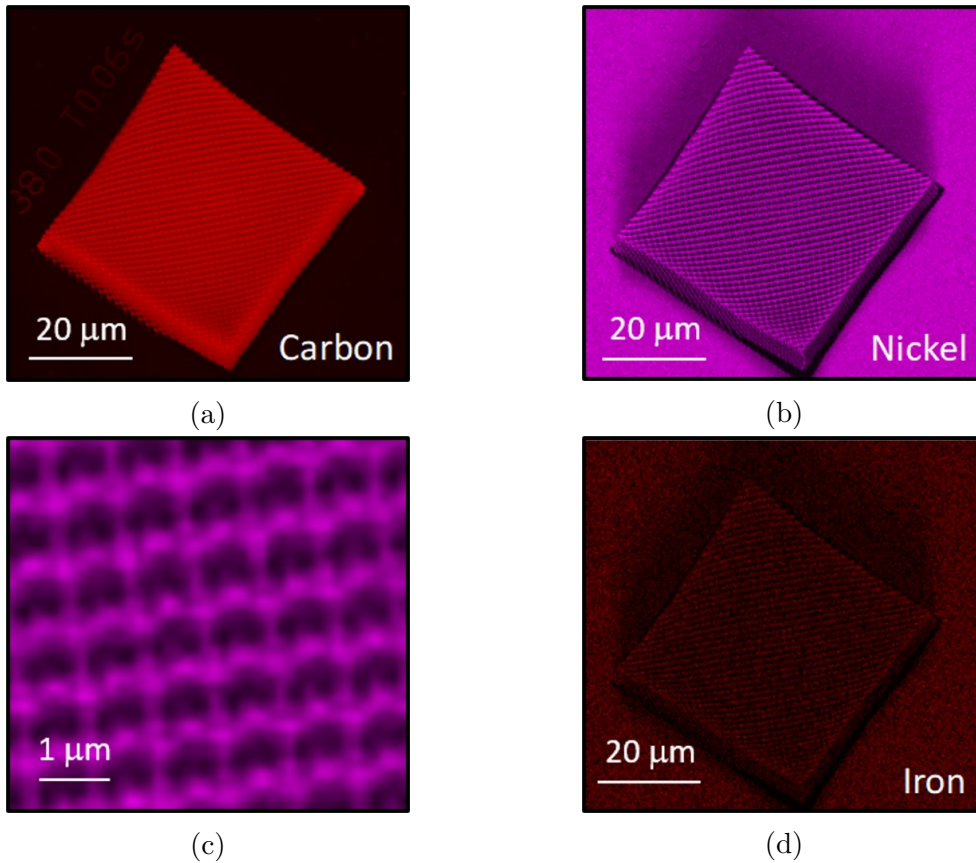


Figure 3.20: EDX measurements, mapping the composition of a $Ni_{81}Fe_{19}$ nanowire lattice upon a polymer scaffold. Colouring refers to relative density of **a**, Carbon. **b-c**, Nickel. **d**, Iron.

3.5.2 MICRO-MAGNETIC SIMULATIONS

Finite-element simulations were performed using the software package NMAG in order to investigate various characteristics of the nanowires present in the 3DNL. Firstly, the geometry of a single wire was studied to gain insight on the remanent state, domain wall structure, and switching mechanisms. Expanding upon this, the geometries of two wires meeting at a central peak (a bipod) and four wires meeting at a central vertex (a tetrapod) were defined, which act as building blocks of the 3DNL. These building blocks were used to simulate hysteresis loops and obtain an approximation of MFM signal, which hugely benefited the understanding of any data produced from experimental MOKE/MFM studies. The first challenge associated with modeling a 3DNL via micro-magnetic simulations, was to define a geometry closely approximating that of a single $Ni_{81}Fe_{19}$ nanowire. One crucial aspect of the $Ni_{81}Fe_{19}$ wires is the crescent shaped cross-section, which had to be closely adhered

to in this simulated geometry. SEM analysis and geometric arguments (fig. 3.21) were used to gain insight into the physical geometry, allowing the production of a virtual counterpart using the software package OpenSCAD (<https://www.openscad.org/>).

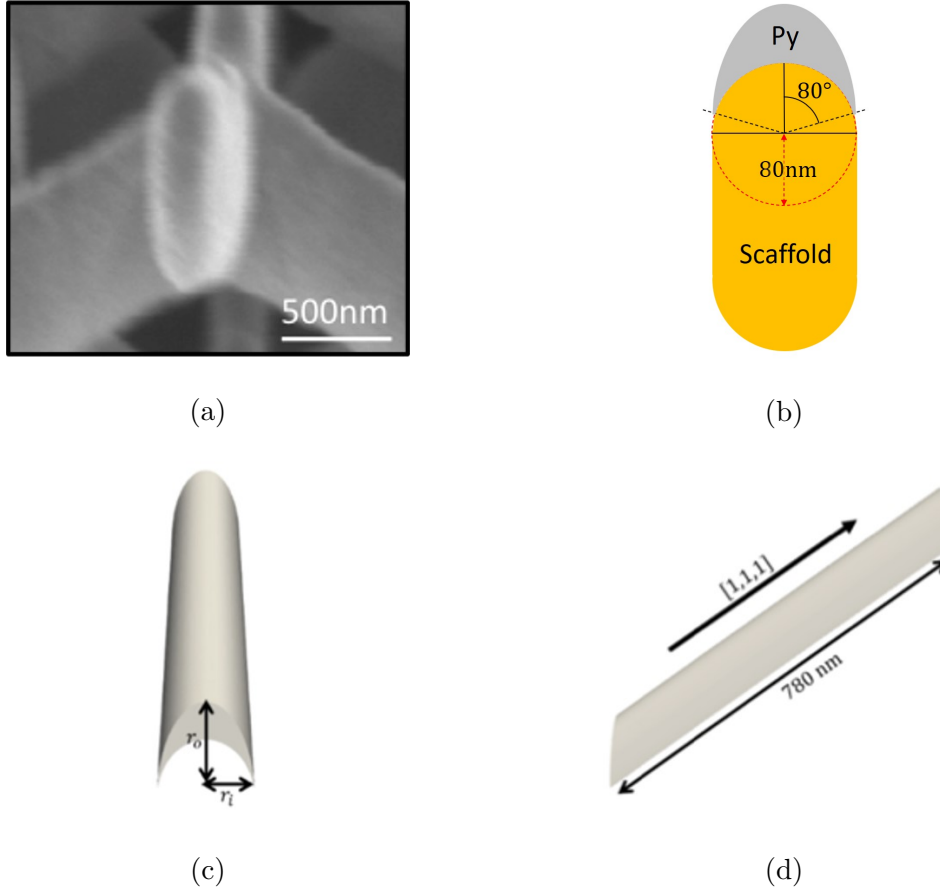


Figure 3.21: Generating the geometry of a single $Ni_{81}Fe_{19}$ nanowire for micro-magnetic simulations. **a**, SEM image observing the cross-section of both the polymer and $Ni_{81}Fe_{19}$ wires. **b**, Schematic of the determined polymer and $Ni_{81}Fe_{19}$ wire cross-sections. **c**, Generated geometry of single $Ni_{81}Fe_{19}$ nanowire, displaying the cross-section. **d**, The same geometry observed from side-view.

Figure 3.21a indicates a lateral feature size of approximately 200 nm, and that the voxel used to defined the polymer scaffold during TPL possessed a cross-sectional area with the shape of a rounded rectangle. A uniform $Ni_{81}Fe_{19}$ film of 50 nm thickness was deposited upon the sample, leading to a maximum thickness of 50 nm at the $Ni_{81}Fe_{19}$ wire peak. However, this thickness is expected to vary away from the peak due to geometric arguments, illustrated earlier in fig. 3.16. The simulated geometry extended 80° from the upper apex, beyond this point the magnetic material was expected to be below the dead-layer thickness of $Ni_{81}Fe_{19}$.

Due to computational restraints, the simulated wire length was set at 780 nm as seen in fig. 3.21d. Hence, setting the inner arc radius to 80 nm led to an aspect ratio that is approximately equivalent to that of wires in the experimental system.

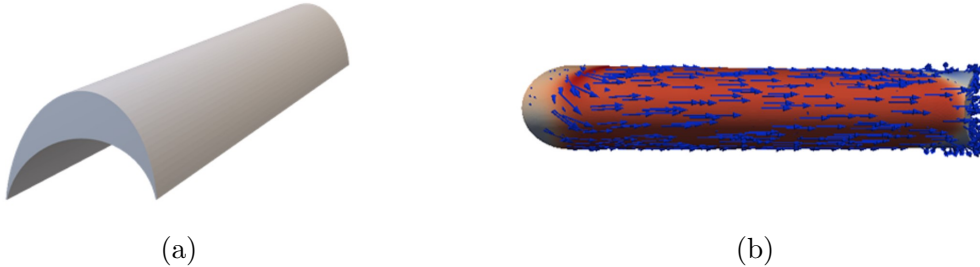


Figure 3.22: Finite-element simulation of a single domain $Ni_{81}Fe_{19}$ nanowire. **a**, Simulated geometry. **b**, Remanent magnetisation profile following relaxation from saturation along principle axes, seen from top view.

Initially, the magnetisation of individual nanowire presented in fig. 3.22b was saturated parallel to its long axis, prior to removal of the applied magnetic field, allowing the wire to relax into a remanent state. The wire is clearly observed to possess a single domain state, in which the magnetisation projects along the length of the wire. An identical single domain state was obtained after relaxation from a saturating magnetic field applied perpendicular to the long axis. Planar magnetic nanowires are the subject of extensive studies within the literature and typically reverse by the propagation of DWs^{16,19,54}, although the type of DW can vary and significantly depends upon a combination of wire width and thickness⁹. However, the curved cross-section and non-uniform thickness of nanowires studied here represent clear differences from the geometry of planar wires. As such, a simulation was performed to determine the DW structure expected within nanowires present in the 3DNL. For this, the central 80% of the wire length was defined with a random magnetisation to avoid any bias over the resulting DW type, whilst the two outer regions were defined with magnetisation vectors orientated towards the wire centre. Figure 3.23a presents the result after a relaxation command was performed, this shows a head-to-head vortex DW has formed between two opposing domains. To discern if the novel crescent shaped cross-section influences the DW structure, this result can be compared with a planar wire of similar dimensions. To do so, the geometry shown in fig. 3.23a must first undergo a co-ordinate transformation to “unroll” the crescent cross-section, allowing the magnetisation profile to be projected onto a planar surface. In the new co-ordinate system M_x is the component parallel

with the wire long-axis, M_y is the component tangential to the wire surface but perpendicular to the long-axis, and M_z is the component normal to the wire surface. Figure 3.23b shows this “unrolled” projection, which is readily comparable with the similar planar wire shown in fig. 3.23c. The planar wire has an identical length to the curved wire, a thickness of 50 nm, and a width of 300 nm, approximately equal to the arc length of the upper surface in the curved wire. Observing the DW structure in the two wires, the DW in the curved wire appears stretched along the y-axis, causing the DW length along the x-axis to be reduced in comparison with the planar wire. This is most likely the result of curvature-induced effects, discussed in section 1.7, as these are most relevant at regions with finite M_y or M_z . Such regions are only present within the DW here, explaining why the regions of uniform magnetisation either side of the DW appear unperturbed by the curvature. Another PhD student within this research group (Mr Arjen van den Berg) has examined the impact of curvature upon DW structure in greater detail.

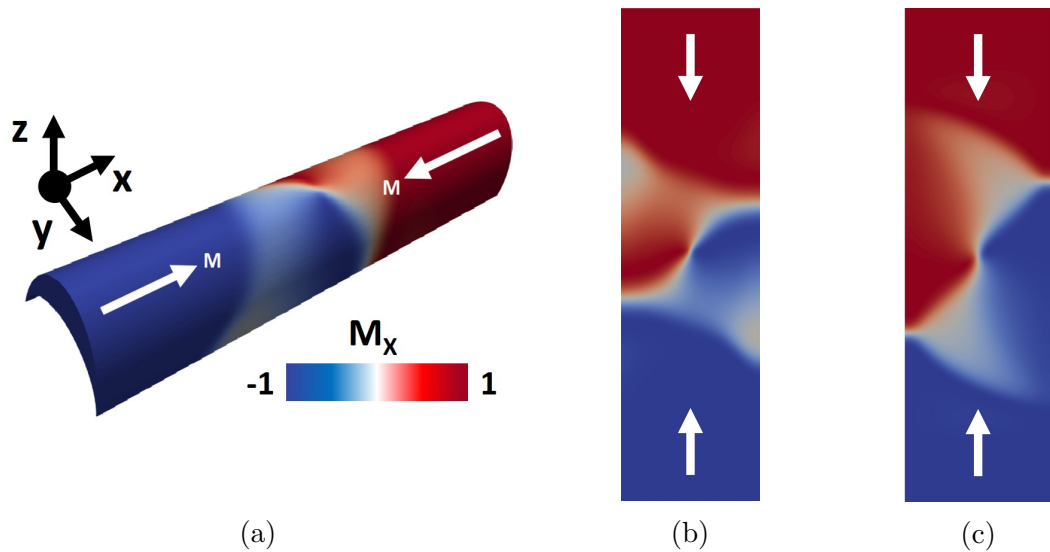


Figure 3.23: Finite-element simulations of DW within a $Ni_{81}Fe_{19}$ nanowire. **a**, The geometry seen in fig. 3.22 at remanence, a vortex DW separates two opposing domains. **b**, The same state, viewed from above. **c**, A planar wire with equivalent dimensions, following relaxation from identical initial conditions.

Having concluded the DW structure for this nanowire geometry to exist in the vortex regime, the next logical step was to investigate the switching mechanisms occurring within these wires. Finite-element simulations were performed to model hysteresis loops for several geometries, given in fig. 3.24. In addition to gaining information regarding the switching mechanisms, comparison of experimental MOKE

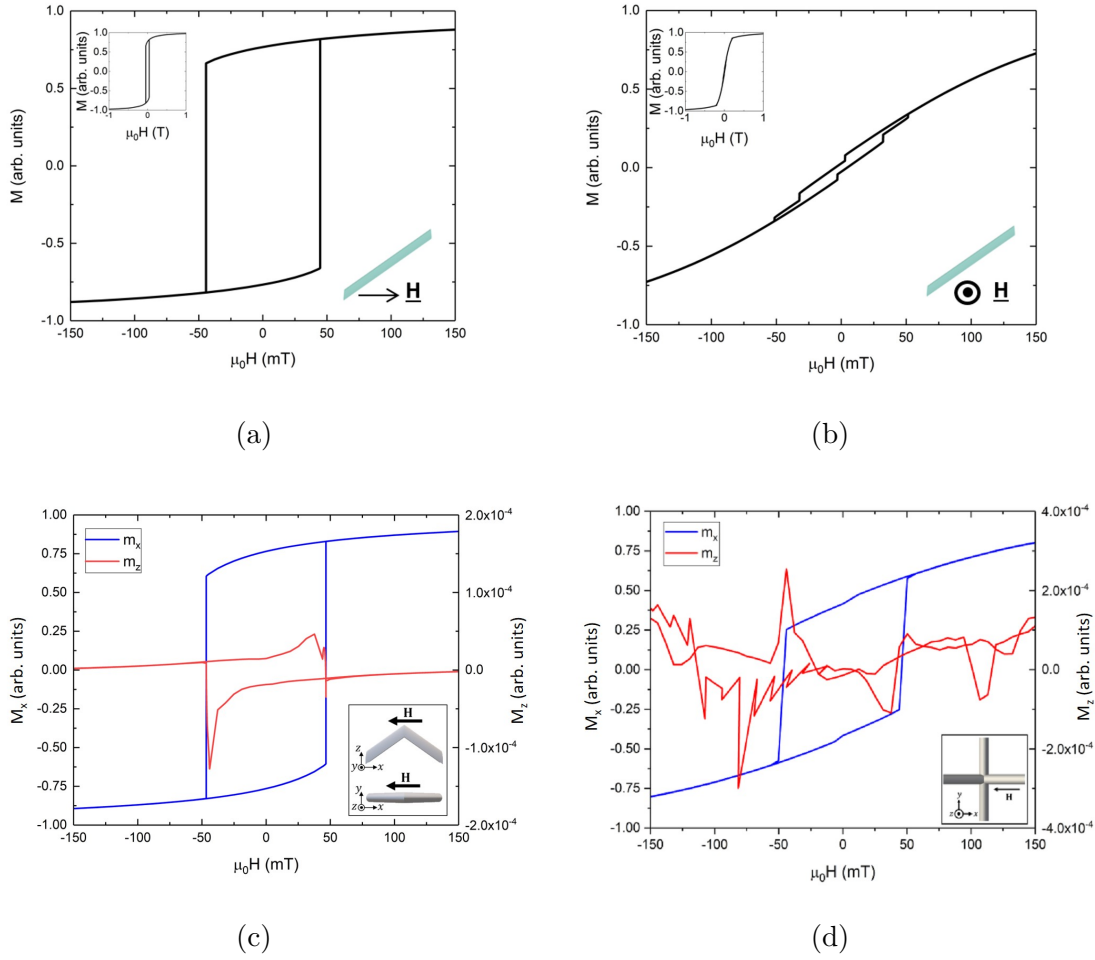


Figure 3.24: Simulated hysteresis loops, insets illustrate direction of the applied magnetic field. **a**, A single magnetic nanowire with the field applied at 35° to the long axis. A second inset shows the loop reaching saturation. **b**, A single magnetic nanowire with the field applied perpendicular to the long axis. **c**, A bipod structure, comprising of two wires meeting at a central junction. **d**, A tetrapod structure comprising of 4 wires meeting at a central vertex

data with the data obtained from these different simulated geometries should provide insight into the sensitivity of experimental measurements to the different sub-lattice layers within the 3DNL. In each case, an applied magnetic field was ramped from -1 T to +1 T, before sweeping back to -1 mT. This ensured each system transitioned between positive and negative saturation states so that no information regarding the reversal mechanism was lost. To aid visual observations of the significant regions in each hysteresis loop only the data in the field range of -150 mT to +150 mT are shown in the main plots.

Figure 3.24a presents a simulated hysteresis loop with the magnetic field applied at a 35° angle with respect to the wire long-axis. This field direction was chosen to emulate experimental measurements of the 3DNL via optical magnetometry, in which a magnetic field was applied parallel to the substrate plane, and therefore at a 35° angle to the nanowire long axis due to the tetrahedral bond angle present throughout the lattice, demonstrated in fig. 3.14 and 3.16. Figure 3.24a was defined with initial conditions such that the plane of magnetisation in the wire lies parallel to the negative saturating field. A gradual increase in magnetisation from negative saturation to $-0.7M_S$ was observed as the applied field swept upwards to +45 mT, associated with rotation due to the plane of magnetisation rotating to align with nanowire long axis. At 45 mT a sharp transition occurred, indicative of DW motion, before a similar gradual increase to positive saturation led the direction of magnetisation to once again rotate, lying parallel with the applied field. The up and down sweeps are seen to be symmetric as expected, with remanence of approximately $0.76M_S$. If this wire was perfectly single domain at remanence, meaning that all moments would be aligned with the wire long-axis, one would expect a remanent magnetisation of $\cos(35^\circ) = 0.82M_S$. Though the true value is reduced slightly, due to demagnetisation fields produced at the wire ends causing nearby moments to diverge from the long-axis. Figure 3.24b modeled an identical nanowire geometry, however the applied magnetic field direction was rotated by 90° about the z-axis (as annotated in fig. 3.24b), meaning that it had no component parallel to the nanowire long axis. The result is reminiscent of a hard axis hysteresis loop with a remanent magnetisation of $< 0.1M_S$, in which the wire reversed via rotation, shown by the gradual change in magnetisation symmetrically along the up and down sweeps. Noticeably, 3 subtle transitions are seen in both the up and down sweeps. Close examination of the micromagnetic spin texture indicates these to be the result of edge defects at either end of the wire. Such defects are not expected to be seen in experiments because the physical system is composed of connected nanowires, and so exposed wire ends are only present at the lattice boundaries. The lack of any pronounced, sharp transitions (as seen in fig. 3.24a), provides further evidence that this wire is single domain and behaves as a suitable approximation to an Ising spin. Mr Arjen van den Berg has furthered this investigation in more detail.

Two individual wires with the long nanowire axis tilted at 35° and joined at a central peak form a bipod, these act as building blocks of sub-lattice layers in the 3DNL, as can be seen in fig. 3.14 and 3.16. Figure 3.24c inset illustrates the geometry of a single bipod as viewed from the side and above. This simulated hysteresis

loop models the longitudinal and polar components of the bipod, as with fig. 3.24a the magnetic field is applied at a 35° angle with respect to the nanowire long axis in order to replicate the field geometry in experimental MOKE magnetometry. Observing the longitudinal component, this is very similar to fig. 3.24a, as both show a symmetric loop with gradual increase in M_x from negative saturation, prior to a sharp transition at approximately +50 mT, and further gradual increase to positive saturation. This is not surprising because the two wires comprising the bipod are both identical in geometry to fig. 3.24a.

Figure 3.24d also shows hysteresis loops for simulated polar and longitudinal signals of a tetrapod geometry, comprising of four individual wires, each identical to fig. 3.24a. Two upper wires are connected by a central vertex to two lower wires, acting as a building block of the combined L1 and L2 sub-lattice layers. Comparison with fig. 3.24c shows an extended tail leading to saturation and a lower remanent magnetisation of approximately $0.4M_S$. This can be attributed to the geometry of the tetrapod as seen in the inset of fig. 3.24d, the two wires projecting along the x-axis are subject to the field geometry seen in fig. 3.24a and so the reversal of these two wires is primarily dominated by DW motion. However, the two wires projecting along the y-axis experience a field that is directed perpendicular to the wire long-axis (as occurred for fig. 3.24b), leading to a reversal dominated by rotation. Assuming no interactions occur at the vertex, the resultant hysteresis loop is expected to be a linear combination of the easy and hard axis loops presented in fig. 3.24a and b. It is also noted that the characteristic polar signal seen in the bipod is not present for the tetrapod, likely because the tetrapod is comprised of two equal and opposite bipods, so any net polar signal generated in one sub-lattice layer would be cancelled out by an opposing signal in the other layer.

Additional simulations were conducted upon the bipod and tetrapod geometries to build an understanding of the expected magnetisation configuration within a 3DNL (fig. 3.25 and 3.26). Simulated MFM contrast is overlaid on these simulations, this was calculated as discussed in section 2.5. Initially, the remanent state of a bipod geometry is examined in fig. 3.25, whereby the magnetisation vectors of the individual wires are relaxed to be orientated parallel and anti-parallel (fig. 3.25a and b respectively). When both wires are magnetised in the same direction, the vector plot shows a rotation in the magnetisation at the vertex, therefore introducing a variation in M_z . Since MFM is sensitive to the second derivative of H_z , both positive and negative MFM contrast are expected to be observed about this peak, as is

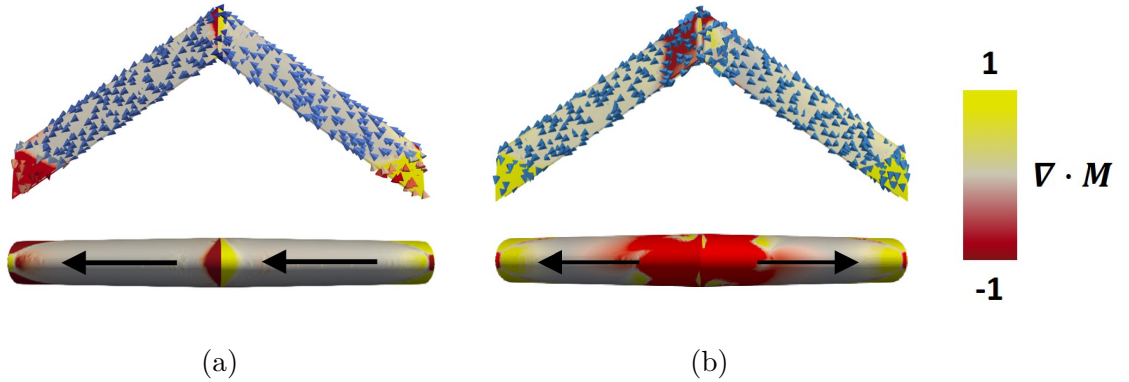


Figure 3.25: Finite-element simulations of bipod structures at remanence, **a**, head-to-tail and **b**, tail-to-tail configurations were defined here. For each state, the spin texture is viewed from the side-on (upper), and simulated MFM contrast is seen from top view (lower). Black arrows indicate the direction in which each individual wire is magnetised.

predicted in fig. 3.25a. This contrast is tightly confined to the peak and the edges of the bipod because no variation in M_z is present along the length of the wire, due to the wires relaxing into a single domain state. Figure 3.25b shows the remanent state of an alternative scenario where the magnetisation vectors of the two wires are defined to orientate away from the vertex. After a relaxation procedure is executed a tail-to-tail vortex DW is formed, indicated by the dark red region at the peak of the vector plot. Vortex DWs in conventional planar magnetic wires only possess a component that is perpendicular to the wire plane at the vortex core⁹⁴. However this is more complex for the 3D arrangement of nanowires present in a bipod, close examination of the vector plot in fig. 3.25b shows significant variation in M_z across the domain wall, resulting in the simulated MFM contrast spreading across a far greater area in comparison with fig. 3.25a.

Magnetic nanowires arranged about a four-wire vertex within 2D systems are well documented within the literature^{33,34,37}. However examples comparable to nanowires constructed in a 3D diamond-bond lattice geometry are far more limited. A crucial factor when considering how significantly these 3D nanowire networks can compare to bulk spin-ice crystals is the available states and their associated relative energy scale. Ideally, individual wires would possess a cylindrical geometry, allowing a four-fold rotational symmetry at a vertex, as is the case for atomic spins positioned at the corners of a pyrochlore lattice within bulk spin-ice, this could therefore be expected to realise degenerate ice-rules states. It is noted that the magnetic

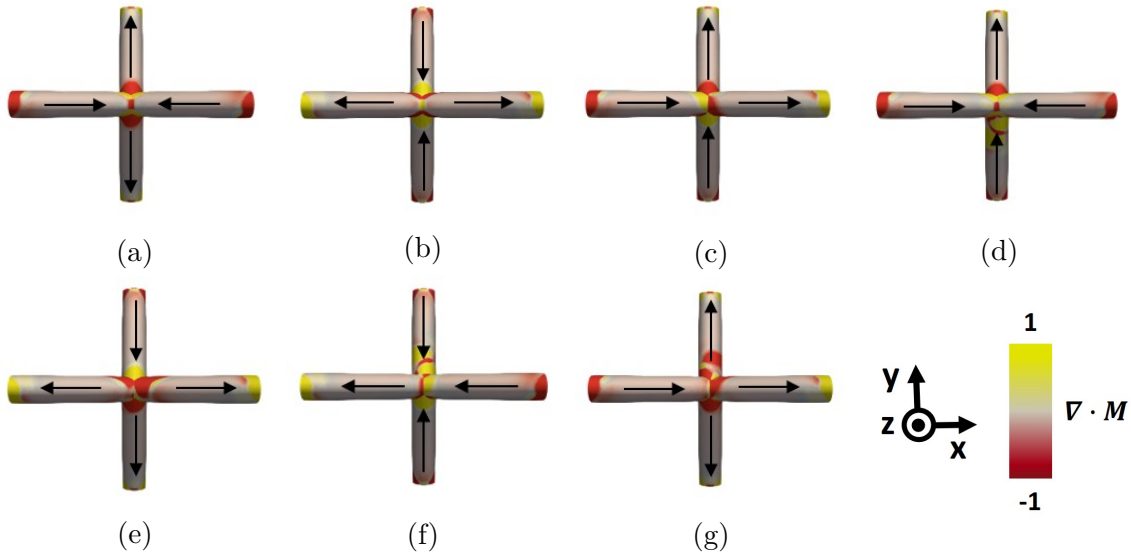


Figure 3.26: Finite element simulations of a tetrapod geometry, red and yellow contrast illustrates simulated MFM signal, black arrows the orientation of the magnetisation vector for each individual wire. **a-b**, Type 1 vertices. **c**, Type 2 vertex. **d-g**, Type 3 vertices.

nanowires presented here do not match this idealised cylindrical geometry. Instead the crescent shaped cross-section results in a broken symmetry. To investigate the extent to which this broken symmetry impacts the degeneracy of available states, finite-element simulations of tetrapod geometries are given in fig. 3.26 to examine the remanent state of all accessible magnetic configurations aside from those which could result from rotational transformations.

Simulation Index	Vertex Configuration	Energy Density (Jm^{-3})
a	Type 1	8342
b	Type 1	8342
c	Type 2	7745
d	Type 3: 3-in/1-out	11683
e	Type 3: 3-out/1-in	11685
f	Type 3: 3-in/1-out	10447
g	Type 3: 3-out/1-in	10447

Table 3.2: Energy density values of different tetrapod remanent states. Simulation index refers to the relevant subfigure label in fig. 3.26.

The notation being used for vertex type is identical to that which is used to describe similar four-wire vertices in 2D ASI. Each simulation resulted in all nanowires relaxing into a single domain state, allowing the wires to behave as effective Ising spins, just as atomic spins do in bulk spin-ice. Only type 1, 2, and 3 vertices were observed in simulations, any attempt at realising a type 4 vertex became unstable and relaxed into a lower energy state. Energy densities for all 7 remanent states are presented in table 3.2. Both type 1 vertices yield a density of 8342 Jm^{-3} , implying that there is negligible difference if the two magnetisation vectors orientated towards the vertex are associated with the lower wires or the upper wires. The energy densities of type 1 and type 2 vertices are seen to agree within 7%. This discrepancy is likely due to the previously discussed broken symmetry in these crescent shaped wires (section 3.5.1). However, this distinction between type 1 and type 2 vertex energy is smaller than previous studies have found in 2D ASI³⁶. This result is a key motivating factor behind the desire to investigate frustration within 3D systems, as it offers hope that research into the 3D nanostructuring of magnetic materials may allow the study of true artificial analogues of bulk frustrated materials. Figure 3.26 also displays simulated MFM contrast for each magnetic configuration, calculated with the same method used for the bipod in fig. 3.25. A distinct, different set of simulated MFM contrast is observed for each of the seven vertices, as this crucially depends upon the magnetisation of each nanowire connected to the junction. This result, as well as the simulated hysteresis loops shown in fig. 3.24, indicates that standard experimental techniques such as MFM and MOKE magnetometry might be able to elucidate a wealth of information from these 3D nanowire networks. To specify, these measurements could reveal the reversal mechanisms by which nanowires within the lattice switch, and the extent to which a near-degenerate set of ice rules are obeyed. Finite-element simulations of bipod and tetrapod structures will be revisited in greater detail in the next chapter.

3.5.3 MAGNETIC CHARACTERISATION

Thus far it has been shown that TPL coupled with thermal evaporation has the ability to construct 3DNLs in the geometry of a diamond-bond lattice (section 3.5.1). By modeling building blocks of this nanowire lattice via finite-element simulations (section 3.5.2), it was predicted that these wires act as an approximation of Ising spins and switch predominantly through the propagation of vortex domain walls. Additionally, vertices between four wires are anticipated to obey a near-degenerate set of ice rules at remanence. Here, an experimental analysis of a physical 3DNL is

presented. MOKE magnetometry probed the coercivity and reversal mechanisms of the $Ni_{81}Fe_{19}$ sheet film and nanowire lattice. Comparison of these revealed whether or not the nanowires of interest could be measured independently of the surrounding film. MFM measurements of the lattice at remanence discerned the extent to which the simulated MFM contrast presented in fig. 3.25 and 3.26 were observed in the physical system, this also provided an opportunity to acquire further evidence that the individual nanowires relaxed into a single domain state.

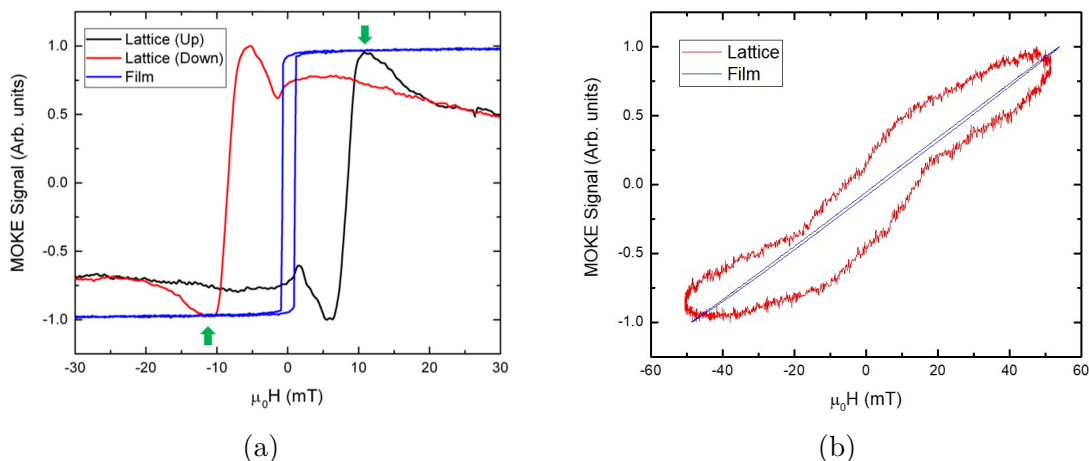


Figure 3.27: MOKE loops measured from both the $Ni_{81}Fe_{19}$ sheet film and nanowire lattice in longitudinal and polar geometries for **a**, and **b**, respectively.

Hysteresis loops given in fig. 3.27 were obtained by focussed MOKE magnetometry in both longitudinal and polar geometries (measurements were performed by Dr Matthew Hunt of Cardiff University). Figure 3.27a used a laser path orientated at 45° with respect to the substrate plane and applied field direction in order to examine the in-plane magnetisation. Here the applied field geometry was identical to fig. 3.24c-d, resulting in a similar loop dominated by a sharp transition associated with domain wall propagation at the coercive field of 8 mT. However, four lobes are present symmetrically in the up and down sweeps taking the measured signal significantly beyond M_S , not seen in the simulated longitudinal signal. Firstly the two lobes positioned at approximately -6 mT and +6 mT on the down and up sweep respectively are believed to be an artefact resulting from specular reflection off the sheet film deposited on the substrate. To substantiate this, the film loop is overlaid on the same plot to illustrate that the initial transition occurs at the coercive field of the film. This highlights a key benefit of 3D lattices in which the nanowires are very densely

spaced, with several lower polymer wire layers acting as scattering centres, thus reducing the proportion of the reflected signal arising from the substrate film. Prior to any measurements, care is taken to precisely align the laser spot centrally upon the 3DNL to maximise the signal associated with the nanowires. Comparison of the loops yielded from the $Ni_{81}Fe_{19}$ film and nanowires demonstrates an increased coercive field by an order of magnitude, as can be expected for nanostructured materials.

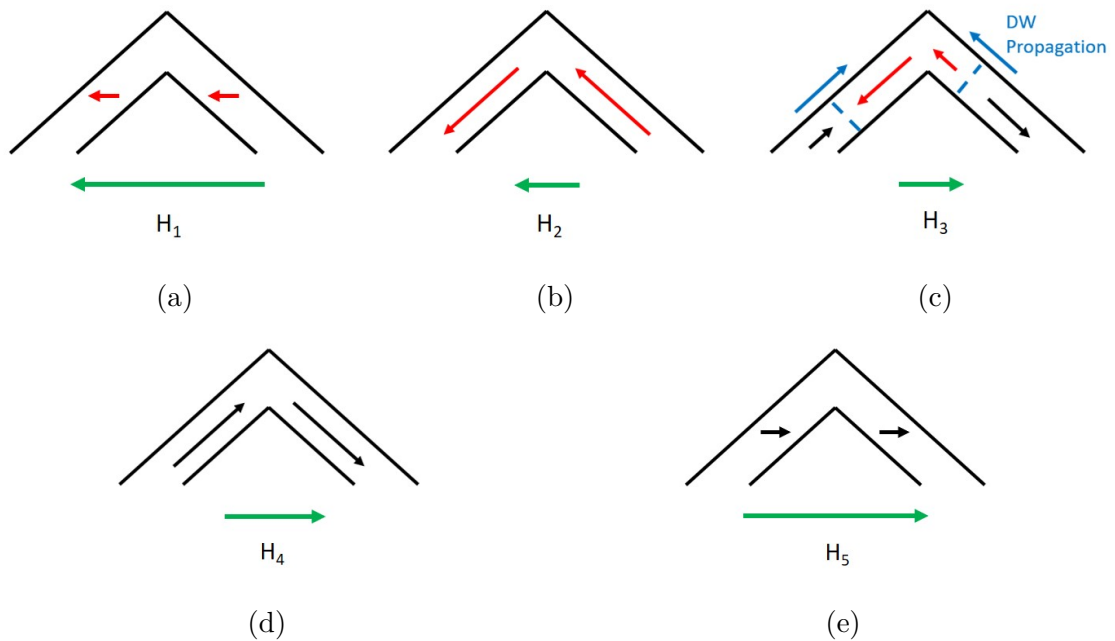


Figure 3.28: Illustrations of a bipod shown side-on at different stages of a reversal from negative to positive saturation. Red and black arrows indicate direction of magnetisation within the nanowire. The direction and magnitude of the external field is annotated by green arrows.

Two further lobes are observed, indicated by green arrows, these are believed to be the result of polar contributions to the MOKE signal. Whilst a polar signal was observed in the simulated bipod hysteresis loop, the scale of this effect is greatly enhanced here. Figure 3.28 presents illustrations of a possible explanation as to why this polar contribution would be exaggerated in experiments. Each diagram shows the plane of magnetisation for both wires at different points as the applied magnetic field sweeps from negative to positive saturation. It is clear that no polar signal should be expected for fig. 3.28a and e, because the magnetisation of both wires lies parallel to the applied magnetic field. Whilst this is not the case for fig. 3.28b and d, the out of plane components of both wires are expected to be equal and opposite,

therefore no net polar component is observed. Figure 3.28c illustrates the period of switching in which DWs are present, where it is expected that opposing DWs would nucleate at either end of the bipod, before propagating towards the vertex and annihilating. In experiments there is likely to be some finite tilt between the substrate plane and that of the applied field, even when great care is taken whilst mounting the sample. If this is the case, one could expect that the nucleation and propagation of the two DWs would be asymmetric, hence leading to a net polar signal. Any signal arising from polar MOKE is expected to be an order of magnitude greater than longitudinal MOKE^{95,96}, meaning that this effect would likely be observed in the resultant signal, if it is indeed occurring. To help understand which sub-lattices were probed via longitudinal MOKE, it is insightful to compare this measured hysteresis loop with the simulated loops for the bipod and tetrapod geometries (fig. 3.24c-d respectively). The large remanence ($\sim 0.85M_S$) seen in the bipod simulation shows a much closer resemblance to the measured loop when compared with the tetrapod simulation, which displayed an extended tail and lower remanence ($\sim 0.40M_S$) not present in the measurement. Additionally the simulated bipod yields both a longitudinal and polar signal which, when combined provide a close comparison to the measured lattice loop. Therefore it is concluded that in this setup the measured MOKE signal is predominantly sensitive to only the L1 sub-lattice layer.

A polar setup was utilised for fig. 3.27b, such that the substrate plane was mounted perpendicular to both the applied field and wave vector of the incident laser path. Therefore the entire 3DNL was expected to be exposed to the incident laser and contribute to the acquired signal, because the incident laser path was identical to the viewing plane in fig. 3.14a-b, where all $Ni_{81}Fe_{19}$ nanowires are visible. Here the coercive field of the nanowire lattice is also enhanced by an order of magnitude with respect to the substrate. A hard axis loop was acquired from the film, this is to be expected due to the applied field being projected perpendicular to the substrate plane, resulting in the film switching via rotation. The film did not saturate within the applied field range, though this is not surprising as $Ni_{81}Fe_{19}$ films typically saturate out-of-plane at ~ 1 T⁹⁷, well above the capability of the electromagnet used in this setup. However, the nanowires were orientated at 35° to the substrate, meaning that both rotation and domain wall propagation are evident in the produced hysteresis loop. Rotation is associated with the gradual increase in applied field from -50 mT to approximately +8 mT, this occurs as the magnetisation vector of each wire is initially aligned parallel to the applied field, before rotating to align with the long nanowire axis. At +8 mT a sharper transition initiates, indicating the propagation of domain

walls, this transition is seen to be less sharp than in fig. 3.27. To understand this the film loop is overlaid, showing that any specular reflection from the substrate film would cause the acquired loop to shear over. In addition, the polar setup is more likely to be sensitive to any nanoislands on the substrate than the longitudinal setup. These islands are expected to yield a hard-axis hysteresis loop with a similar trend to that of the film for an out-of-plane field direction. Hence, islands on the substrate may well be a contributing factor behind why the hysteresis loop measured from the lattice is sheared over in comparison with the lattice data in the longitudinal setup.

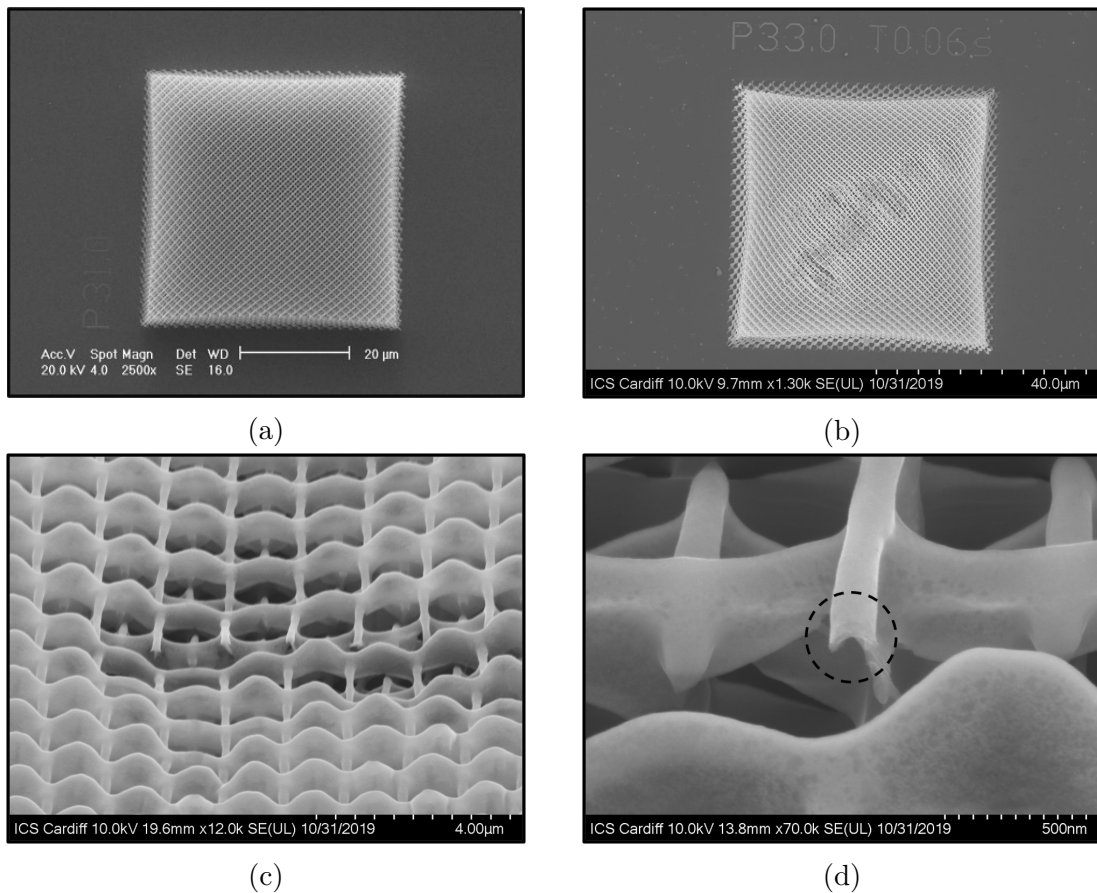


Figure 3.29: SEM images displaying deformation of a 3DNL and underlying polymer structures. **a**, Diamond-bond lattice which has not been exposed to intense electron or laser beams. **b**, Diamond-bond lattice seen from top-view after exposure to a 6 mW laser for a long duration (several hours), to obtain the data presented in fig. 3.27. **c**, The central region of the same lattice seen from a 45° angle with respect to the substrate. **d**, Magnified image of the same region. A dotted circle indicates the end of wire that has been sheared off.

Many measurement techniques typically used to probe magnetic nanostructures require the use of highly intense electrons, x-rays, or laser beams, as such it

is crucial that the structures of interest are significantly robust, to prevent these methods becoming destructive. To this end, the extent to which a 3DNL may deform under these potentially destructive methods will be investigated next. Figure 3.29a, displays a structure which has received no exposure to intense electrons or laser beams, and is included for reference. Figure 3.29b-d presents the structure from which the MOKE data given in fig. 3.27 was extracted. During this analysis a 6 mW laser was focused upon the upper surface of the lattice for a long period of time (minimum of one hour). Repetitions were performed whilst incrementally moving the laser spot between the upper-right and lower left corners, based on the viewing orientation seen in fig. 3.29b. Whilst the metallic $Ni_{81}Fe_{19}$ nanowires are expected to possess relatively high thermal and electrical conductivity, the same cannot be said for the underlying polymer scaffold, which insulates the 3DNL from the surrounding sheet film. The resulting deformation of the polymer scaffold and hence the $Ni_{81}Fe_{19}$ nanowire lattice is clear to be observed and is localised to only regions exposed to the 6 mW laser spot. Interestingly, in fig. 3.29d a polymer wire which should be present in the region highlighted by a black dotted circle has disappeared altogether, whilst the deposited $Ni_{81}Fe_{19}$ remains in place. This $Ni_{81}Fe_{19}$ wire has also sheared off from the adjoining wire, allowing the cross-section to be seen. Observations of this magnified view provide further evidence for the crescent cross-section with a graded thickness discussed previously.

Deformation under intense electron/laser beams raises serious concerns over the potential to characterise these structures via MOKE, SEM, and a host of other measurement techniques. The most likely reason for this deformation occurring is the poor electrical and thermal conductivity of the polymer scaffold, which isolates the 3DNL from the surrounding film. In an attempt to alleviate this issue, new structures were fabricated for which four layers of gold are first deposited at a $\sim 60^\circ$ angle with respect to the substrate (see section 2.2), thus coating the lattice side walls and acting as a conductance layer. Once suitable samples were produced, an individual four-wire vertex was observed via SEM under high magnification (fig. 3.30), to investigate the effect of this gold deposition. For this example, each of the four gold depositions was 10 nm in thickness. Images were captured at 10 minute intervals over 120 minutes, during which the electron path remained positioned on the vertex. Comparison of fig. 3.30b and c indicates no obvious deformation occurred during exposure. Additionally, fig. 3.30d shows a darkening of the exposed region, but no deformation to the lattice, this discolouration is likely due to carbon deposited during imaging.

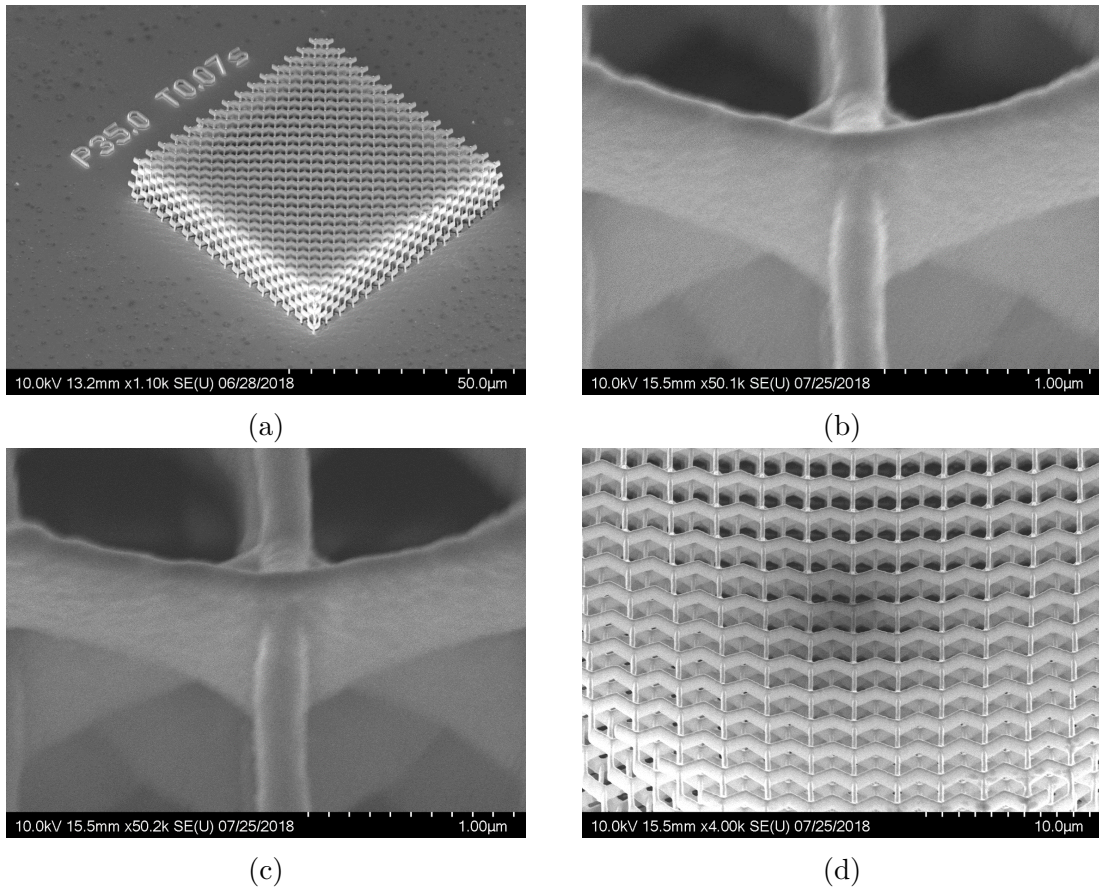


Figure 3.30: SEM images of a diamond-bond lattice with four gold depositions at a 30° angle with respect to the substrate, prior to a top-down $Ni_{81}Fe_{19}$ deposition. **a**, Entire lattice viewed from 45° , before exposure to an intense electron beam. **b**, An individual four-wire vertex viewed at 45° with 50000x magnification. **c**, The same vertex after 120 minutes of exposure to the electron beam, no deformation is observed. **d**, The same region viewed at 4000x magnification, the lattice is seen to be darkened in the exposed region.

With this positive result of a 3DNL which can withstand intense electron beams, the next logical step was to return to MOKE measurements. Hysteresis loops obtained from a diamond lattice structure nominally identical to that which was studied in fig. 3.27 are presented in fig. 3.31, with the only difference being the addition of a conductive gold layer. A laser power of 6 mW resulted in the deformation seen in fig. 3.29, whereas here no damage could be observed (via optical microscopy) after extended exposure beyond 10 mW. However, to exercise caution and ensure repeatability, 7 mW was used, as this produced MOKE loops of sufficient signal-to-noise ratio in a relatively short time period (~ 10 minutes).

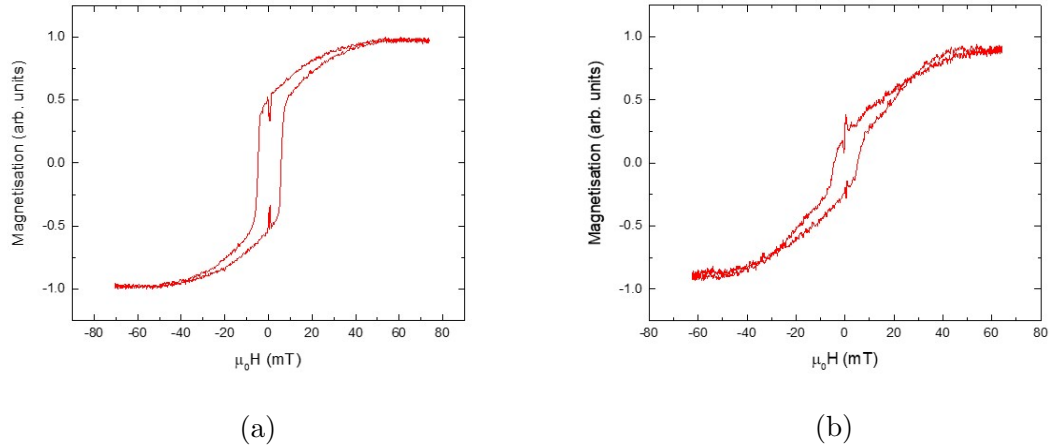


Figure 3.31: MOKE loops obtained in a longitudinal geometry, from a 3DNL with an underlying gold layer. **a**, Data acquired with the applied magnetic field parallel to the projection of L1. **b**, Applied field perpendicular to the projection of L1.

Observing fig. 3.31a where the projection of L1 is orientated parallel to the applied magnetic field, the wires once again switch via both rotation and domain wall propagation. Although here, the gradual increase in magnetisation associated with rotation as the field sweeps from -70 mT to +6 mT, is greatly extended. Thus leading to a lower remanent magnetisation of approximately $0.5M_S$. This falls between the remanence found for the simulated bipod and tetrapod geometries, suggesting that these MOKE measurements are predominantly sensitive to L1, but not entirely, with L2 also contributing to the resultant signal. This conclusion is substantiated by fig. 3.31b, in which the lattice is rotated by 90° about the z-axis, such that the projection of L1 is perpendicular to the applied magnetic field. A similar appearing loop is produced, expressing both rotation and domain wall propagation. However here, rotation dominates because no component of the nanowire long axis in L1 extends parallel to the field, yielding a result similar to that of fig. 3.24b. Despite this, an abrupt transition does occur at the nanowire coercive field, albeit a small transition in comparison to fig. 3.31a, with a remanence of approximately $0.2M_S$. This sharp transition indicates the propagation of DWs is being measured, which can only be originating from L2, given the applied field geometry. As such, the acquired MOKE signal must be sensitive to at least the upper two sub-lattices. Figure 3.31a-b exhibit coercive fields of 6.5 T and 5.4 mT respectively, both of which are reduced in comparison with the 8.0 mT coercivity that was measured in fig. 3.27. A reduced coercivity is expected here because the gold depositions increase the width of the resulting $Ni_{81}Fe_{19}$ wires. It is also noted that whilst great care was taken to position

the laser spot centrally upon the lattice, contributions from the surrounding sheet film could not be eliminated altogether. As seen by the small, abrupt transition in both MOKE loops at an applied field of $< 1 \text{ mT}$.

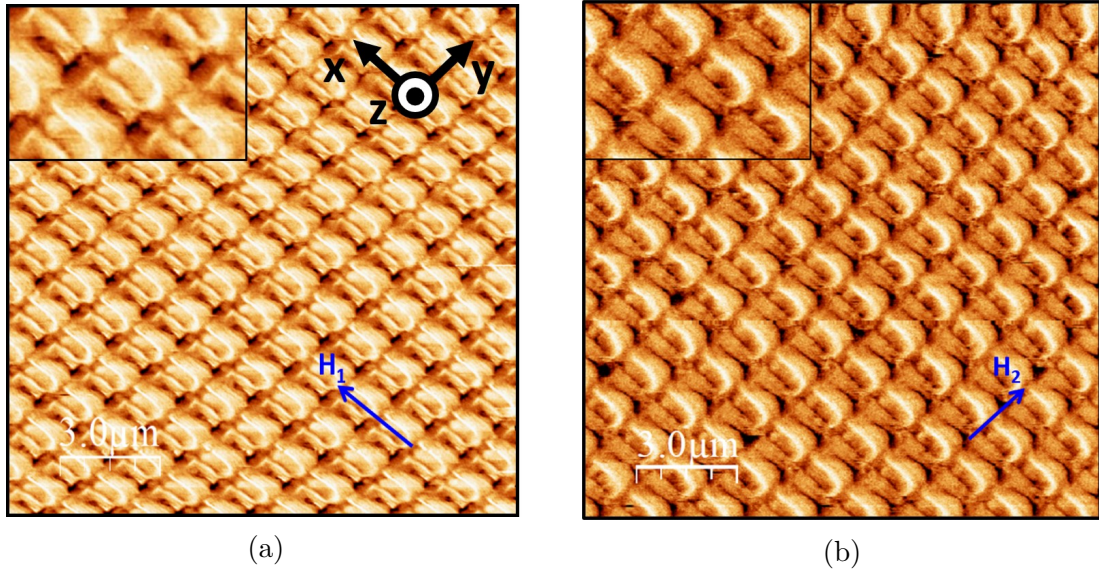


Figure 3.32: MFM images captured from a 3DNL at remanence following the application of a saturating magnetic field parallel to L1 and L2 for **a**, and **b**, respectively. Insets display magnified regions.

As discussed in section 3.5.1, AFM has the ability to closely track the complex 3D topography of the upper sub-lattice layers of the nanowire lattice. It is therefore possible to study the magnetic configuration at individual microsites on the lattice using MFM, paving the way for a vast array of potential experiments. Firstly, fig. 3.32a-b shows MFM images of a $15 \mu\text{m} \times 15 \mu\text{m}$ region of a 3DNL at remanence following the application of an external magnetic field aligned parallel and perpendicular to L1 respectively. The two images show identical remanent states, indicating the nanowires to be single domain and Ising-like.

It is well known that artefacts can arise in MFM data if the topography is not being sufficiently closely tracked and corrected for in the AFM scan. To investigate if the observed MFM contrast is indeed magnetic in origin and not an artefact associated with the 3D topography, the nanowire lattice was captured before and after inverting the magnetisation vector of the MFM probe (fig. 3.33b and d respectively). Prior to this imaging, the lattice was once again relaxed from saturation along L1. Figure 3.33b displays a complex pattern of MFM contrast

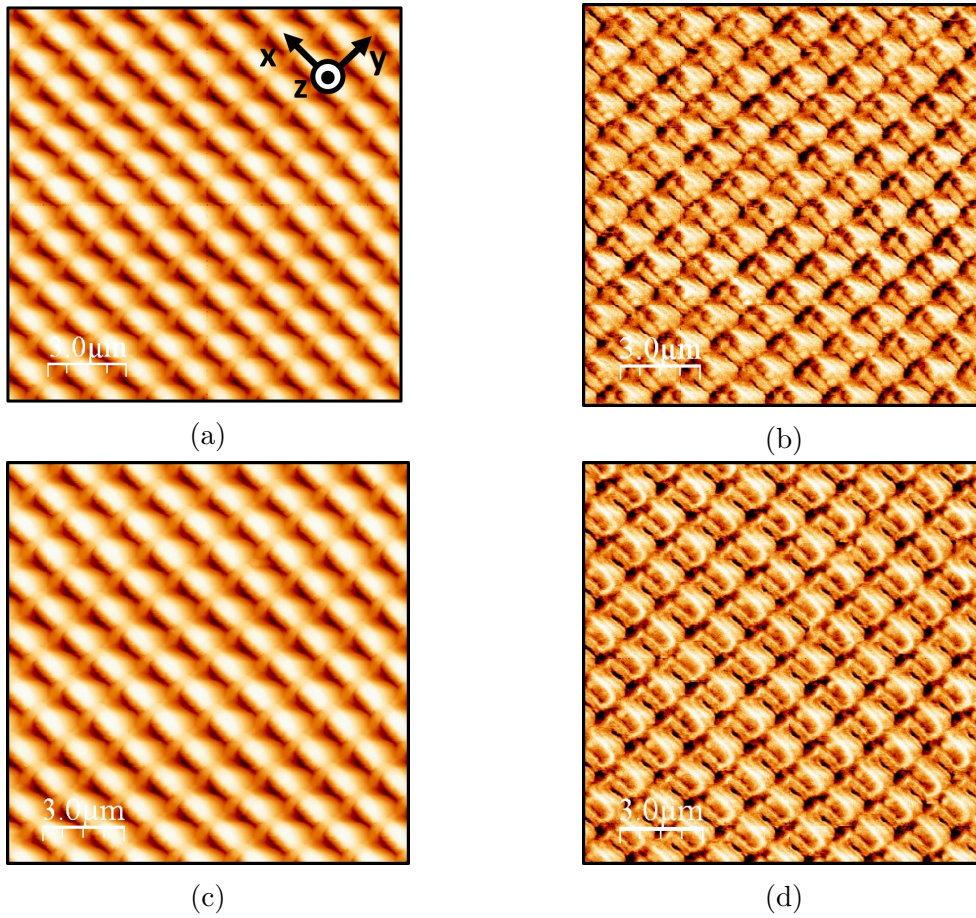


Figure 3.33: AFM and MFM scans of a 3DNL at remanence, following the application of a saturating magnetic field. **a-b**, AFM and MFM scans respectively, taken with the tip magnetised down. **c-d**, AFM and MFM scans respectively, captured from the same region after inverting the tip magnetisation.

originating from the nanowires as well as the voids in between. After inverting the probe magnetisation, the MFM signal originating from L1 shows clear differences, indicating this signal to be magnetic in origin. However, visual inspection of this data is made difficult by the bright regions associated with voids in the lattice. To aid visual observations, the MFM data was multiplied by the associated topography, before the result was rotated and cropped to yield the images shown in fig. 3.34. Here, fig. 3.33a-b were multiplied to produce fig. 3.34a, whilst multiplying fig. 3.33c-d yielded fig. 3.34b. This process allows one to more easily focus upon the contrast associated with the L1 sub-lattice.

Figure 3.34a yields clear MFM contrast in a complex pattern which is repeated across all L1 bipods within the image, this pattern is better shown in fig. 3.34c

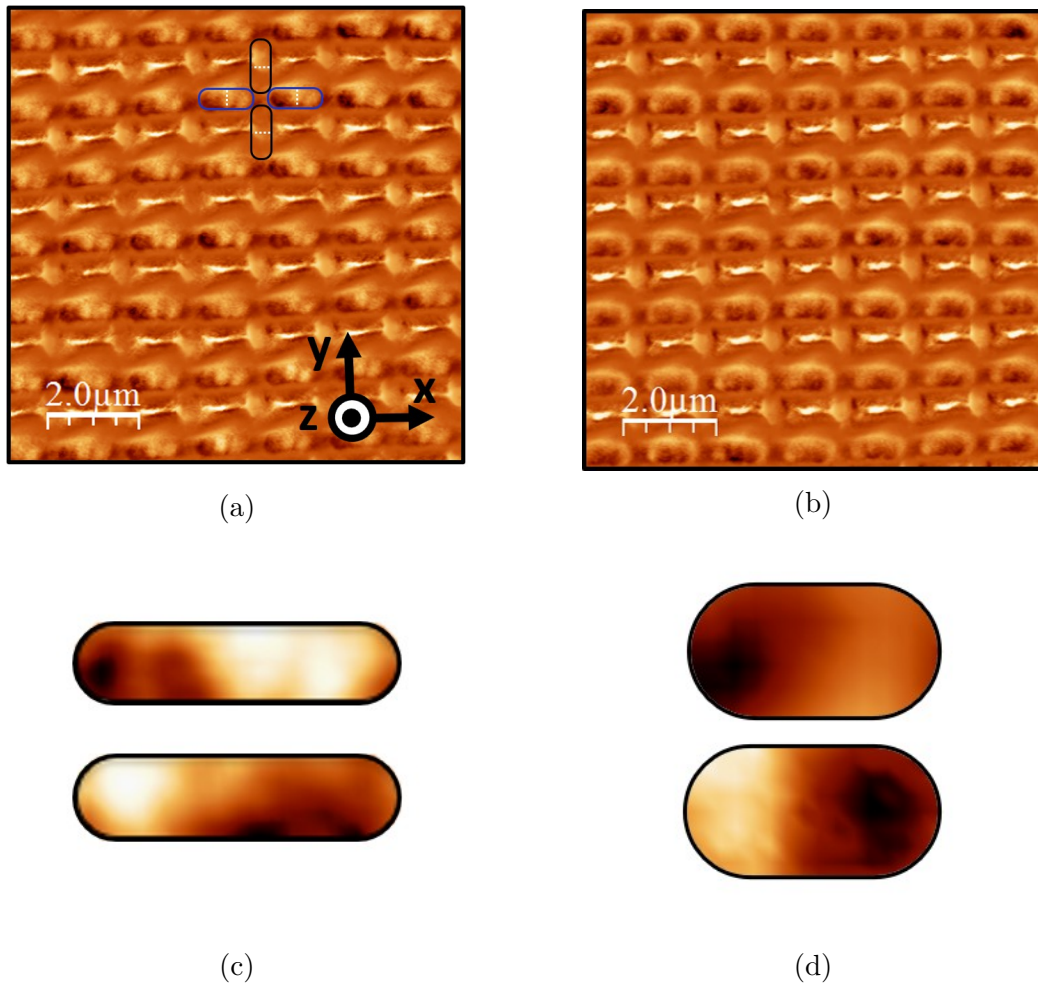


Figure 3.34: MFM scans of a 3DNL. **a-b**, Image of the same area on the lattice before and after reversing the tip magnetisation. To aid analysis, the data has been processed in WSxM, minimising any artefacts due to topography and enhancing the contrast originating from L1. Raw data is presented and analysed in fig. 3.33. **c**, MFM contrast associated with a single bipod before (upper) and after (lower) reversal of the tip magnetisation. **d**, MFM contrast produced at a four wire vertex before (upper) and after (lower) reversing the tip magnetisation.

(upper). Relaxation from an identical field geometry produced the simulated MFM contrast given in fig. 3.25a. Visual inspection gives a close agreement between experimental data and simulations, both yield contrast at the edges of the bipod structure as well as at the central peak. Experimentally, the contrast spreads along the wire far more than is seen in the simulations, however this is to be expected because the minimum resolvable feature size approximately scales with the lift height of the MFM probe during data acquisition. Additionally, contrast is discerned from the four wire vertices (fig. 3.25d) between two upper wires (part of L1) and two lower perpendicular wires (part of L2), adjacent lobes of opposite MFM contrast are

measured here. A close approximation of these four wire vertices are the simulated tetrapods in fig. 3.26, where only type 2 vertices (fig. 3.26c) yields adjacent lobes of opposing MFM contrast, similar to those observed in the experimental data. This infers that type 2 vertices are present at all L1-L2 junctions upon relaxation from a saturating field applied parallel to the projection of L1. An explanation for these observations is that the nanowires associated with L1 remain aligned with the applied field as it is reduced to zero, whilst the lower wires align head-to-tail along L2 to satisfy one of the low energy ice-rule states.

Once the tip magnetisation was reversed, the MFM contrast associated with the magnetic material can also be seen to have inverted, whereby positive contrast (bright) became negative (dark) and vice-versa. This effect is most clearly visualised in the magnified individual bipod and four wire vertex (fig. 3.25c-d respectively), showing that this MFM contrast is indeed magnetic in origin. Conversely the bright narrow strips of contrast between L1 wires are not seen to invert, therefore this is likely to be a topography related artefact associated with the deep gaps in these regions (see fig. 3.14). To reinforce the qualitative observation of inverted contrast, fig. 3.35 displays a quantitative analysis of this data. Here, 50 line profiles of individual vertices have been measured before and after the tip magnetisation was inverted, with the average of these plotted. A clear inversion of MFM phase is seen after the tip magnetisation is reversed, providing further evidence that the observed MFM contrast associated with these regions is indeed magnetic in origin.

Results presented within this chapter offer strong evidence that TPL and line-of-sight deposition provide a means to nanostructure single domain magnetic nanowires into complex 3D geometries. It is also possible to probe the magnetic properties of such systems, using standard in-house techniques such as MFM and MOKE magnetometry. Further insight into the switching mechanism within these could be gained through imaging the dynamics of domain walls propagating through 3 dimensions via MFM.

3.6 SUMMARY

A brief summary of the key findings and results presented in this chapter.

- Depositing a 50 nm $Ni_{81}Fe_{19}$ film upon a pre-fabricated template can yield

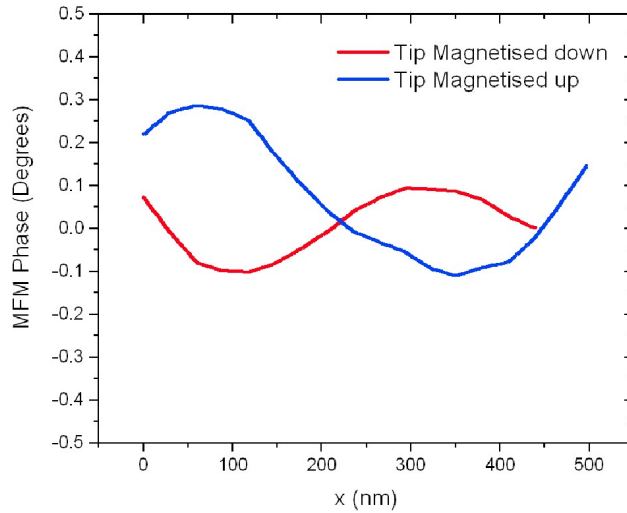


Figure 3.35: Quantitative analysis of fig. 3.33a and c. Line profiles of 50 L1-L2 vertices in each image were taken using WSxM and an average of these is plotted.

microwires and pads possessing a variety of remanent domain structures, dependant upon the local shape anisotropy, which can be directly observed via MFM.

- AFM and MFM can probe the topography and magnetic configuration of nano/micro wires and pads suspended above the substrate, a number of which are seen to be single domain.
- TPL and line-of-sight deposition can yield a $Ni_{81}Fe_{19}$ nanowire lattice upon a polymer scaffold in a diamond-bond lattice geometry, with strong user-control over the structure design.
- The 3D topography of the upper two sub-lattices can be probed via AFM.
- Micromagnetic simulations indicate nanowires within the lattice to be single domain and to reverse via the propagation of vortex DWs.
- Simulating tetrapod building blocks reveals a near-degenerate ice rule manifold, where type 2 vertices are the minimum energy state.
- Optical magnetometry can probe the reversal mechanism of the upper nanowire layers in a 3DNL, with the vast majority of the detected signal thought to originate from the L1 sub-lattice. MOKE measurements were seen to be a

destructive technique, unless a conductive layer is deposited upon the scaffold sidewalls prior to the $Ni_{81}Fe_{19}$ deposition.

- MFM also indicates wires within the lattice to be single domain, and inversion of the tip magnetisation demonstrates the complex pattern of MFM contrast associated with the L1 sub-lattice to be magnetic origin.

Chapter 4

Imaging Magnetic Monopole Excitations on a 3D Frustrated Magnetic Lattice

‘There’s something that doesn’t make sense. Let’s go and poke it with a stick.’

DOCTOR WHO

In chapter 3 the fabrication of 3D $Ni_{81}Fe_{19}$ nanowire lattices was optimised, before simple magnetic measurements were conducted. Here, analysis of these structures is furthered by testing the extent to which the magnetic configuration of a 3DNL can be controlled. MFM was used to visualise the lattice spin texture following precisely applied in-plane magnetic fields, allowing the observation of different sub-lattices switching independently. By capturing images at regular field increments, one can generate and observe excited states, the behaviour of which could then be studied on different sub-lattices. Two related physical perspectives can be used to understand the behaviour of such systems. Firstly, since the nanowire lattice captures the arrangement of spins in bulk spin-ice crystals, excitations can be treated as magnetically charged monopole-like states. A Monte-Carlo approach is well suited for modeling a large collection of pseudo spins, where each nanowire can be approximated by an individual Ising spin. Alternatively, one can focus upon more local physics which governs the switching of individual nanowires upon the lattice and in particular how domain walls pin to form the relevant states. This perception requires a more detailed

model to capture the impact of DW structure and pinning, hence finite-element simulations were used for this. Whilst finite-element simulations allowed the calculation of detailed spin textures within nanowires, this approach cannot be scaled up to full 3D lattices due to computational constraints. For this reason, finite-element simulations focused upon two key building blocks of the diamond lattice. Firstly, a four-wire junction known as a tetrapod was considered, which is a fundamental unit within the bulk of the lattice. Secondly, a two-wire junction known as a bipod was studied, this is the unit that terminates the surface of diamond lattices (when grown along [001]). In connected nanowire lattices it is the propagation of DWs that mediates the transport of emergent magnetic charges. Therefore, both monopole physics and DW physics have been considered when investigating excitations above the ice-rule manifold. Although, it must be stated that monopoles and DWs are two separate entities which can not be treated as one and the same. Monopoles are composite micromagnetic entities that arise when the configuration of a nanowire junction violates the ice-rule, resulting in a net magnetic charge. DWs are the intermediate spins between domains of differing magnetisation, numerous permutations of DW structure are available in connected nanowire lattices, as discussed in section 1.5. In complex systems, one or more DWs may be present at nanowire junctions, forming a portion of the spin texture that comprises a monopole.

4.1 DIRECT OBSERVATION AND MANIPULATION OF A 3D SPIN TEXTURE

In the previous chapter, it was shown that AFM can closely track the 3D topography of the upper nanowire layers on a 3DNL. Furthermore, a magnetic signal can be extracted from the uppermost nanowire layer via MFM, closely agreeing with simulations of a saturated state. To further understand the physics of this system, including what vertices are possible and how the system switches upon a global scale, the next logical step is to apply external magnetic fields to the sample, and discern any variations in the observed MFM contrast. For this, the most practical solution is to fix an electromagnet in place around a sample which is mounted on the AFM stage (see fig. 2.16), as this allows for successive measurements of a particular region following various applied field protocols. Section 2.5 describes the mounting procedure and current-field calibration, which demonstrated a linear relationship of $\sim 10 \text{ mTA}^{-1}$.

Before embarking on any complex field-driven experiments, it was crucial to initially build a confident understanding of how the MFM contrast originating from each sub-lattice related to the associated magnetic configuration. Therefore, MFM measurements were captured after the system was placed into several well defined states, as seen in fig. 4.1. Here, saturating fields of 30 mT were applied parallel with the projection of each sub-lattice, yielding saturation of L1 (uppermost sub-lattice) and L2 (sub-lattice below L1) along the negative x and y directions respectively (fig. 4.1b). During field applications, the piezotube was raised by several centimetres above the sample, to avoid affecting the probe magnetisation. MOKE magnetometry presented in section 3.5.3 indicates 30 mT to be well above the external field required to saturate both sub-lattices. To be clear, here saturation is referring to the in-plane magnetisation component of all wires on a particular sub-lattice being aligned along the long-axis. Since these images were captured at remanence, the magnetisation of each wire possessed an out-of-plane component as shape anisotropy constrains the magnetisation to orientate parallel with the wire long-axis. To preserve the signal originating from wires below the surface layer, these images have not been processed by multiplying the MFM signal with the topography, as was done for fig. 3.34. Whilst this post-processing step was helpful to highlight the contrast originating from L1, any magnetic signal associated with wires below this surface layer was lost. Therefore, MFM data presented in this chapter has only undergone minor processing, as outlined in section 2.5. Figure 4.1c illustrates the 3DNL after a field of 30 mT has been applied along the positive x-direction. Here it can be seen that the MFM contrast only changes on L1, whilst the L2 sub-lattice is seen to be unchanged. The contrast originating from all L1 wires within the observed area inverted with respect to fig. 4.1b, indicating that L1 has reversed to the opposite saturation state. Figure 4.1d shows the system after 30 mT was applied along the negative x and y directions, returning it to the initial state seen in fig. 4.1b, before a 30 mT field was applied along the positive y direction. Here, it is the contrast originating from L2 that has inverted, whilst the L1 signal remains unchanged with respect to fig. 4.1b. These measurements crucially show that the switching of individual sub-lattices can be clearly discerned using MFM.

MFM contrast originating from positively and negatively saturated L1 and L2 bipods is presented in fig. 4.1e-h. For both sub-lattice reversals, distinctly opposing states are readily identified through visual inspection, each of which are seen throughout the measured area of the corresponding saturated state. It is noteworthy that the MFM contrast observed in fig. 4.1e-f closely matches fig. 3.34c, where the

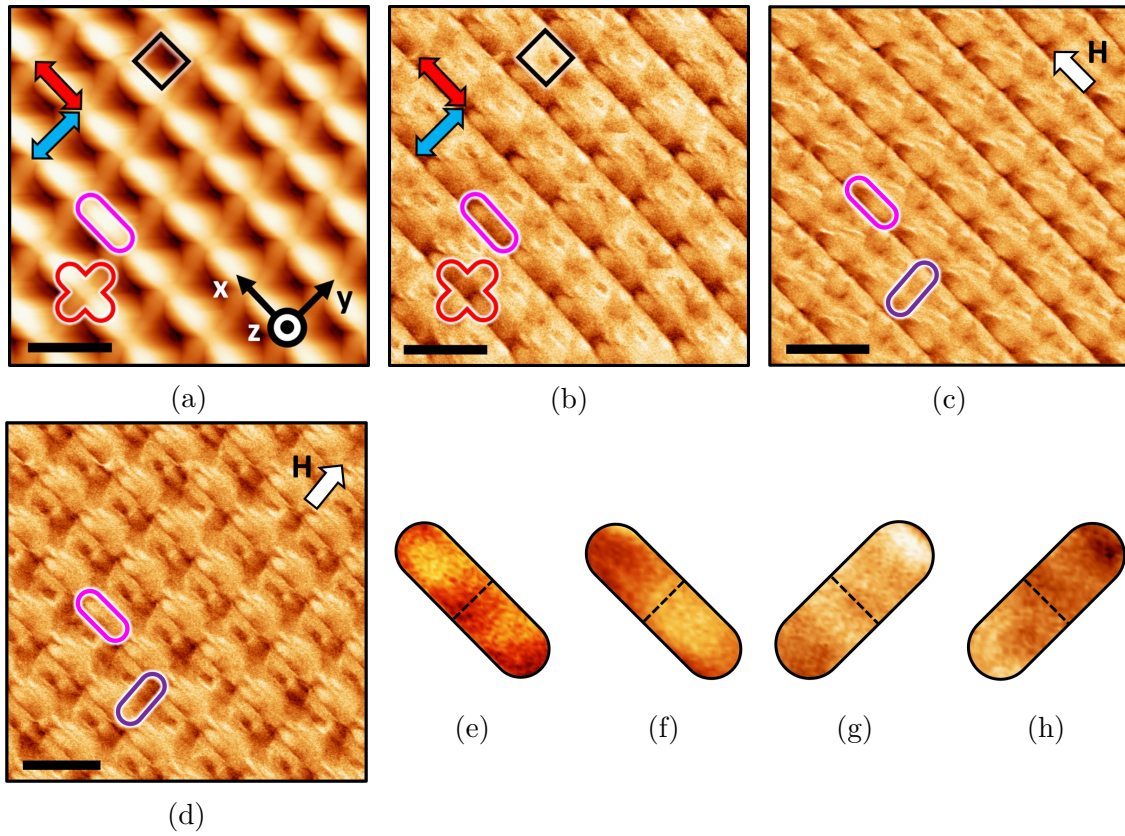


Figure 4.1: AFM and MFM images of opposing saturation states. **a**, AFM image of a 3DNL. L1 (red arrow) and L2 (blue arrow) are clearly visible. An L1 bipod and a tetrapod are annotated with pink and red outlines respectively, and a black outline encompasses a void region. Scale bar is $2\mu\text{m}$. **b**, Associated MFM image in which L1 and L2 are saturated along the negative x and y axes respectively. **c**, L1 is now saturated in the positive x -direction, whilst L2 is unchanged. A purple outline annotates an L2 bipod. **d**, L2 is now reversed, with saturation along the positive y -direction, L1 is once again saturated with negative x -component. **e-f**, MFM contrast associated with individual L1 bipods saturated with negative and positive M_x respectively. Dotted lines indicate the bipod vertex. **g-h**, MFM contrast associated with L2 bipods saturated with negative and positive M_y respectively.

sample was unchanged and the tip magnetisation was reversed, providing further confidence that these images represent oppositely magnetised states. Interestingly, the MFM signal originating from L2 always appears stronger in the upper-right region of each bipod, when compared with the lower-left, whereas this asymmetry is not seen on L1. This is likely due to the effects described in section 2.4, where the MFM probe tracks the topography less closely immediately following a drop in height. Therefore, after the MFM probe passes over the L1-L2 vertex there is a slight delay in the descent to L2. Hence, the sample-probe distance is expected to be greater when scanning over the lower-left region of L2 bipods, resulting in weaker

probe-stray field interactions and weaker MFM contrast when compared with the upper-right section.

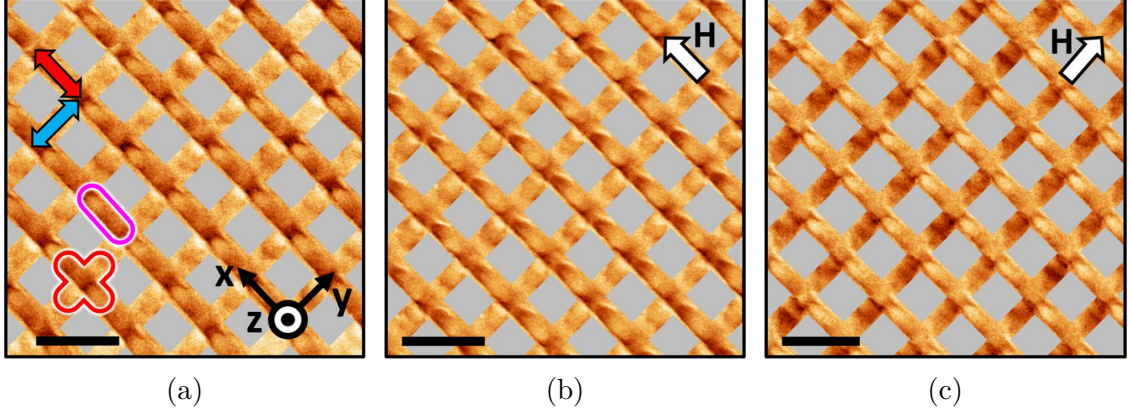


Figure 4.2: Identical MFM data to fig. 4.1. Here, masks are annotated over the void regions. This aids visual analysis of the MFM contrast originating from L1 and L2. Scale bars are $2 \mu m$.

Whilst the L1 and L2 MFM contrast is well defined, the signal originating from the square regions that aren't associated with either of these sub-lattices (see fig. 4.1b) is more difficult to interpret. These square regions are comprised of L3 and L4 wires as well as void space. The topography of these lower sub-lattices was less closely tracked, likely due to a greater probe-wire separation since the probe quickly scans across this gap without fully descending into this space. As a result, any probe-stray field interactions were substantially weaker for L3 and L4 compared with the upper layers. Therefore, MFM studies in this chapter have focused on the L1 and L2 sub-lattices, from which a distinctive signal can be repeatably measured. To aid visual observations of the upper two sub-lattices, it was helpful to cover these square regions with masks, as shown in fig. 4.2. Here, masking is the only alteration from the data given in fig. 4.1, this greatly aids data interpretation by allowing one's eyes to focus on the signal associated with the upper two sub-lattices.

Having now confirmed that saturated states along principal directions can be directly confirmed using MFM, the next step was to understand the switching in these complex systems. MOKE measurements shown in the previous chapter examined the switching properties on the surface of a 3DNL, within the lateral extent of the laser spot size. Here, MFM is utilised to visualise the magnetic configuration and track the switching process as the system tends towards saturation^{14,41}. A small number

of images were initially captured at coarsely spaced field intervals, in order to gauge the approximate field range over which each sub-lattice reverses. Figure 4.3 shows one such measurement of an intermediately magnetised state, where an immediately striking feature is the long, dark strip of MFM contrast (annotated by a black arrow) that extends across seven L1 bipods. No such features were witnessed in saturated samples, suggesting that this could be the result of a DW. However, DWs in nanowires tend to be localised features, and would certainly not be expected to span such a significant proportion of the lattice. In fact, micromagnetic simulations presented in fig. 3.26 predict the MFM contrast associated with a DW to remain localised to a single nanowire junction, as previous MFM studies of connected nanowire systems have seen^{41,43,98}. Bearing this in mind, the dark strip is likely the result of a DW being

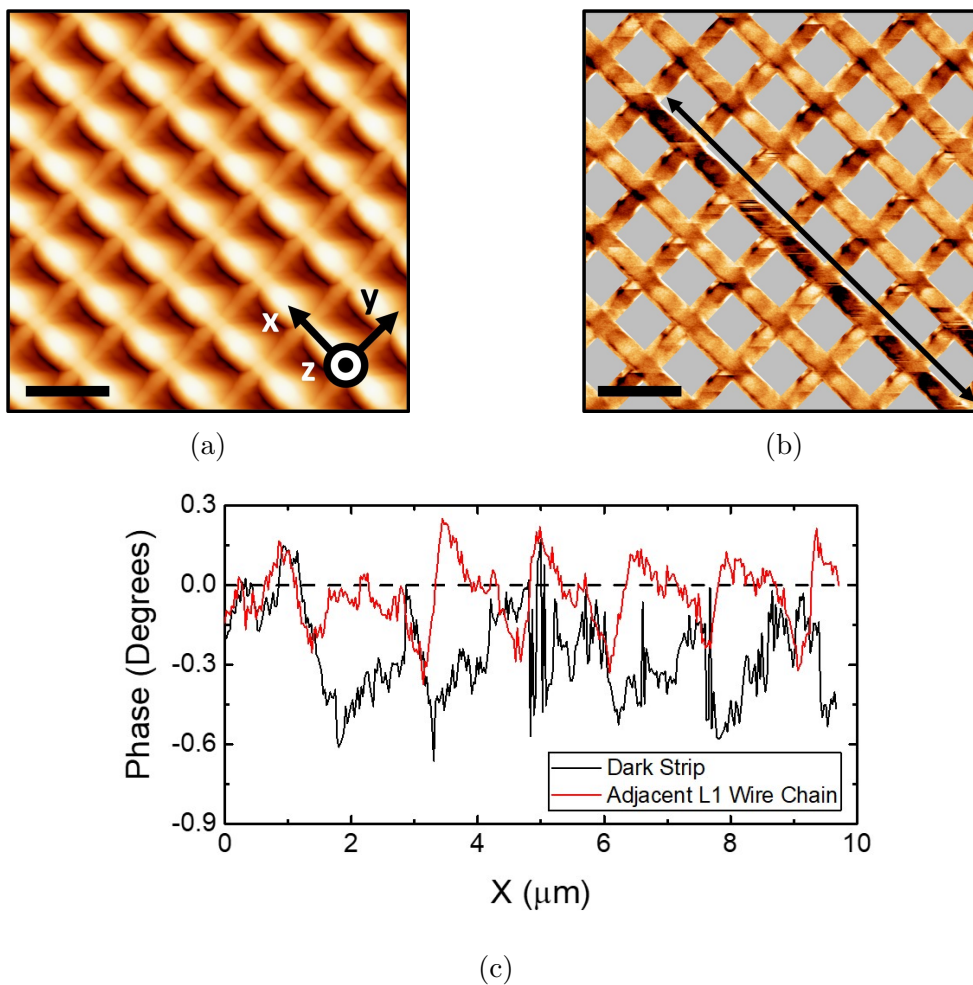


Figure 4.3: A non-saturated 3DNL. **a**, AFM scan of an approx. $9 \mu m \times 9 \mu m$ region. **b**, Associated MFM scan, annotated arrow indicates a dark strip along a L1 wire chain. Both scales are $2 \mu m$. **c**, Line profiles of a MFM scan along the dark strip (black) and an adjacent wire chain (red).

moved by the stray field of the probe. This hypothesis is supported by the relatively intense signal detected in the dark strip. Figure 4.3c compares this measured phase with that of an adjacent L1 wire chain. A different phase is clearly detected from the region associated with the dark strip, likely due to a DW producing a large gradient of stray field, causing a greater phase shift when compared with saturated wire chains.

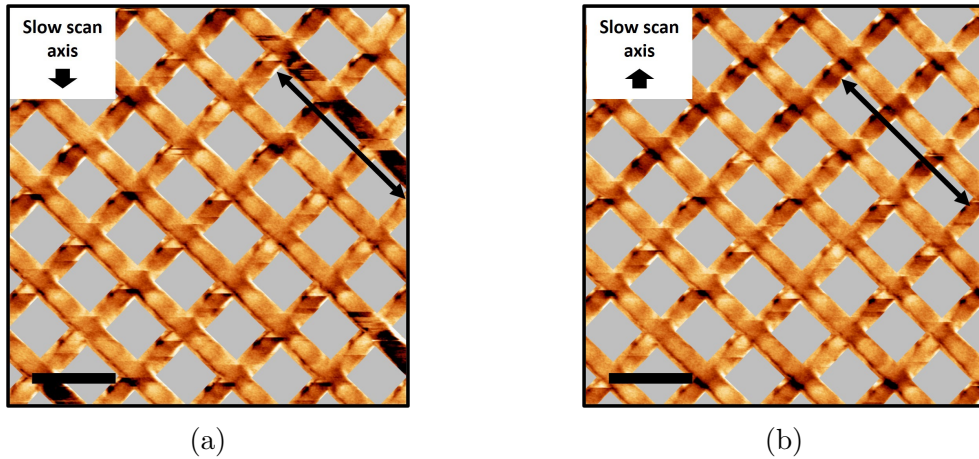


Figure 4.4: Two successive scans of the same $8 \mu m \times 8 \mu m$ region, with the probe slow scan axis orientating **a**, Down. **b**, Up. A black arrow is annotated in the same position on both images. Both scale bars are $2 \mu m$.

To test this hypothesis, an external field was applied along the L1 axis to yield a non-saturated state, before successive images were captured with the slow scan axis orientated in opposite directions. Figure 4.4a shows an image that was scanned from top to bottom, three dark strips are seen, although only one spans multiple L1-L2 junctions within the measured area. After this scan had completed, the probe was allowed to continue scanning from bottom to top over the same region (see fig. 4.4b), the slow-scan axis was the only difference between the acquisition of the two images. A black arrow is annotated in the same position on both images. Interestingly, the dark strips are not observed when the probe scans back over the same area, despite no external fields being applied to the sample, demonstrating that the probe must be altering the sample magnetisation as it scans across the 3DNL. An effect which can occur if the probe-sample interactions are strong enough to manipulate the lattice spin texture. This explains why such behaviour is only observed at intermediately magnetised states, because these interactions may be too weak to nucleate a DW, though if an external field generates a DW prior to the data acquisition, this could be moved with relative ease. Clearly this presents an issue, as it is very difficult to draw reliable conclusions from data

which was influenced by the measuring instrument. To resolve this issue, a survey of commercially available MFM tips was performed, the findings of which are presented in table 4.1. As can be seen, the Nanosensors SSS-MFMR tips have a moment of just 0.25×10^{-13} emu, the lowest found to be commercially available, a $\sim 17\%$ reduction compared to the previously used MESP-LM-V2. These tips also possess the advantage of a reduced tip radius in comparison with standard probes, allowing higher resolution AFM and MFM. Therefore, SSS-MFMR tips were sourced for further measurements, all proceeding MFM data was captured using these probes.

Make	Model	m (10^{-13} emu)	H_c (Oe)	Tip Radius (nm)
SPM Tips	CO-CR COATED	1.00	300 – 400	< 60
Bruker	MESP-HM-V2	3.00	400	80
Bruker	MESP-V2	1.00	400	35
Bruker	MESP-LM-V2	0.30	< 400	25
Nanosensor	PPP-MFMR	1.00	300	< 50
Nanosensor	PPP-LC-MFMR	0.75	0.75	< 30
Nanosensor	PPP-LM-MFMR	0.50	250	< 30
Nanosensor	SSS-MFMR	0.25	125	< 15

Table 4.1: Survey of commercial MFM probes comparing magnetic moment, coercivity, and nominal tip radius of curvature. These data were recorded from the specifications given on the web page for each probe.

After acquiring Nanosensors SSS-MFMR probes, another set of images were captured following coarsely spaced field increments. Two examples of MFM images captured using these softer probes are presented in fig. 4.5. The difference with fig. 4.3 is clear, both of fig. 4.5b-c display a single region of particularly intense contrast (highlighted with black arrows), each localised to a single L1-L2 junction. In both cases the enhanced contrast separates regions of opposing magnetisation on the L1 wire chain, as the two bipods to the upper-left of the excitation in fig. 4.5c resemble fig. 4.1f, whilst the 4.5 bipods seen to the lower-right resemble fig. 4.1e. This, along with the enhanced phase (quantified in fig. 4.5d), demonstrates that these regions of intense contrast must signify vertices that are excited above the ice-rule manifold. Excited vertices with opposing magnetic charge (i.e. 3-in/1-out and 3-out/1-in) exhibit opposing MFM contrast, due to the differing net stray field

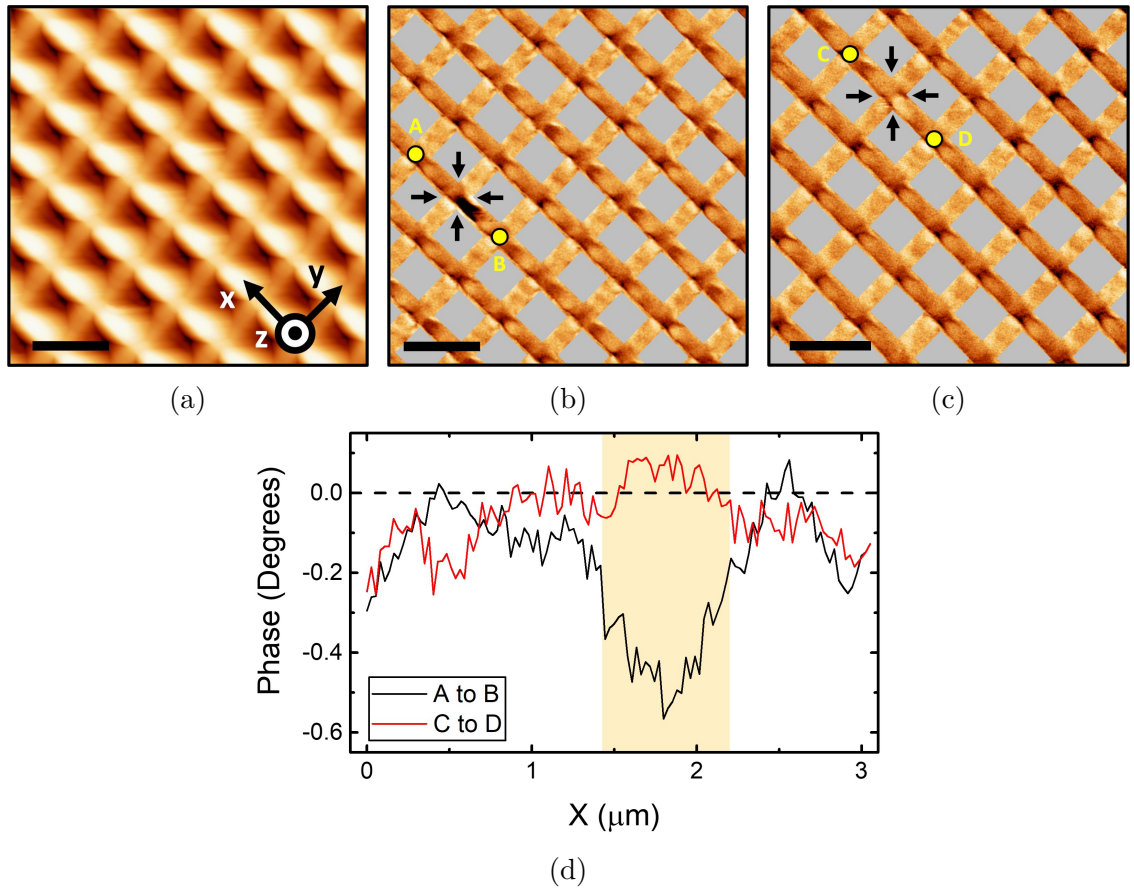


Figure 4.5: $9 \mu\text{m} \times 9 \mu\text{m}$ scans of a non-saturated 3DNL using a Nanosensors SSS-MFMR probe. **a**, AFM scan. **b**, Associated MFM scan, arrows highlight a dark, intense region of contrast, situated between oppositely magnetised sections of an L1 wire chain. **c**, Example of a similarly intense region, exhibiting an opposing phase. All scale bars are $2 \mu\text{m}$. **d**, Line profiles for each excitation, markers are annotated on the images to show the approx. start and end points. A shaded region indicates the phase associated with each excitation.

associated with either state. It is noteworthy that both intense regions of contrast extend partway along one of the wires connected to the L1-L2 junction, suggesting that the DW associated with each monopole is pinned slightly off the centre of each vertex. In 2D connected systems DWs have been found to pin off vertices⁴¹. The DW equilibrium position will depend upon local energetics and will be explored in detail later in this chapter. Micromagnetic simulations, shown in fig. 3.26, also predicted the MFM contrast to spread partway along one or more of the adjoining wires. Changing to the SSS-MFMR probes was therefore judged to be a success, as repeated measurements indicated that these probes were not manipulating the sample magnetisation, whilst the configuration of L1 and L2 could still be interpreted.

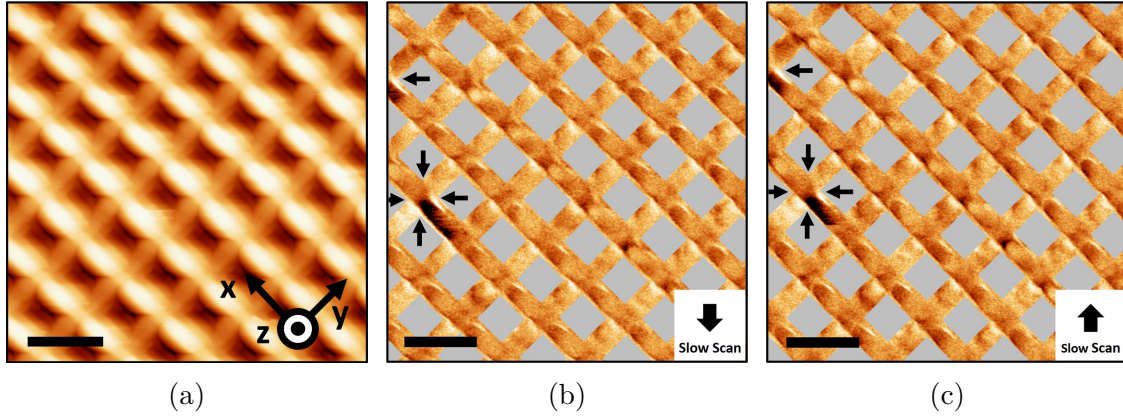


Figure 4.6: $9 \mu\text{m} \times 9 \mu\text{m}$ scans of a non-saturated 3DNL using a Nanosensors SSS-MFMR probe. **a**, AFM scan. **b**, MFM image with a downwards slow-scan direction. Arrows highlight two dark, intense regions of contrast on the L1 sub-lattice. **c**, Subsequent MFM image under identical conditions, with an upwards slow-scan direction. All scale bars are $2 \mu\text{m}$.

To further test the SSS-MFMR probes, a 3DNL was once again placed into an intermediately magnetised state by applying a field along the L1 projection. Next, an initial scan was performed to ensure a monopole excitation was present within the measured area. Once an excitation had been found, successive images of this area were captured under identical conditions, with the slow scan direction alternating between up and down for consecutive scans. Figure 4.6b-c shows examples of images with the slow scan axis orientating downwards and upwards respectively. Two regions of intense contrast indicating monopole excitations are witnessed, one is entirely within the measured area (highlighted with four arrows), whilst the other is partially observed (highlighted with one arrow). Once again each monopole remains localised to one nanowire junction. Furthermore, visual analysis determined negligible variations between images, demonstrating that the SSS-MFMR probes allow repeatable scans without manipulating the sample magnetisation.

As discussed in section 1.8, ice-rule-obeying vertices possess a net zero magnetic charge (Q), whereas type 3 vertices violate the ice rule and possesses $Q = \pm 2q$. To quantify the magnetic charge associated with an individual wire (q), one only needs to consider the wire geometry and composition⁹⁹

$$q = \frac{m}{l} = M_S A \quad (4.1)$$

where the magnetic moment is related to the magnetisation by $m = M_S V$, for

a $Ni_{81}Fe_{19}$ composition $M_S = 8.6 \times 10^5 \text{ Am}^{-1}$. For planar wires, the cross-sectional area is simply found by multiplying together the wire width and thickness. This is less straightforward here since nanowires studied in this thesis exhibit a crescent shaped cross-section, as outlined in the previous chapter. One method for approximating this cross-sectional area is illustrated in fig. 4.7. The area of a semi-circle is subtracted from half of an ellipse to leave the area of a crescent shaped cross-section with a peak thickness of 50 nm. Defining $W = 200 \text{ nm}$ as is indicated by SEM measurements, yields $A = 7.9 \times 10^{-15} \text{ m}^2$. Therefore, applying eq. (4.1) yields $q = 6.8 \times 10^{-9} \text{ Am}^{-1}$, hence a type 3 vertex possesses $Q = \pm 1.4 \times 10^{-8} \text{ Am}^{-1}$.

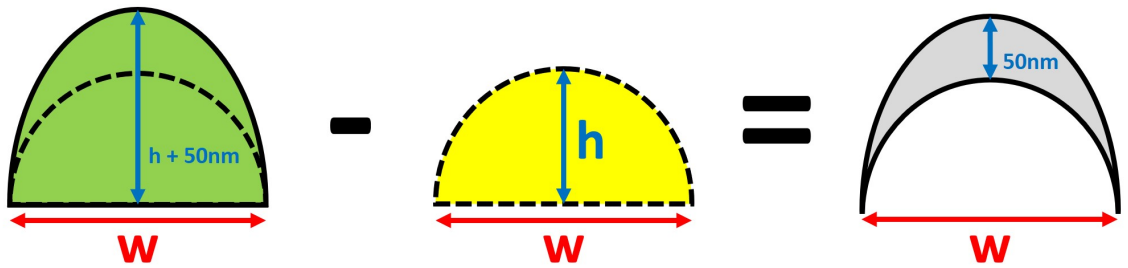


Figure 4.7: Nanowire cross-section calculation. A semicircle (yellow) of width w and height h is subtracted from an ellipse (green) of minor-axis w and major axis $h + 50 \text{ nm}$ to yield a crescent cross-section (grey) with a peak thickness of 50 nm. The dotted semicircle outline is overlaid on the ellipse for comparison.

Having demonstrated that excited states can now be observed without altering the sample, the logical next step was to investigate the extent to which monopoles can be resolved and tracked as they propagate across the nanowire network. To do so requires extensive knowledge of the MFM signal associated with different states. Figure 4.8 has been compiled to aid the interpretation of complex MFM images, where individual L1-L2 junctions are observed in different magnetic configurations. Firstly, the topography of an L1-L2 junction is shown in fig. 4.8a-c via SEM and AFM. Comparison of the two techniques once again shows that AFM is mostly sensitive to the upper two layers of the 3DNL and that it exaggerates the lateral feature, most notably on L1. Although this is expected, since scanning probe techniques are typically used to measure 2D samples. Figure 4.8d-f show magnified examples of the saturated states that were seen in fig. 4.2a-c respectively, hence each pair of colinear wires exhibit a matching pattern of contrast. These saturated states also clearly show that upon reversal of each sub-lattice, the signal associated with the relevant wires is seen to invert. Figure 4.8g-j present examples of L1-L2 junctions

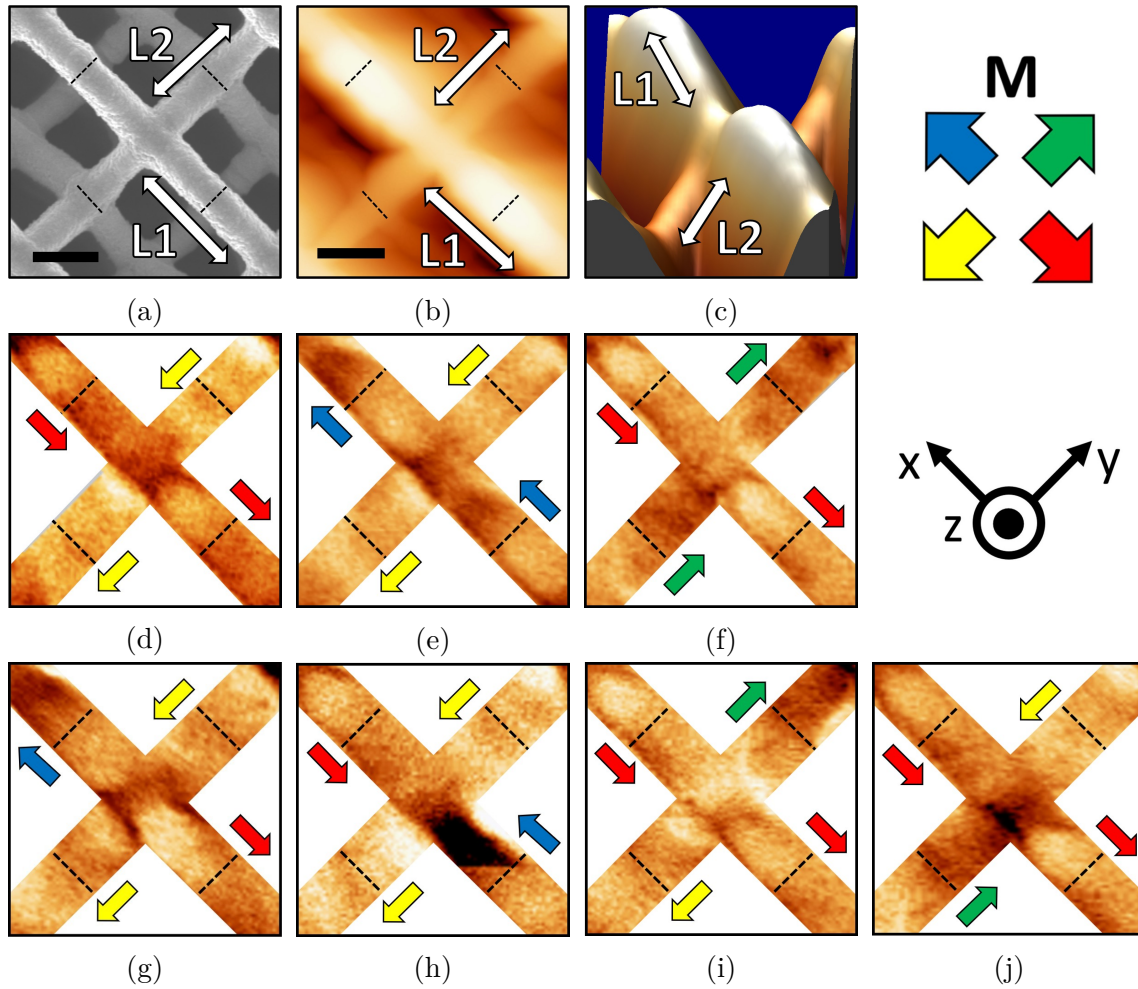


Figure 4.8: Identifying different states for an individual L1-L2 junction. **a**, SEM image focused upon an individual L1-L2 junction, dotted lines are annotated on neighbouring nanowire junctions. Scale bar indicates 500 nm. **b**, Topography associated with an individual L1-L2 junction, measured via AFM. Scale bar indicates 300 nm; this is consistent for all AFM/MFM images. **c**, 3D representation of AFM data. **d-f**, MFM contrast associated with L1-L2 junctions exhibiting 3 variations of a type 2 configuration. Arrows indicate in-plane magnetisation orientation. **g-h**, Examples of type 3 vertices with opposing L1 wires. **i-j**, Examples of type 3 vertices with opposing L2 wires.

displaying type 3 configurations, readily identified due to the enhanced MFM signal. Examples are given for $Q = \pm 2q$ with opposing L1 wires (fig. 4.8g-h) and opposing L2 wires (fig. 4.8i-j), other examples which would be effectively identical following a rotational transformation are not shown here. These have been extracted from several different images, each of which was captured following the application of an in-plane magnetic field sequence which yielded an intermediately magnetised state along one sub-lattice, whilst the other sub-lattice remains saturated. In each

case, one pair of colinear wires exhibits opposing contrast with respect to one another, whilst the other pair of colinear wires show matching patterns of contrast, immediately indicating either a 3-in/1-out or a 3-out/1-in state. To deduce the specific configuration, one must consider the spatial arrangement of contrast both at the vertex and on nearest neighbour wires. When observing the signal associated with nearest neighbour wires, it is particularly useful to refer back to saturated examples (such as fig. 4.1e-h) to help interpret the local magnetisation.

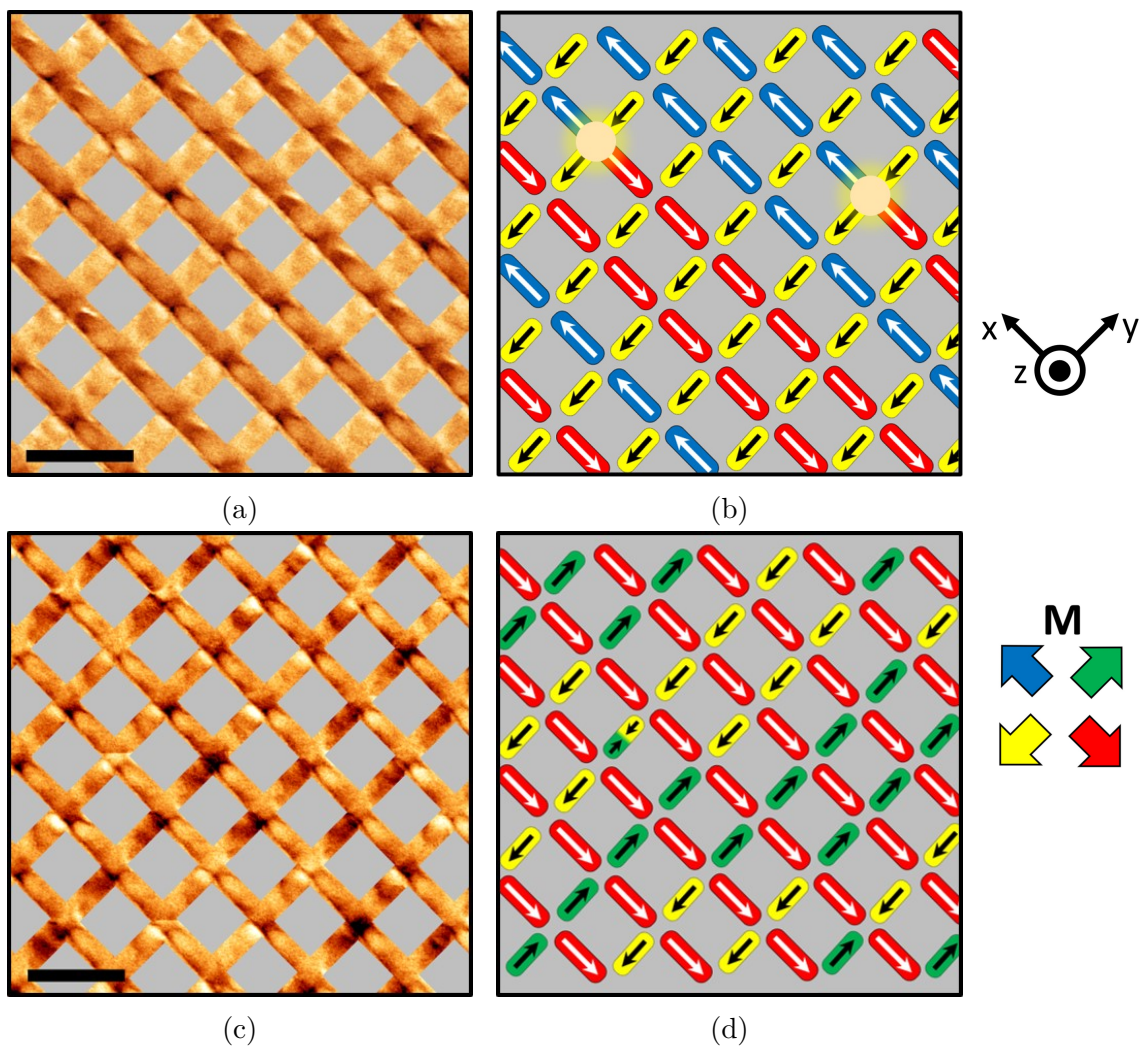


Figure 4.9: **a**, $8 \mu\text{m} \times 8 \mu\text{m}$ MFM scan of a 3DNL following relaxation from a 9.5 mT in-plane magnetic field, applied along the L1 projection (x-axis). L2 remains saturated. **b**, Vector map illustrating the magnetic configuration in the associated MFM data. Each ellipse illustrates a bipod, coloured by the local in-plane magnetisation. **c-d**, Similar MFM data and associated vector map following 8.0 mT applied along the L2 projection (y-axis), L1 is saturated. Both scale bars are $2 \mu\text{m}$.

Figure 4.9a shows an MFM scan following a $H = 9.5$ mT in-plane magnetic field applied parallel to the L1 projection, whilst L2 remains saturated. Optical magnetometry shown in the previous chapter indicates this to be within the field range that switching is expected to occur across. A vector map of the magnetic configuration (fig. 4.9b) has been produced through observations of the MFM contrast associated with each L1-L2 junction as well as the surrounding wires. Comparison with the magnified data presented in fig. 4.8 and fig. 4.1e-h also aided data interpretation. Here, every L1-L2 junction in the observed area resembles one of the patterns seen in fig. 4.8d-e, with two exceptions. These are two monopole-excitations, each with a charge of $Q = -2q$, which distinctly resemble the contrast pattern seen in fig. 4.8g. Figure 4.9c-d shows a similar intermediate state following relaxation from a $H = 8.0$ mT in-plane magnetic field applied along the L2 projection, L1 is saturated. Here, 9 monopoles are identified through observations of the contrast associated with each L1-L2 junction, as well as the surrounding wires. In both intermediate states, the sub-lattice that extends along the field direction is effectively demagnetized ($M < 0.1M_S$), so it is intriguing that a vast difference in the density of monopole-excitations is seen between the two images. At this point it is worth noting that the L1 sub-lattice possesses an alternating sequence of two-wire, surface-like nanowire junctions and four-wire, ice-like junctions. In contrast, the sub-surface L2 layer only contains four-wire, ice-like junctions, so the observed distinction in monopole behaviour could be the result of surface-driven effects resulting from the broken lattice symmetry at the upper boundary.

To form a more complete picture of the monopole behaviour on the surface and sub-surface, MFM scans were captured following 0.25 mT field increments between opposing saturation states. This facilitates direct observations of the reversal sequences for the L1 and L2 sub-lattices. Having acquired significant experience applying external fields to these samples, it was known that the L1 sub-lattice typically begins switching at approximately 8 mT. Therefore, saturating fields of 30 mT were applied along the negative x and y directions, before the field was applied in the positive x-direction with a magnitude of 7.50 mT (see fig. 4.10). Here, the contrast shown in fig. 4.8d is present throughout the image, meaning that no wires within the measured area have switched yet, indicated by the adjacent vector map. Successive images were then captured at 0.25 mT increments until negative saturation was reached. At 8.25 mT, the first switching event is observed, where a single L1-L2 junction (in the upper-left corner) now exhibits contrast which is similar to fig. 4.8g, indicating this is a type 3 vertex with a magnetic charge of $-2q$.

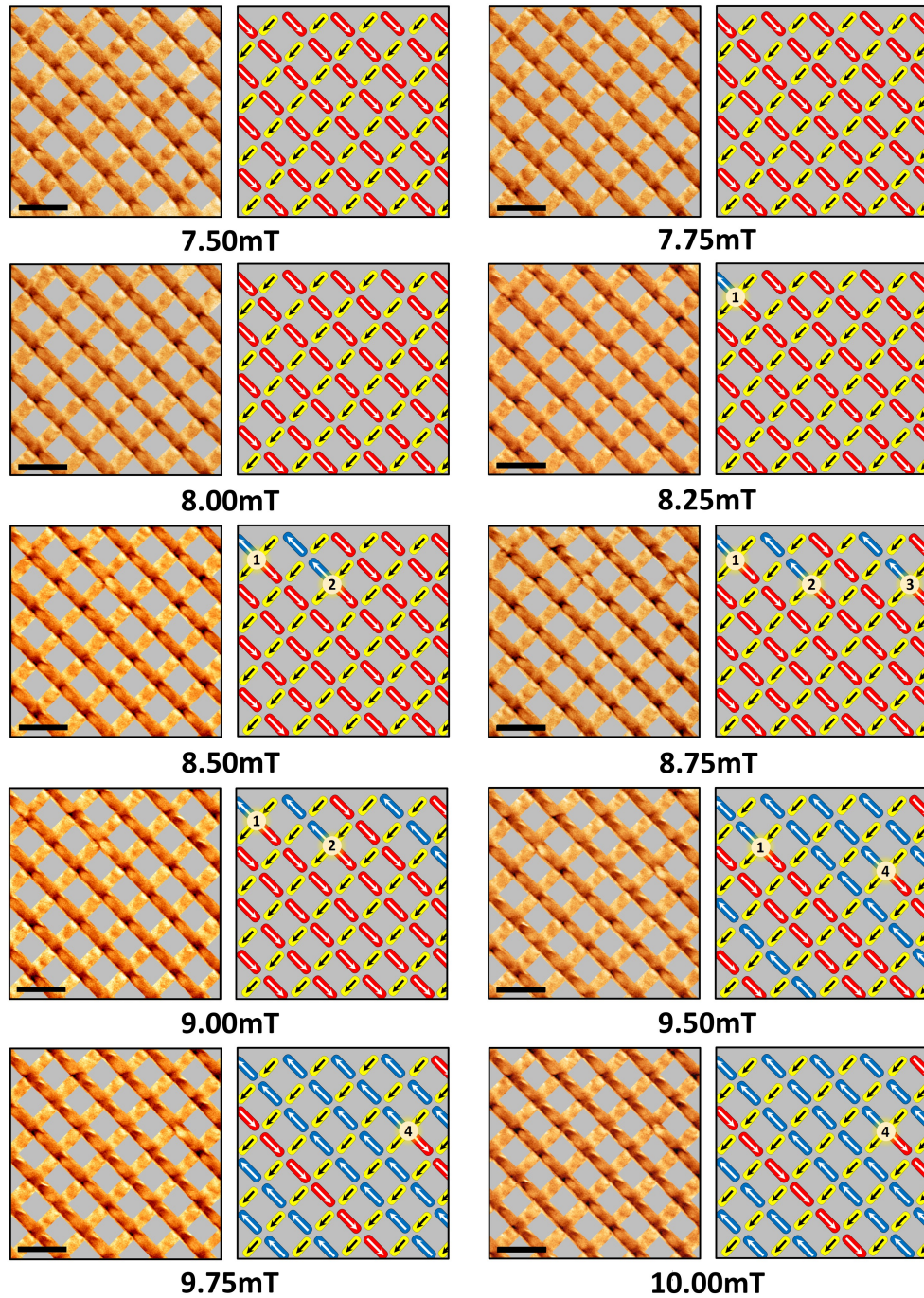


Figure 4.10: MFM dataset probing a $8 \mu\text{m} \times 8 \mu\text{m}$ region of a 3DNL. Firstly, a 30 mT external field saturated both sub-lattices, then the field was aligned to the negative x-direction to incrementally reverse L1 from negative to positive saturation. An arrow map illustrating the in-plane magnetic configuration is placed beside every MFM image, these were constructed through visual analysis. Each ellipse denotes a bipod. Each monopole is assigned a unique index. All scale bars are $2 \mu\text{m}$.

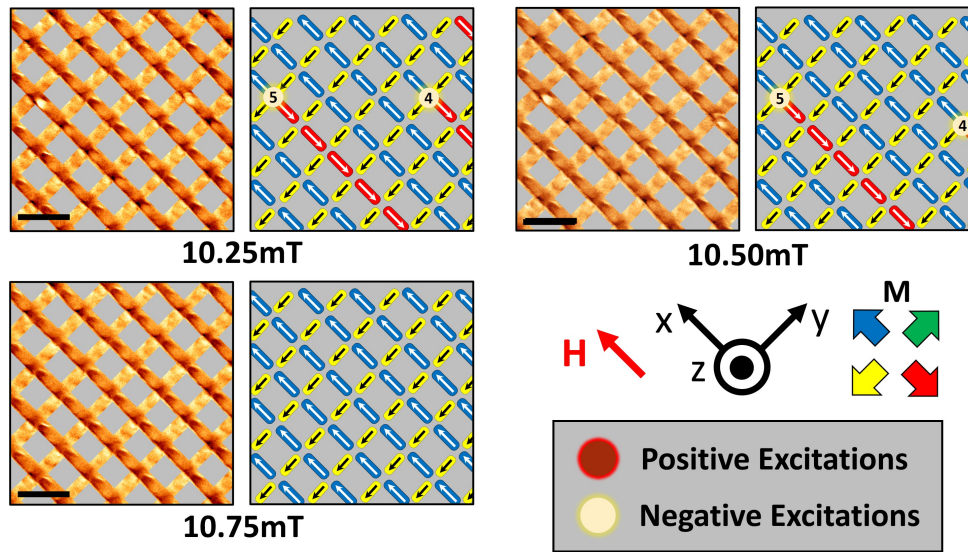


Figure 4.10: Continued L1 reversal. All scale bars are $2 \mu m$.

All other measured vertices are still in the initial type 2 configuration, as shown in the associated arrow map.

Further field increments yield additional nucleation and propagation of excitations until the opposing saturation state is reached at 10.75 mT, where the resulting contrast is equivalent to fig. 4.1b. During this dataset, five excitations are observed within the measured area, which propagate via cascading chains of wires switching. All of these L1 excitations possess a magnetic charge of $-2q$, none of which appear as part of a correlated, charge neutral, monopole pair. Also, net charges are only observed at four-wire junctions, suggesting that positioning a charge upon a bipod peak (2-in or 2-out) is energetically unfavourable.

With L1 and L2 saturated along the positive x and negative y directions respectively, the field was aligned to the positive y-axis to perform a similar switching experiment upon L2 (see fig. 4.11). Initial coarse measurements suggested that L2 displays a reduced coercive field in comparison with L1, in agreement with MOKE magnetometry. Therefore, a lower initial field step of 6.50 mT was applied, which immediately resulted in the nucleation of a correlated, charge neutral pair of monopole excitations, separated by a single L2 bipod. This is visually determined since one L2 bipod has similar contrast to fig. 4.1g, where the L1-L2 vertex at the upper-right end of this bipod is dark, whilst the lower-left end is bright, indicating a positive and negative excitation respectively. All other L1-L2 junctions at this

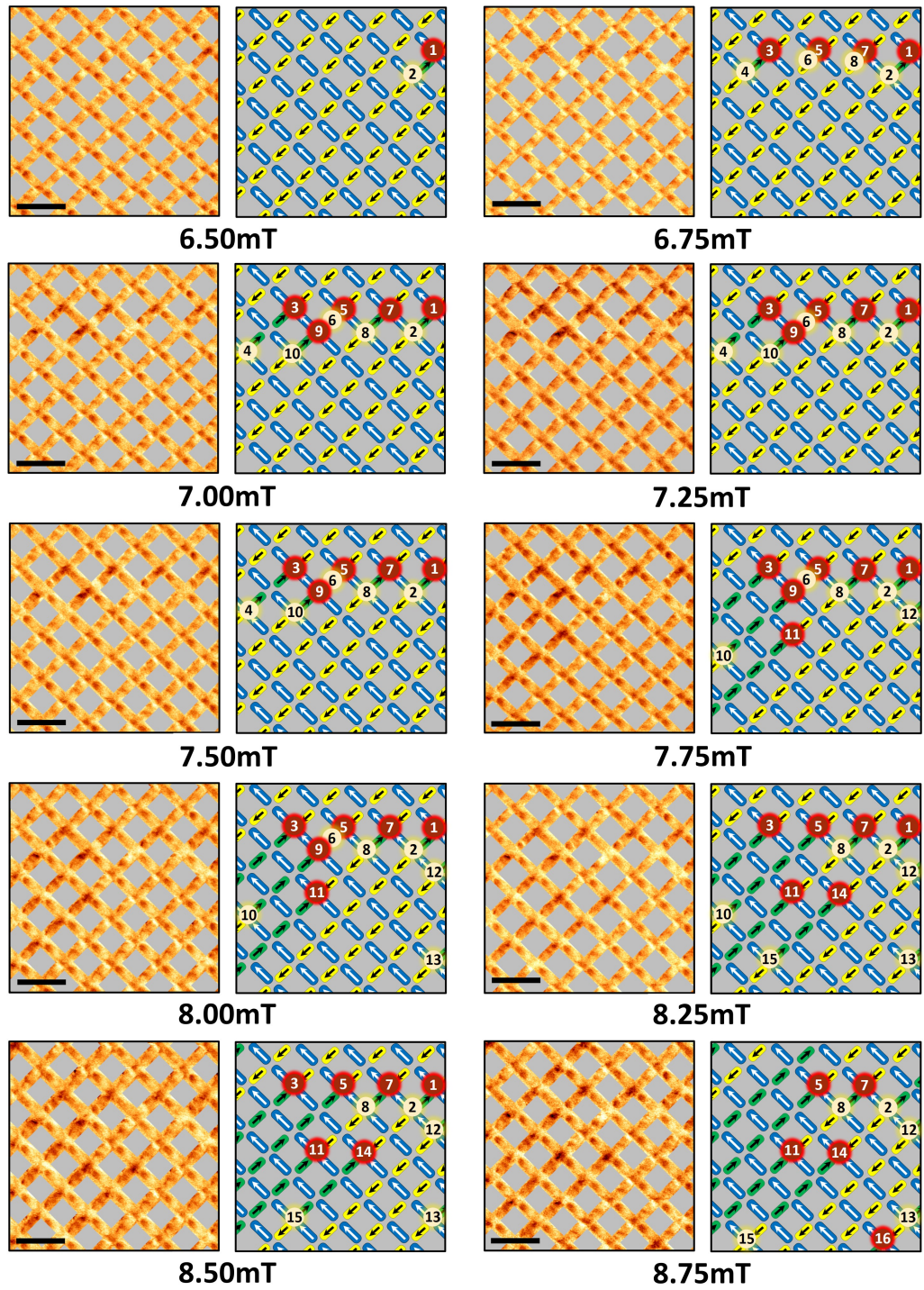


Figure 4.11: Masked MFM dataset of L2 reversal. A 30 mT external field saturated L2 along the positive y-direction, before the field direction was reversed to incrementally switch L2 to negative saturation. Each ellipse indicates a bipod. Each monopole is assigned a unique index. All scale bars are $2 \mu m$.

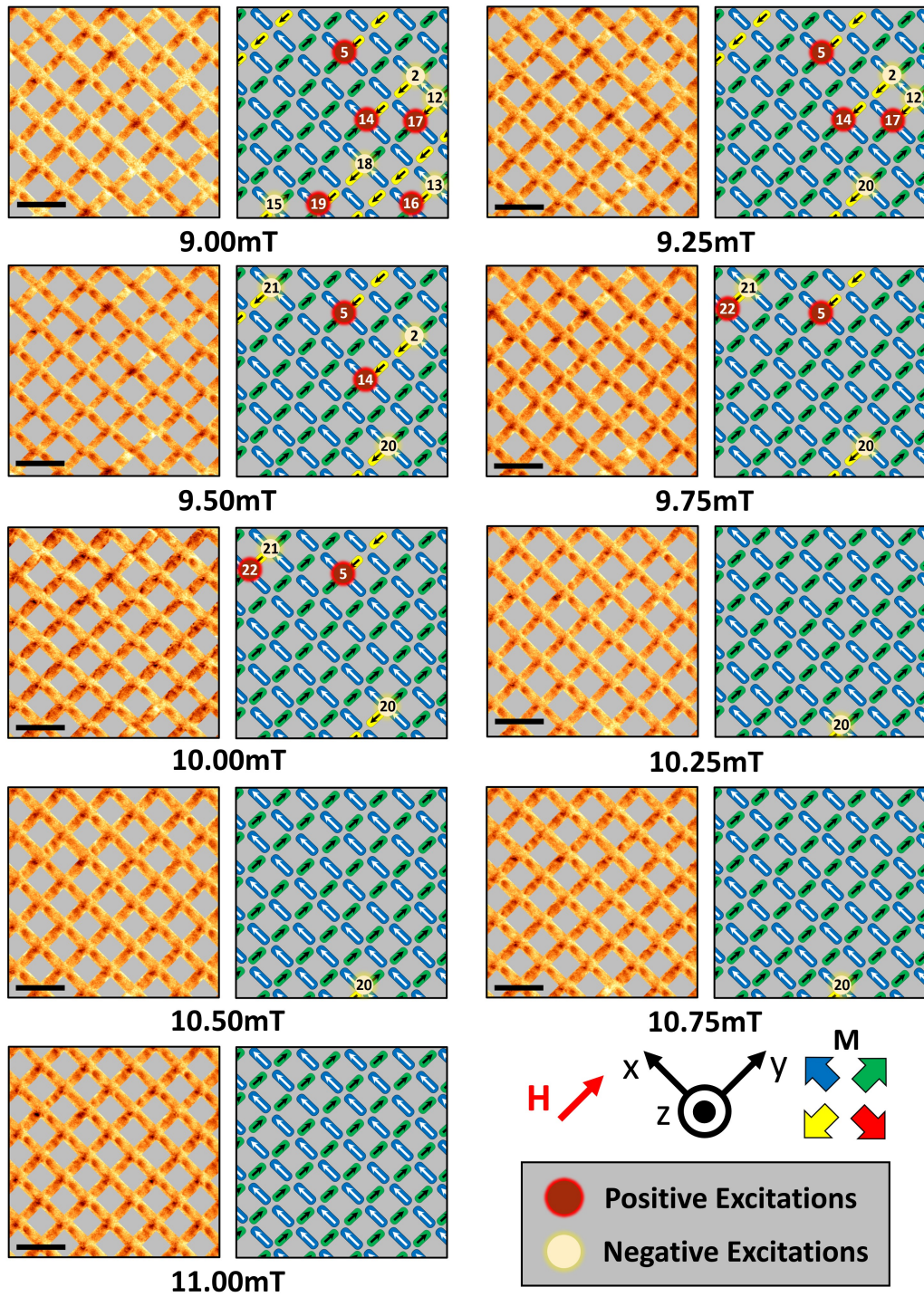


Figure 4.11: Continued L2 reversal. All scale bars are $2 \mu m$.

field step are reminiscent of fig. 4.8e, so remain in the initial type 2 configuration. A second field step of 6.75 mT gives rise to an additional three correlated, charge neutral, monopole pairs, where two excitations are positioned on L2-L3 vertices,

and the remaining are found at L1-L2 junctions. Further field increments produce more excitations, continuing with this trend of highly correlated pairs. During the L1 reversal sequence, excitations appeared to cascade across long chains of wires, but this is not the case here. Excited states in the L2 reversal appear with a larger frequency, meaning that each excitation only propagates a short distance before annihilating with an opposing charge, or exiting the sampled area. The first example of annihilation occurs during the 8.25 mT field step, where monopoles 6 and 9 have annihilated. At 11.00 mT, the observed region is fully saturated in the positive y-direction, visually determined as every pictured L2 bipod exhibits a distinctive dark lobe on the upper-right boundary, similar to fig. 4.1g. L2 switching is therefore detected over a field range of 4.5 mT, greater than the 2.5 mT range seen in the L1 data. During this field sweep, only two instances are observed of an excitation at a L2-L3 junction, all other pinning events are only seen to occur at L1-L2 vertices.

Figure 4.12a-b displays the number of excitations observed as a function of applied field in the L1 and L2 datasets respectively, separated into positive and negative charges. These data summarise the pronounced differences between the upper two sub-lattices noted during visual inspection of fig. 4.10 and fig. 4.11. A total of 5 excitations are seen in the L1 data, all of which are negatively charged, whilst 21 are measured during L2 switching, with almost equal proportions of magnetic charge throughout. By assigning a value of $\pm 2q$ to each excitation (typical of type 3 vertices), the net magnetic charge at each field step could be discerned (fig. 4.12c). Intriguingly, despite containing a significantly greater number of excitations, the L2 data remains within a single monopole ($\pm 2q$) of charge neutrality throughout the field sweep. Conversely, L1 shows far fewer excitations, though the observed magnetic charge deviates substantially from net zero. L2 excitations appear to nucleate locally as part of charge neutral pairs, many of which annihilate upon encountering an opposite charge within the measured region, meaning that a net charge is rarely obtained. In contrast, excitations in the L1 data are never seen with an associated opposing monopole. This suggests that L1 monopole-antimonopole pairs

hl(MAPs) deconfine from one another almost immediately following nucleation, allowing the two opposing states to move apart with relative ease. Figure 4.12d summarises the switching characteristics of both sub-lattices in the up sweeps of digital hysteresis loops. These were constructed by counting the number of wires that are aligned parallel and antiparallel with the applied field direction at each increment, this data was normalised between -1 and +1. Coercive fields of 9.5 mT and 8.8 mT

are seen in the L1 and L2 data sets respectively, in close agreement with MOKE magnetometry (shown in fig. 3.27 and 3.31), which also indicated an enhanced coercivity when the applied field is aligned to the L1 projection. Additionally, the L2 data displays significantly more plateaus, associated with monopole creation events, again inferring that L2 excitations are more confined than the L1 counterparts. It is also noteworthy that the up sweeps for both sub-lattices appear more square and with sharper transitions than was seen in the MOKE data, this a result of the data being captured at remanence here. Therefore, any gradual transitions associated magnetic moments partially rotating towards the field direction are not observed,

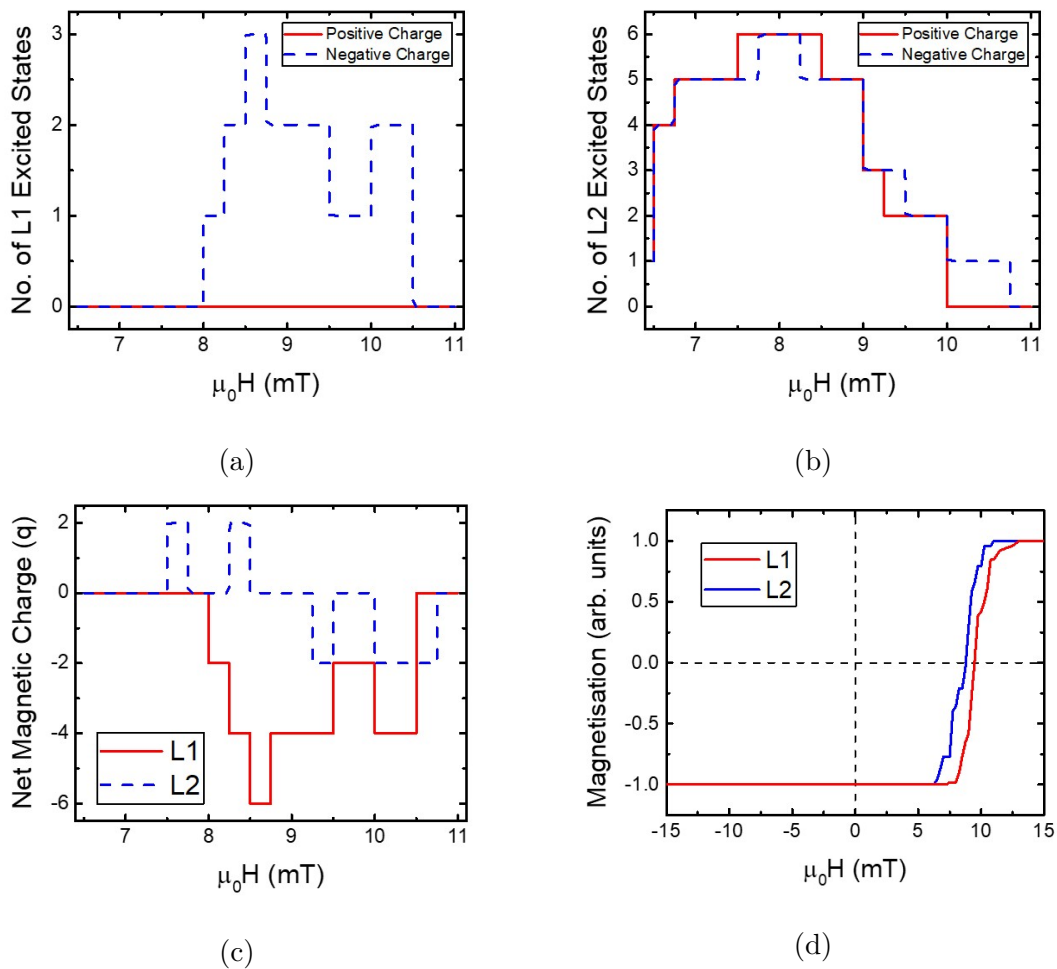


Figure 4.12: Analysis of the L1 and L2 MFM data. **a-b**, Number of excitations plotted as a function of applied field, for the L1 and L2 datasets respectively. Positively charged monopoles are red and the opposing state is blue. **c**, Net magnetic charge within the measured area, plotted as a function of applied field for both sub-lattices. **d**, Up sweeps of normalised digital hysteresis loops, representing the MFM reversal data for the L1 and L2 sub-lattices.

since these moments would relax back to their initial state once the applied field is removed. The underlying physical mechanisms for this curious distinction between the upper two sub-lattices will be revisited later in this chapter

Now armed with a more comprehensive understanding of the 3DNL switching characteristics, we seek to investigate two further questions of practicality:

- Can MFM extract any useful information from sub-lattices below L2, to further map the micro-state of these interesting systems?
- Is it possible to move monopole excitations in a controlled manner? As would be required for DW-based technologies such as racetrack memory.

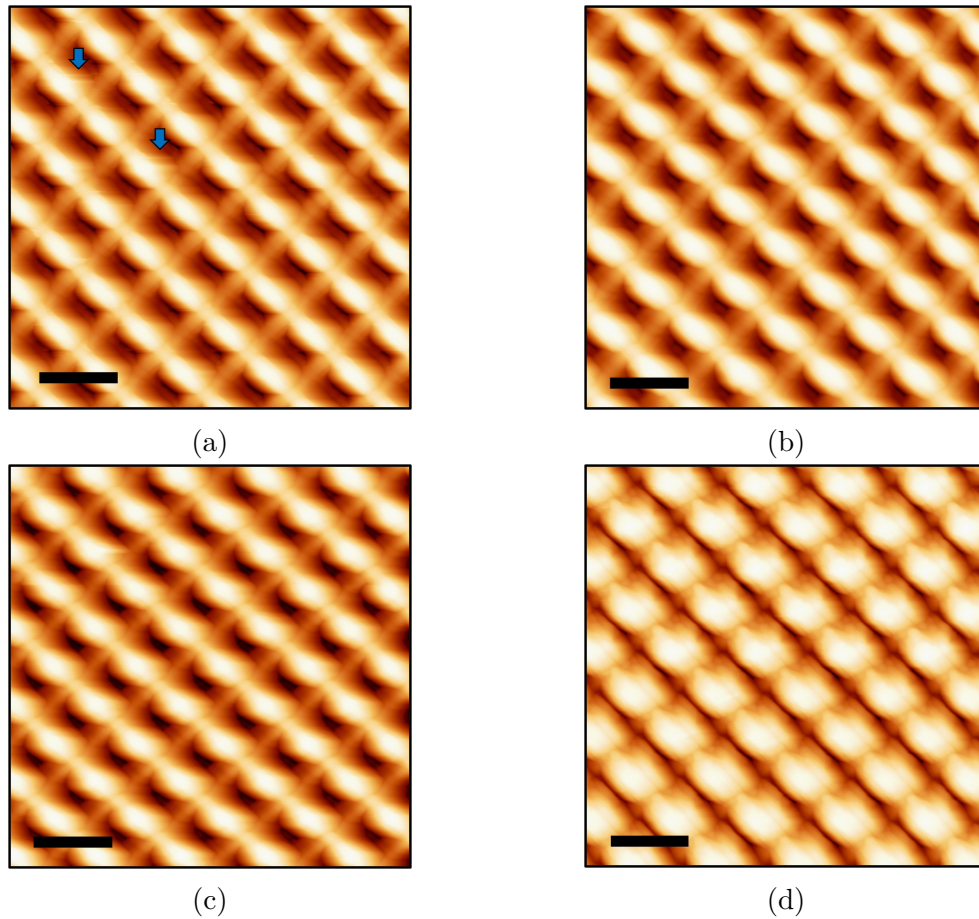


Figure 4.13: $10\ \mu\text{m} \times 10\ \mu\text{m}$ AFM scans of a 3DNL. The degree of probe degradation increases from **a** to **d**.

To address the first question, one must consider the vertical distance between L3 and the 3DNL surface. L3 nanowires extend between L2-L3 and L3-L4 junctions.

Wires are $1 \mu m$ in length, and the tetrahedral bond angle infers that the wire long-axis subtends an angle of 35.25° from the x-y plane. Using these values, basic trigonometry shows that L2-L3 and L3-L4 junctions are $1.16 \mu m$ and $1.74 \mu m$ below the uppermost points on the 3DNL respectively. This height variation is at least one order of magnitude greater than those which are typically studied in AFM/MFM experiments. As such, the L3 topography is only resolved with highly optimised feedback settings and when using probes that have seen very little usage. To show this, Figure 4.13 presents examples of AFM scans captured with probes that have endured different amounts of degradation. Directly characterising the extent to which a probe has degraded is very challenging, though this can be examined indirectly through observations of the resulting data. Figure 4.13a was captured with a probe which had very little usage. Here, L1 and L2 wires appear sharp and distinct, L3 topography is also seen though is less clear than the upper two sub-lattices. It should be noted that brand new tips often encounter greater tip strike than probes which have been used numerous times, likely because tips are sharpest when they are new. The SSS-MFMR probe is ultra sharp, with a tip radius of curvature of $< 15 \text{ nm}$, approximately half of the tip radius seen in standard low moment MFM probes. The sharper a probe is, the more closely it scans the topography, which is why L3 is visualised in fig. 4.13a. However, scanning more closely will increase the risk of tip strike, minor events of which cause the streaks that are indicated by blue arrows. This also explains why the period in which L3 can be visualised tends to be short lived. Figure 4.13b was captured with a probe that had a small level of degradation, hence the probe is expected to be less sharp than was the case for fig. 4.13a. L1 and L2 are still distinctive, though L1 wires do appear rounder and less sharp. Very subtle topography is detected from L3. Figure 4.13c was captured using a further degraded probe, hence L1 and L2 are more blurred, also only the very upper edges of L3 wires are detected. For studies concerning only L1 and L2, this is still expected to resolve suitable MFM data. Finally, fig. 4.13d was captured using a probe that had suffered significant degradation, such that data is not suitably representing the 3DNL topography. At this point, the probe is not expected to render any useful information and should not be used any further. Typically, probes will degrade to the standard of fig. 4.13b-c after a small number of uses. After which, the probe degradation tends to plateau until a significant tip strike event occurs, causing an abrupt change in the appearance of the captured data.

Unfortunately, even in cases such as fig. 4.13a, the probe-stray field interactions are too weak to reliably discern the MFM contrast of individual L3 wires

in opposing saturated states, as was done for L1 and L2 (fig. 4.1e-h). As discussed earlier, MFM resolution is approximately equal to lift height, and the probe is not thought to closely track the topography of these lower layers. Hence, if the probe-L3 separation is significantly greater than the wire lateral width ($\sim 200 \text{ nm}$) then signal originating from L3 wires will not be resolved. Although, stray fields are minimised in these saturated cases, so it is not surprising that the L3 MFM signal in these configurations is difficult to decipher. A more promising route to extracting information from this lower layer is to observe a non-saturated state, where excitations are expected to be found at L2-L3 junctions. We have already seen that excited vertices produce an enhanced phase detected by MFM probes, due to the increased stray field gradient associated with monopole excitations. Therefore, if a saturating field is applied parallel to L2, before an intermediate switching field of 8.0 mT is projected along L3 (also L1), it is reasonable to assume that any L2-L3 monopole excitations are formed due to oppositely magnetised L3 wires. It should be noted that L3 projects along the x-axis, just as L1 does, and 8.0 mT did not produce an intermediate state in fig. 4.10. However L3 is in the lattice bulk, with four-wire junctions at either end of all wires. So this sub-lattice is expected to more closely resemble L2, where 11 excitations were found after a switching field of 8.0 mT, hence this is a reasonable starting point to investigate monopole excitations upon L3. The upper panel in fig. 4.14 shows an AFM measurement of five L2-L3 vertices (annotated with dotted lines), where L3 extends along the x-axis. An associated MFM scan and line profile are below this, where the phase measured at pinning site 1 (P1) is increased by a factor of ~ 1.7 compared with the other L2-L3 junctions, indicating the presence of a monopole. This result suggests that whilst L3 is more difficult to reliably probe, it is possible to infer the magnetic profile through monitoring of these excited states. To maximise the chance of observing this monopole moving between adjacent L2-L3 vertices, the applied field was increased in 0.1 mT increments, with a MFM image of the remanent state captured after each field step. Images taken between 8.1 mT and 8.5 mT showed no significant changes. At 8.6 mT the normalised phase at P1 reduced to ~ 1 , whilst P2 increases to ~ 1.7 showing the monopole had moved between the two pinning sites. Likewise at 9.3 mT, P3 exhibits a normalised phase of ~ 1.7 and P2 reduces to ~ 1 , indicating the monopole had moved once again between L2-L3 vertices. After this point, the tracked excitation annihilated with an opposing charge, as often occurred in the L2 switching dataset.

Whilst the promising data displayed in fig. 4.14 opens the door for future

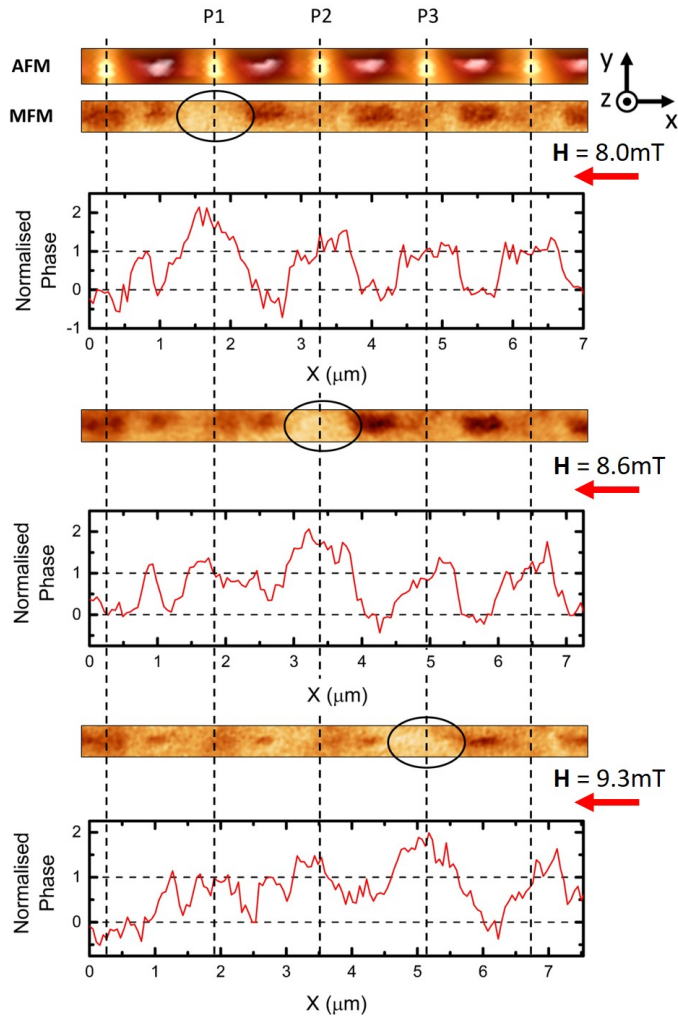


Figure 4.14: Propelling an excitation along a buried sub-lattice. The upper panel shows an AFM scan of L3, spanning five L2-L3 vertices, including the pinning sites P1, P2, and P3. Associated MFM scans and line profiles following three applied field increments are presented. At each step, an enhanced phase by a factor of ~ 1.7 identifies the excitation (highlighted by an ellipse). Phase data is normalised such that unexcited L2-L3 vertices possess a phase of 1.

studies to explore controlled monopole movement on buried sub-lattices within 3D devices, it is unlikely that MFM is the most suitable technique to probe this. As was alluded to earlier, information concerning L3 could only be extracted when using probes that had seen very little usage. In addition, variation in sensitivity was noticed between different probes, meaning that in some cases even brand new probes were unable to discern a reliable MFM signal from L3. As a result, this study shall predominantly focus upon L1 and L2, from which MFM can repeatedly yield

a signal with a high degree of reliability. Though it is noted that future studies are expected to advance upon the observations made here, by making use of x-ray synchrotron techniques to fully characterise the magnetisation profile of nanowire networks arranged in 3D. With experimental results obtained, the next step is to use relevant modelling in order to further understand the system.

4.2 MODELLING SWITCHING IN 3D ARTIFICIAL SPIN-ICE.

As is often the case in the modern world of nanomagnetism, we now turn to simulations for additional insight into the curious behaviour discussed in the previous section. In an ideal scenario, one would model a full 3DNL transitioning between opposing saturation states (emulating the experimental reversals), using a micromagnetic simulation package to study a true approximation of the experimental system in copious detail. However, current available technologies (including a recently upgraded supercomputer cluster) simply do not possess the necessary memory requirements to simulate a full lattice. An alternative approach with significantly reduced memory requirements, is to instead model building blocks of the lattice, whereby a tetrapod represents a L1-L2 junction, and a bipod represents a L1 surface termination. Here, these two geometries were defined in an identical manner to the bipod and tetrapod NMAG simulations presented in the previous chapter. Simulating such building blocks with NMAG allows one to investigate the on-site energetics of both ground state vertices and excitations. In addition one can apply field protocols along directions analogous to L1 and L2 in experimental samples. This provides a detailed picture of the micromagnetic spin texture composing a monopole and how this evolves in the presence of an external field.

First to be studied is the bipod, which raised interesting questions upon analysis of the experimental data. Bipods represent a broken symmetry between the lattice surface and bulk, so may be important in explaining the differences between the two sub-lattices. Furthermore, why are monopole states never observed upon bipod vertices? With these questions in mind, two studies were undertaken to understand these surface terminations via micromagnetic simulations. Firstly, the energetics of the bipods and tetrapods were compared. Secondly, more detailed calculations were performed to determine how the spin texture and local energetics

change upon the vertex.

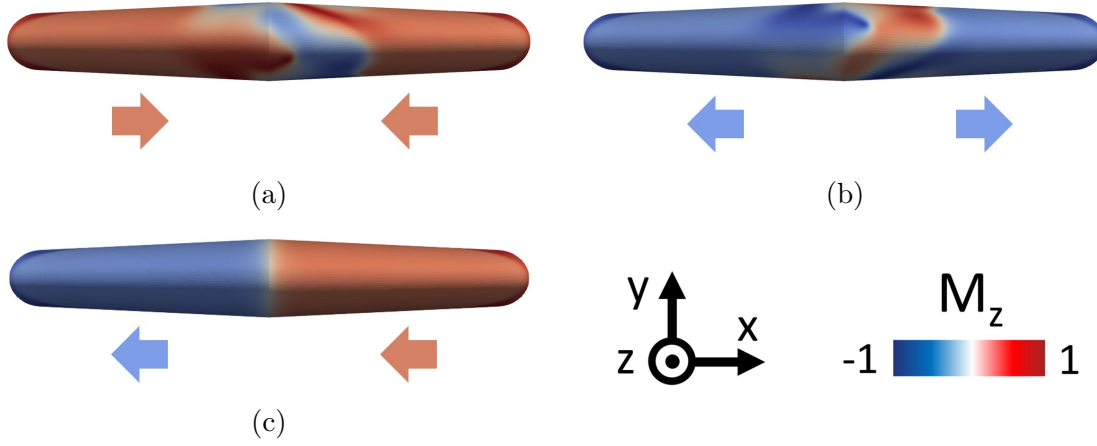


Figure 4.15: NMAG simulations of three bipod remanent states. **a**, 2-in. **b**, 2-out. **c**, 1-in/1-out.

The former route, studying the energetics of differing nanowire junctions, simply requires knowledge of the energy terms of each possible bipod and tetrapod configuration at remanence. Total energy density (E_{tot}) values for the relevant tetrapod configurations are already presented in table 3.2, whereas the three possible bipod states are shown at remanence in fig. 4.15. Here, the magnetisation of each nanowire was defined parallel or antiparallel to the wire long axis as required, before a relaxation procedure brought the system to remanence. As expected for the case of a bipod structure, the monopole states with positive (2-in) and negative (2-out) charge contain a HH DW and a TT DW respectively. Both DWs exhibit a vortex formation just as occurred in fig. 3.23. Here the energetics are the focus, finer details of the DW structure will be discussed later in this chapter. E_{tot} was obtained from each of these simulations to produce an updated table of nanowire junction energetics (table 4.2). These values represent the energy density of the final states, since the simulations are effectively time-independent. Hence, these energy values cannot precisely calculate the energy barriers that were present during the simulations, although they do provide useful indication. To approximate the energy required to produce an excitation, one must consider the energy difference between the ground state and the excited state. The ground state of a bipod is clearly 1-in/1-out, so to transition from this to an excited state requires $E_{2-in} - E_{1-in/1-out} = 8985 \text{ Jm}^{-3}$. Whereas a L1-L2 junction is minimised in a type 2 configuration, so transitioning to an excited state requires $E_{T3} - E_{T2} = 2702 \text{ Jm}^{-3}$ if the lower wires oppose one

another in the excited state, or 3938 Jm^{-3} if the upper wires oppose. Therefore, the necessary energy to excite a bipod is 2.3 or 3.3 times greater than the energy needed to form an excitation at a L1-L2 junction with opposing L1 or L2 wires respectively. These simple energy considerations make it clear that the high energy 2-in and 2-out bipod states are unpreferable and so are unlikely to be seen in the real system. Table 4.2 also indicates that the energetics of a 2-in and a 2-out bipod are effectively identical.

Structure	Index	Vertex Type	$E_{\text{tot}} \text{ (Jm}^{-3}\text{)}$
Bipod	10	1-in/1-out	7021
Bipod	11	2-in	16006
Bipod	00	2-out	16007
Tetrapod	0011	Type 1	8342
Tetrapod	1100	Type 1	8342
Tetrapod	1010	Type 2	7745
Tetrapod	1011	Type 3	11683
Tetrapod	1000	Type 3	11685
Tetrapod	1110	Type 3	10447
Tetrapod	0010	Type 3	10447

Table 4.2: Total system energy density for each simulated remanent state of a bipod and tetrapod. An index is assigned to each simulation, whereby 1 indicates a wire magnetised towards the vertex and 0 is the opposite. For tetrapods, the first two digits describe the lower two wires, the next two digits describe the upper wires.

For the second investigation - studying the finer details of the spin texture at the vertex as a function of applied field - a number of additional NMAG simulations were required. These were analogous to the field-driven MFM experiments, where an excited vertex was formed by defining the initial magnetisation as shown in fig. 4.16. A VDW formed after a relaxation procedure was executed in the absence of an external field, this was pinned near to the central nanowire junction. To replicate the experimental procedure, an external field was applied with an incrementally increasing magnitude until the DW depinned. These simulations provide an understanding of the local energy barriers that need to be surpassed in order to move monopole excitations.

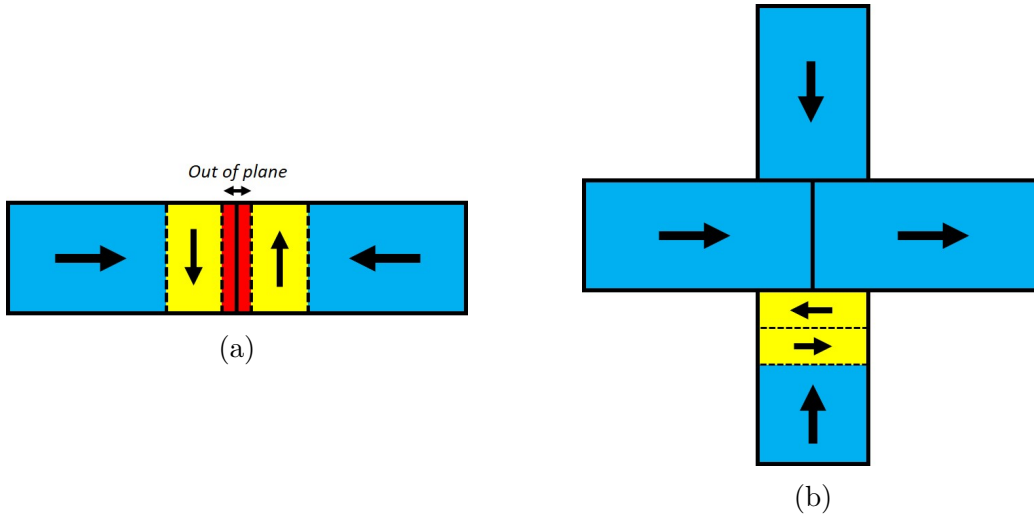


Figure 4.16: Schematics of the initial conditions set for NMAG simulations to obtain specified chirality and polarity combinations, seen from top view. Regions are defined with magnetisation parallel to the z -axis (red), $\langle 111 \rangle$ axis (blue), and orthogonal to the wire long-axis (yellow). Conducted for **a**, bipod and **b**, tetrapod geometries.

Figure 4.17a-b once again presents the two opposing excited bipod states at remanence. Here, both states were subjected to identical field protocols, whereby an external field was aligned to the x -axis and the magnitude was increased in 0.1 mT increments until the DW depinned. Figure 4.17c-d illustrate the field increments immediately following the HH and TT DWs depinning towards and past the central vertex (negative x -direction) respectively. The HH DW depinned towards the vertex at 2.9 mT, whilst the TT DW depinned in the same direction at 2.8 mT. Figure 4.17e-f shows the opposite scenarios, the HH and TT DWs both depinned away from the vertex at 2.5 mT. By combining this result with the essentially equal energetics of simulations containing HH or TT DWs (seen in table 4.2), it is clear there is a similarity between these two DW types. Therefore, further analysis of bipod structures focused only on HH DWs, to avoid unnecessary repetitions.

As explained in section 1.5, four permutations of vortex DW exist, due to the polarity and chirality each possessing two possible states. Previous studies have suggested these vortex parameters influence the DW dynamics, so have been considered throughout this analysis. To study the impact of DW structure, it was first necessary to produce four remanent states of a 2-in bipod, where each state possessed a unique combination of DW chirality and polarity. A schematic illustrating how this was achieved is given in fig. 4.16a. Here, a central region extending 10 nm either side of

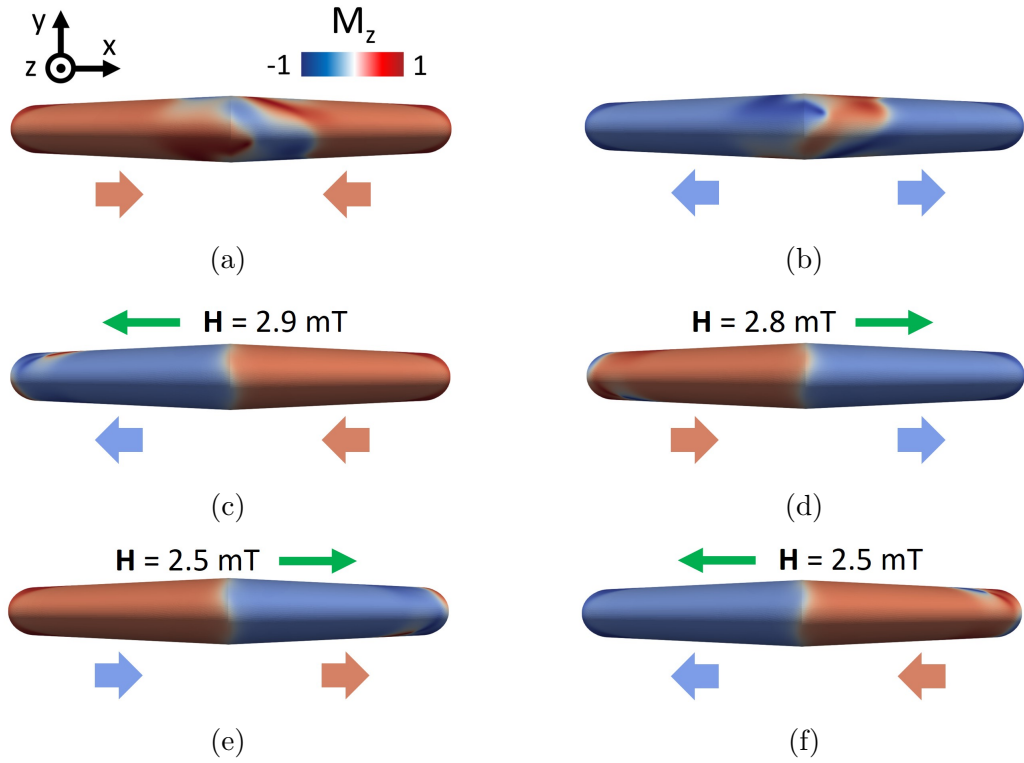


Figure 4.17: N MAG simulations of DWs depinning in a bipod, seen from top-view. **a-b**, Remanent 2-in and 2-out states respectively, in both cases a vortex DW is pinned on the right hand side of the vertex. **c-d**, States immediately following the DW depinning towards the vertex, associated with (a) and (b) respectively. **e-f**, States immediately following the DW depinning away from the vertex, associated with (a) and (b) respectively.

the vertex was defined with an out-of-plane magnetisation, the direction of which determined the resulting DW polarity following a relaxation. Likewise, either side of this central region a further 90 nm was defined with a magnetisation perpendicular to the bipod projection, to control the resulting DW chirality. The configuration seen in fig. 4.16a would lead to a HH DW with anti-clockwise chirality, whilst a clockwise chirality could be obtained by simply inverting the magnetisation of both yellow regions.

Figure 4.18 shows the resulting four permutations of VDW structure for a 2-in bipod, in each case the vortex core is positioned just off the bipod vertex. It is immediately noticeable that none of the vortices sit upon the apex of the cross-sectional curvature, with the chirality appearing to dictate which side of this apex the vortex core will reside. Apart from the obvious reversal in the vortex circulation, changing the chirality has little impact on the DW appearance. However, alternating the polarity appears to yield a more significant impact, particularly concerning the

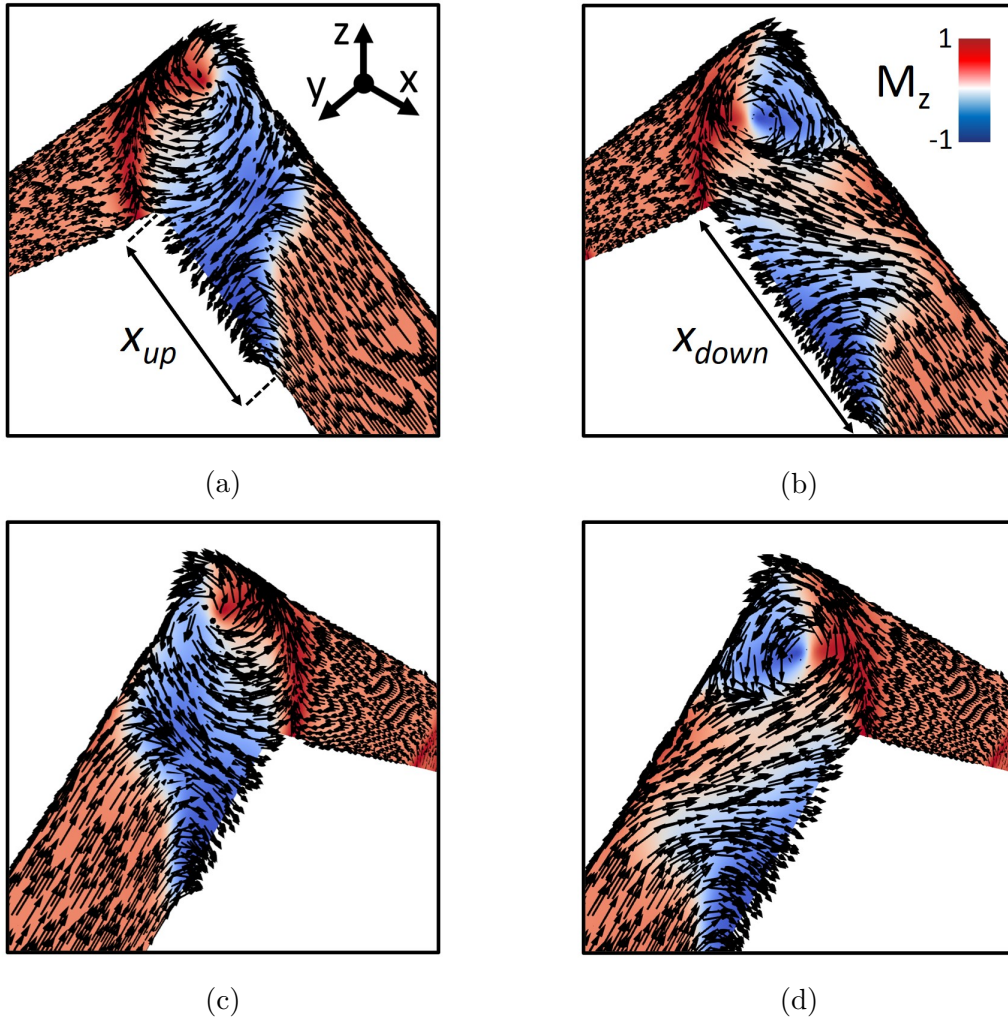


Figure 4.18: NMAG simulations of relaxed 2-in bipods possessing the four permutations of vortex DW structure. **a**, Clockwise chirality, upwards polarity. **b**, Clockwise chirality, downwards polarity. **c**, Anti-clockwise chirality, upwards polarity. **d**, Anti-clockwise chirality, downwards polarity.

DW size, as shown in fig. 4.18a-b where the distance each DW extends from the vertex is annotated as X_{up} and X_{down} for the two polarities. At remanence, X_{up} is (254 ± 5) nm and X_{down} is (353 ± 5) nm. To accurately compare the various DW permutations within different systems, the DW energy terms have been isolated by subtracting off the energetics from an equivalent geometry that is in a ground state configuration¹⁰⁰. For a bipod, this would involve subtracting the energy terms of a 1-in/1-out configuration from a 2-in or a 2-out state. Although, NMAG only outputs energy density values, so this subtraction would result in the DW energy divided by the total system volume. To resolve this issue, one can multiply the subtracted result by the system volume to approximate the DW energy (see eq. (4.2)).

$$E_{DW} \approx (E^* - E_{GS})V_{system} \quad (4.2)$$

E^* represents the energetics of an excited state where a DW is present between two regions with opposing magnetisation, whilst E_{GS} represents the equivalent energy terms in the ground state of an identical geometry. The reason eq. (4.2) does not exactly yield the DW energy is because a DW is also present in the ground state (1-in/1-out), since two well-defined regions of magnetisation are separated by the spin texture at the vertex. However, it is likely that E_{DW} is much greater for the excited state when compared with the ground state, and so eq. (4.2) is expected to provide a suitable approximation. In addition, any error introduced in this calculation by the ground state DW is expected to be systematic, meaning that the energetics of differing DWs in excited states can still be reliably compared with one another in relative terms. Just as occurred in fig. 4.17, an external field was applied in 0.1 mT increments until each DW depinned to create a 1-in/1-out state. Depinning fields in opposing field directions are compiled in table 4.3 along with remanent DW energetics, calculated using eq. (4.2). Here, one can see that chirality has negligible impact on the DW energy or depinning fields, which agrees with visual observations of the remanent states. In contrast vortex polarity has a minor effect on the DW energetics, whereby an upwards polarity is favourable, due to a reduced E_{ex} in comparison with the downwards polarity. This effect is once again the result of curvature-induced effects discussed in section 1.7, which may also explain why a downwards polarity leads to a larger DW. An increased DW size is necessary to minimise the angle between neighbouring spins, so this DW growth allows the increased E_{ex} to be distributed across a larger number of spins. Interestingly, the difference in E_{tot} is not as large as one might expect because the downwards polarity DW exhibits a lower E_{ms} .

Structure	Chirality	Polarity	E_{tot} ($10^{-17} J$)	E_{ex} ($10^{-17} J$)	E_{ms} ($10^{-17} J$)	$+H_D$ (mT)	$-H_D$ (mT)
Bipod - TT	CW	Down	13.21	3.82	9.39	2.5	2.8
Bipod - HH	CW	Up	13.21	3.81	9.39	2.5	2.9
Bipod - HH	CW	Down	13.34	4.69	8.65	0.8	6.5
Bipod - HH	ACW	Up	13.21	3.82	9.39	2.5	2.8
Bipod - HH	ACW	Down	13.34	4.70	8.64	0.7	6.5
Tetrapod: L1 - TT	CW	Up	7.68	2.35	5.33	41	44
Tetrapod: L1 - HH	CW	Up	7.80	2.34	5.47	44	40
Tetrapod: L1 - HH	CW	Down	7.68	2.34	5.34	44	41
Tetrapod: L1 - HH	ACW	Up	7.80	2.34	5.46	40	43
Tetrapod: L1 - HH	ACW	Down	7.68	2.35	5.33	41	43
Tetrapod: L2 - TT	CW	Up	5.27	2.07	3.19	19	20
Tetrapod: L2 - HH	CW	Up	5.37	2.07	3.30	19	14
Tetrapod: L2 - HH	CW	Down	5.27	2.08	3.19	18	19
Tetrapod: L2 - HH	ACW	Up	4.25	1.30	2.95	22	7
Tetrapod: L2 - HH	ACW	Down	4.22	1.33	2.88	22	10

Table 4.3: Domain wall characteristics within micromagnetic simulations of 2-in bipods and type 3 tetrapods possessing opposing L1 (upper) and L2 (lower) magnetisation respectively. Each permutation of DW chirality and polarity is presented, alongside the DW energetics at remanence, and the external field required to depin each DW away from the central vertex ($+H_D$) and towards it ($-H_D$).

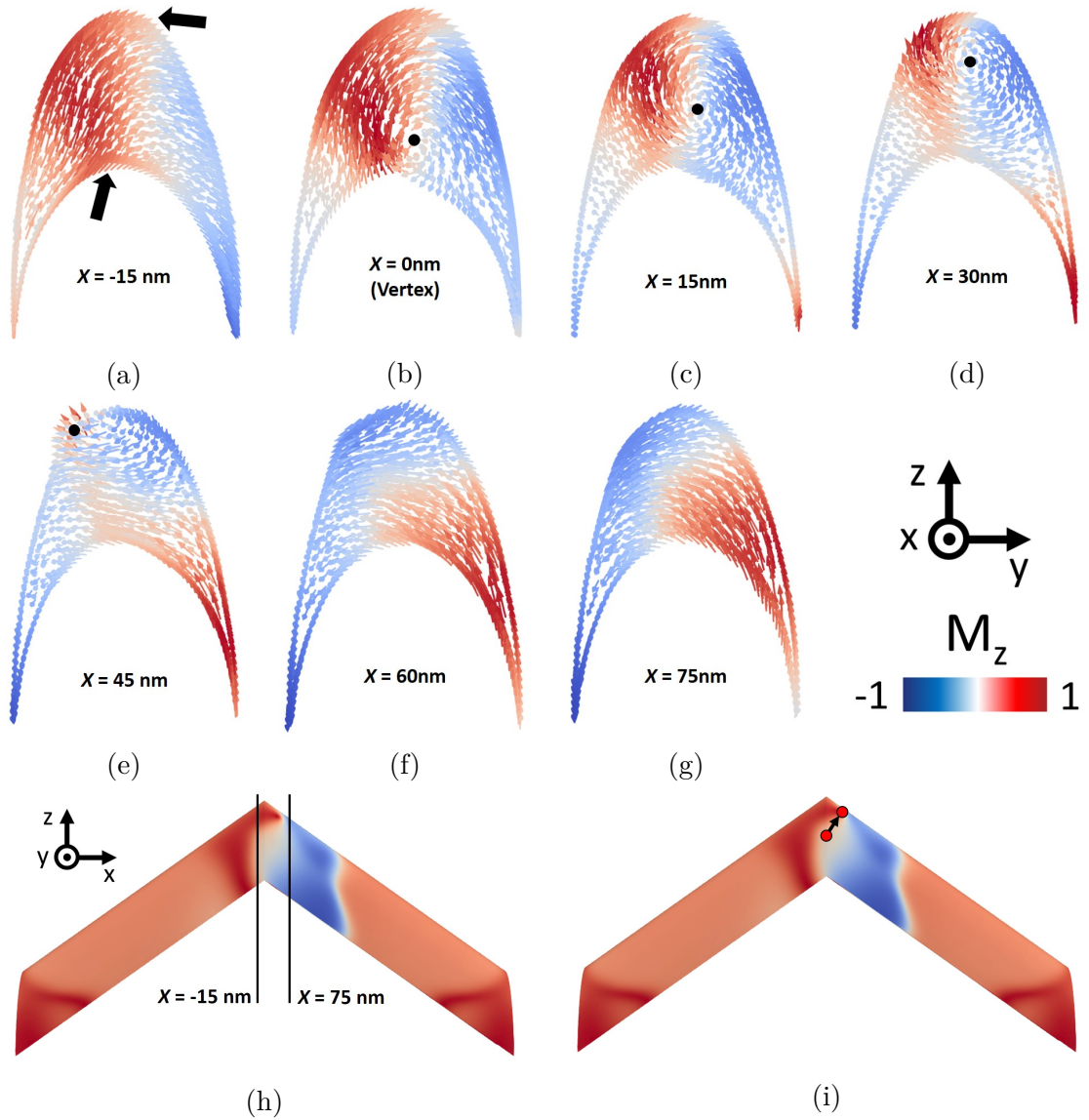


Figure 4.19: Spin texture of a 2-in bipod with upwards polarity. **a-g**, Cross sections taken at 15 nm intervals. **h**, Side-on view with lines annotated on the approximate positions of $x = -15$ nm and $x = 75$ nm, for reference. **i**, Approximate positions of the upper and lower vortex boundaries, the connecting arrow points towards the upper boundary.

The vortex polarity has a significant effect on the DW depinning field. A HH DW with upwards polarity and clockwise chirality depins towards and away from the vertex at 2.9 mT and 2.5 mT respectively, (shown in fig. 4.17) indicating an approximately symmetric pinning potential. Although the equivalent depinning fields for a DW with an opposing polarity are 6.5 mT and 0.8 mT, which is clearly asymmetric. Additionally, the vortices with downwards polarity are far more mobile whilst pinned, before depinning towards the vertex X_{down} shrinks to (232 ± 5) nm

and extends to (408 ± 5) nm before depinning in the opposite direction, a range of 176 nm. In comparison, X_{up} shrinks to (212 ± 5) nm and extends to (280 ± 5) nm, a range of just 68 nm.

To understand this substantial variation, one must consider the spin texture below the upper-surface. Figure 4.19 presents snapshots of the cross-sectional spin texture at 15 nm intervals along the bipod projection for the simulation containing a HH DW with clockwise chirality and upwards polarity. At $x = -15$ nm, the edge of the vortex is seen, where much of the magnetisation is orientated perpendicular to the wire long-axis. Interestingly, at points of high curvature, spins are seen to cant out-of-plane, black arrows indicate where this is most prominent. This is the result of an effective-DMI due to competing exchange and magnetostatic interactions, as was predicted in section 1.7. At the bipod vertex ($x = 0$), the upper-surface spin texture is unchanged in comparison with the previous snapshot, however a vortex is seen to be circulating about the x-axis (highlighted by a black dot) near to the apex of the lower surface. This is a surprising observation, since vortex DWs are well studied in planar systems, typically vortices only circulate about the z-axis and hence are translationally symmetric in the z-direction. $X = 15$ nm and $X = 30$ nm are similar views, though the vortex core is increasing in height as it progresses along the x-axis. The vortex core emanates from the upper surface at $X = 45$ nm, as was also seen in fig. 4.18a. Here, the core is once again seen to position away from the upper-apex, likely because the density of charges forming where the out-of-plane spins meet the boundary would increase at higher curvature, which is unfavourable for the magnetostatic energy. Subsequent cross-sections (fig. 4.19f-g) show the outer regions of the DW, which exhibit an opposing M_y compared with fig. 4.19a, as is to be expected for opposite edges of a vortex. Figure 4.19i summarises these cross-sectional observations, where unlike 2D planar wires, the vortex core projects along both the x and z directions due to the 3D nature of a bipod geometry. Here, two vortices can be imagined, one which emerges on the upper wire boundary and a second that intersects the lower surface, as is annotated using red circles. It was seen in fig. 4.19b that the lower vortex core is positioned directly on the apex of the bipod junction, indicating this could govern the DW pinning. Upon application of an external field, the lower core gradually shifts position, with the DW depinning once the lower core leaves this vertex. Therefore, a 2-in bipod with upwards polarity forms with the upper vortex boundary positioned off the junction, however this is still pinned in place as it is effectively tethered to the lower vortex which is pinned at the vertex. This ‘tethering’ occurs because if the upper vortex were to propagate

along the wire, the DW would increase in size leading to an increased E_{ex} . When an external field is applied, this supplies energy to the system, allowing the DW to expand or contract as the more mobile upper part of the vortex shifts slightly along the wire. Eventually the lower part of the vortex depins when sufficient energy is supplied by the external field to allow the DW to overcome the energy barrier imposed by the vertex. At which point the DW rapidly propagates in the field direction, switching one of the wires.

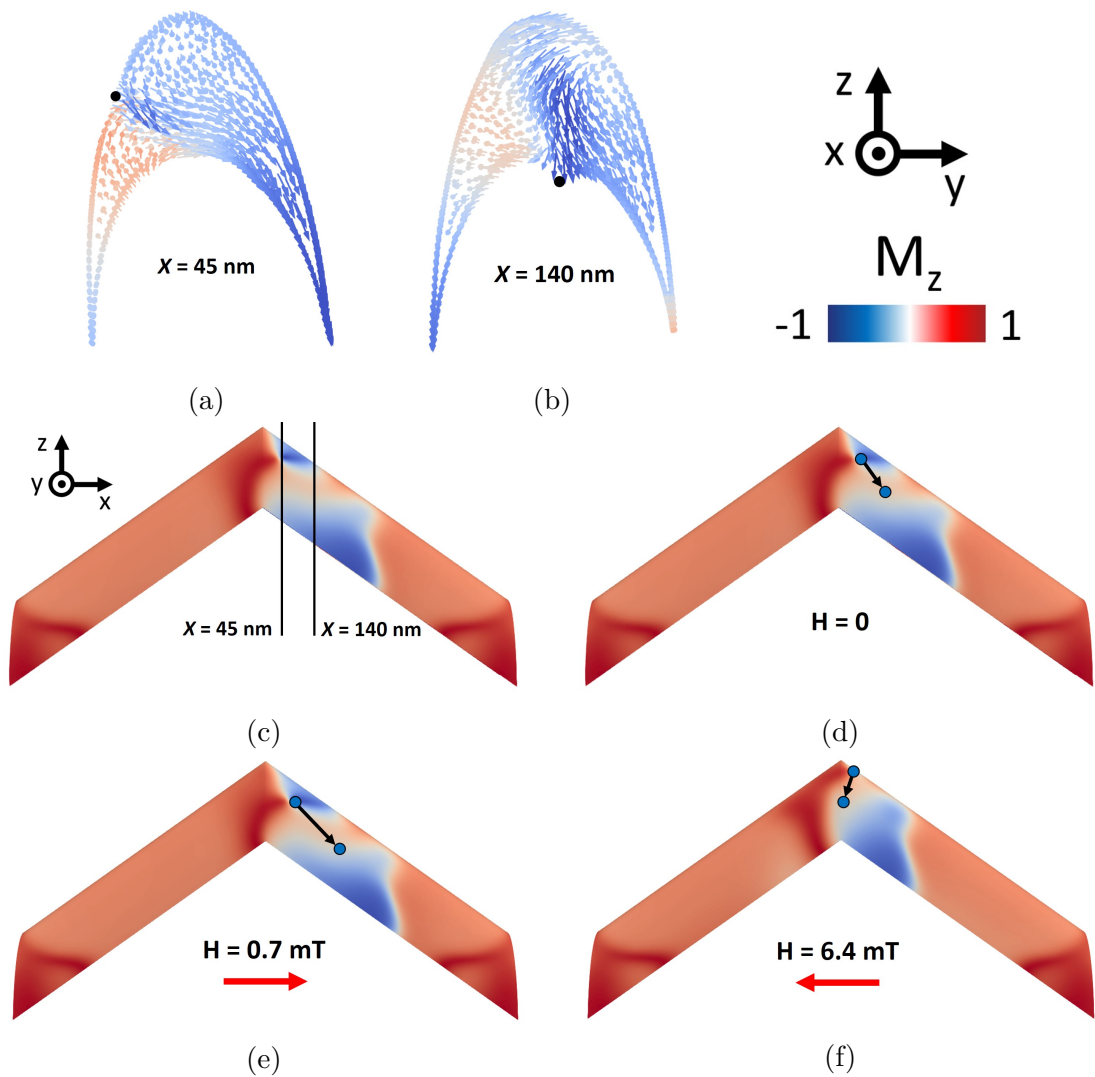


Figure 4.20: Spin texture of a 2-in bipod with downwards polarity. **a-b**, Cross-sections where the vortex core intersects the upper and lower wire surfaces respectively. **c**, Side-on view with lines at the cross-section positions for reference. **d-f**, Approximate upper and lower vortex core positions at remanence and at the last field steps before depinning occurs. The connecting arrow points towards the lower vortex boundary.

Figure 4.19 has provided insight into the mechanism by which an excited bipod transitions to the ground state, however further analysis is required to explain why the polarity so greatly affects the DW characteristics. This becomes clear after performing similar analysis on a VDW with downwards polarity (see fig. 4.20). Here, the upper vortex boundary (fig. 4.20a) is observed in approximately the same position as was seen in fig. 4.19e. However, now the lower vortex core is found at $X = 140$ nm, so the DW appears to only be pinned to the vertex by an edge defect, as is conventional in planar nanowire junctions. This result is actually not altogether surprising, it is once again likely the result of curvature-driven energy terms causing it to be unfavourable for the polarity to oppose the out-of-plane component of the incoming wire magnetisation. As the lower vortex is positioned further from the junction than the upper vortex, this offers a second explanation for the downwards polarity DW extending further along the wire than the upwards polarity equivalent. Additionally, the reduced depinning field of $H_D = 0.8$ mT when pushing the wall away from the vertex is explained since here only an edge defect pins the wall, which exhibits a weaker pinning potential than the vortex core. In contrast, to depin this wall in the negative x-direction both vortices must be pushed towards and over the energy barrier imposed by the vertex, hence H_D is increased to 6.5 mT here.

To truly comprehend the significance of a broken symmetry upon the surface layer, the surface termination (bipod) simulations are now placed into context, with comparison to similar simulations of four-wire junctions (tetrapods) present in the lattice bulk. To recreate the experimental field protocols, two remanent tetrapod configurations were studied, corresponding to the two sub-lattice reversals. Firstly, an excited 3-in/1-out state was defined with the magnetisation of both upper wires orientating towards the central vertex, whilst the lower wires resemble a 1-in/1-out bipod. This configuration emulates an excitation during the L1 reversal MFM data, hence external fields were then applied along the x-axis to depin the simulated DW in either direction along the upper wires. After setting the required magnetisation along the length of each wire and relaxing the system at $H = 0$, a VDW forms on the lower wire that opposes the two upper wires. (see fig. 4.21). This agrees with the bipod simulations and MFM measurements, as excitations are consistently seen adjacent to nanowire junctions, suggesting that it is energetically unpreferable for the DW to be positioned centrally on the junction. Before embarking on any significant analysis, it was necessary to generate remanent states with each of the four VDW permutations, particularly since the DW structure was seen to play a

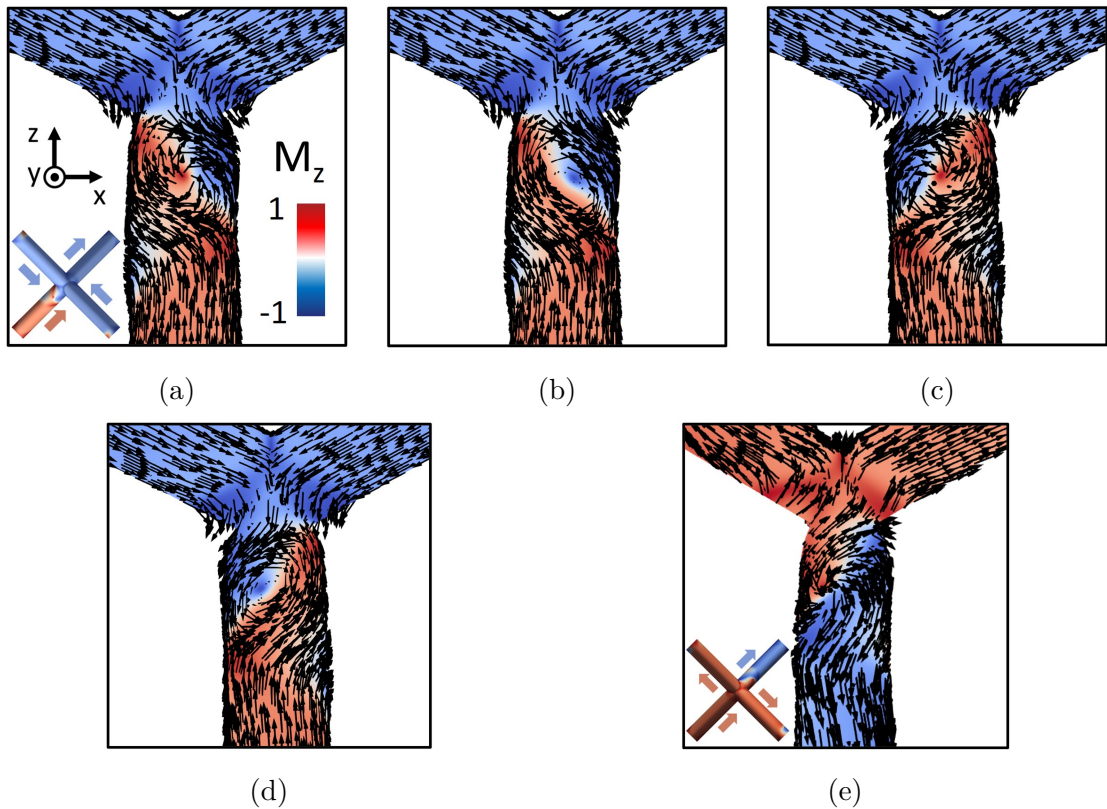


Figure 4.21: Relaxed type 3 tetrapods with opposing upper wires. **a**, HH, clockwise chirality, upwards polarity. Inset: Top view, without glyphs. **b**, HH, clockwise chirality, downwards polarity. **c**, HH, anti-clockwise chirality, upwards polarity. **d**, HH, anti-clockwise chirality, downwards polarity. **e**, TT, clockwise chirality, upwards polarity. Inset: Top view, without glyphs.

crucial role within a 2-in bipod. Figure 4.16b illustrates how DWs with opposing chiralities were defined, to attain examples of both polarities this process was simply repeated several times, since the relaxation provides an element of randomness.

Visually examining fig. 4.21, once again the chirality has little effect on the DW appearance aside from the obvious circulation reversal. Just as occurred in bipods, the cores of vortices with opposing chirality are positioned on opposite side of the wire apex. Though this affect is more subtle here, with each core residing closer to the apex than was seen in a bipod. Most likely this is due to the upper wires providing a symmetric repulsion, pushing the vortex towards the central apex. Again, a DW with downwards polarity is larger in order to distribute the E_{ex} over a greater area, however here the increase in size is marginal. Figure 4.22 illustrates the reasoning that the difference in polarity has only a slight effect, where the approximate vortex core positions are annotated for the upper and lower

wire surface. Unlike in the bipod, there is very little difference in the positions of cores with opposing polarity, so these annotations are approximately correct for all four VDW permutations. Here, the offset along the y -axis between the upper and lower vortex boundaries is only due to the wire long-axis being orientated along the $\langle 111 \rangle$ axis (i.e. in a reference frame where the wire extends along the horizontal, the upper core is directly above the lower).

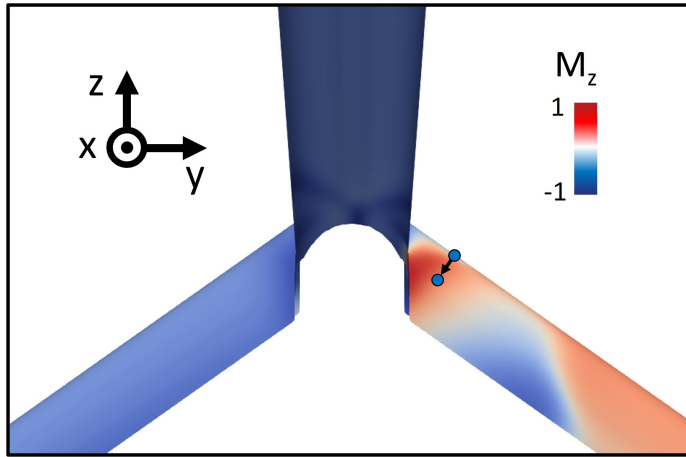


Figure 4.22: Side-view of a tetrapod with clockwise chirality and downwards polarity. Approximate positions of the vortex core intersecting the upper and lower wire surfaces are annotated with blue circles. The arrow points towards the lower vortex boundary.

Lastly, fig. 4.21e shows a negatively excited 3-out/1-in remanent state, with magnetic charge of $-2q$. A VDW with clockwise chirality and upwards polarity has formed on the opposite side of the vertex, compared with fig. 4.21a-d, since in this configuration the lower wire with a magnetisation orientated away from the vertex opposes the upper wires. This was performed to investigate if HH and TT DWs also show effectively equivalent characteristics in a tetrapod, as was seen in the bipod geometry. Remanent energetics for each simulation are recorded in table 4.3. Once again, chirality shows negligible impact on the DW energetics, whilst polarity has a minor effect. Interestingly, here both polarities exhibit effectively equal E_{ex} , leading to the downwards polarity VDWs being the energy minimum. One explanation for this is that the upwards polarity VDWs (which are expected to exhibit a lower E_{ex}) are marginally smaller as discussed previously. So the upwards polarity DWs can sit closer to the vertex, therefore reducing the transition space between the oppositely magnetised wires, which increases E_{ex} . Finally, the TT DW energetics are effectively identical to the HH DWs which possess the opposite polarity, just as occurred in the

bipod.

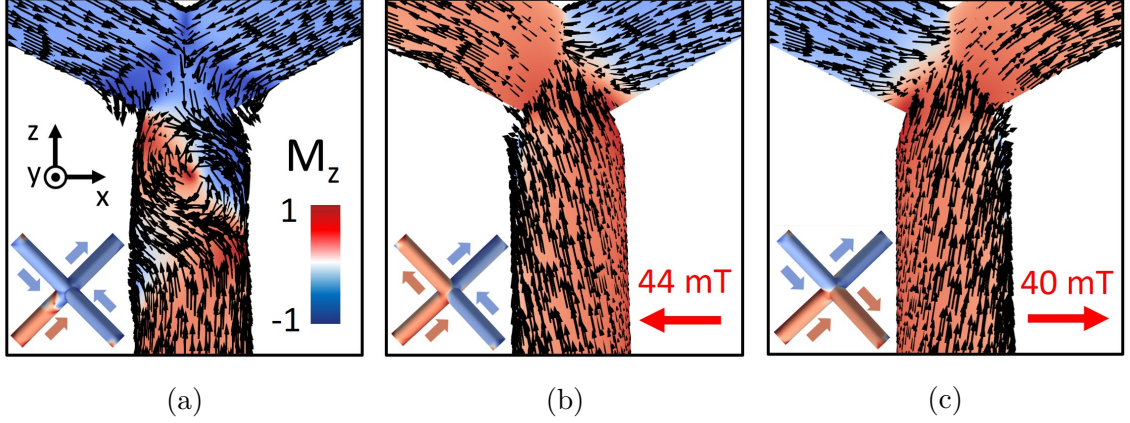


Figure 4.23: Depinning a VDW with clockwise chirality and upwards polarity from a 3-in/1-out tetrapod with opposing upper wires. **a**, Remanent state. Inset: Top view without glyphs. **b-c**, States immediately following the DW depinning along the negative and positive x-direction respectively.

Next, identical field protocols were applied to each VDW (see fig. 4.23), with the resulting depinning fields also compiled in table 4.3. Initial measurements indicated depinning fields in a tetrapod to be substantially larger than for a bipod, therefore the external field magnitude was increased in steps of 1 mT. In contrast to the bipod simulations, polarity displays negligible impact over the pinning potential here, whilst chirality has a subtle effect. For the CW vortex fig. 4.23, depinning fields of 44 mT and 40 mT are seen with the field applied in the negative and positive x-direction respectively. Whereas the ACW vortex that is otherwise equivalent, exhibits depinning fields of 40 mT and 43 mT in the negative and positive x-directions, effectively mirroring the CW vortex. Chirality has significance because the cores of the oppositely circulating DWs are positioned on opposing sides of the cross-sectional apex at remanence. Figure 4.24 clearly shows this, where the CW core (fig. 4.24a-b) is ~ 5 nm to the right of centre, whilst the ACW core (fig. 4.24c-d) is ~ 5 nm to the left. Therefore, in each case a stronger H_D is required when the vortex core must be pushed towards and over the apex of curvature. In addition, HH and TT DWs with otherwise identical vortex parameters also have cores that reside on opposite sides of this apex. Hence, the pinning properties of the TT DW (which displays a clockwise chirality and upwards polarity) are most closely aligned with the anti-clockwise, downwards polarity HH DW.

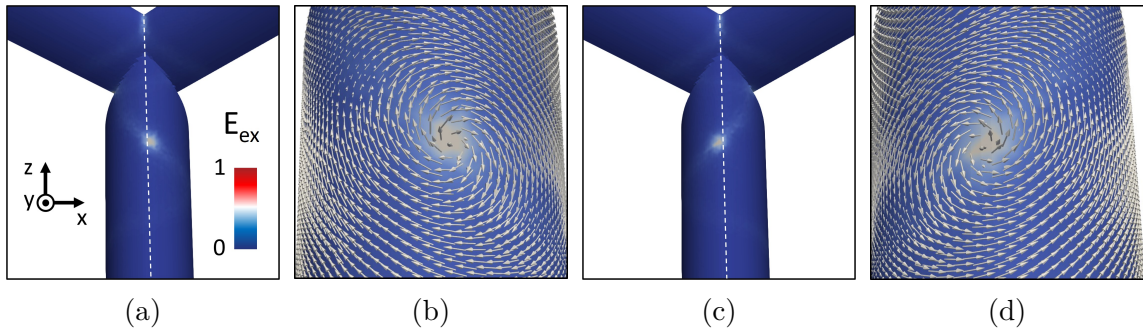


Figure 4.24: A 3-in/1-out tetrapod with opposing upper wires. **a**, A CW VDW with upwards polarity, colour coded with exchange energy. A white dotted line annotates the $y = 0$ plane, indicating the apex of curvature for the lower wires. **b**, Magnified view of the vortex, including glyphs. **c-d**, An equivalent DW with ACW chirality.

The two geometries considered thus far in this section emulate the two energy barriers encountered by an excitation propagating during the L1 reversal. It is therefore noteworthy that the minimum H_D observed at a L1-L2 junction (40 mT) is a factor of 6.2 greater than the maximum H_D seen at a surface termination (6.5 mT). This severe disparity in the pinning potential of two-wire and four-wire junctions offers a second explanation for the lack of excited bipods witnessed in the experimental data. That is to say, if an excitation obtains sufficient energy to overcome the energy barrier imposed at a L1-L2 junction during a field protocol, it will depin and propagate along L1. Upon encountering a bipod vertex, the excitation will already possess ample energy to pass over this barrier.

Next, the L2 reversal sequence is considered, which only requires examination of four wire junctions. Here, an excited L1-L2 junction is composed of one upper wire magnetised towards the vertex and the other magnetised away, whilst the lower wires resemble a 2-in bipod for positively charged excitations (fig. 4.25a-d), or a 2-out bipod for a negative charge (fig. 4.25e). In similar fashion to the previously considered simulations, each combination of vortex parameters were studied for HH DWs, as well as a clockwise, TT DW. Just as occurred in fig. 4.21, vortex polarity has little effect on the DW appearance. However, in contrast with previous simulations chirality now alters the DW structure drastically, due to the asymmetric configuration of the upper two wires. Two states are observed, for a clockwise vortex the core sits near to the central apex, whilst an anti-clockwise chirality causes the core to position far closer to the wire edge. Lastly, a TT DW exhibits a very similar appearance to the equivalent HH DW, though once again the core is positioned on the opposing side of the apex. It should be noted that if the vortex were formed on

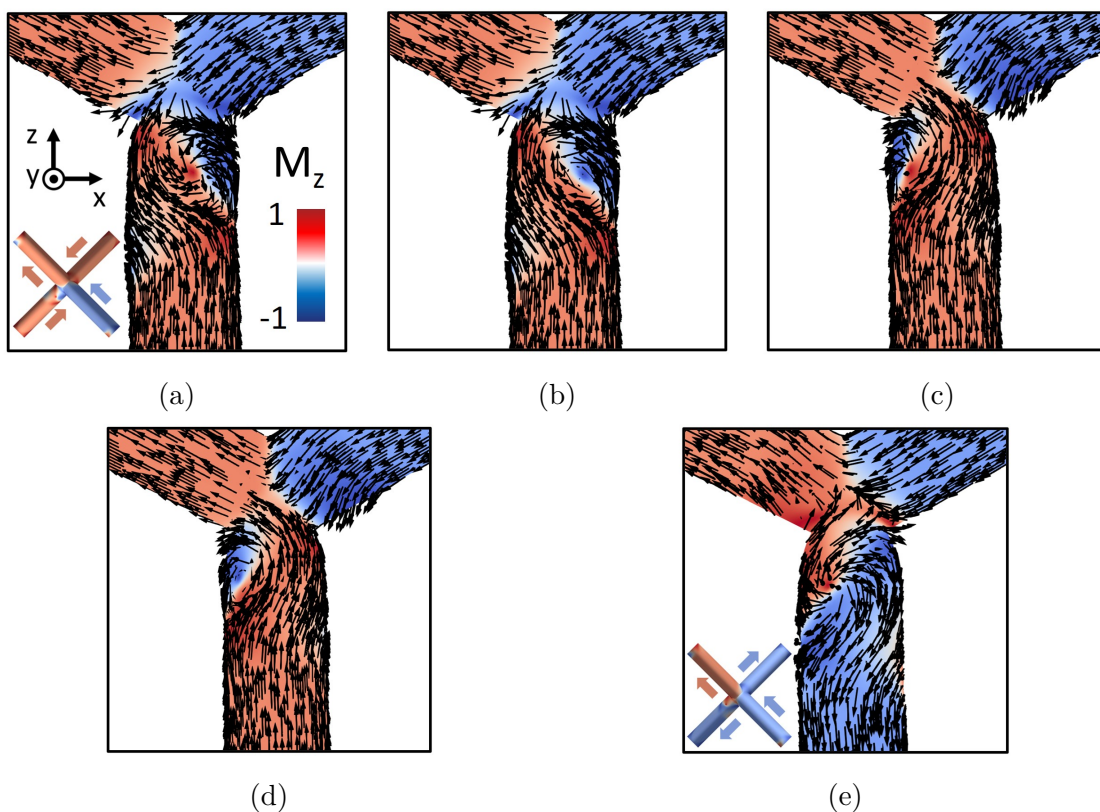


Figure 4.25: Relaxed excited tetrapods with opposing lower wires. **a**, HH, Clockwise, upwards polarity. Inset: Top view, without glyphs. **b**, HH, Clockwise, downwards polarity. **c**, HH, Anti-clockwise, upwards polarity. **d**, HH, Anti-clockwise, downwards polarity. **e**, TT, clockwise, upwards polarity. Inset: Top view, without glyphs.

the other lower wire, the anti-clockwise vortex would sit near the apex, whilst the clockwise DW would position towards the wire edge. To understand this, one must consider how the spin texture of the upper wires feeds into the vortex. Figure 4.25c-d are the two lowest energy states here, which is intuitive when observing the gradual, smooth transition between the upper-left wire and the right-hand side of the vortex. As a result, the E_{ex} of a anti-clockwise wall is reduced by a factor of 1.6 compared with the clockwise equivalent where this smooth transition is not possible.

This effect also poses consequences for the DW pinning potential. To depin the vortex away from the junction requires an enhanced H_D by 3-4 mT for the ACW example compared with the CW DW. However, when pushing the wall towards the vertex, an ACW DW requires a H_D that is 7-9 mT lower than the CW equivalent vortex. Interestingly, propelling this DW towards the vertex is the only example whereby depinning does not result in a wire switching. Instead, the DW moves

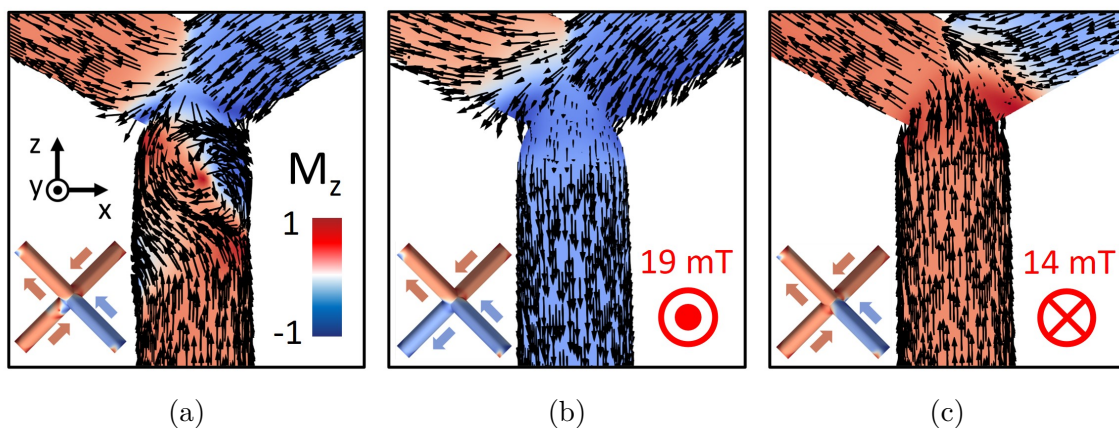


Figure 4.26: Depinning a VDW with clockwise chirality and upwards polarity from a 3-in/1-out tetrapod with opposing lower wires. **a**, Remanent state. Inset: Top view without glyphs. **b**, Immediately following the DW depinning away from the vertex. **c**, Immediately following the DW depinning towards the vertex, although the L2 wire on the opposite side of the vertex hasn't switched. At 46mT, a DW is emitted from the vertex, which switches this wire (upper-right wire in inset).

up to the vertex in an intermediate step (see fig. 4.26c), where a transverse DW separates the magnetisation of the incoming upper wire with each of the two lower wires. Further increments in the applied field yield little change until a DW is emitted from the vertex and switches the wire that opposes the field direction in a single step, at $H = 46$ mT.

Significant insight has been gained through conducting this suite of micro-magnetic simulations. Firstly, excited bipods are shown to be a severely unfavourable state, since producing this excitation requires an energy density ≥ 2.3 times greater than generating a tetrapod excitation, providing an explanation as to why they are rarely seen experimentally. Applying field protocols to each simulated geometry compounded this finding with a second reason for the experimental omission of excited bipods. The energy barrier imposed on a DW propagating along L1 is ≥ 6.2 times greater at a L1-L2 junction when compared with a bipod vertex, meaning that bipod pinning events are expected to be highly unlikely. Next, DW structure is an important factor when considering DW pinning characteristics at a nanowire junctions, with the exact impact of polarity and chirality depending upon both the junction geometry and magnetic configuration.

Simulations have also reproduced multiple aspects of the experimental results. One example is that excitations propagate along L2 at lower fields than on L1, though this effect is more subtle in the experimental data. Additionally, in each

configuration a range of H_D values are observed across the different permutations of vortex structure. which may be a contributing factor as to why experimental excitations are seen to propagate across a range of applied field steps (see fig. 4.12), rather than in a single sharp transition. Experimental data (fig. 4.12d) indicated that L2 experiences pinning events across a wider field range (4.25 mT) than L1 (2.75 mT). Whilst these specific field values are not directly comparable to the simulations, this trend is recreated by NMAG. Modeling, in which an external field applied along the L1 projection yields a 4 mT range of H_D , and a field orientated along the L2 projections yields a 15 mT H_D range.

Considerable information has been attained through finite-element simulations, concerning the energetics and pinning potentials of nanowire junctions with different magnetic configurations, both on the lattice surface and in the bulk. However, to truly understand the macroscopic dynamics seen in these systems one has to take into account dipolar fields from nearest neighbours and beyond. Here, one could investigate the nucleation and propagation of MAPs on different sub-lattices.

4.3 THE IMPLICATIONS OF BROKEN SYMMETRY

As discussed previously, it would be impractical to model an extended 3DNL using a micromagnetics package, but a suitable alternative that requires a substantially lower memory allocation is a Monte-Carlo approach. Here, each nanowire is approximated as an infinitesimally thin compass needle, effectively acting as an individual spin. Clearly this method does not capture the finer details of the lattice spin texture, this mostly has implications at wire junctions where non-uniformities are found, particularly in the presence of a DW. Such Monte-Carlo simulations may therefore suggest if the experimental observations are purely a result of the diamond lattice geometry, namely the broken symmetry upon the surface, or if an additional factor is at play.

Dr Michael Saccone of the University of California, Santa Cruz developed and performed all Monte-Carlo simulations presented herein. Monte-Carlo algorithms are useful tools for efficiently evaluating systems with many degrees of freedom, herein Monte-Carlo simulations were conducted at zero temperature using MATLAB¹⁰¹. In the experimental 3DNL each wire is approximating an Ising spin, which by definition has two possible states, therefore an extended system containing N wires (or spins) has 2^N possible states. A single cubic unit cell of a pyrochlore lattice contains 16

spins⁹³, and hence $2^{16} = 65536$ possible configurations, so one can see how the number of available states increases rapidly as the system grows in size. To model the experimental system, compass needles were arranged into a diamond-lattice geometry of $15 \times 15 \times 1$ unit cells (see fig. 4.27). Needles possess a uniform, linear magnetic moment density m/L aligned with the needle long-axis, where the island length (l) is set as 1000 nm to match experimental parameters. Each needle is defined with a magnetic moment which matches that of a nanowire in the 3DNL, this is calculated as $|\mathbf{m}| = M_S V$, where the saturation magnetisation of $Ni_{81}Fe_{19}$ is set as $M_S = 8.60 \times 10^5 \text{ Am}^{-1}$ to agree with previous studies^{54,56,102}. To approximate the cross-sectional area of the experimental wires, the procedure that was illustrated in fig. 4.7 was once again used to estimate $A = 7.9 \times 10^{-15} \text{ m}^2$. Finally, the cross-sectional area can simply be multiplied by the wire length to yield a volume of $7.9 \times 10^{-21} \text{ m}^3$.

To govern the needle-needle interactions, a dumbbell model (see section 1.8.1) is implemented, where equal yet opposite charges are placed at the two needle ends. The interaction energy between needles i and j obeys a modified Coulomb's law, as defined by

$$E_{ij} = \alpha_{ij} \frac{\mu_0 |\mathbf{m}|^2}{4\pi l^2} \left[\frac{1}{|\mathbf{r}_{ai} - \mathbf{r}_{aj}|} - \frac{1}{|\mathbf{r}_{ai} - \mathbf{r}_{bj}|} - \frac{1}{|\mathbf{r}_{bi} - \mathbf{r}_{aj}|} + \frac{1}{|\mathbf{r}_{bi} - \mathbf{r}_{bj}|} \right] - \mathbf{m}_i \cdot \mathbf{B}. \quad (4.3)$$

where \mathbf{r}_{ai} and \mathbf{r}_{bi} are the positive and negative charge positions respectively at either end of the i th needle, α_{ij} is the modification parameter, which governs the relative strength of interaction between needles at specific vertices. This parameter was introduced to capture the enhanced energetics which micromagnetic simulations revealed to be present at L1 surface terminations, compared with four-wire junctions in the bulk (see table 4.2). At all four-wire vertices α_{ij} is set to 1, meaning that when $\alpha_{ij} > 1$ is defined at bipod vertices, neighbouring needles that form a bipod will exhibit stronger interactions between one another than with other adjacent needles. Effectively, defining α_{ij} in this way renders excited bipods as an unpreferable state, which is known to be the case from analysis of MFM and micromagnetic data. Therefore increasing α_{ij} at bipod vertices reduces the probability of excited bipods forming. In an attempt to closely align these simulations with the experimental system, the energy density values computed in NMAG were evaluated to calculate a realistic value for α_{ij} . To do this, one must consider the energy cost of transitioning a bipod from the ground to an excited state, relative to the energy cost of an equivalent

transition of a four-wire junction. Using table 4.2, 8985 Jm^{-3} is the energy density difference between a 1-in/1-out and a 2-in bipod, whilst 2785 Jm^{-3} is the difference between the mean ice-rule obeying tetrapod and the mean type 3 state. Therefore, the energy required to produce an excited bipod is a factor of 3.23 greater than to generate a type 3 tetrapod. It should be noted that the Monte-Carlo simulations are not expected to be directly comparable to the micromagnetics, however, setting α_{ij} to 3.23 is a reasonable starting point.

To maintain analogy with the experimental switching protocols, the simulated system was first placed into a saturated state, before an external field was applied along the x-axis to incrementally reverse L1 and L3. To update the system, a needle is randomly selected and the energy required to reverse the needle magnetisation is calculated. This reversal is only performed if the resulting energy change exceeds a threshold value that is associated with the needle coercivity. To allow the system to reach equilibrium, this updating process is repeated $10N$ times where N is the total number of needles in the lattice. Upon initial investigation, it quickly became evident that whilst using eq. (4.3) the reversal of each sub-lattice occurred entirely in a single transition, clearly this is not representative of the experimental data. Although this result is not wholly unexpected, since the simulated needles are all identical, so possess exactly the same coercivity. In reality, every nanowire will not be utterly identical, as samples will exhibit surface roughness and are susceptible to minor imperfections. In addition, different combinations of DW chirality and polarity lead to a variety of depinning fields, as discussed in section 4.2. It is these subtle variations that are largely responsible for DWs nucleating and propagating over a range of applied field steps in experimental systems. One can attempt to capture this effect in Monte-Carlo simulations by modifying eq. (4.3) to include a disorder parameter (δ) which is unique to the i th needle.

$$E_{ij} = \alpha_{ij}\delta_i \frac{\mu_0 |\mathbf{m}|^2}{4\pi l^2} \left[\frac{1}{|\mathbf{r}_{ai} - \mathbf{r}_{aj}|} - \frac{1}{|\mathbf{r}_{ai} - \mathbf{r}_{bj}|} - \frac{1}{|\mathbf{r}_{bi} - \mathbf{r}_{aj}|} + \frac{1}{|\mathbf{r}_{bi} - \mathbf{r}_{bj}|} \right] - \mathbf{m}_i \cdot \mathbf{B} \quad (4.4)$$

where the inclusion of disorder adds an element of randomness to the coercivity of each needle. This is achieved by defining a Gaussian probability distribution (eq. (4.5)), from which δ_i is randomly selected for the i th needle.

$$P(\delta) = \frac{1}{\sigma\sqrt{2\pi}} \exp \left[-\frac{(\delta - 1)^2}{2\sigma^2} \right]. \quad (4.5)$$

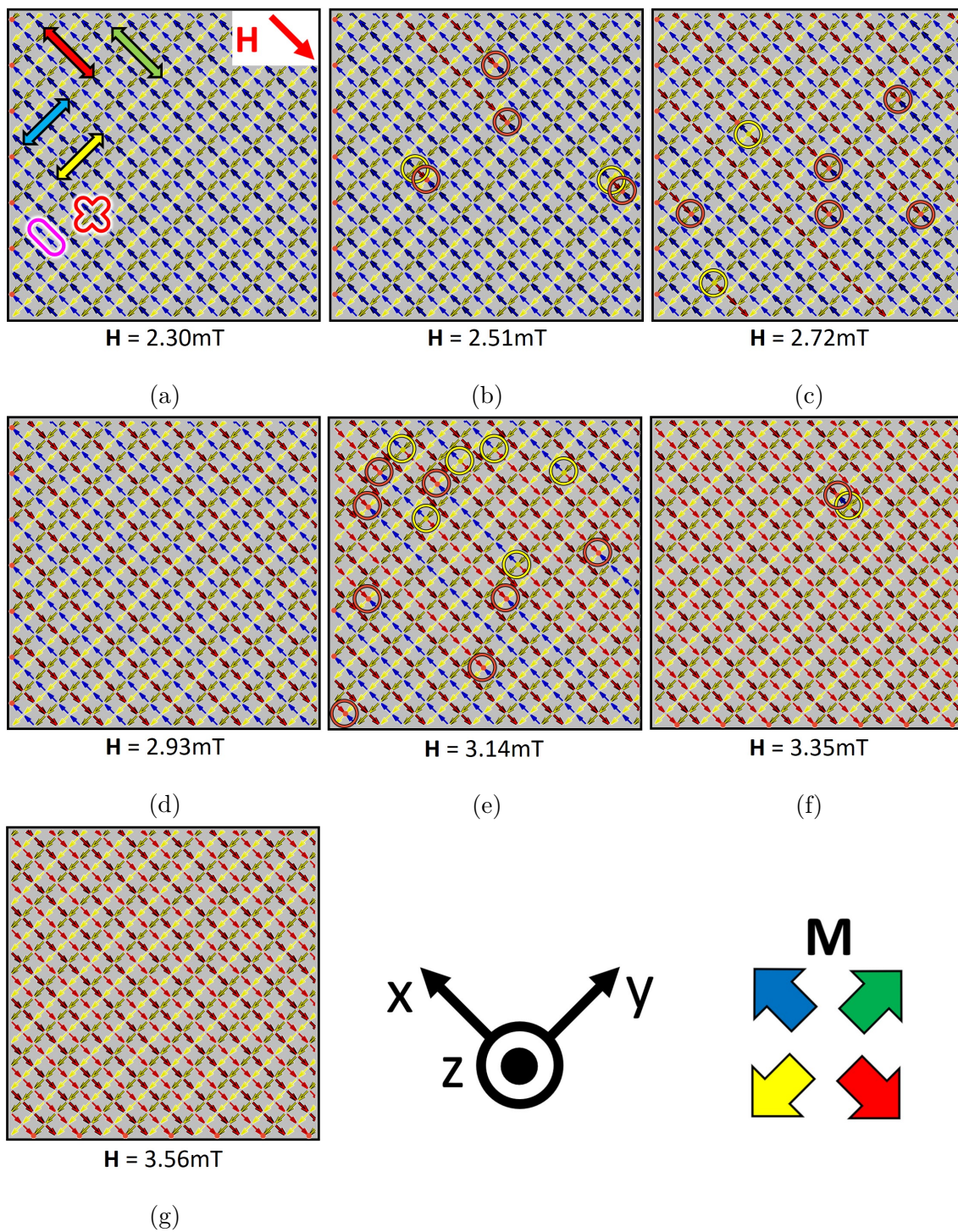


Figure 4.27: Monte-Carlo L1 reversal where $\alpha = 6.45$ and $\sigma = 30\%$. Positive and negative excitations are indicated with red and yellow rings respectively.

The variance (σ) controls the Gaussian peak width, effectively governing the degree of disorder in the coercive field of the simulated needles. Nominally identical simulations of L1/L3 and L2/L4 reversals were conducted for $\sigma = 10\%$, 20% , 30% ,

and 40%, as well as $\alpha_{ij} = 1, 3.23,$ and 6.45 at bipod junctions. Visual inspection of each dataset determined $\sigma = 30\%$ and $\alpha_{ij} = 6.45$ to yield switching which most closely resembled the experimental measurements. Therefore, these simulations are presented in fig. 4.27 and fig. 4.28, whilst the equivalent datasets with other combinations of σ and α_{ij} can be found in the appendices. Ten field steps were applied in each simulation, though only one snapshot of each saturated state is included here. Initially the lattice was placed into a saturated state before a field was applied anti-parallel with the in-plane magnetisation of L1 and L3. Figure 4.27a shows the state immediately before the field is sufficient to induce switching, so is still saturated along all four sub-lattices. Five intermediate states are observed (fig. 4.27b-f), where L1 and L3 are seen to reverse independently, each of which show two intermediate steps between opposing saturation points. Interestingly, L1 entirely reverses prior to any spin flips upon L3 (see fig. 4.27d), a consequence of the enhanced bipod interaction strength. Throughout this dataset, a total of 30 excitations are observed, with 16 found at L2-L3 vertices, 10 at L1-L2 junctions, and 4 upon bipods.

Next, the manner in which each sub-lattice switches shall be considered. In fig. 4.27, excitations are mostly uncorrelated, appearing as isolated charges. Although two instances are observed of correlated MAPs separated by a Dirac string of a single reversed spin. This indicates that once nucleated, a charge pair is weakly correlated such that a slight increase in the external field results in a cascade of reversed spins, facilitating the rapid separation and deconfinement of each monopole pair. In contrast, fig. 4.28 illustrates that a rather different reversal mechanism is observed when the external field is applied orthogonal to the L1 projection. Figure 4.28a depicts a similar saturated state to fig. 4.27a, though the two datasets diverge in appearance once L2 and L4 begin to reverse at $\mathbf{H} = 2.72$ mT. MFM was unable to determine the magnetic configuration of L4, however the L2 arrangement in fig. 4.28b shows a strong agreement with experimental observations. Here, closely correlated MAPs are densely spaced throughout the observed region, whilst L1 and L3 remain saturated. Since these excitations are so densely packed, rings enclosing excited vertices have not been used for annotations (see fig. 4.27) as this would have negatively impacted visual observations. Figure 4.28c is where Monte-Carlo simulations deviate from the MFM results, since many excited L1 bipods are generated despite the external field aligning orthogonal to this surface layer. As a result, many high-energy type 4 vertices are seen at L1-L2 junctions, leading to a lattice configuration resembling a charge crystal. This raises an interesting point

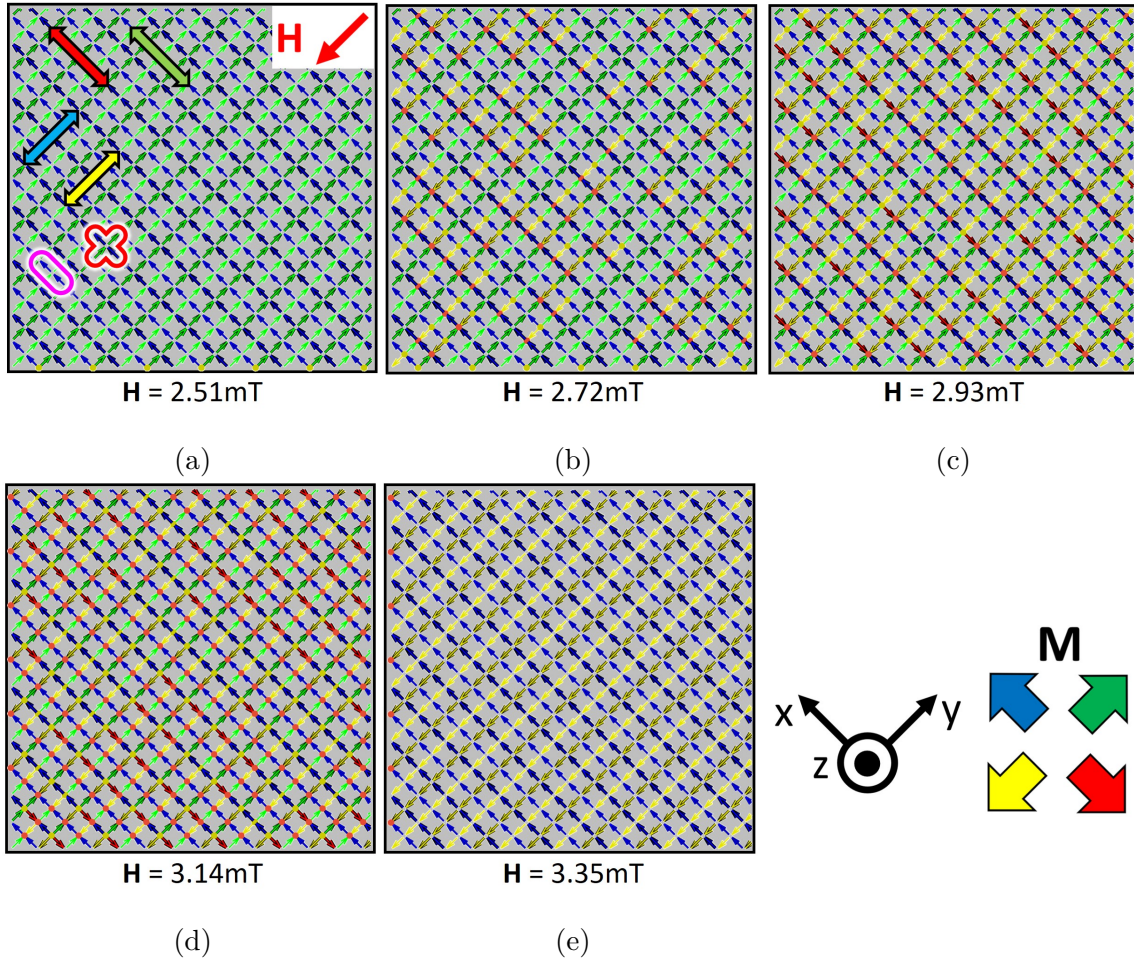


Figure 4.28: Monte-Carlo L2 reversal where $\alpha_{ij} = 6.45$ and $\sigma = 30\%$.

that during a reversal it is energetically preferable for the lattice to pass through a demagnetised state, although, there are multiple possible spin textures for achieving $M = 0$. A charge crystal possessing many excitations may seem to be a very high energy state, although a net-zero magnetic charge is maintained throughout allowing this to form. In addition, this Monte-Carlo system of individual spins is not incurred with the energy cost of nucleating/propagating a DW upon every spin flip, likely to be a key distinguishing factor from the physical 3DNL. Whilst excitations in fig. 4.27 propagated via a cascade of reversing spins, charges here move between adjacent vertices via single spin flips. This is noticeable as excited L1-L2 junctions are almost entirely positively charged at $\mathbf{H} = 2.93$ mT, and negatively charged at $\mathbf{H} = 3.14$ mT, whilst the reverse is true for L2-L3 junctions. At $\mathbf{H} = 3.35$ mT, L2 and L4 reach the opposing saturation state whilst L1 returns to the original state seen in fig. 4.28a, reinforcing the hypothesis that the L1 surface charges form to balance the system net magnetic charge.

Lastly, the reasoning behind the choice of α_{ij} will be discussed. When increased surface energetics are not considered ($\alpha_{ij} = 1$), the simulated L1 reversal yields many closely correlated charges, that are densely spaced and often positioned upon bipod vertices. Clearly this is not reminiscent of the experimental observations. To consider the enhanced surface energetics that were indicated by micromagnetic simulations, α_{ij} can be set to 3.23. This is the factor by which the mean energy difference between a $Q = +2q$ and a $Q = 0$ bipod is increased with respect to the equivalent energy difference in a tetrapod. It is important to note that when $\alpha_{ij} = 3.23$, the simulated reversals bear a far closer resemblance to experiments than when $\alpha_{ij} = 1$, in terms of string length, monopole density, and frequency of charges positioning upon bipods. However, it is necessary to increase this further to gain an even closer resemblance to experiments. To determine why the value of α_{ij} used in Monte-Carlo simulations must be increased beyond the value indicated by micromagnetic simulations, one must consider the fundamental differences between the two approaches. The Monte-Carlo model is composed of disconnected needles, so clearly the two methods will not treat interactions at the vertex identically. Perhaps an even larger distinction is that a micromagnetic simulation of an excited bipod exhibits a net magnetic charge of $\pm 2q$, whereas an extended lattice produces MAPs, so is capable of incorporating excitations whilst maintaining a demagnetised state with net zero charge. Hence, monopole nucleation is more probabilistic in the system where a magnetic charge equilibrium can be continuously sustained. Additionally, the finer detail offered by micromagnetic simulations allows much of the system energy to be densely focussed at the vertex. Whereas Monte-Carlo simulations evenly distribute the wire energy across each needle, effectively reducing the energy barrier for monopoles to form. Generally speaking, if a system presents a lower energy barrier for monopole nucleation upon bipods, then a higher value of α_{ij} is required to suppress this, and hence to approximate the experimental results. Finally, it should be noted that for $\alpha_{ij} = 6.45$ significantly fewer L1 excitations are found upon bipods (29%), compared with L1 four-wire junctions (71%), though this factor has not eliminated 2-in or 2-out states altogether. In theory, α_{ij} could be increased to some massive value in an attempt to entirely inhibit excited bipods, though in doing so one would considerably deviate from parameters thought to be realistic, which may induce unanticipated consequences for the lattice behaviour.

Monte-Carlo modeling, coupled with enhanced surface energetics as deduced through micromagnetic simulations, has broadly captured much of the distinguishing features between the upper two sub-lattices witnessed experimentally. This implies

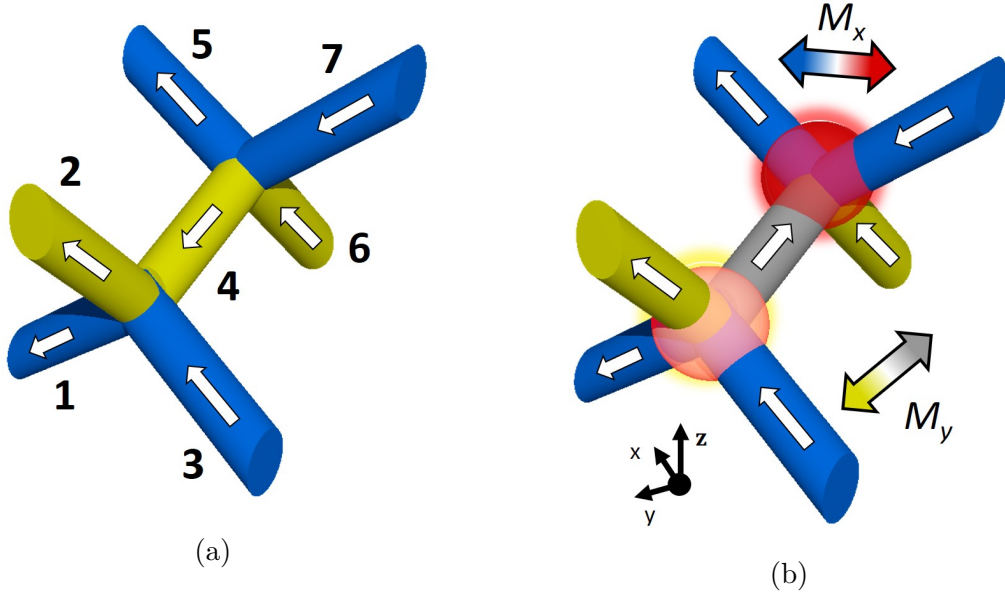


Figure 4.29: Illustrations of adjacent four-wire junctions in the bulk of a diamond-lattice **a**, before and **b**, after nucleation of a MAP. Each wire is assigned a unique index. The co-ordinate system is defined such that the magnetisation of wires 3 and 5 extend along the $[1,1,1]$ axis.

the broken symmetry present at surface terminations is a key factor in directional-dependent excitation dynamics. To show the physical origin for this more explicitly, one can consider a quantity known as the chemical potential (μ_{pot}). Generally speaking, this quantity defines the change in energy resulting from a change in the number of a specific type of particle. Hence, within the spin-ice and ASI communities μ_{pot} typically refers to the energy required to nucleate a monopole-excitation. To calculate this parameter, one must consider the difference in energy between two adjoining ice-rule obeying nanowire junctions (U_{ice}) and two otherwise equivalent junctions which harbour a MAP (U_{MAP}), hence

$$\mu_{pot} = \frac{U_{MAP} - U_{ice}}{2} \quad (4.6)$$

where the factor of $1/2$ corrects for the fact that two monopole-excitations are formed in a single nucleation event. Figure 4.29 illustrates how a MAP nucleates in the lattice bulk via a single wire reversal, the pair of charges are then positioned at adjacent four-wire junctions, separated by a single wire, as is the case in traditional 2D ASI. To quantify the chemical potential for this scenario, one must first calculate U_{ice} and U_{MAP} by discerning the total energy of pairwise interactions before and after the nucleation event. An expression for the interaction energy between two spins i

and j , separated by r_{ij} , is³⁵

$$u_{ij} = \frac{D |\hat{\mathbf{m}}_i \cdot \hat{\mathbf{m}}_j - 3(\hat{\mathbf{m}}_i \cdot \hat{\mathbf{r}}_{ij})(\hat{\mathbf{m}}_j \cdot \hat{\mathbf{r}}_{ij})|}{\left(\frac{|r_{ij}|}{a}\right)^3} \quad (4.7)$$

here, these calculations are performed in a deunitised framework where the geometric parameters are derived from a lattice where the lattice constant (a) = 1. The constant D is given by

$$D = \frac{\mu_0 |\mathbf{m}|^2}{4\pi a^3}. \quad (4.8)$$

By approximating the states shown in fig. 4.29 within a dipolar framework, one can calculate the energy of every pairwise interaction within each system using eq. (4.7). The values used to calculate the energy of each pairwise interaction for the pre-nucleation, sub-surface scenario (fig. 4.29a) are given in table 6.1. It is noticeable that for every interaction between two spins that are within the same tetrahedron, $u_{ij} = \pm 0.59D$, this value is significantly reduced for spins that do not share a tetrahedron, due to the $1/r_{ij}^3$ dependence. In every case, $u_{ij} > 0$ if the spins i and j are orientated such that their interaction energy is maximised (HH or TT), whilst

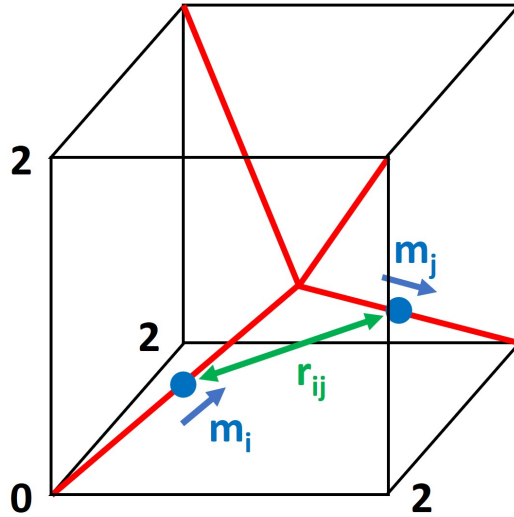


Figure 4.30: Schematic of a tetrapod geometry using a dipolar approximation. The co-ordinate system is defined such that the central vertex is at $(1, 1, 1)$. The magnetic moments and separation of spins i and j are annotated, whereby $m_i = (1, 1, 1)$, $m_j = (1, 1, -1)$, and $r_{ij} = (1, 1, 0)$.

the opposing scenarios (head-to-tail) yields $u_{ij} < 0$. To evaluate the total system energy (u_{system}), one simply needs to summate u_{ij} for all pairwise spin-spin interactions within the system.

$$u_{system} = \sum_{ij} u_{ij}. \quad (4.9)$$

Applying eq. (4.9), yields $u_{system} = -2.36D$ for the pre-nucleation, sub-surface scenario that is presented in table 6.1. The same method can be applied to the post-nucleation scenario (fig. 4.29b), to determine the sub-surface, effective chemical potential. To simplify matters, one can define an effective chemical potential (μ_{pot}^*) whereby

$$\mu_{pot}^* = \frac{\mu_{pot}}{D}. \quad (4.10)$$

This parameter is a measure of the extent to which a MAP remains correlated following nucleation¹⁰³. Charges become increasingly correlated as the effective chemical potential approaches half of the Madelung constant (M_c), at which point a charge crystal is energetically favourable. M_c is a physical constant associated with the crystal geometry, for a diamond lattice¹⁰³ $M_c/2 = 0.82$. Equation (4.10) leads to $\mu_{pot}^* = 1.18$ for the sub-surface nucleation event. This is only a factor of 1.44 above ($M_c/2$), possibly explaining why a state resembling a charge crystal was observed during the Monte-Carlo simulation of an L2 reversal. To add context to this result, and to determine the implications of broken lattice symmetry at the surface, the scenario of a MAP nucleation on the lattice surface shall now be considered. Figure 4.31a-b show the states which must be considered to determine the energy required to nucleate a MAP on the surface. Although, it is noted that experiments and simulations have indicated that 2-in or 2-out bipods are energetically unfavourable, and so are likely to be unstable states. Hence, the monopole which is positioned upon the bipod vertex would be expected to propagate down to the adjacent four-wire junction immediately following nucleation (shown in fig. 4.31c). When calculating μ_{pot}^* upon the surface, it is the transition from fig. 4.31a-b which will be considered in the first instance, since this is the nucleation event. Applying the same method that determined the sub-surface, effective chemical potential to fig. 4.31a-b, yields $\mu_{pot}^* = 1.23$ on the surface. At first this result seems unexpected, since the distinctive differences in monopole dynamics that were observed experimentally imply a significant difference in μ_{pot}^* on the surface and sub-surface. However, this simple dipolar model has not yet considered the implications of the enhanced surface

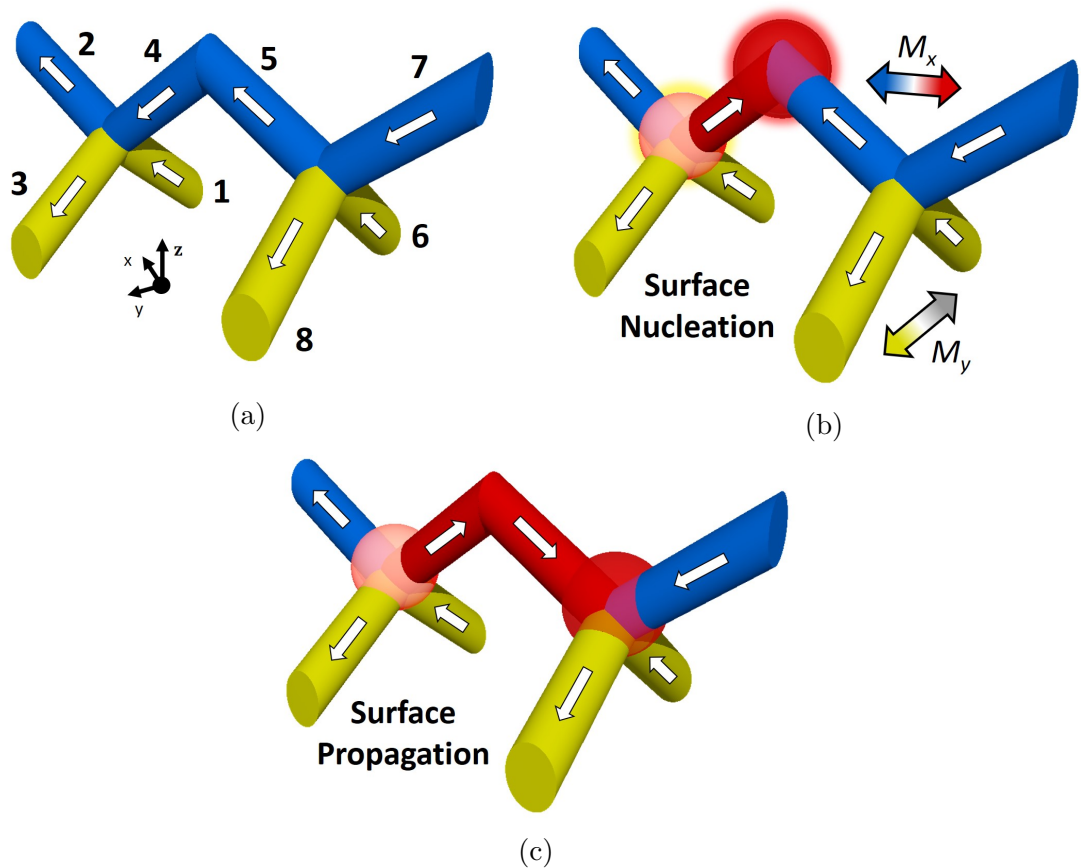


Figure 4.31: Illustrations of adjacent four-wire junctions on the surface of a diamond-bond lattice. **a**, Both tetrahedra exhibit type 2 vertices. Each wire is assigned a unique index. The co-ordinate system is defined such that the magnetisation of wires 2 and 5 extend along the $[1,1,1]$ axis. **b**, A MAP has nucleated via a single wire reversal. **c**, The charge upon the bipod immediately propagates down to the adjacent four-wire junction, since the 2-in bipod is a highly energetically dense state.

energetics. For this, two concepts must be taken into account. Firstly, the MAP will be separated by two wires in the final state of the surface nucleation process (shown in fig. 4.31c), here the long-range interactions increase the system energy. Secondly, the dipolar framework assumes that the energy required to reverse a single spin is identical on the surface and sub-surface. Although, micromagnetic simulations have indicated that the energy barrier to reverse a spin is enhanced on the surface, due to the broken lattice symmetry.

To address the first implication, enhanced monopole separation, one can define the position of both charges in a co-ordinate system where the bipod vertex is positioned at $(0, 0, 0)$. Figure 4.32 illustrates this, where $\hat{r}_1 = \frac{1}{\sqrt{3}}(-1, -1, -1)$ and $\hat{r}_2 = \frac{1}{\sqrt{3}}(1, 1, -1)$, hence it follows that $\hat{r}_{charge} = \frac{2}{\sqrt{3}}(1, 1, 0)$ and so $|\hat{r}_{charge}| = \frac{2\sqrt{2}}{\sqrt{3}}$.

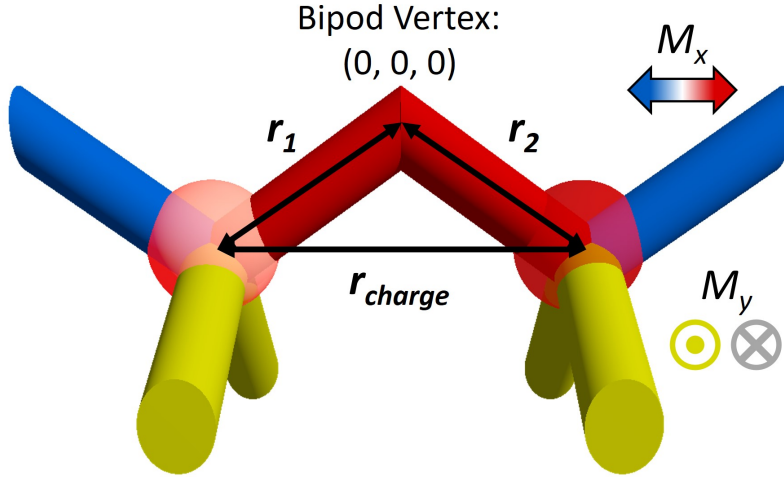


Figure 4.32: Illustration of a monopole-antimonopole pair at adjacent L1-L2 junctions. The co-ordinate system is defined such that left and right charges are positioned at $(-1, -1, -1)$ and $(1, 1, -1)$ respectively.

This result can be used to approximate the energy increase via the dumbbell model's long-range interactions (E_{lr})³¹.

$$E_{lr} = \frac{D}{r_{charge}/a} \quad (4.11)$$

when considering these long-range interactions, the system energy rises by the difference between the interaction strength of a MAP separated by one wire and that of a MAP separated by more than one wire. Hence, U_{MAP} is raised by $D(1 - E_{lr}) = D(1 - \frac{\sqrt{3}}{2\sqrt{2}}) = 0.39D$, resulting in $\mu_{pot}^* = 1.62$ on the lattice surface. Now a notable distinction is seen between the surface and sub-surface. However, this model still doesn't incorporate the enhanced energy barrier that must be overcome when reversing a wire to nucleate a charge upon a bipod. To do so, one can consider the individual building block associated with each monopole, and modify the energy to produce a monopole upon a bipod by the value α_{ij} , which represents the enhanced surface energetics discussed previously. Firstly, recall that favourable interactions between spins in a tetrapod geometry exhibit $u_{ij} = -0.59D$ and unfavourable interactions exhibit $u_{ij} = 0.59D$. The tetrapod (wires 1-4 in fig. 4.31) transitions from 4 favourable and 2 unfavourable interactions, $u_{tetra} = -1.18D$, to 3 favourable and 3 unfavourable interactions, $u_{tetra} = 0$. Similarly, the bipod (wires 4-5) transitions from 1 favourable interaction, $u_{bipod} = -0.59\alpha_{ij}D$, to 1 unfavourable interaction,

$u_{bipod} = 0.59\alpha_{ij}D$. The average energy cost to nucleate a monopole is then given by

$$\mu_{pot}^* = \frac{1}{D} \left(\left. \frac{u_{tetra} + u_{bipod}}{2} \right|_{MAP} - \left. \frac{u_{tetra} + u_{bipod}}{2} \right|_{ice} \right). \quad (4.12)$$

Micromagnetic simulations indicated $\alpha_{ij} = 3.23$, although Monte-Carlo simulations showed a closer resemblance to experiments when $\alpha_{ij} = 6.45$, hence both values shall be considered here. For $\alpha_{ij} = 3.23$, eq. (4.12) yields $\mu_{pot}^* = 2.50$, whilst $\alpha_{ij} = 6.45$ results in $\mu_{pot}^* = 4.39$. Hence, it has been calculated that the effective chemical potential on the surface of a diamond-bond lattice is increased by a factor of 2.12 - 3.72 compared with the sub-surface equivalent, when enhanced surface energetics are incorporated. This difference comprehensively explains the behaviour witnessed in both experiments and simulations. An increased μ_{pot}^* on L1 means that, once nucleated, charges that are part of a MAP are more weakly confined to one another, so only require a small amount of energy to rapidly separate. In contrast, sub-surface charge pairs are more strongly constrained to one another, leading to a greater density of correlated MAPs being observed, which separate more gradually. In addition, μ_{pot}^* is far closer to $M_c/2$ in the lattice bulk, which clarifies why intermediate steps in the Monte-Carlo L2 reversal (fig. 4.28) resembled a charge crystal, whilst steps in the L1 reversal did not. The various scenarios and results of the μ_{pot}^* calculations are summarised in table 4.4.

Scenario	μ_{pot}^*
Sub-surface: Purely dipolar model	1.18
Surface: Purely dipolar model	1.23
Surface: Including E_{lr}	1.62
Surface: Including $\alpha_{ij} = 3.23$	2.50
Surface: Including $\alpha_{ij} = 6.45$	4.39

Table 4.4: Calculated values of the effective chemical potential for a diamond-bond lattice geometry. Firstly, a purely dipolar framework where the MAP are separated by one wire was considered. Next, this was modified on the surface to account for the long-range interactions of a MAP separated by two wires. Lastly, a hybrid approach was taken which incorporates the enhanced energy barrier to position a monopole upon a bipod, due to surface energetics.

4.4 SUMMARY

A brief summary of the key findings and results presented in this chapter.

- A relationship between the lattice spin texture and associated MFM signal has been understood, through analysis of MFM images following in-plane saturating fields in each principle direction.
- After sourcing lower moment MFM tips, intermediately magnetised states could be repeatably imaged, allowing individual vertex types to be reliably identified.
- Successive MFM measurements at systematic field steps between saturation states revealed uncorrelated, highly mobile excitations upon the surface layer, and a greater density of excitations in the bulk appearing in strongly correlated MAPs.
- NMAG simulations demonstrated excited bipods to be severely unpreferable states, and provided significant insight into the pinning characteristics of nanowire junctions in the diamond lattice.
- Monte-Carlo simulations broadly captured the excitation dynamics witnessed experimentally, inferring the broken symmetry upon the surface to be a primary factor in the distinction between monopole behaviour on L1 and L2.
- Effective chemical potential calculations, using a dipolar approximation, mathematically demonstrated the difference in MAP confinement on the surface and sub-surface, explaining experimental observations.

Chapter 5

Conclusions and Future Work

‘There is no real ending. It is just the place where you stop the story.’

FRANK HERBERT

The aims of the research conducted in this thesis can be summarised in three core objectives. The progress made herein, relating to each of these objectives, is summarised and concluded next.

1. Evaluate the potential of TPL to engineer magnetic nanowires into a 3D frustrated geometry.
2. Explore the possibilities offered by standard, in-house magnetometry techniques for the characterisation of any fabricated structures
3. Combine experimental observations with simulations and modeling to gain insight into the underlying physical mechanisms occurring within these novel 3D systems.

5.1 REALISING A 3D ARTIFICIAL SPIN-ICE

Naturally, objective 1 was the first to be addressed during this study, due to practicality. Other technologies in the field of 3D nanomagnetism have reported promising results in recent years, but have so far struggled to declare themselves as the primary candidate to offer a route towards a multitude of next-generation technologies. Here, the intention has been to establish the immense capability

and versatility offered by TPL, thus demonstrating that this technique should be considered a firm contender within 3D nanomagnetism. One of the key benefits of TPL is that it has the potential to be coupled with numerous secondary techniques to yield different types of magnetic nanostructure. At an early stage of this study, thermal evaporation was chosen to be this secondary technique. In part this was chosen for simplicity, since thermal evaporation has been widely used for decades to deposit ultra-high purity magnetic films, with relatively little setup time and a strong degree of repeatability. In addition, this approach was expected to be most comparable with previous examples of 2D ASI, as these are also typically fabricated via a line-of-sight deposition following a lithographic technique.

Before attempting to produce a complex 3DNL, simpler structures were first fabricated to build confidence and experience in this fabrication process. Initially, planar $Ni_{81}Fe_{19}$ micropads and microwires were created directly upon a glass substrate. This facilitated a calibration of the deposition thickness, via AFM, and demonstrated that distinctive domain patterns, which depend upon the shape anisotropy, can be directly observed in 50 nm thick structures via MFM. Next, similar in-plane, $Ni_{81}Fe_{19}$ pads and wires were fabricated upon a polymer scaffold with feature sizes in the range of 0.3 to 4.1 μm and aspect ratios in the range of 1:1 to $\sim 10:1$. Scanning probe techniques are typically used to measure 2D surfaces, although AFM was found to closely track the high ranging topography ($\sim 1.5 \mu m$) of this 3D scaffold. After optimising the AFM feedback settings, MFM revealed the remanent domain pattern of almost every structure, these clearly demonstrated the effect of shape anisotropy. A combination of finite resolution and tip convolution meant that the smallest structures were not sufficiently resolved in the MFM data. Flux-closure domain patterns were seen at the lowest aspect ratios, whereas single domain states were found for aspect ratios greater than ~ 4 . Hence, proof-of-principle was provided that this technique can form magnetic nanowires, suspended above the substrate, which act as effective Ising spins.

Having gained experience and confidence in this technique, attention now turned towards fabricating a diamond-bond lattice polymer scaffold, which emulates the arrangement of atomic Ising spins in bulk spin-ice. After considering several methods of defining a scaffold with this complex geometry, it was determined that the most suitable approach was to define a disconnected series of individual points. Using the galvo scan mode each co-ordinate could then be exposed in a layer-by-layer approach, this ensured that the minimum possible feature was achieved, whilst also

maintaining sharp, well-defined vertices. In the first instance, a diamond-bond lattice scaffold that extended by only one unit-cell in the z-direction was fabricated, primarily due to simplicity and speed of production. After gaining proof-of-principle that the desired geometry could be created, it was next necessary to isolate the $Ni_{81}Fe_{19}$ nanowire array from the surrounding sheet film. Without a convenient lift-off method to remove the sheet film, the most obvious solution was to construct a scaffold extending by several unit cells in the z-direction. A simple calculation revealed that any stray field from $Ni_{81}Fe_{19}$ on the substrate would be negligible at a separation of 10 μm , hence, a scaffold which is five unit-cells in height was constructed. This solution truly isolated the 3DNL upon the polymer scaffold, because shadowing effects during the line-of-sight deposition prevent any magnetic material from depositing on scaffold layers below the uppermost unit-cell. A crescent shaped wire cross-section is expected in these systems, due to the ellipsoidal voxel and line-of-sight deposition, this prediction is supported through SEM observations. No noteworthy variation between different scaffold layers was found, shown by analysis of SEM data which determined no significant trend in lateral or axial feature size exists as a function of height. In addition, AFM measurements indicated RMS surface roughness values of (10.8 ± 4.3) nm and (16.1 ± 3.2) nm for the L1 and L2 sub-lattices respectively, agreeing within error.

5.2 MAGNETIC CHARACTERISATION

Once satisfactory structures could be repeatably produced in the geometry of a 3D ASI, attention then turned towards the magnetic characterisation of these complex systems. Magnetometry techniques are typically optimised for bulk materials, thin films, or 2D nanostructured systems, and so careful data interpretation is required when considering the 3D nanostructures studied here. In this thesis, MOKE and MFM measurements have been used to examine the switching characteristics of the 3DNL in field-driven experiments, as these allow one to study how the lattice geometry impacts monopole transport on different sub-lattices. MOKE magnetometry, performed in a longitudinal setup, was seen to be predominantly sensitive to the uppermost sub-lattice. Although, the resulting hysteresis loops were thought to be a superposition of the signal associated with L1, L2, and the surrounding film with varying relative contributions, depending on the exact configuration during measurement. The laser used in this technique significantly deformed the polymer scaffold, an issue which was resolved by coating the sidewalls of the structure with gold prior to the $Ni_{81}Fe_{19}$ deposition. A coercivity of 8.0 mT was measured from a

structure which did not possess an underlying gold layer, with the field aligned to the L1 sub-lattice projection. Similar measurements were then performed on a structure which did possess an underlying gold layer, these indicated coercive fields of 6.5 mT and 5.4 mT when the field was aligned to the L1 and L2 projections respectively. Here, it is likely that the coercive fields were reduced due to the enhanced wire width that results from the underlying gold layer.

Whilst MOKE measurements provided useful insight into the switching properties of the 3DNL, this technique could offer limited information regarding the impact of the lattice geometry upon monopole behaviour. MFM is proven to be a more suitable approach for this, since one can directly image the magnetic configuration, allowing the signal associated with different sub-lattices to be disentangled, without any contribution from material on the substrate. A key result of this thesis is that AFM and MFM can in fact be used to probe 3D nanostructured systems, providing the wires are sufficiently closely spaced to prevent the probe from falling too far into any void regions, which could damage the sample and probe. After surveying different low moment MFM probes and gaining significant experience in measuring these structures, the signal associated with a variety of different states could be reliably identified. This understanding was built up by initially considering saturated states, which are the simplest scenario to interpret because every wire is expected to align with the applied field and hence exhibits a matching pattern of MFM contrast. During this data collection, it was noted that the signal associated with a sub-lattice did not change when a saturating field was applied perpendicular to the projection of that sub-lattice, indicating the wires to be single domain.

Using this knowledge, the configuration of intermediately magnetised states could then be mapped out, allowing monopole transport to be directly observed and tracked by using an incremental field protocol to independently reverse each sub-lattice. Having gained considerable experience measuring 3DNLs in field-driven MFM experiments, a number of recurring features have been observed. When applying a field along the L1 projection, monopole excitations are only seen at four-wire junctions, never at two-wire surface terminations. These typically appear as isolated charges which propagate via long cascading chains of reversing wires. As a result, nucleation/annihilation events are rarely seen in the observed window for this field geometry, it is more common for existing monopoles to simply propagate into and out of the measured area, often within a single field step. Monopole behaviour is found to be rather different when applying a field parallel to the L2 projection, as monopoles

must now travel through a sub-surface nanowire layer. In this field geometry, a greater density of monopole excitations is regularly seen. Charges propagate via short chains of wire reversals and often appear as part of a closely correlated charge neutral pair. Hence, many nucleation/annihilation events tend to occur within the measured area. These features are highly prominent during the incremental reversal sequences of the L1 and L2 sub-lattices, shown in this thesis. Only 5 monopole excitations are observed during the L1 reversal, none of which are part of a correlated, charge neutral pair. This allows a significant net magnetic charge ($0 \geq Q \geq -6q$) to be present within the measured area throughout this dataset. In contrast, 22 monopole excitations are found during the L2 reversal, 14 of which are part of charge neutral pairs that have nucleated within the observed region. Hence, despite the vastly increased number of monopoles, the net charge within this measured remains close to zero throughout ($+2q \geq Q \geq -2q$).

5.3 SIMULATIONS AND MODELING

To gain further insight into the curious physical behaviour of these systems, they have been modeled using three methods. Firstly, micromagnetic simulations allow the energetics and spin texture of lattice building blocks to be studied in intricate detail. Secondly, Monte-Carlo simulations provide a broader view of the system, whereby the user can modify certain parameters to understand their impact on the lattice behaviour. Finally, a dipolar model has been used to approximate the effective chemical potential on different sub-lattices, providing a physical origin for the behaviour observed experimentally.

NMAG served as the primary micromagnetic simulation package herein, this facilitated the modeling of a single wire, a bipod, and a tetrapod in a variety of scenarios. A key result is that in each geometry all wires were found to be single domain at remanence and are hence Ising-like, despite the novel wire geometry. These wires switch via the propagation of VDWs, the structure of which is perturbed, due to the crescent shaped cross-section, in comparison with more commonly studied VDWs in planar wires. By comparing simulated hysteresis loops of a bipod and a tetrapod with experimental data, it could be inferred that MOKE measurements in a longitudinal setup are predominantly, though not entirely, sensitive to the uppermost sub-lattice. Next, each configuration of a bipod and a tetrapod was simulated, all of which proved to be possible remanent states with the exception of type 4 vertices. These revealed type 2 vertices to be the energy minimum in four-wire junctions,

agreeing with a recently reported theoretical study considering connected 2D ASI⁴². Another key result was discovered by comparing the energy density difference between low energy and excited states for the bipod and tetrapod geometries. This difference is a factor of 3.23 greater for the bipod relative to the tetrapod, indicating that it is a very high energy state for a monopole to be positioned upon a bipod. Coupling this finding with experimental observations led to the conclusion that 2-in or 2-out states are effectively forbidden due to these enhanced surface energetics.

Next, field-driven NMAG simulations were conducted to assess the role of DW structure and pinning in the bipod and tetrapod geometries. These results consistently showed that a bipod exhibits a far weaker pinning potential ($0.7mT \geq H_D \geq 6.5mT$) than a tetrapod ($7mT \geq H_D \geq 45mT$). In each case, the vortex structure was found to be intimately connected to the vertex pinning potential. For a bipod the chirality has relatively little impact, though the polarity is of great importance because this governs how the vortex pins to the central vertex due to curvature-induced effects. In a tetrapod, the vortex is positioned further from the central vertex and so polarity is relatively insignificant, whereas the importance of chirality depends upon the tetrapod configuration. For initially opposing upper wires, the DW is in an effectively symmetric potential well, meaning that chirality poses little significance. For initially colinear upper wires this is not the case, in this scenario the two chiralities interact differently with the upper wires, leading to pronounced differences in the DW energetics and depinning fields.

To assess the implications of the enhanced energetics, predicted through micromagnetics, a different technique was required which is better optimised to model an extended, many-body system. For this purpose, Monte-Carlo simulations are often called upon within the ASI community and beyond. Here, the 3DNL was modeled using infinitesimally thin needles to approximate each wire. The purpose of this was to recreate the experimental field protocol both with and without any enhanced surface energetics to comprehend the consequences of the broken lattice symmetry. It was found that when surface energetics were considered ($\alpha_{ij} > 1$), the simulated reversals showed a far greater resemblance to the experimental data for both the L1 and L2 switching sequences. For this, considered factors include monopole density, typical string length, and number of charges upon bipods.

The distinction in monopole behavior on the surface and sub-surface has been explained in the context of an effective chemical potential. This considers the

tetrahedral geometry in a dipolar framework, within which the energy of interaction between any two spins is calculated as ± 0.59 in reduced units. By evaluating the total energy change during the nucleation of a monopole-antimonopole pair due to a single spin flip, one can determine the sub-surface, effective chemical potential to be 1.18. When considering a purely dipolar framework, a very similar value of 1.23 is found for a surface nucleation event, which increases to 1.62 when accounting for the long-range dipolar interactions in the remanent state. However when the enhanced surface barrier to reverse a bipod spin is incorporated into this model, predicted through simulations and experiments, an effective chemical potential of 2.50 - 4.39 is found. Here, the exact value of μ_{pot}^* depends upon the method by which the value of α_{ij} is determined. This significant distinction means that monopoles are expected to be less correlated and propagate more freely on the surface than sub-surface, as was observed in experiments.

Finally, to reflect upon the main achievements of the work presented in this thesis:

- TPL and line-of-sight deposition can yield single domain $Ni_{81}Fe_{19}$ nanowires arranged in a complex, 3D geometry, positioned upon a polymer scaffold.
- AFM and MFM can probe the topography and magnetic configuration of these 3D nanostructures.
- A relationship between the lattice spin texture and associated MFM signal has been understood, allowing type 1, 2, and 3 vertices to be reliably identified.
- Applied field protocols revealed uncorrelated, highly mobile excitations upon the surface layer of a 3DASI, and a greater density of excitations in the bulk appearing in strongly correlated monopole-antimonopole pairs.
- Simulations and theory predict that this discrepancy in monopole behaviour could be the result of a difference in effective chemical potential between the lattice surface and bulk, due to the broken lattice symmetry on the surface.

5.4 FUTURE WORK

This thesis serves as a proof-of-principle study that TPL, coupled with a secondary deposition technique, can yield complex 3D magnetic nanostructures with significant user-control over the desired geometry. In addition, in-house

magnetometry techniques can probe the magnetic properties of these 3D systems. With this demonstrated, there are many further avenues of research which can build upon the work presented herein that would be of great interest to the nanomagnetism community. Perhaps the most direct extension of this work would be to incorporate a lift-off procedure into the sample fabrication, to remove any material deposited on the substrate. Doing so would greatly simplify the collection and interpretation of data via optical magnetometry. This would also make various synchrotron-based techniques more accessible, since these often require the user to tune towards a specific element, which is complicated when the $Ni_{81}Fe_{19}$ nanowires are surrounded by a $Ni_{81}Fe_{19}$ film. Though incorporating a lift-off procedure is not a trivial modification, since this requires a material which can withstand the solvents used during sample development, and can then be removed following evaporation without damaging the scaffold. Another student is undertaking this significant challenge and has already made encouraging progress.

The enhanced energy difference between low energy and excited states at the lattice surface, relative to sub-surface vertices, is a key result of this thesis. Hence, it would be fascinating to gain further insight into the physical origin of this, and to examine how this varies for different boundary conditions. One possible explanation lies in the distribution of magnetic charge across the vertex. Here, one would have to examine micromagnetic simulations, since 2-in or 2-out bipods have not been seen experimentally. It is clear that a four-wire junction offers an additional degree of freedom for the magnetic charge, associated with the monopole state, to be distributed in comparison with a two-wire junction. More detailed analysis of this charge distribution could establish if this is a viable explanation for the enhanced surface energetics. It is also noted that this thesis has only considered diamond-bond lattice structures which terminate along a plane perpendicular to the [001] crystallographic axis, though in reality bulk spin-ice crystals can terminate along any arbitrary plane. Therefore, it would be of great interest to investigate diamond-bond lattice geometries which terminate along a variety of crystallographic axes, and the impact of surface terminations in each case.

A topic which is often discussed in bulk spin-ice and 2D ASI is the ground state which is expected in these massively degenerate systems. For this, some studies make use of a field-driven demagnetisation procedure in an attempt to realise the ground state. Although, in connected nanowire systems this is expected to preferentially form type 2 vertices since DWs would be efficiently propagated

to the lattice boundaries. A more promising possibility is to study samples which have never been exposed to a significant external magnetic field, and are hence in the ‘as-deposited’ state. Here it is expected that some minimum energy state is reached during growth, whilst the nanowires are sufficiently thin to be thermally active. Once the thickness increases beyond a point where the wires exhibit a stable magnetisation, this state is effectively ‘locked in’ until the sample is exposed to a significant magnetic field. MFM measurements of as-deposited samples have already taken place, interestingly these displayed ferromagnetic order upon the surface and disorder below this. However, this study has not yet been conducted thoroughly enough to be included in this thesis. It is also noted that ferromagnetic ordering could be the result of a small magnetic field, present during growth. A more reliable method of investigating the ground state would be to fabricate nanowires that are sufficiently thin to be thermally active, as has been studied recently in 2D and 2.5D ASI^{35,104}. Although, it is unlikely that MFM could probe the magnetic configuration of such structures, due to the reduced magnetisation and stray fields associated with these thinner wires. Hence, it is expected that x-ray magnetometry techniques would be required, such as magnetic transmission x-ray microscopy.

Finally, to consider the broader perspective of the possibilities offered by TPL, it has previously been shown that this technique can be coupled with electrochemical deposition to produce complex, self-supporting 3D magnetic nanostructures⁷⁸. Hence, one can envisage the production of a diamond-bond lattice structure that is composed entirely of cylindrical magnetic nanowires, without the requirement of a supporting polymer scaffold. One could even use a multi-layer deposition to produce non-magnetic vertices, such that the Ising-like nanowires would be effectively disconnected. Such a structure would likely exhibit the closest approximation of bulk frustrated materials that is possible through the engineering of magnetic nanowires.

It is hoped that the research discussed herein is of great interest to the wider scientific community. The fabrication techniques used in this thesis have been demonstrated to possess immense opportunities for the field of 3D nanomagnetism, which could well be applied to a sweeping variety of applications, such as the potentially revolutionary technology of racetrack memory¹⁴. In addition, the extension of artificial spin-ice into 3D sets a precedent which could lead to the exploration of a host of new lattice geometries, which have not previously been accessible for 2D and 2.5D systems. This offers new avenues for research into statistical mechanics within these model frustrated systems.

Chapter 6

Appendices

6.1 UNMASKED MFM DATA

In chapter 4, a number of partially masked MFM images are shown. Here, the unmasked MFM is given, this data has undergone minor processing as described in chapter 2.

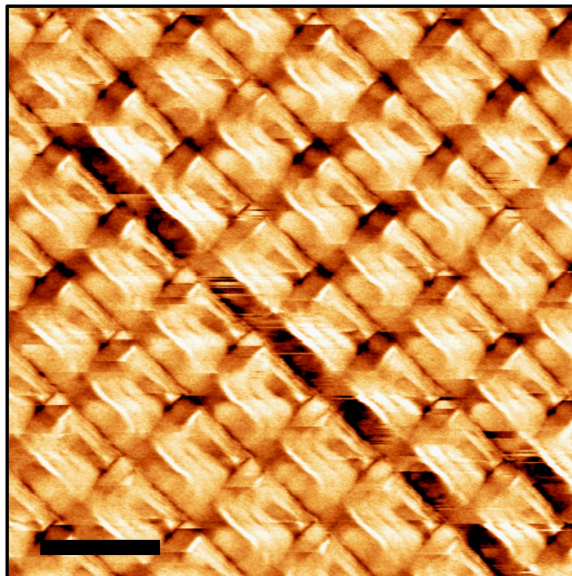
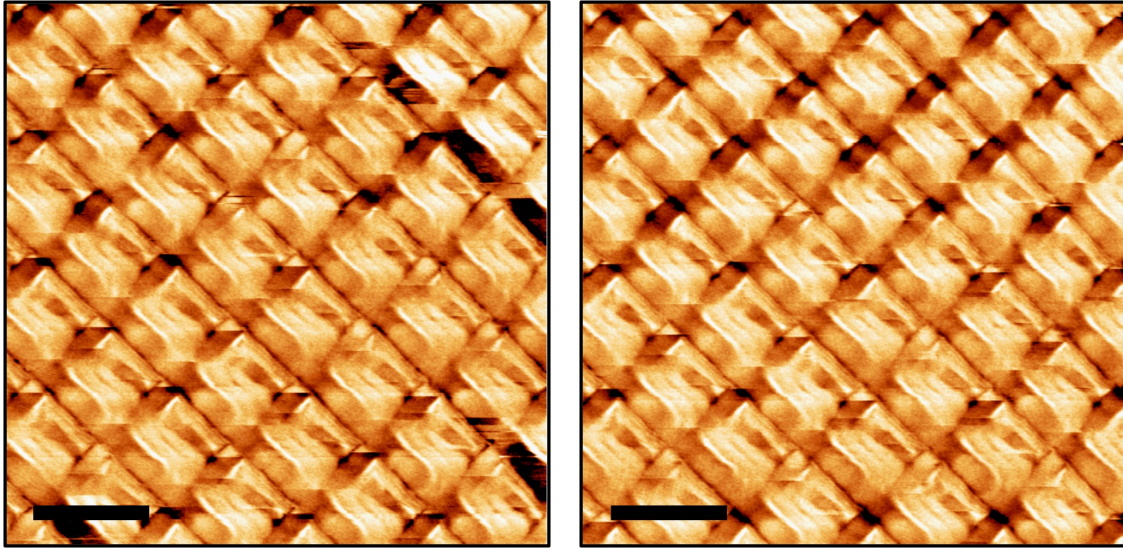


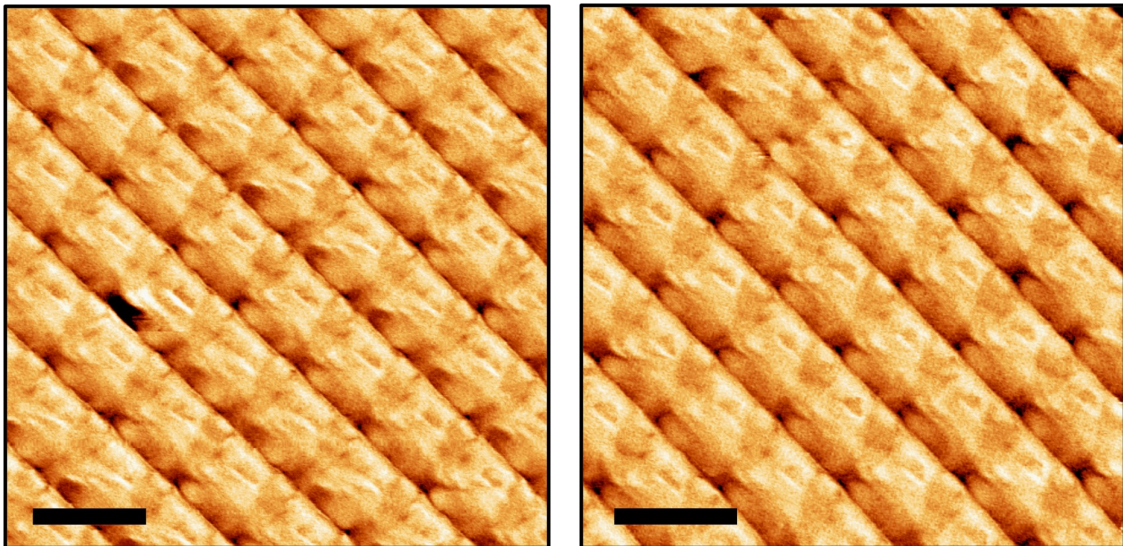
Figure 6.1: Unmasked MFM data from fig. 4.3b. Scale bar indicates $2 \mu m$.



(a)

(b)

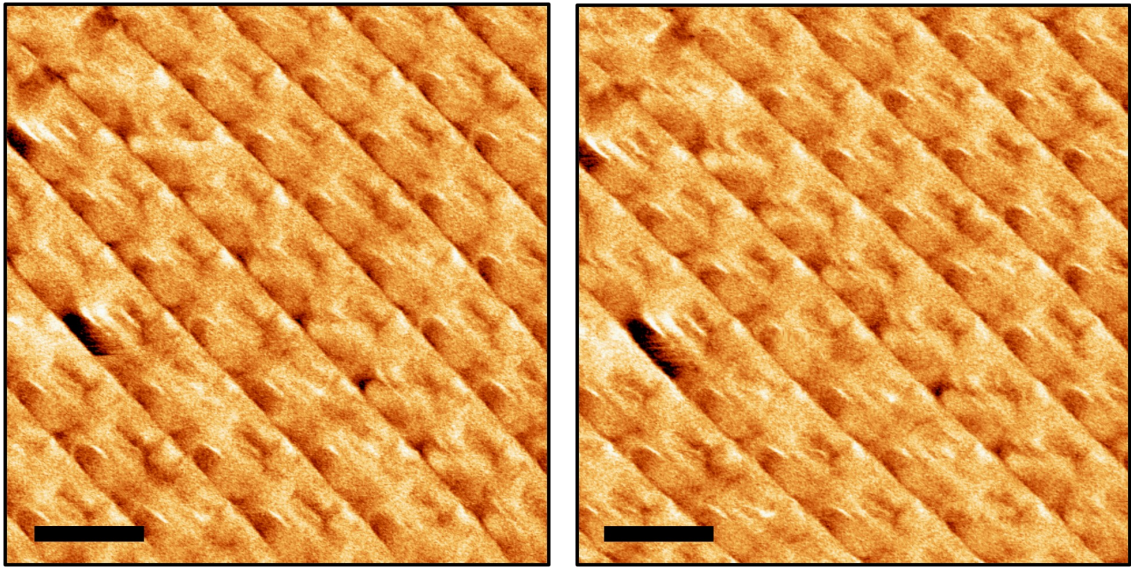
Figure 6.2: Unmasked MFM data from fig. 4.4a-b respectively. Scale bars indicates $2 \mu m$.



(a)

(b)

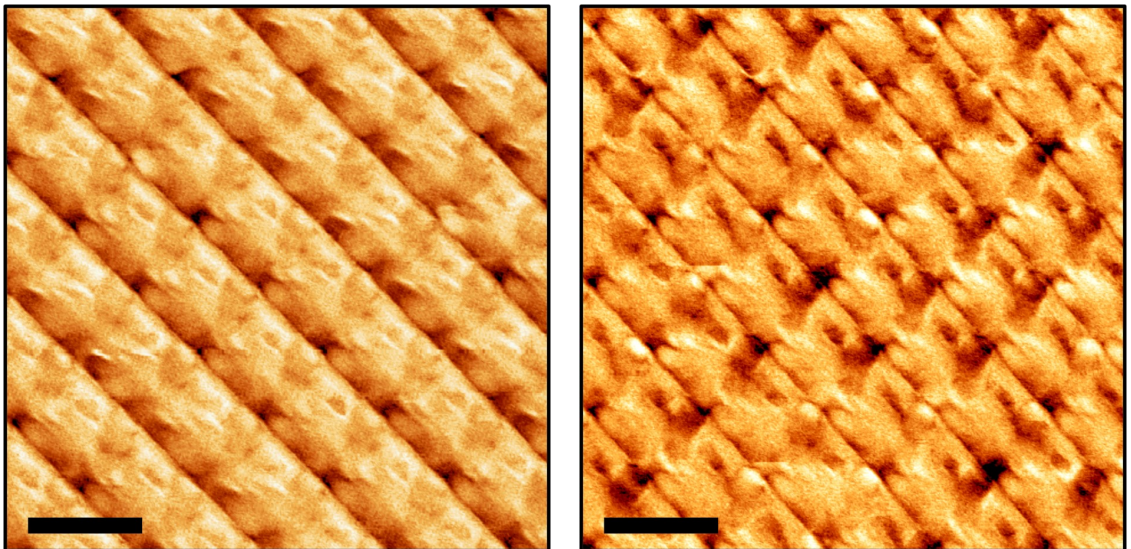
Figure 6.3: Unmasked MFM data from fig. 4.5b-c respectively. Scale bar indicates $2 \mu m$.



(a)

(b)

Figure 6.4: Unmasked MFM data from fig. 4.6b-c respectively. Scale bar indicates $2 \mu\text{m}$.



(a)

(b)

Figure 6.5: Unmasked MFM data from fig. 4.9a and c respectively. Scale bar indicates $2 \mu\text{m}$.

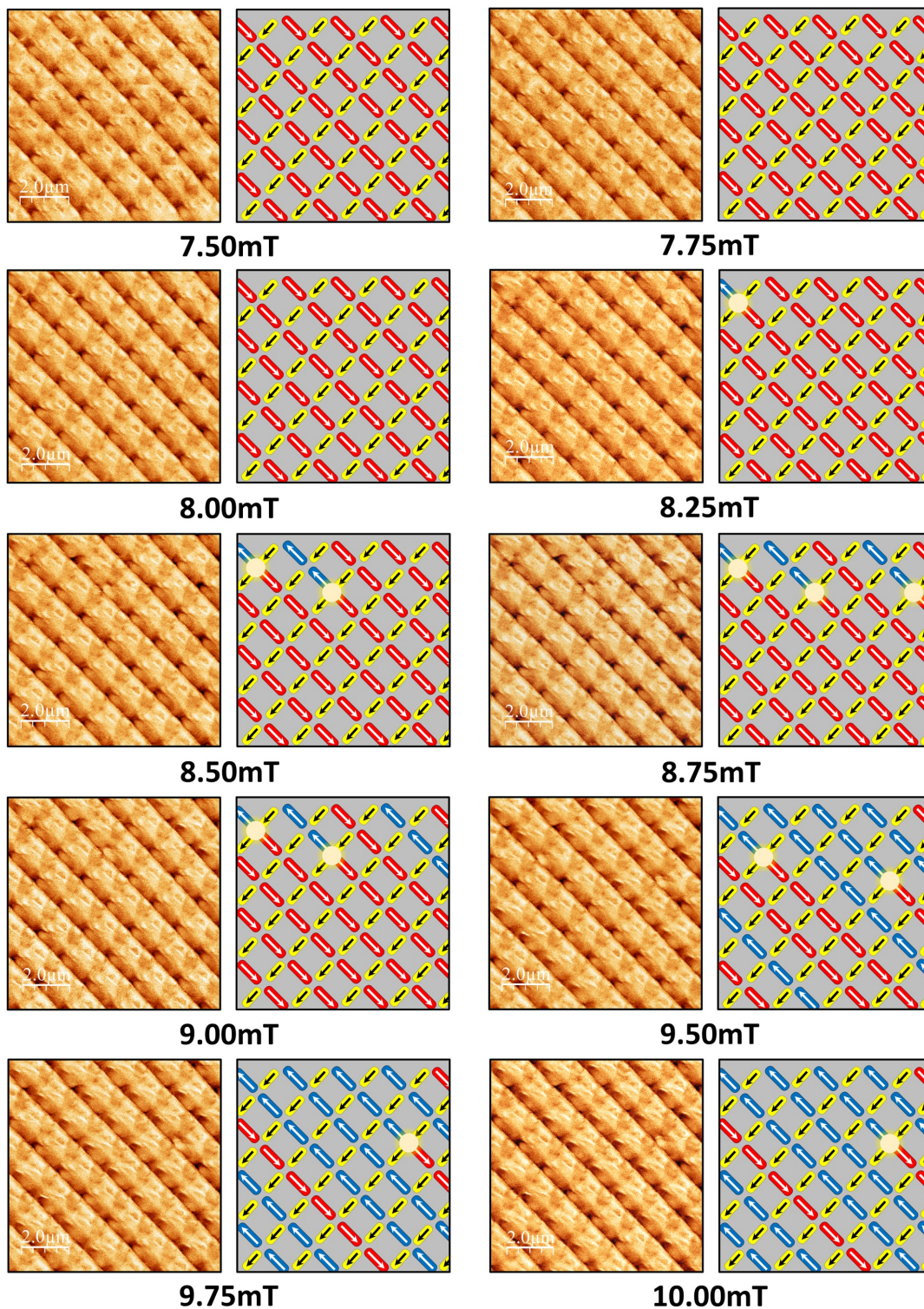


Figure 6.6: Unmasked MFM data from fig. 4.10. All scale bars are $2 \mu m$.

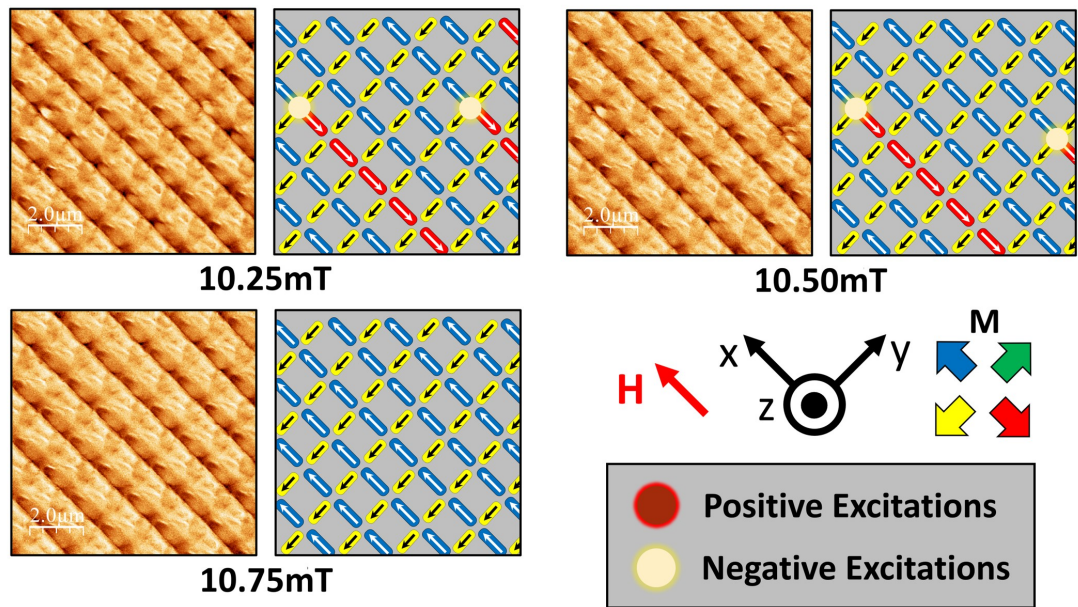


Figure 6.6: Continued.

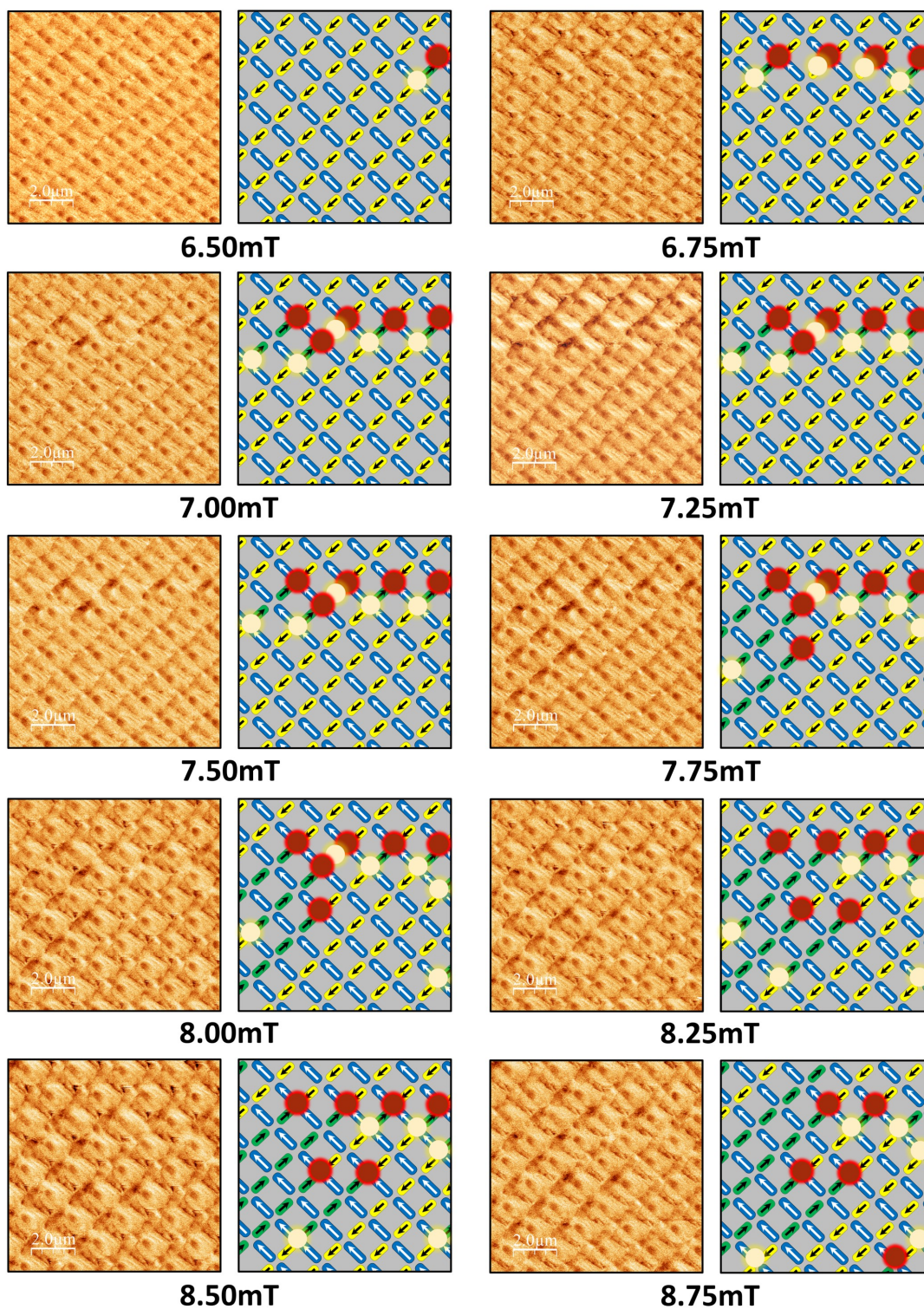


Figure 6.7: Unmasked MFM data from fig. 4.11. All scale bars are 2 μm .

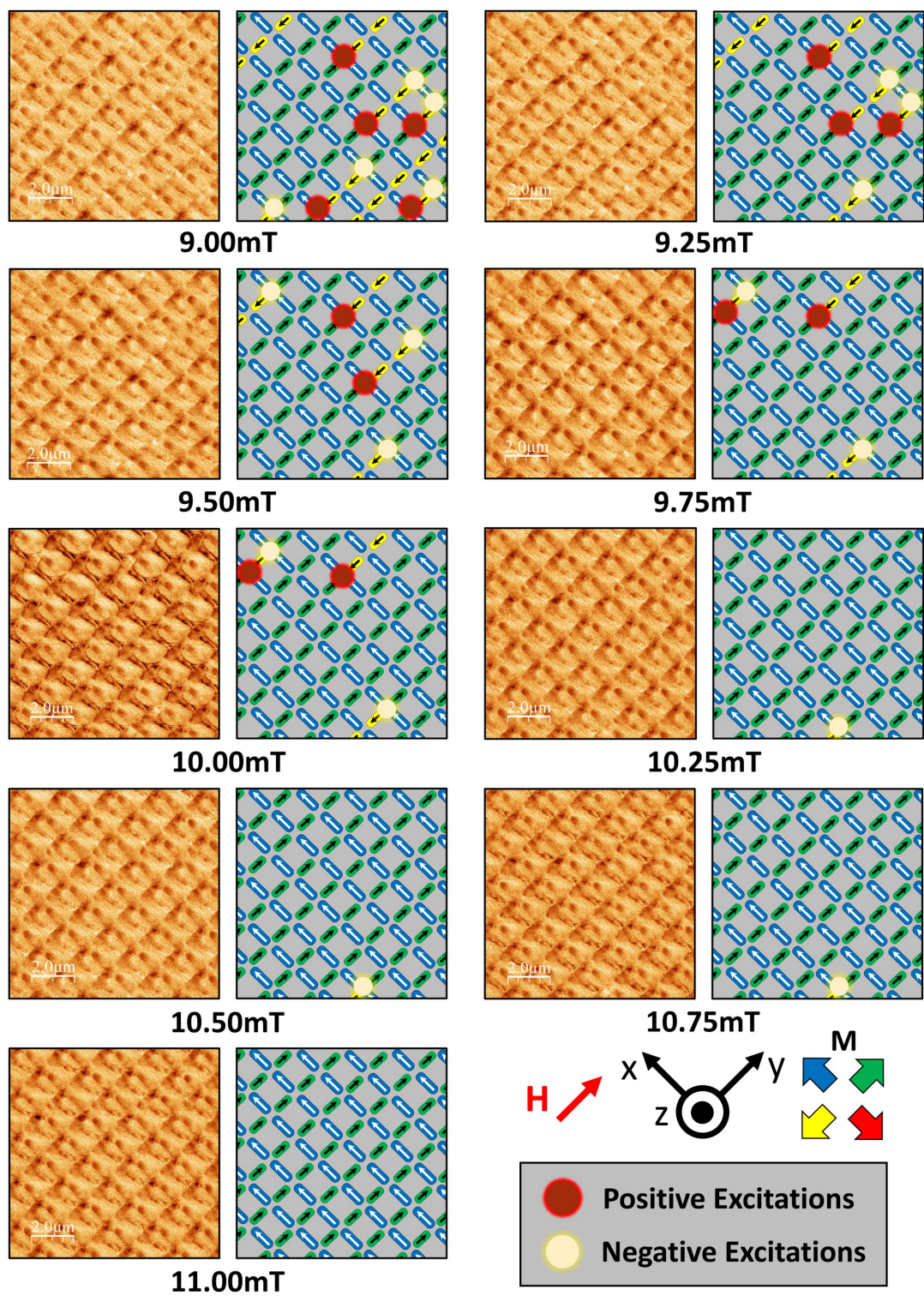


Figure 6.7: Continued.

6.2 DIPOLAR FRAMEWORK CALCULATIONS

i	j	m_i	m_j	r_{ij}	$u_{ij}(D)$
1	2	(1, 1, -1)	(-1, 1, 1)	(-1, 0, 1)	0.59
1	3	(1, 1, -1)	(1, 1, 1)	(-1, -1, 0)	-0.59
1	4	(1, 1, -1)	(-1, 1, -1)	(0, -1, 1)	-0.59
1	5	(1, 1, -1)	(1, 1, 1)	(1, -1, 2)	0.07
1	6	(1, 1, -1)	(-1, 1, 1)	(1, -2, 1)	-0.07
1	7	(1, 1, -1)	(1, 1, -1)	(0, -2, 2)	-0.04
2	3	(-1, 1, 1)	(1, 1, 1)	(0, -1, -1)	-0.59
2	4	(-1, 1, 1)	(-1, 1, -1)	(-1, 1, 0)	-0.59
2	5	(-1, 1, 1)	(1, 1, 1)	(2, -1, 1)	0.07
2	6	(-1, 1, 1)	(-1, 1, 1)	(2, -2, 0)	-0.04
2	7	(-1, 1, 1)	(1, 1, -1)	(1, -2, 1)	-0.07
3	4	(1, 1, 1)	(-1, 1, -1)	(1, 0, 1)	0.59
3	5	(1, 1, 1)	(1, 1, 1)	(2, 0, 2)	-0.04
3	6	(1, 1, 1)	(-1, 1, 1)	(2, -1, 1)	0.07
3	7	(1, 1, 1)	(1, 1, -1)	(1, -1, 2)	0.07
4	5	(-1, 1, -1)	(1, 1, 1)	(1, 0, 1)	0.59
4	6	(-1, 1, -1)	(-1, 1, 1)	(1, -1, 0)	-0.59
4	7	(-1, 1, -1)	(1, 1, -1)	(0, -1, 1)	-0.59
5	6	(1, 1, 1)	(-1, 1, 1)	(0, -1, -1)	-0.59
5	7	(1, 1, 1)	(1, 1, -1)	(-1, -1, 0)	-0.59
6	7	(-1, 1, 1)	(1, 1, -1)	(-1, 0, 1)	0.59

Table 6.1: The pairwise spin-spin interactions within two adjoining, type 2, four-wire junctions. Specifically, these are the interactions present in the pre-nucleation, sub-surface state (displayed in fig. 4.29a). u_{ij} is expressed as a function of D , which is defined in eq. (4.8).

6.3 MONTE-CARLO SIMULATIONS

Simulated field reversals of the L1 and L2 sub-lattices were performed with varying surface energetics factor ($\alpha_{ij} = 1, 3.23$ and 6.45) and disorder ($\sigma = 10\%$, 20% , 30% , and 40%). Two datasets were shown in chapter 4, these are the L1 and L2 reversals with $\alpha_{ij} = 6.45$ and $\sigma = 30\%$. All other datasets are given here, the coordinate system and colour scale are consistent across all Monte-Carlo simulations. Ten field steps were performed in each simulation, though only one image of each saturation state is included here.

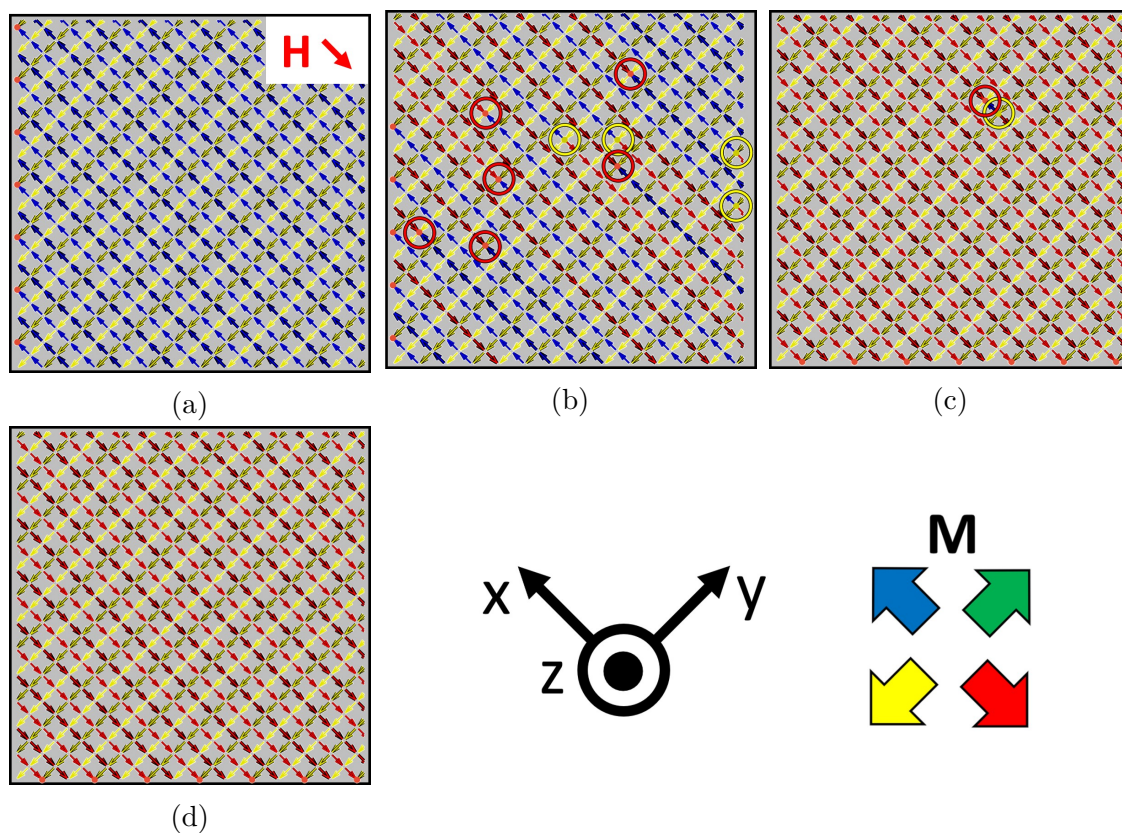


Figure 6.8: Monte-Carlo L1 reversal where $\alpha_{ij} = 1$ and $\sigma = 10\%$. Positive and negative excitations are indicated with red and yellow rings respectively. **a-d**, Applied field values are 2.72 mT, 2.93 mT, 3.14 mT, and 3.35 mT respectively.

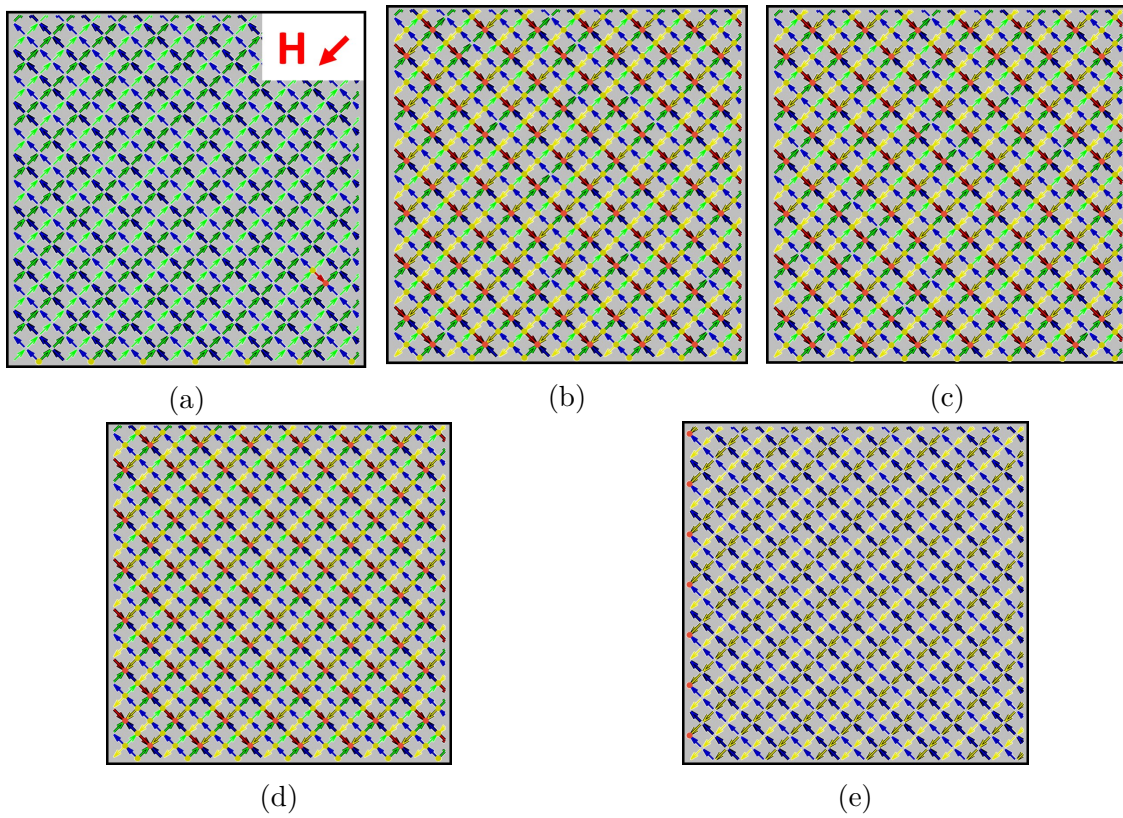


Figure 6.9: Monte-Carlo L2 reversal where $\alpha_{ij} = 1$ and $\sigma = 10\%$. **a-e**, Applied field values are 2.51 mT, 2.72 mT, 2.93 mT, 3.14 mT, and 3.35 mT respectively.

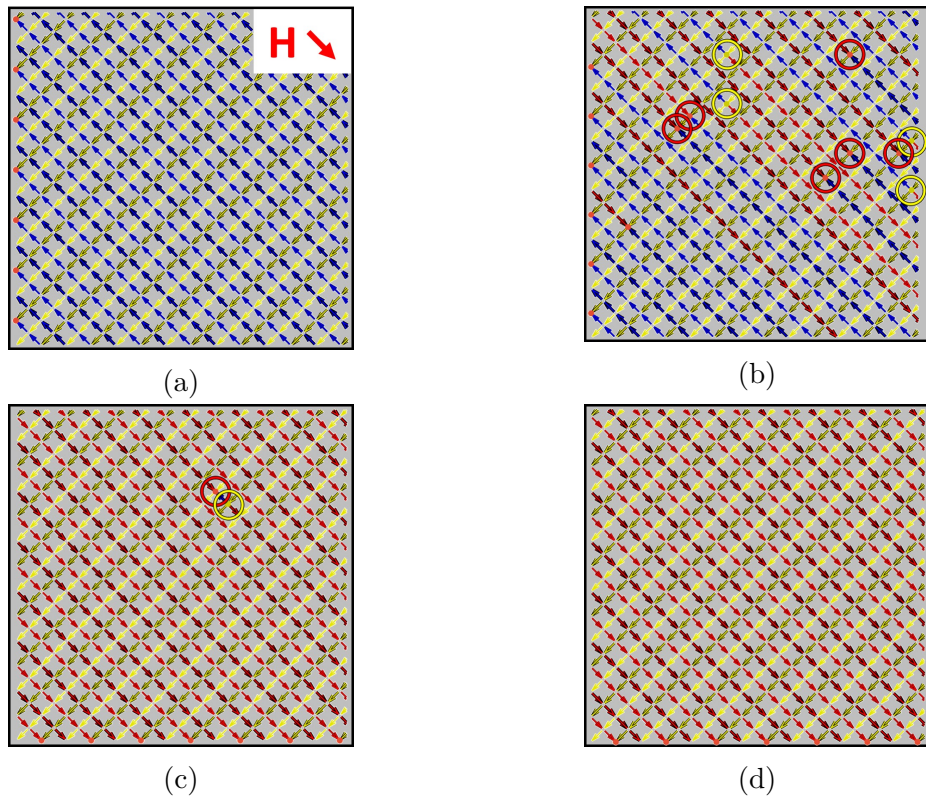


Figure 6.10: Monte-Carlo L1 reversal where $\alpha_{ij} = 1$ and $\sigma = 20\%$. Positive and negative excitations are indicated with red and yellow rings respectively. **a-d**, Applied field values are 2.72 mT, 2.93 mT, 3.14 mT, and 3.35 mT respectively.

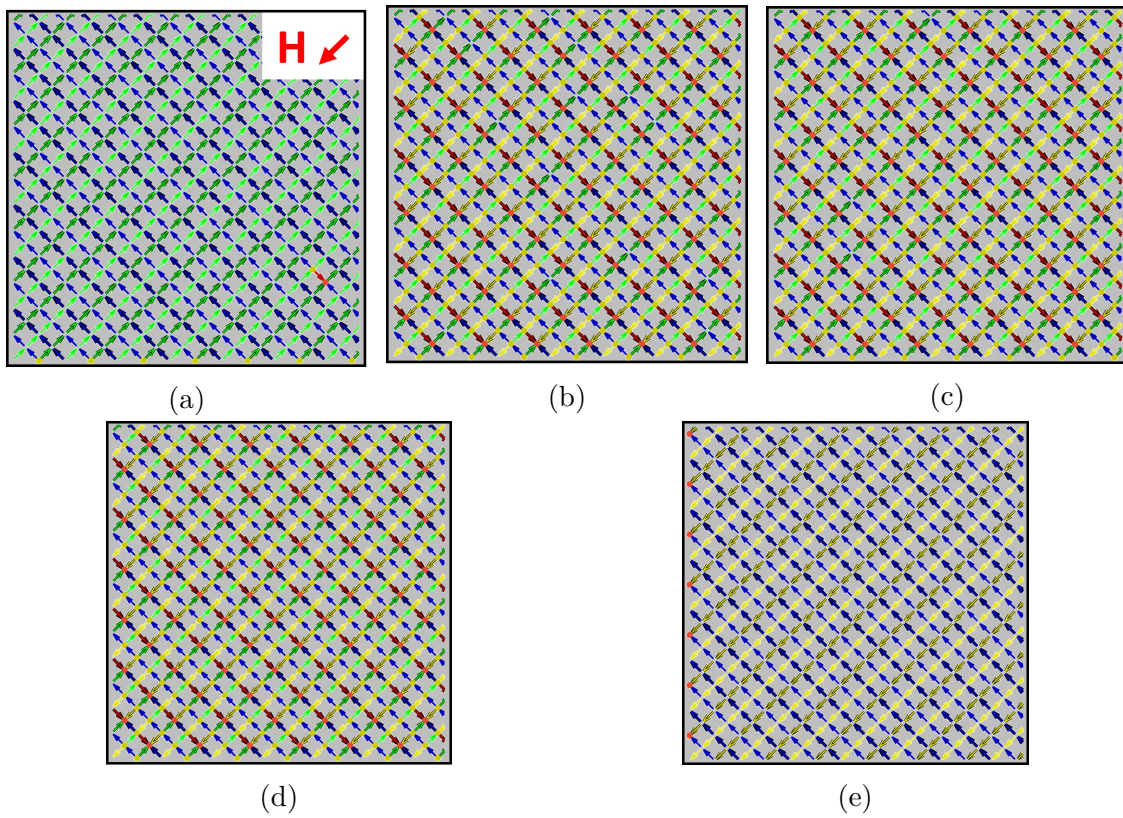


Figure 6.11: Monte-Carlo L2 reversal where $\alpha_{ij} = 1$ and $\sigma = 20\%$. **a-e**, Applied field values are 2.51 mT, 2.72 mT, 2.93 mT, 3.14 mT, and 3.35 mT respectively.

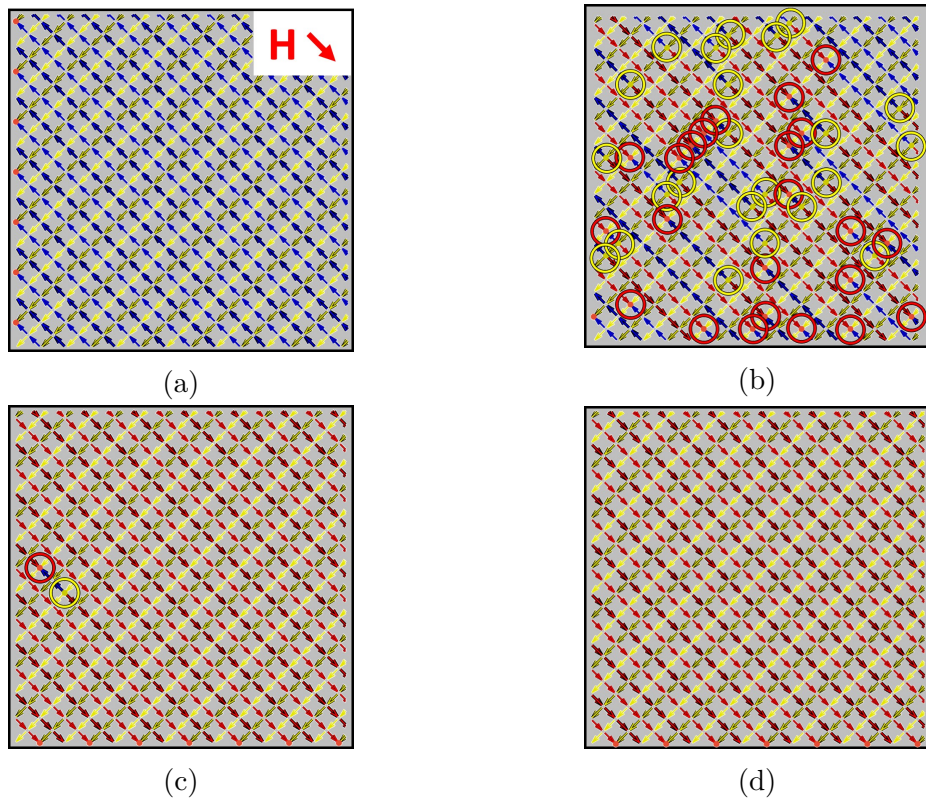


Figure 6.12: Monte-Carlo L1 reversal where $\alpha_{ij} = 1$ and $\sigma = 30\%$. Positive and negative excitations are indicated with red and yellow rings respectively. **a-d**, Applied field values are 2.93 mT, 3.14 mT, 3.35 mT, and 3.56 mT respectively.

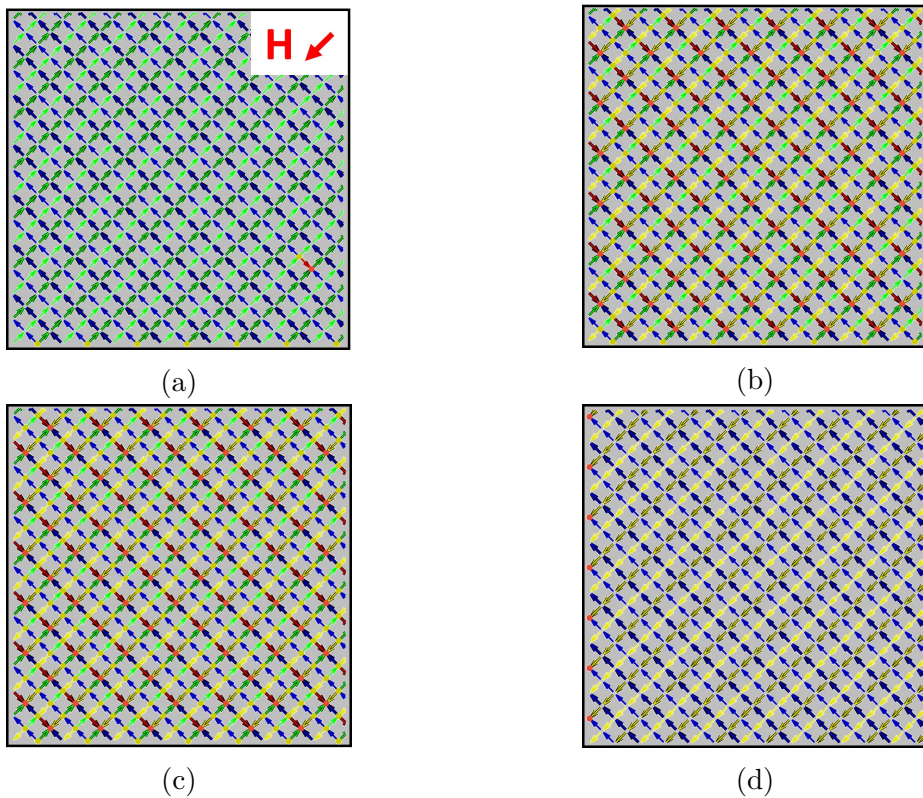


Figure 6.13: Monte-Carlo L2 reversal where $\alpha_{ij} = 1$ and $\sigma = 30\%$. **a-d**, Applied field values are 2.72 mT, 2.93 mT, 3.14 mT, and 3.35 mT respectively.

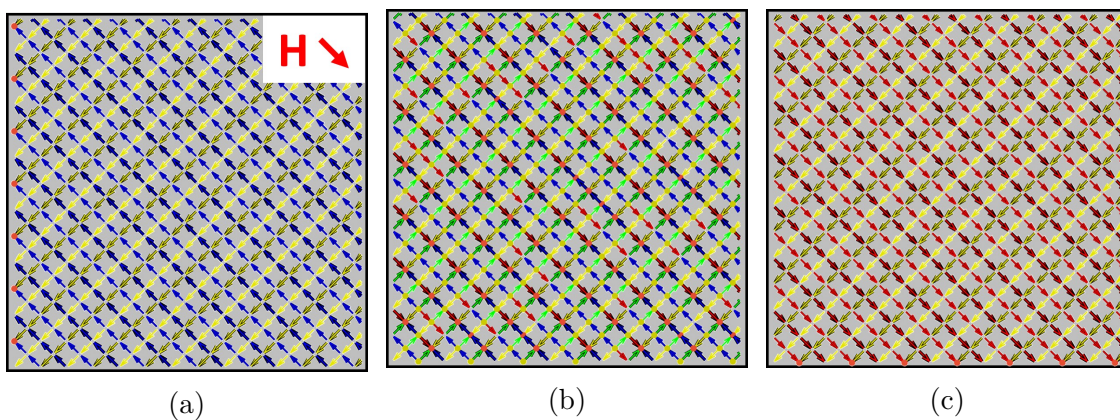


Figure 6.14: Monte-Carlo L1 reversal where $\alpha_{ij} = 1$ and $\sigma = 40\%$. **a-c**, Applied field values are 2.93 mT, 3.14 mT, and 3.35 mT respectively.

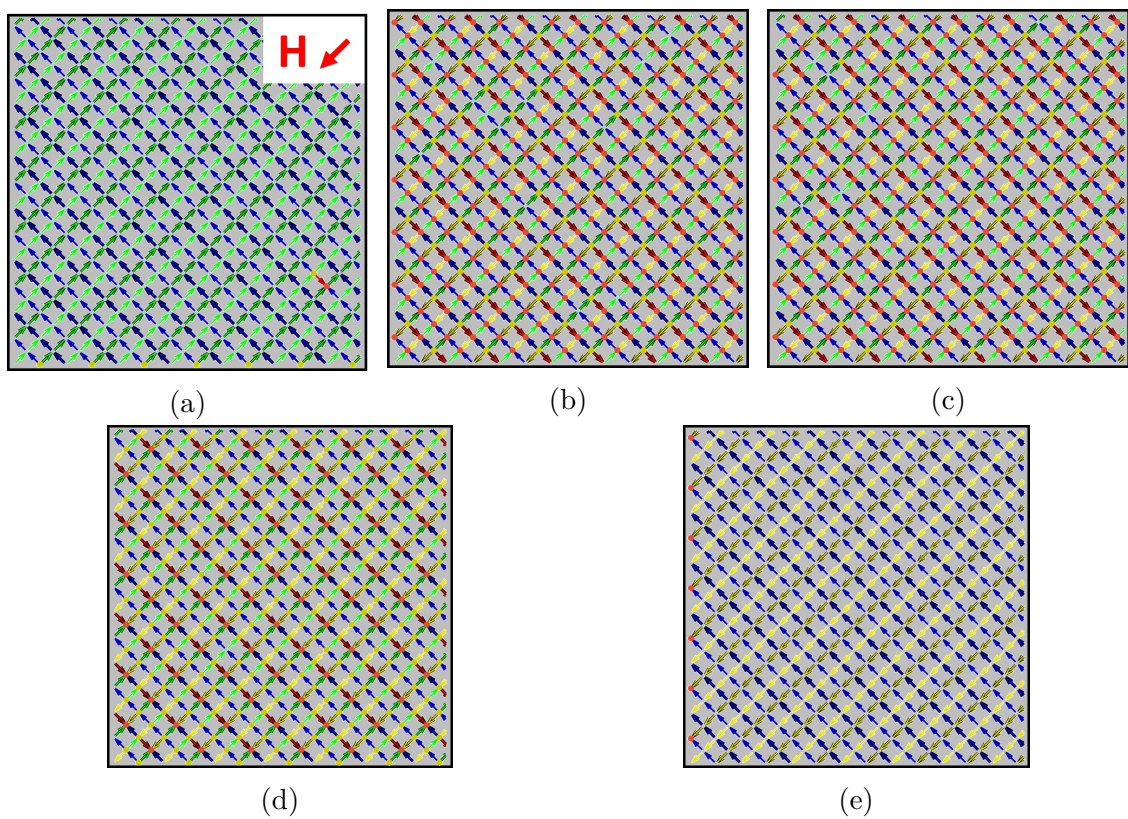


Figure 6.15: Monte-Carlo L2 reversal where $\alpha_{ij} = 1$ and $\sigma = 40\%$. **a-e**, Applied field values are 2.51 mT, 2.72 mT, 2.93 mT, 3.14 mT, and 3.35 mT respectively.

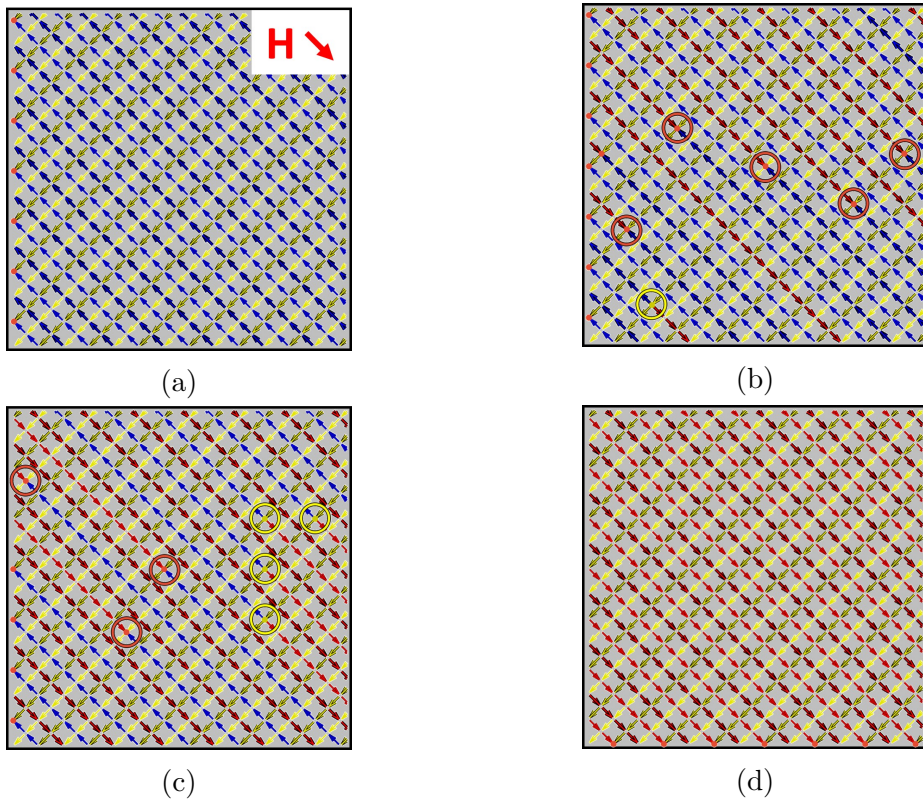


Figure 6.16: Monte-Carlo L1 reversal where $\alpha_{ij} = 3.23$ and $\sigma = 10\%$. Positive and negative excitations are indicated with red and yellow rings respectively. **a-d**, Applied field values are 2.72 mT, 2.93 mT, 3.14 mT, and 3.35 mT respectively.

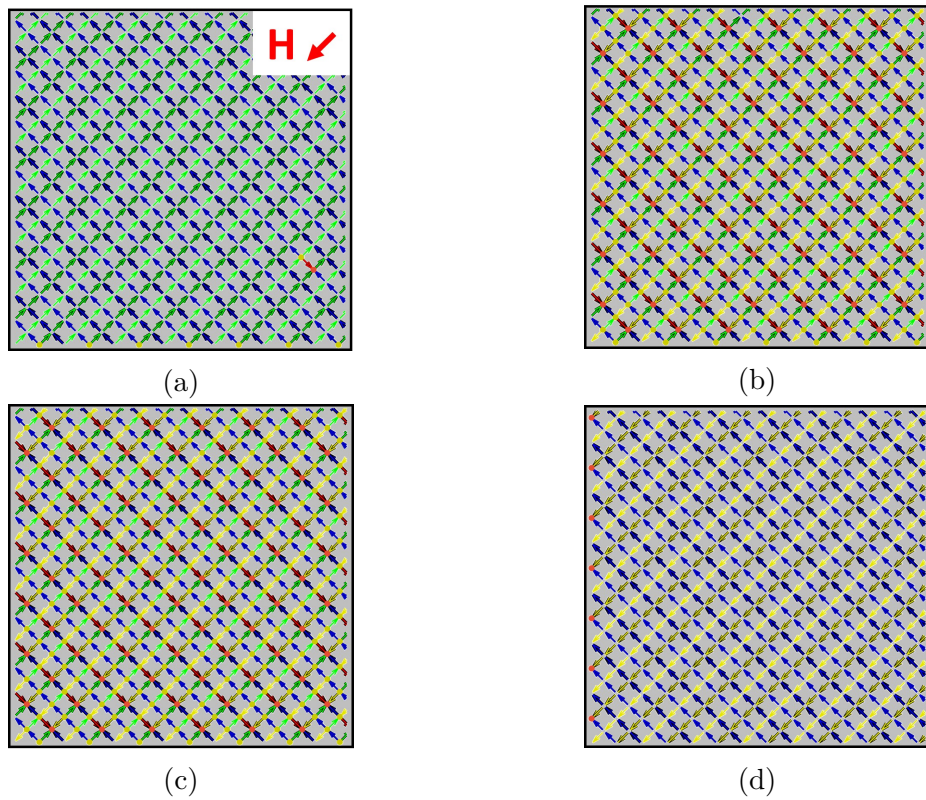


Figure 6.17: Monte-Carlo L2 reversal where $\alpha_{ij} = 3.23$ and $\sigma = 10\%$. **a-d**, Applied field values are 2.72 mT, 2.93 mT, 3.14 mT, and 3.35 mT respectively.

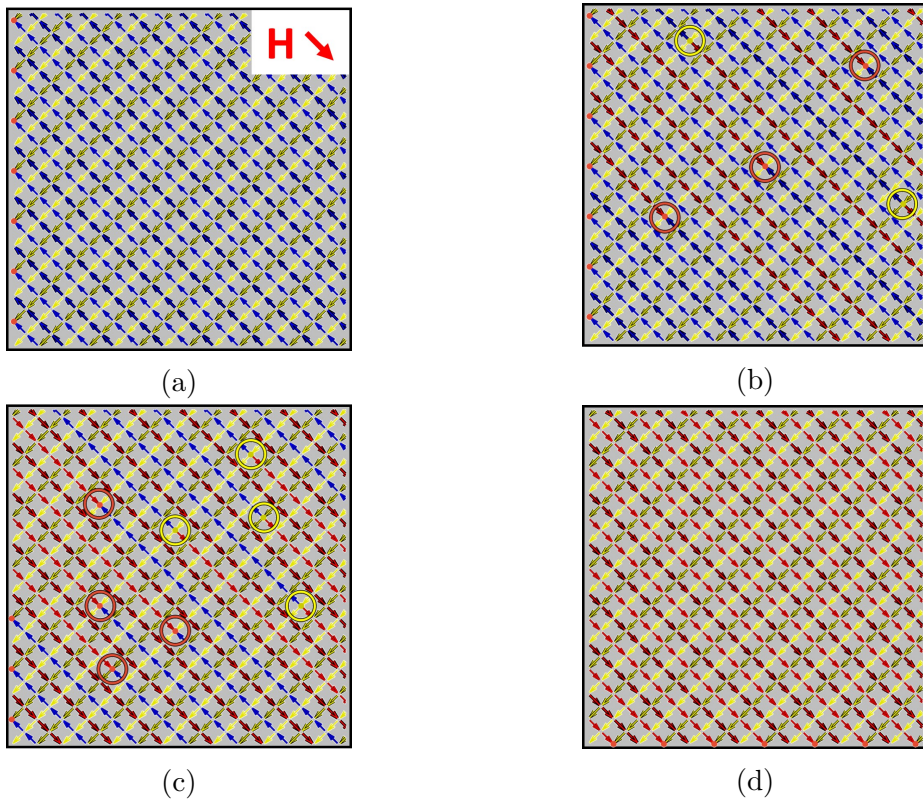


Figure 6.18: Monte-Carlo L1 reversal where $\alpha_{ij} = 3.23$ and $\sigma = 20\%$. Positive and negative excitations are indicated with red and yellow rings respectively. **a-d**, Applied field values are 2.72 mT, 2.93 mT, 3.14 mT, and 3.35 mT respectively.

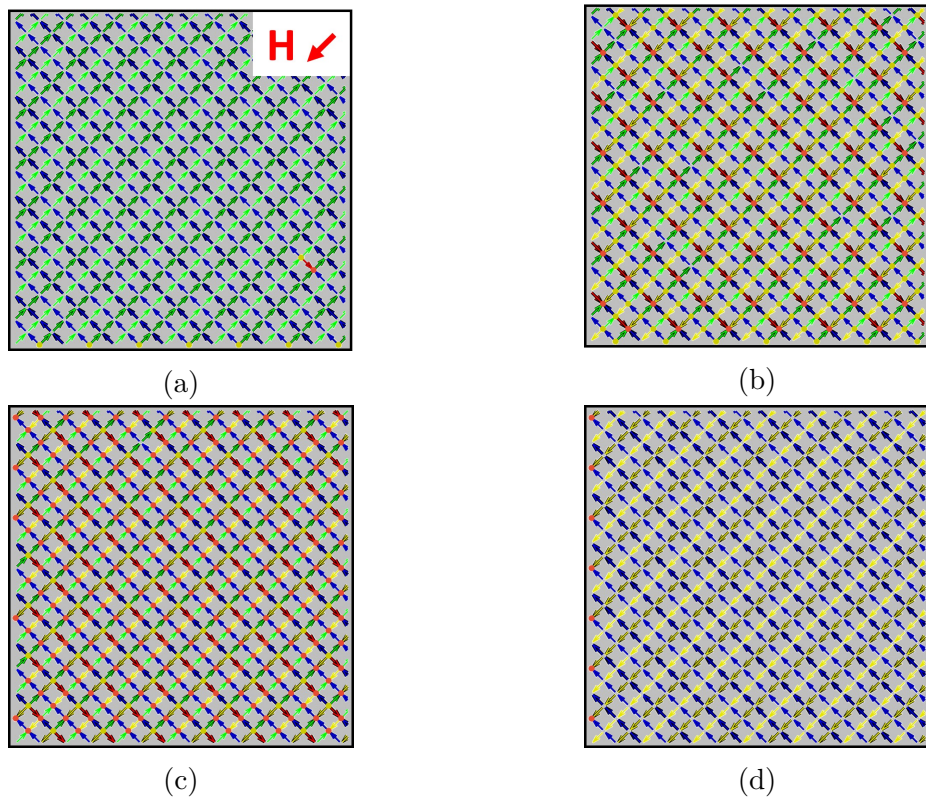


Figure 6.19: Monte-Carlo L2 reversal where $\alpha_{ij} = 3.23$ and $\sigma = 20\%$. **a-d**, Applied field values are 2.51 mT, 2.72 mT, 2.93 mT, and 3.14 mT respectively.

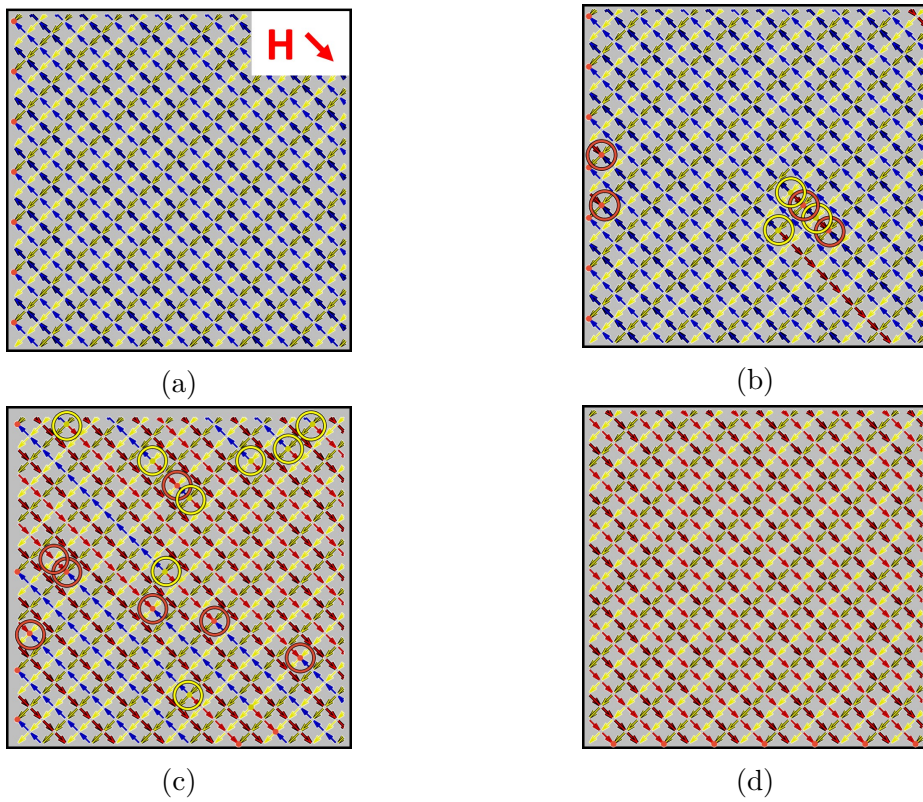


Figure 6.20: Monte-Carlo L1 reversal where $\alpha_{ij} = 3.23$ and $\sigma = 30\%$. Positive and negative excitations are indicated with red and yellow rings respectively. **a-d**, Applied field values are 2.72 mT, 2.93 mT, 3.14 mT, and 3.35 mT respectively.

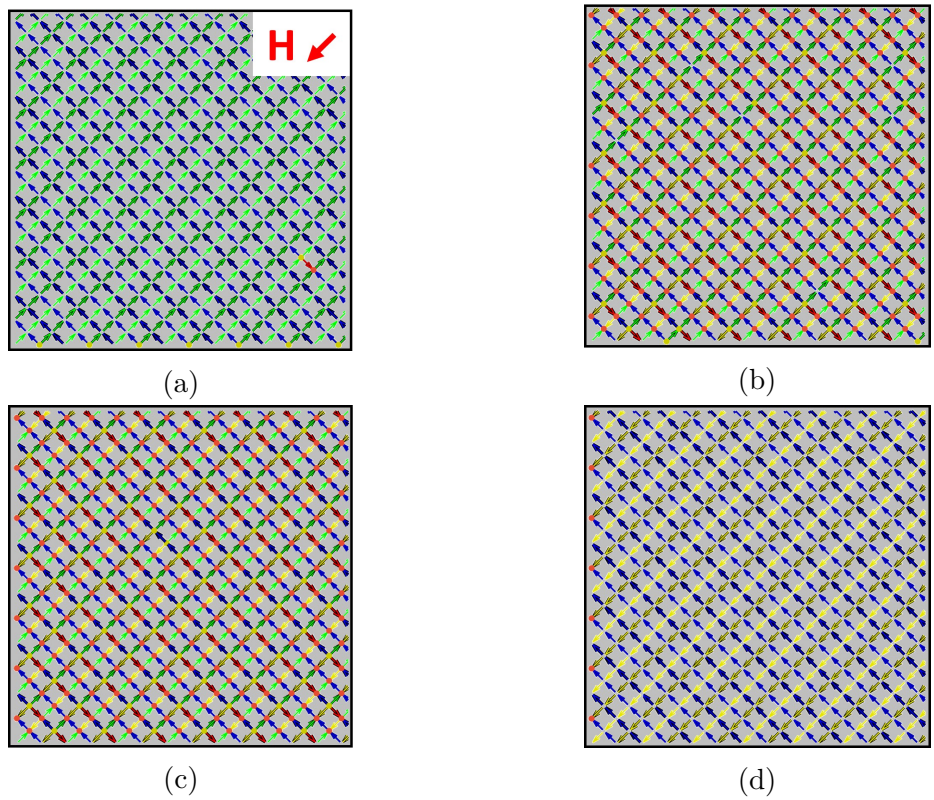


Figure 6.21: Monte-Carlo L2 reversal where $\alpha_{ij} = 3.23$ and $\sigma = 30\%$. **a-d**, Applied field values are 2.72 mT, 2.93 mT, 3.14 mT, and 3.35 mT respectively.

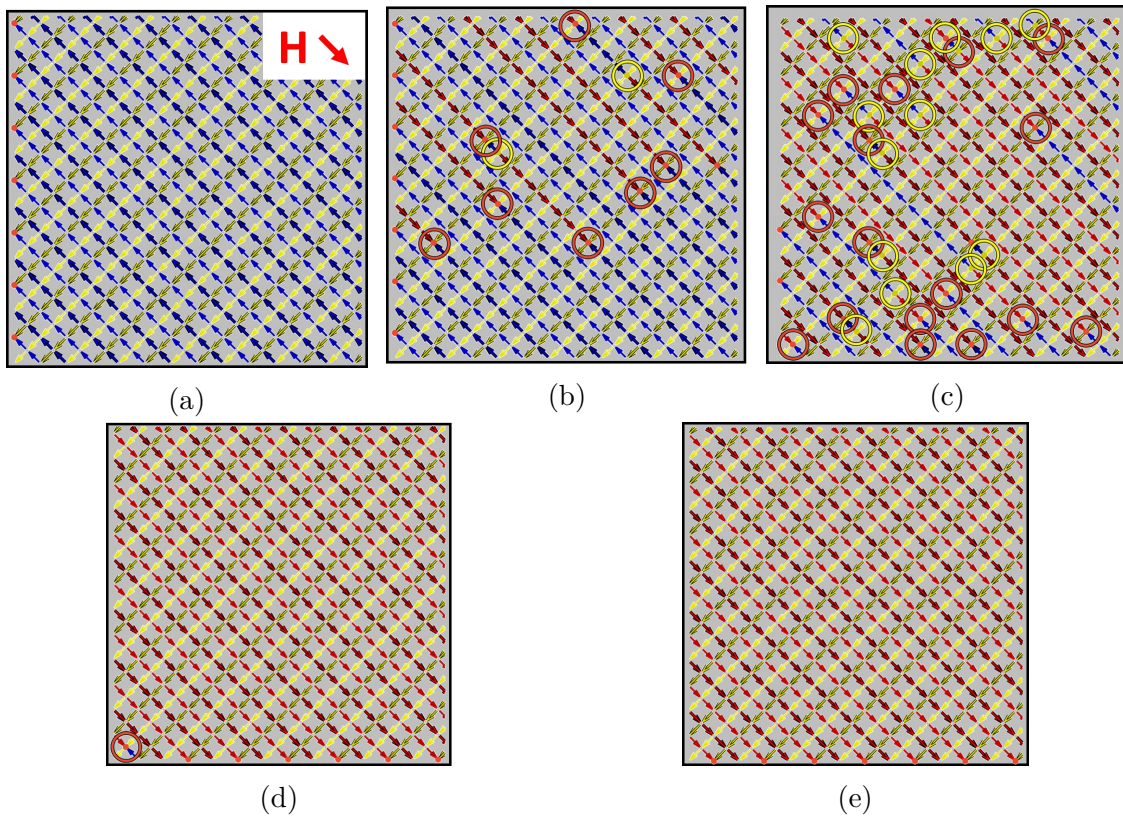


Figure 6.22: Monte-Carlo L1 reversal where $\alpha_{ij} = 3.23$ and $\sigma = 40\%$. Positive and negative excitations are indicated with red and yellow rings respectively. **a-e**, Applied field values are 2.72 mT, 2.93 mT, 3.14 mT, 3.35 mT, and 3.56 mT respectively.

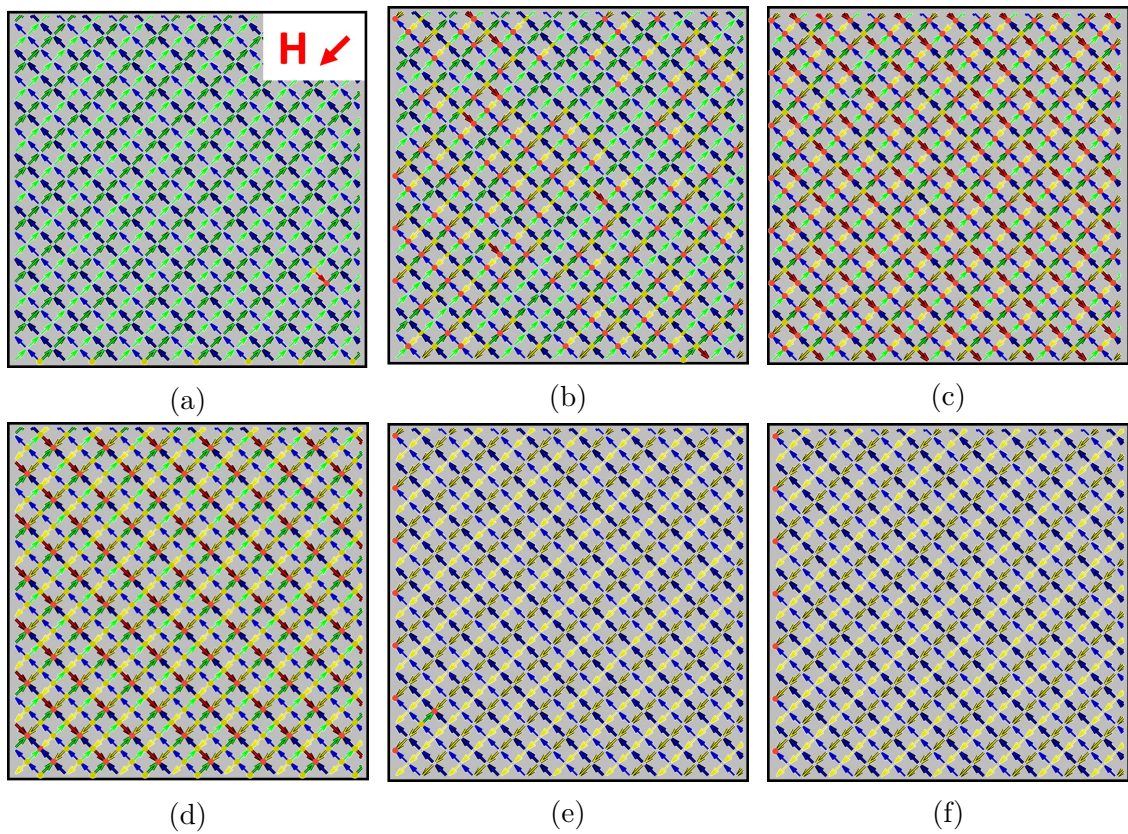


Figure 6.23: Monte-Carlo L2 reversal where $\alpha_{ij} = 3.23$ and $\sigma = 40\%$. **a-f**, Applied field values are 2.51 mT, 2.72 mT, 2.93 mT, 3.14 mT, 3.35 mT, and 3.56 mT respectively.

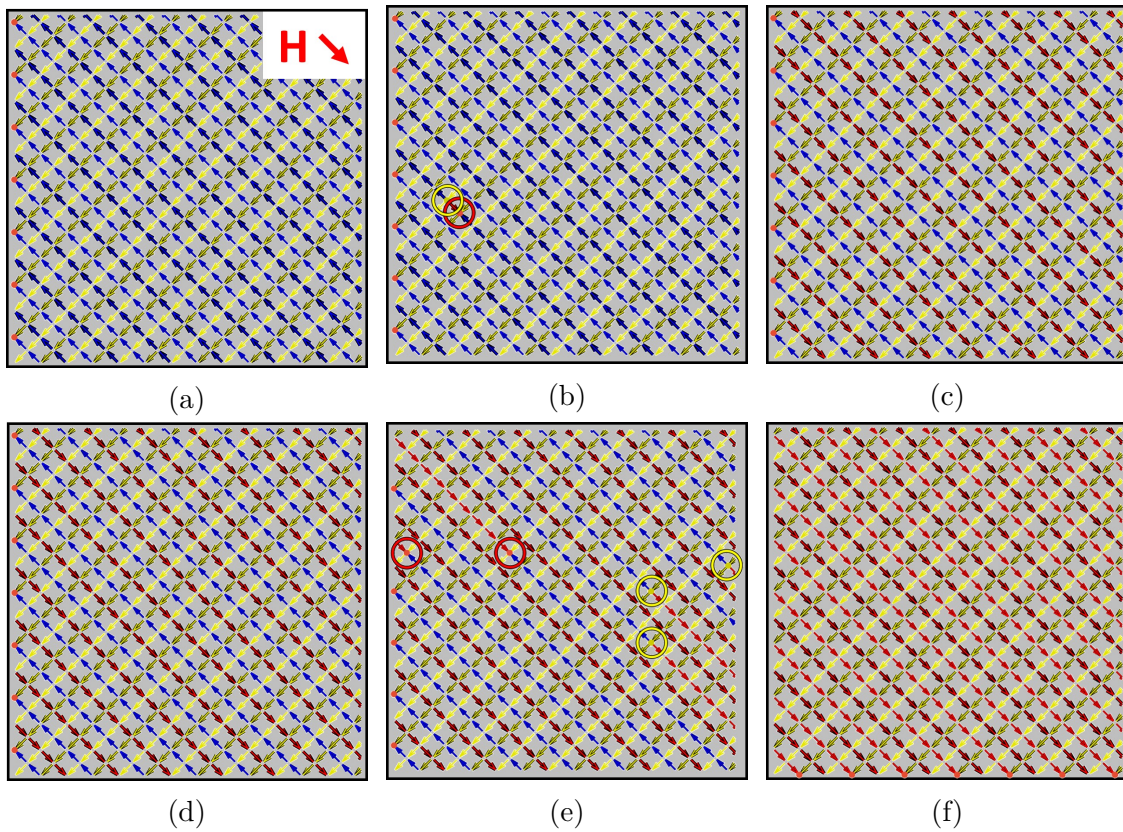


Figure 6.24: Monte-Carlo L1 reversal where $\alpha_{ij} = 6.45$ and $\sigma = 10\%$. Positive and negative excitations are indicated with red and yellow rings respectively. **a-f**, Applied field values are 2.30 mT, 2.51 mT, 2.72 mT, 2.93 mT, 3.14 mT, and 3.35 mT respectively.

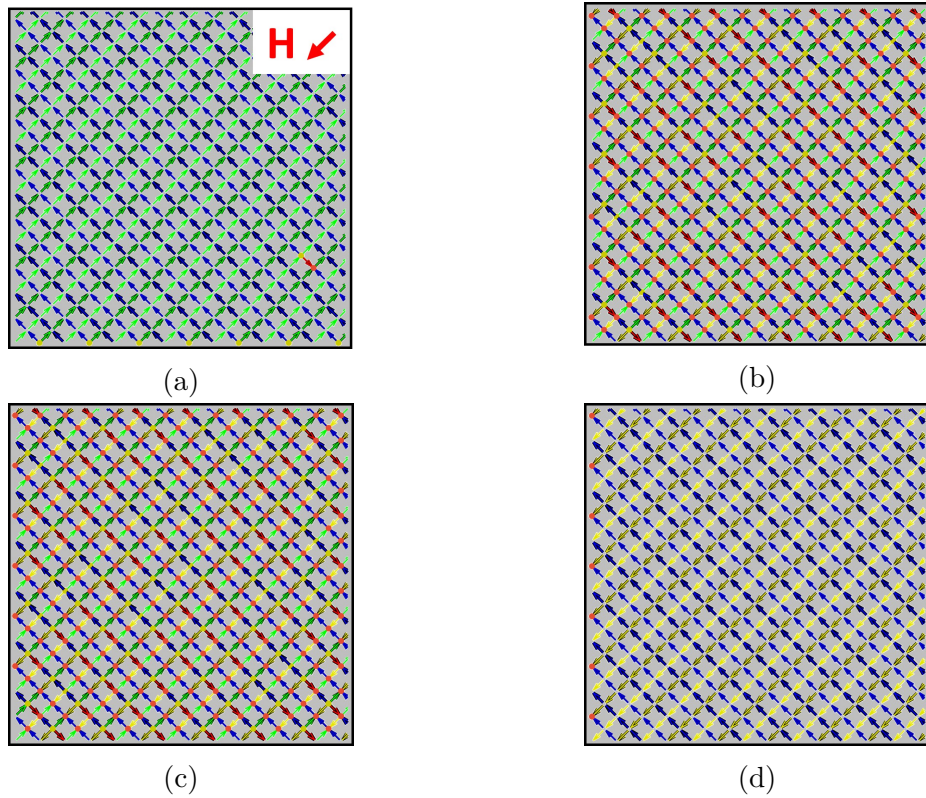


Figure 6.25: Monte-Carlo L2 reversal where $\alpha_{ij} = 6.45$ and $\sigma = 10\%$. **a-d**, Applied field values are 2.72 mT, 2.93 mT, 3.14 mT, and 3.35 mT respectively.

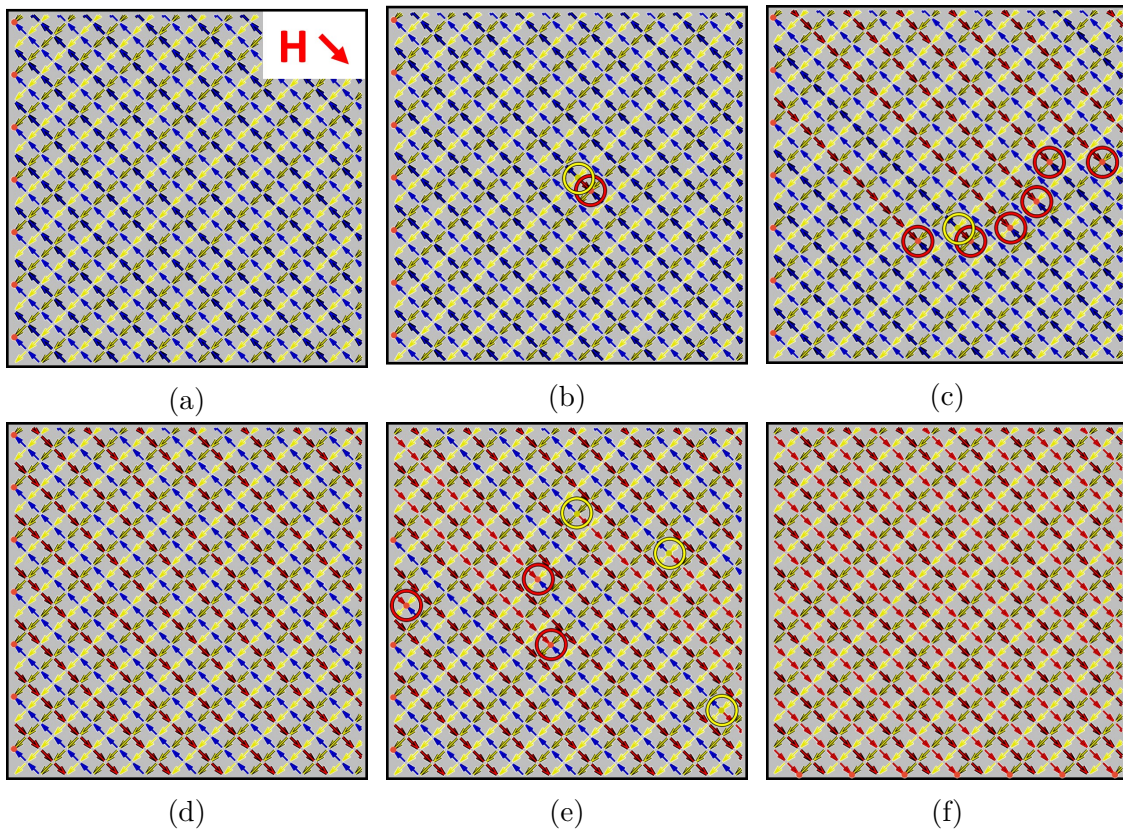


Figure 6.26: Monte-Carlo L1 reversal where $\alpha_{ij} = 6.45$ and $\sigma = 20\%$. Positive and negative excitations are indicated with red and yellow rings respectively. **a-f**, Applied field values are 2.30 mT, 2.51 mT, 2.72 mT, 2.93 mT, 3.14 mT, and 3.35 mT respectively.

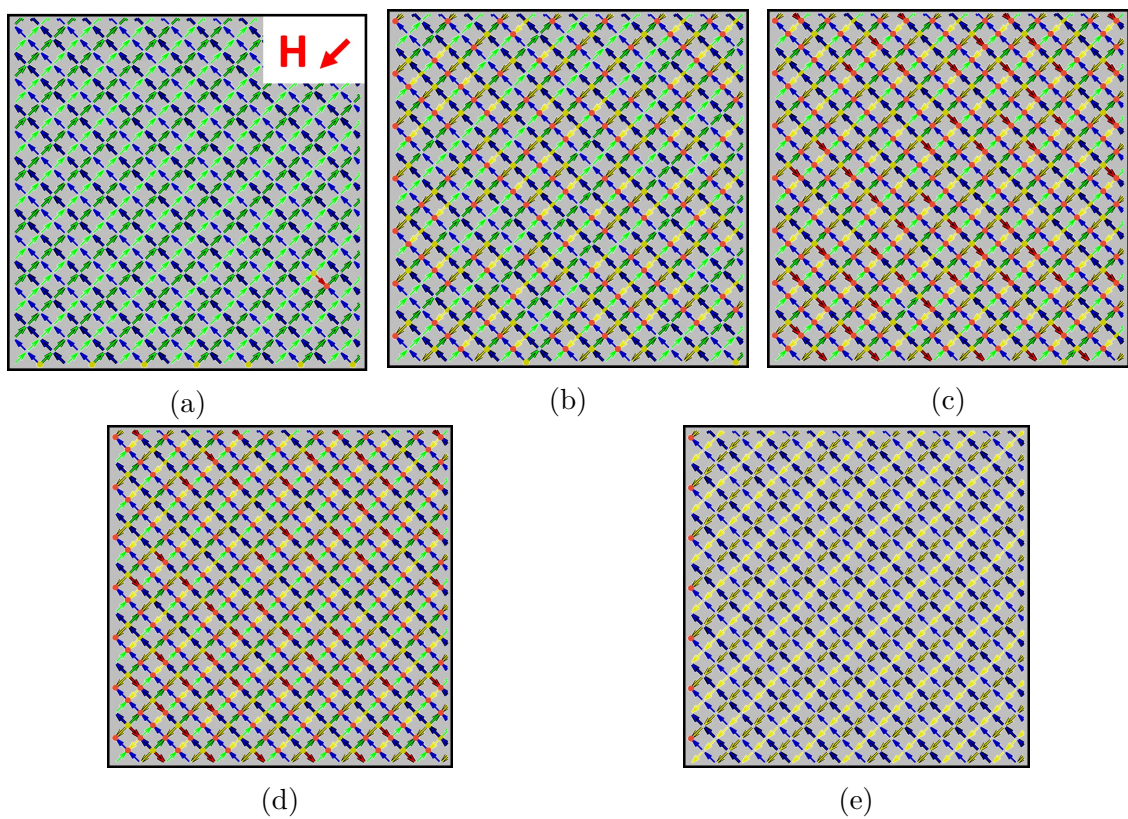


Figure 6.27: Monte-Carlo L2 reversal where $\alpha_{ij} = 6.45$ and $\sigma = 20\%$. **a-e**, Applied field values are 2.51 mT, 2.72 mT, 2.93 mT, 3.14 mT, 3.35 mT respectively.

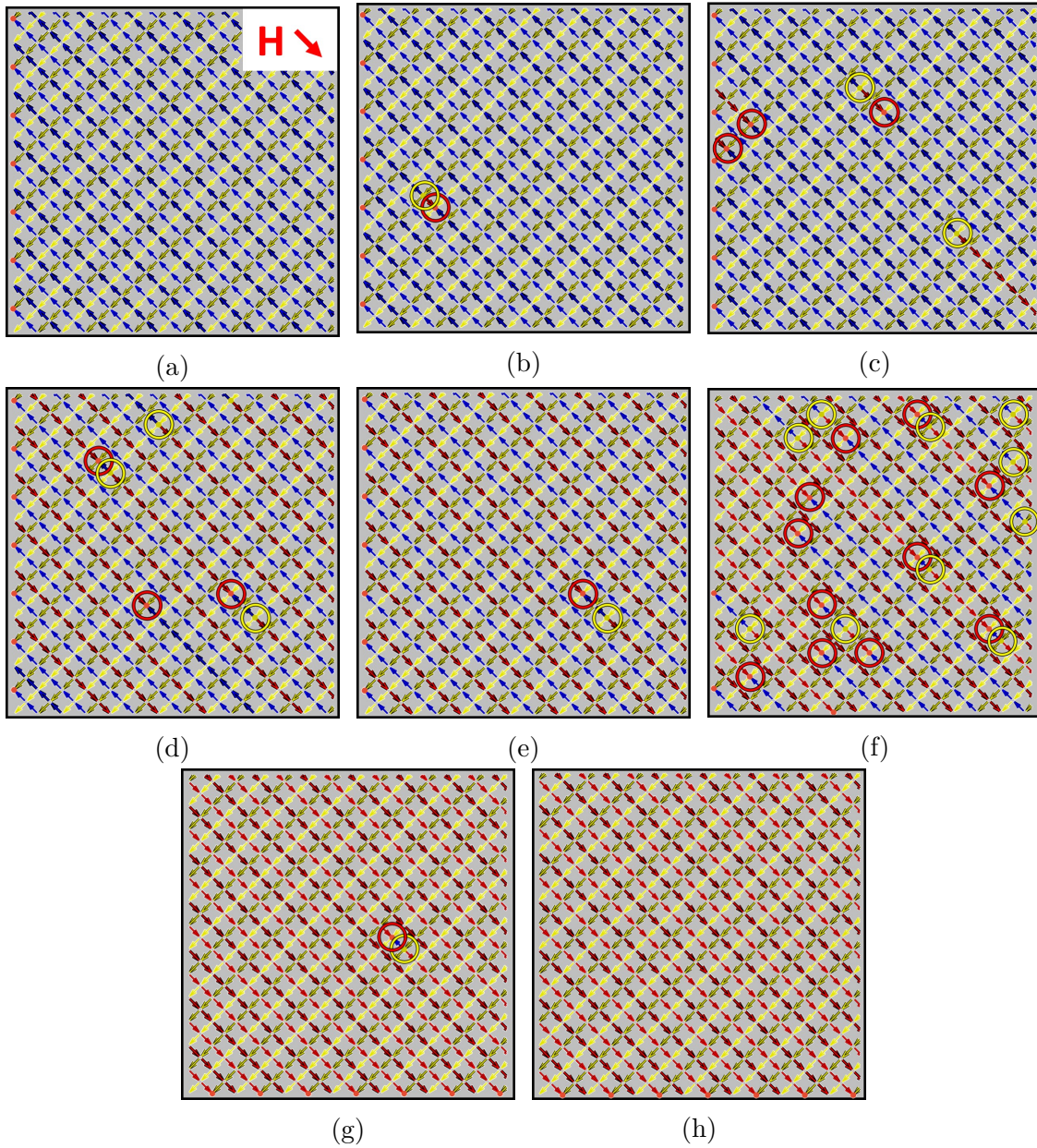


Figure 6.28: Monte-Carlo L1 reversal where $\alpha_{ij} = 6.45$ and $\sigma = 40\%$. Positive and negative excitations are indicated with red and yellow rings respectively. **a-h**, Applied field values are 2.09 mT, 2.30 mT, 2.51 mT, 2.72 mT, 2.93 mT, 3.14 mT, 3.35 mT, and 3.56 mT respectively.

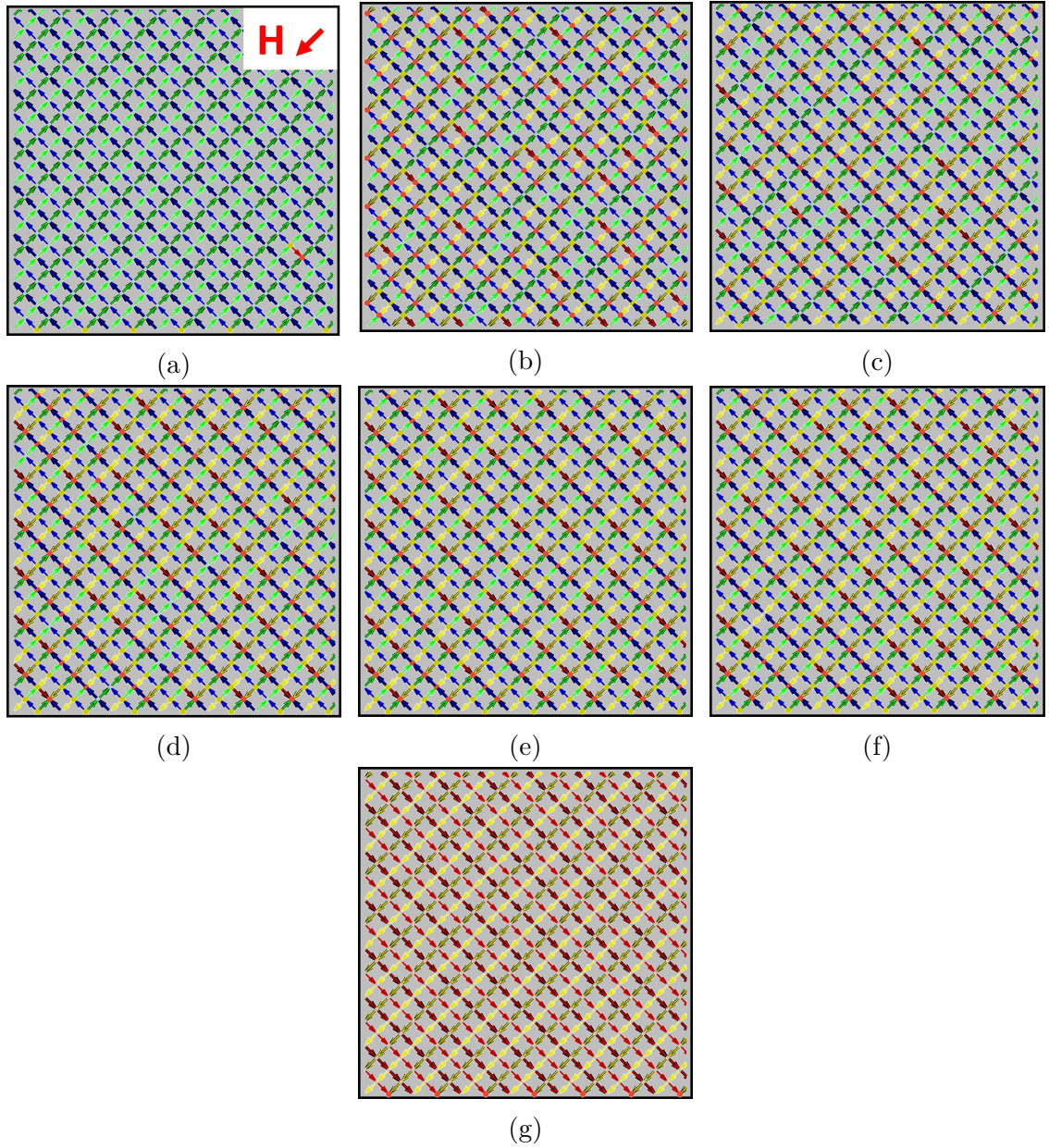


Figure 6.29: Monte-Carlo L2 reversal where $\alpha_{ij} = 6.45$ and $\sigma = 40\%$. **a-g**, Applied field values are 2.30 mT, 2.51 mT, 2.72 mT, 2.93 mT, 3.14 mT, 3.35 mT, and 3.56 mT respectively.

Chapter 6

Bibliography

- [1] K. M. Krishnan. *Fundamentals and Applications of Magnetic Materials*. Oxford University Press, 2016.
- [2] B. Canals, I. A. Chioar, V. D. Nguyen, M. Hehn, D. Lacour, F. Montaigne, A. Locatelli, T. O. Montes, B. S. Burgos, and N. Rougemaille. Fragmentation of magnetism in artificial kagome dipolar spin ice. *Nature Communications*, 7(1):1–6, 2016. ISSN 20411723. doi: 10.1038/ncomms11446.
- [3] I. A. Chioar, N. Rougemaille, and B. Canals. Ground-state candidate for the classical dipolar kagome Ising antiferromagnet. *Physical Review B*, 93(21):214410, 2016. ISSN 24699969. doi: 10.1103/PhysRevB.93.214410.
- [4] P. C. Guruciaga, S. A. Grigera, and R. A. Borzi. Monopole ordered phases in dipolar and nearest-neighbors Ising pyrochlore: From spin ice to the all-in-all-out antiferromagnet. *Physical Review B - Condensed Matter and Materials Physics*, 90(18):184423, 2014. ISSN 1550235X. doi: 10.1103/PhysRevB.90.184423.
- [5] R. C. O’Handley. *Modern Magnetic Materials*. John Wiley and Sons, 2000.
- [6] J. Winterlik, S. Chadov, A. Gupta, V. Alijani, T. Gasi, K. Filsinger, B. Balke, G. H. Fecher, C. A. Jenkins, F. Casper, J. Kübler, G. D. Liu, L. Gao, S. S. P. Parkin, and C. Felser. Design scheme of new tetragonal heusler compounds for spin-transfer torque applications and its experimental realization. *Advanced Materials*, 24(47):6283–6287, 2012. ISSN 09359648. doi: 10.1002/adma.201201879.
- [7] C. L. Dennis, R. P. Borges, L. D. Buda, U. Ebels, J. F. Gregg, M. Hehn, E. Jouguelet, K. Ounadjela, I. Petej, I. L. Prejbeanu, and M. J. Thornton. The defining length scales of mesomagnetism: A review. *Journal*

- of *Physics Condensed Matter*, 14(49):R1175, 2002. ISSN 09538984. doi: 10.1088/0953-8984/14/49/201.
- [8] R. Hertel. Ultrafast domain wall dynamics in magnetic nanotubes and nanowires. *Journal of Physics Condensed Matter*, 28(48):483002, 2016. ISSN 1361648X. doi: 10.1088/0953-8984/28/48/483002.
- [9] Y. Nakatani, A. Thiaville, and J. Miltat. Head-to-head domain walls in soft nano-strips: A refined phase diagram. *Journal of Magnetism and Magnetic Materials*, 290:750–753, 2005. ISSN 03048853. doi: 10.1016/j.jmmm.2004.11.355.
- [10] R. Allenspach. Magnetic domain walls in nanowires. In *2007 International Conference on Electromagnetics in Advanced Applications, ICEAA '07*, volume 31, pages 603–604, 2007. ISBN 1424407672. doi: 10.1109/ICEAA.2007.4387373.
- [11] S. Da Col, S. Jamet, N. Rougemaille, A. Locatelli, T. O. Mendes, B. S. Burgos, R. Afid, M. Darques, L. Cagnon, J. C. Toussaint, and O. Fruchart. Observation of Bloch-point domain walls in cylindrical magnetic nanowires. *Physical Review B - Condensed Matter and Materials Physics*, 89(18):180405, 2014. ISSN 1550235X. doi: 10.1103/PhysRevB.89.180405.
- [12] A. Fernández-Pacheco, R. Streubel, O. Fruchart, R. Hertel, P. Fischer, and R. P. Cowburn. Three-dimensional nanomagnetism. *Nature Communications*, 8(1):1–14, 2017. doi: 10.1038/ncomms15756.
- [13] A. De Riz, J. Hurst, M. Schöbitz, C. Thirion, J. Bachmann, J. C. Toussaint, O. Fruchart, and D. Gusakova. Mechanism of fast domain wall motion via current-assisted Bloch-point domain wall stabilization. *Physical Review B*, 103(5):054430, 2021. ISSN 24699969. doi: 10.1103/PhysRevB.103.054430.
- [14] S. S. P. Parkin, M. Hayashi, and L. Thomas. Magnetic domain-wall racetrack memory. *Science*, 320(5873):190–194, 2008. ISSN 00368075. doi: 10.1126/science.1145799.
- [15] D. A. Allwood, G. Xiong, C. C. Faulkner, D. Atkinson, D. Petit, and R. P. Cowburn. Magnetic domain-wall logic. *Science*, 309(5741):1688–1692, 2005. ISSN 00368075. doi: 10.1126/science.1108813.
- [16] D. Atkinson, D. A. Allwood, G. Xiong, M. D. Cooke, C. C. Faulkner, and R. P. Cowburn. Magnetic domain-wall dynamics in a submicrometre ferromagnetic

- structure. *Nature Materials*, 2(2):85–87, 2003. ISSN 14761122. doi: 10.1038/nmat803.
- [17] C. C. Faulkner, M. D. Cooke, D. A. Allwood, D. Petit, D. Atkinson, and R. P. Cowburn. Artificial domain wall nanotraps in Ni₈₁Fe₁₉ wires. *Journal of Applied Physics*, 95(11):6717–6719, 2004. ISSN 00218979. doi: 10.1063/1.1652391.
- [18] M. Y. Im, L. Bocklage, P. Fischer, and G. Meier. Direct observation of stochastic domain-wall depinning in magnetic nanowires. *Physical Review Letters*, 102(14):1–4, 2009. ISSN 00319007. doi: 10.1103/PhysRevLett.102.147204.
- [19] L. O’Brien, D. Petit, E. R. Lewis, R. P. Cowburn, D. E. Read, J. Sampaio, H. T. Zeng, and A. V. Jausovec. Tunable remote pinning of domain walls in magnetic nanowires. *Physical Review Letters*, 106(8):1–4, 2011. ISSN 00319007. doi: 10.1103/PhysRevLett.106.087204.
- [20] K. A. Omari and T. J. Hayward. Chirality-based vortex domain-wall logic gates. *Physical Review Applied*, 2(4):044001, 2014. ISSN 23317019. doi: 10.1103/PhysRevApplied.2.044001.
- [21] M. Al Bahri, B. Borie, T. L. Jin, R. Sbiaa, M. Kläui, and S. N. Piramanayagam. Staggered Magnetic Nanowire Devices for Effective Domain-Wall Pinning in Racetrack Memory. *Physical Review Applied*, 11(2):024023, 2019. ISSN 23317019. doi: 10.1103/PhysRevApplied.11.024023. URL <https://doi.org/10.1103/PhysRevApplied.11.024023>.
- [22] R. Streubel, P. Fischer, F. Kronast, V. P. Kravchuk, D. D. Sheka, Y. Gaididei, O. G. Schmidt, and D. Makarov. Magnetism in curved geometries. *Journal of Physics D: Applied Physics*, 49(36):363001, 2016. ISSN 13616463. doi: 10.1088/0022-3727/49/36/363001.
- [23] S. Rohart and A. Thiaville. Skyrmion confinement in ultrathin film nanostructures in the presence of Dzyaloshinskii-Moriya interaction. *Physical Review B - Condensed Matter and Materials Physics*, 88(18):184422, 2013. ISSN 10980121. doi: 10.1103/PhysRevB.88.184422.
- [24] K. V. Yershov, V. P. Kravchuk, D. D. Sheka, and Y. Gaididei. Curvature-induced domain wall pinning. *Physical Review B - Condensed Matter and Materials Physics*, 92(10):104412, 2015. ISSN 1550235X. doi: 10.1103/PhysRevB.92.104412.

- [25] L. Pauling. The Structure and Entropy of Ice and of Other Crystals with Some Randomness of Atomic Arrangement. *Journal of the American Chemical Society*, 57(12):2680–2684, 1935. ISSN 15205126. doi: 10.1021/ja01315a102.
- [26] L. A. Pustil’nik. Solar flare phenomena as phase transition caused by frustration of current percolation. *Astrophysics and Space Science*, 264(1):171–182, 1998. ISSN 0004640X. doi: 10.1007/978-94-011-4203-8_13.
- [27] D. U. Ferreira, E. A. Komives, and P. G. Wolynes. Frustration in biomolecules. *Quarterly Reviews of Biophysics*, 47(4):285–363, 2014. ISSN 14698994. doi: 10.1017/S0033583514000092.
- [28] D. J. P. Morris, D. A. Tennant, S. A. Grigera, B. Klemke, C. Castelnovo, R. Moessner, C. Czternasty, M. Meissner, K. C. Rule, J. U. Hoffmann, K. Kiefer, S. Gerischer, D. Slobinsky, and R. S. Perry. Dirac Strings and Magnetic Monopoles. *Science (New York, N.Y.)*, 326(5951):411–414, 2009. doi: 10.1126/science.1178868.
- [29] M. J. Harris, S. T. Bramwell, D. F. McMorrow, T. Zeiske, and K. W. Godfrey. Geometrical frustration in the ferromagnetic pyrochlore $\text{Ho}_2\text{Ti}_2\text{O}_7$. *Physical Review Letters*, 79(13):2554–2557, 1997. ISSN 10797114. doi: 10.1103/PhysRevLett.79.2554.
- [30] L. D. C. Jaubert and P. C. W. Holdsworth. Magnetic monopole dynamics in spin ice. *Journal of Physics Condensed Matter*, 23(16):164222, 2011. ISSN 09538984. doi: 10.1088/0953-8984/23/16/164222.
- [31] C. Castelnovo, R. Moessner, and S. L. Sondhi. Magnetic monopoles in spin ice. *Nature*, 451(7174):42–45, 2008. ISSN 14764687. doi: 10.1038/nature06433.
- [32] L. D. C. Jaubert and P. C. W. Holdsworth. Signature of magnetic monopole and Dirac string dynamics in spin ice. *Nature Physics*, 5(4):258–261, 2009. ISSN 1745-2473. doi: 10.1038/nphys1227. URL <http://arxiv.org/abs/0903.1074><http://dx.doi.org/10.1038/nphys1227>.
- [33] R. F. Wang, C. Nisoli, R. S. Freitas, J. Li, W. McConville, B. J. Cooley, M. S. Lund, N. Samarth, C. Leighton, V. H. Crespi, and P. Schiffer. Artificial ‘spin ice’ in a geometrically frustrated lattice of nanoscale ferromagnetic islands. *Nature*, 439(7074):303–306, 2006. ISSN 14764687. doi: 10.1038/nature04447.

- [34] S. H. Skjærvø, C. H. Marrows, R. L. Stamps, and L. J. Heyderman. Advances in artificial spin ice. *Nature Reviews Physics*, 2(1):13–28, 2020. doi: 10.1038/s42254-019-0118-3.
- [35] A. Farhan, M. Saccone, C. F. Petersen, S. Dhuey, R. V. Chopdekar, Y. L. Huang, N. Kent, Z. Chen, M. J. Alava, T. Lippert, A. Scholl, and S. van Dijken. Emergent magnetic monopole dynamics in macroscopically degenerate artificial spin ice. *Science Advances*, 5(2):eaav6380, 2019. ISSN 23752548. doi: 10.1126/sciadv.aav6380.
- [36] J. M. Porro, A. Bedoya-Pinto, A. Berger, and P. Vavassori. Exploring thermally induced states in square artificial spin-ice arrays. *New Journal of Physics*, 15(5):055012, 2013. ISSN 13672630. doi: 10.1088/1367-2630/15/5/055012.
- [37] J. P. Morgan, A. Stein, S. Langridge, and C. H. Marrows. Thermal ground-state ordering and elementary excitations in artificial magnetic square ice. *Nature Physics*, 7(1):75–79, 2011. ISSN 17452481. doi: 10.1038/nphys1853.
- [38] Y. Perrin, B. Canals, and N. Rougemaille. Extensive degeneracy, Coulomb phase and magnetic monopoles in artificial square ice. *Nature*, 540(7633):410–413, 2016. ISSN 14764687. doi: 10.1038/nature20155.
- [39] I. R.B. Ribeiro, F. S. Nascimento, S. O. Ferreira, W. A. Moura-Melo, C. A. R. Costa, J. Borme, P. P. Freitas, G. M. Wysin, C. I. L. De Araujo, and A. R. Pereira. Realization of Rectangular Artificial Spin Ice and Direct Observation of High Energy Topology. *Scientific Reports*, 7(1):1–9, 2017. ISSN 20452322. doi: 10.1038/s41598-017-14421-w.
- [40] E. Östman, H. Stopfel, I. A. Chioar, U. B. Arnalds, A. Stein, V. Kapaklis, and B. Hjörvarsson. Interaction modifiers in artificial spin ices. *Nature Physics*, 14(4):375–379, 2018. ISSN 17452481. doi: 10.1038/s41567-017-0027-2.
- [41] S. Ladak, D. E. Read, G. K. Perkins, L. F. Cohen, and W. R. Branford. Direct observation of magnetic monopole defects in an artificial spin-ice system. *Nature Physics*, 6(5):359–363, 2010. ISSN 17452473. doi: 10.1038/nphys1628.
- [42] Y. Perrin, B. Canals, and N. Rougemaille. Quasidegenerate ice manifold in a purely two-dimensional square array of nanomagnets. *Physical Review B*, 99(22):224434, 2019. ISSN 24699969. doi: 10.1103/PhysRevB.99.224434.

- [43] Y. Qi, T. Brintlinger, and J. Cumings. Direct observation of the ice rule in an artificial kagome spin ice. *Physical Review B - Condensed Matter and Materials Physics*, 77(9):094418, 2008. ISSN 10980121. doi: 10.1103/PhysRevB.77.094418.
- [44] S. Ladak, D. E. Read, G. K. Perkins, L. F. Cohen, and W. R. Branford. Direct observation of magnetic monopole defects in an artificial spin-ice system. *Nature Physics*, 6(5):359–363, 2010. ISSN 17452481. doi: 10.1038/nphys1628. URL <http://dx.doi.org/10.1038/nphys1628>.
- [45] M. Hunt, M. Taverne, J. Askey, A. May, A. van den Berg, Y. L. D. Ho, J. Rarity, and S. Ladak. Harnessing multi-photon absorption to produce three-dimensional magnetic structures at the nanoscale. *Materials*, 13(3):761, 2020. ISSN 19961944. doi: 10.3390/ma13030761.
- [46] T. Baldacchini. *Three-Dimensional Microfabrication Using Two-Photon Polymerization*. Elsevier, 2016.
- [47] J. Fischer. *Three-dimensional optical lithography beyond the diffraction limit*. PhD thesis, Karlsruhe Institute of Technology, 2012. URL <https://publikationen.bibliothek.kit.edu/1000028704>.
- [48] X. Zhou, Y. Hou, and J. Lin. A review on the processing accuracy of two-photon polymerization. *AIP Advances*, 5(3):030701, 2015. ISSN 21583226. doi: 10.1063/1.4916886.
- [49] B. Jia, H. Kang, J. Li, and M. Gu. Use of radially polarized beams in three-dimensional photonic crystal fabrication with the two-photon polymerization method. *Optics Letters*, 34(13):1918–1920, 2009. ISSN 0146-9592. doi: 10.1364/ol.34.001918.
- [50] C. Liberale, G. Cojoc, P. Candeloro, G. Das, F. Gentile, F. De Angelis, and E. Di Fabrizio. Micro-optics fabrication on top of optical fibers using two-photon lithography. *IEEE Photonics Technology Letters*, 22(7):474–476, 2010. ISSN 10411135. doi: 10.1109/LPT.2010.2040986.
- [51] A. Accardo, M. C. Blatché, R. Courson, I. Loubinoux, C. Vieu, and L. Malaquin. Two-photon lithography and microscopy of 3D hydrogel scaffolds for neuronal cell growth. *Biomedical Physics and Engineering Express*, 4(2):027009, 2018. ISSN 20571976. doi: 10.1088/2057-1976/aaab93.

- [52] S. H. Liou, R. F. Sabiryanov, S. S. Jaswal, J. C. Wu, and Y. D. Yao. Magnetic domain patterns of rectangular and elliptic arrays of small permalloy elements. *Journal of Magnetism and Magnetic Materials*, 226:1270–1272, 2001. ISSN 03048853. doi: 10.1016/S0304-8853(01)00073-7.
- [53] L. O’Brien, D. Petit, H. T. Zeng, E. R. Lewis, J. Sampaio, A. V. Jausovec, D. E. Read, and R. P. Cowburn. Near-field interaction between domain walls in adjacent permalloy nanowires. *Physical Review Letters*, 103(7):1–4, 2009. ISSN 00319007. doi: 10.1103/PhysRevLett.103.077206.
- [54] T. C. Chen, C. Y. Kuo, A. K. Mishra, B. Das, and J. C. Wu. Magnetic domain wall motion in notch patterned permalloy nanowire devices. *Physica B: Condensed Matter*, 476:161–166, 2015. ISSN 09214526. doi: 10.1016/j.physb.2015.04.004.
- [55] C. Vieu, F. Carcenac, A. Pépin, Y. Chen, M. Mejias, A. Lebib, L. Manin-Ferlazzo, L. Couraud, and H. Launois. Electron beam lithography: Resolution limits and applications. *Applied Surface Science*, 164(1-4):111–117, 2000. ISSN 01694332. doi: 10.1016/S0169-4332(00)00352-4.
- [56] A. May, M. Hunt, A. van den Berg, A. Hejazi, and S. Ladak. Realisation of a Frustrated 3D Magnetic Nanowire Lattice. *Communications Physics*, 2(1):1–9, 2018. ISSN 2399-3650. doi: 10.1038/s42005-018-0104-6. URL <http://dx.doi.org/10.1038/s42005-018-0104-6><http://arxiv.org/abs/1812.02442>.
- [57] A. Tanuševski and D. Poelman. Optical and photoconductive properties of SnS thin films prepared by electron beam evaporation. *Solar Energy Materials and Solar Cells*, 80(3):297–303, 2003. ISSN 09270248. doi: 10.1016/j.solmat.2003.06.002.
- [58] Y. K. Ko, D. S. Park, B. S. Seo, H. J. Yang, H. J. Shin, J. Y. Kim, J. H. Lee, W. H. Lee, P. J. Reucroft, and J. G. Lee. Studies of cobalt thin films deposited by sputtering and MOCVD. *Materials Chemistry and Physics*, 80(2):560–564, 2003. ISSN 02540584. doi: 10.1016/S0254-0584(03)00085-3.
- [59] S. M. George. Atomic layer deposition: An overview. *Chemical Reviews*, 110(1):111–131, 2010. ISSN 00092665. doi: 10.1021/cr900056b.
- [60] K. Sun, K. Wang, T. Yu, X. Liu, G. Wang, L. Jiang, Y. Bu, and G. Xie. High-performance Fe-Co-P alloy catalysts by electroless deposition for overall water

- splitting. *International Journal of Hydrogen Energy*, 44(3):1328–1335, 2019. ISSN 03603199. doi: 10.1016/j.ijhydene.2018.11.182.
- [61] M. Huth, F. Porrati, and O. V. Dobrovolskiy. Focused electron beam induced deposition meets materials science. *Microelectronic Engineering*, 185: 9–28, 2018. ISSN 01679317. doi: 10.1016/j.mee.2017.10.012.
- [62] A. Salman, R. Sharif, K. Javed, S. Shahzadi, K. T. Kubra, A. Butt, S. Saeed, H. Arshad, S. Parajuli, and J. Feng. Controlled electrochemical synthesis and magnetic characterization of permalloy nanotubes. *Journal of Alloys and Compounds*, 836:155434, 2020. ISSN 09258388. doi: 10.1016/j.jallcom.2020.155434.
- [63] W. F. Van Dorp, I. Lazić, A. Beyer, A. Gölzhäuser, J. B. Wagner, T. W. Hansen, and C. W. Hagen. Ultrahigh resolution focused electron beam induced processing: The effect of substrate thickness. *Nanotechnology*, 22(11):115303, 2011. ISSN 09574484. doi: 10.1088/0957-4484/22/11/115303.
- [64] M. Ohring. *The Materials Science of Thin Films*. 2013. ISBN 012524990X. doi: 10.1016/C2009-0-22199-4.
- [65] M. A. Sutton, N. Li, D. C. Joy, A. P. Reynolds, and X. Li. Scanning electron microscopy for quantitative small and large deformation measurements Part I: SEM imaging at magnifications from 200 to 10,000. *Experimental Mechanics*, 47(6):775–787, 2007. ISSN 00144851. doi: 10.1007/s11340-007-9042-z.
- [66] K. W. Lee and J. T.L. Thong. Improving the speed of scanning electron microscope deflection systems. *Measurement Science and Technology*, 10(11):1070, 1999. ISSN 09570233. doi: 10.1088/0957-0233/10/11/316.
- [67] R. F. Fung and S. C. Huang. Dynamic modeling and vibration analysis of the atomic force microscope. *Journal of Vibration and Acoustics, Transactions of the ASME*, 123(4):502–509, 2001. ISSN 15288927. doi: 10.1115/1.1389084.
- [68] N. Jalili and K. Laxminarayana. A review of atomic force microscopy imaging systems: Application to molecular metrology and biological sciences. *Mechanics*, 14(8):907–945, 2004. ISSN 09574158. doi: 10.1016/j.mechatronics.2004.04.005.
- [69] Veeco Instruments. *Dimension 3100 Manual*. 2004. URL <https://www.scu.edu/media/school-of-engineering/photos/cns/Dimension3100D-Manual.pdf>.

- [70] A. Gimeno, P. Ares, I. Horcas, A. Gil, J. M. Gómez-Rodríguez, J. Colchero, and J. Gómez-Herrero. 'Flatten plus': A recent implementation in WSxM for biological research. *Bioinformatics*, 31(17):2918–2920, 2015. ISSN 14602059. doi: 10.1093/bioinformatics/btv278.
- [71] U. Hartmann. *Magnetic force microscopy*. 1999. doi: 10.1146/annurev.matsci.29.1.53.
- [72] J. M. García, A. Thiaville, and J. Miltat. MFM imaging of nanowires and elongated patterned elements. *Journal of Magnetism and Magnetic Materials*, 249(1-2):163–169, 2002. ISSN 03048853. doi: 10.1016/S0304-8853(02)00525-5.
- [73] M. Hunt. *Optical Magnetometry and Micromagnetic Simulations of Three-Dimensional Magnetic Nanostructures*. PhD thesis, Cardiff University, 2017. URL <http://orca.cf.ac.uk/110072/>.
- [74] H. Fangohr, T. Fischbacher, M. Franchin, G. Bordignon, J. Generowicz, A. Knittel, M. Walter, and M. Albert. *NMAG User Manual Documentation*. Release 0. edition, 2012. URL <http://nmag.soton.ac.uk/nmag/current/manual/manual.pdf>.
- [75] Y. Zhao, Q. Song, S. H. Yang, T. Su, W. Yuan, S. S. P. Parkin, J. Shi, and W. Han. Experimental Investigation of Temperature-Dependent Gilbert Damping in Permalloy Thin Films. *Scientific Reports*, 6(1):1–8, 2016. ISSN 20452322. doi: 10.1038/srep22890.
- [76] T. Fischbacher, M. Franchin, G. Bordignon, and H. Fangohr. A systematic approach to multiphysics extensions of finite-element-based micromagnetic simulations: Nmag. *IEEE Transactions on Magnetics*, 43(6):2896–2898, 2007. ISSN 00189464. doi: 10.1109/TMAG.2007.893843.
- [77] A. Vansteenkiste, J. Leliaert, M. Dvornik, M. Helsen, F. Garcia-Sanchez, and B. Van Waeyenberge. The design and verification of MuMax3. *AIP Advances*, 4(10):107133, 2014. ISSN 21583226. doi: 10.1063/1.4899186.
- [78] G. Williams, M. Hunt, B. Boehm, A. May, M. Taverne, D. Ho, S. Giblin, D. Read, J. Rarity, R. Allenspach, and S. Ladak. Two-photon lithography for 3D magnetic nanostructure fabrication. *Nano Research*, 11(2):845–854, 2018. ISSN 19980000. doi: 10.1007/s12274-017-1694-0.

- [79] J. Garcia, V. M. Prida, V. Vega, W. O. Rosa, R. Caballero-Flores, L. Iglesias, and B. Hernando. 2D and 3D ordered arrays of Co magnetic nanowires. *Journal of Magnetism and Magnetic Materials*, 383:88–93, 2015. ISSN 03048853. doi: 10.1016/j.jmmm.2014.10.165.
- [80] J. Martín, M. Martín-González, J. Francisco Fernández, and O. Caballero-Calero. Ordered three-dimensional interconnected nanoarchitectures in anodic porous alumina. *Nature Communications*, 5(1):1–9, 2014. ISSN 20411723. doi: 10.1038/ncomms6130.
- [81] T. L. Wade, X. Hoffer, A. D. Mohammed, J. F. Dayen, D. Pribat, and J. E. Wegrowe. Nanoporous alumina wire templates for surrounding-gate nanowire transistors. *Nanotechnology*, 18(12):125201, 2007. ISSN 09574484. doi: 10.1088/0957-4484/18/12/125201.
- [82] W. Rave and A. Hubert. Magnetic ground state of a thin-film element. *IEEE Transactions on Magnetics*, 36(6):3886–3899, 2000. ISSN 00189464. doi: 10.1109/20.914337.
- [83] M. A. Akhter, D. J. Mapps, Y. Q. Ma Tan, Amanda Petford-Long, and R. Doole. Thickness and grain-size dependence of the coercivity in permalloy thin films. *Journal of Applied Physics*, 81(8):4122–4124, 1997. ISSN 00218979. doi: 10.1063/1.365100.
- [84] C. Nistor, E. Faraggi, and J. L. Erskine. Magnetic energy loss in permalloy thin films and microstructures. *Physical Review B - Condensed Matter and Materials Physics*, 72(1):014404, 2005. ISSN 10980121. doi: 10.1103/PhysRevB.72.014404.
- [85] L. F. Yin, D. H. Wei, N. Lei, L. H. Zhou, C. S. Tian, G. S. Dong, X. F. Jin, L. P. Guo, Q. J. Jia, and R. Q. Wu. Magnetocrystalline anisotropy in permalloy revisited. *Physical Review Letters*, 97(6):067203, 2006. ISSN 00319007. doi: 10.1103/PhysRevLett.97.067203.
- [86] K. Takada, H. B. Sun, and S. Kawata. Improved spatial resolution and surface roughness in photopolymerization- based laser nanowriting. *Applied Physics Letters*, 86(7):071122, 2005. ISSN 00036951. doi: 10.1063/1.1864249.
- [87] S. Hankemeier, R. Frömter, N. Mikuszeit, D. Stickler, H. Stillrich, S. Pütter, E. Y. Vedmedenko, and H. P. Oepen. Magnetic ground state of single and

- coupled permalloy rectangles. *Physical Review Letters*, 103(14):147204, 2009. ISSN 00319007. doi: 10.1103/PhysRevLett.103.147204.
- [88] R. D. Gomez, T. V. Luu, A. O. Pak, K. J. Kirk, and J. N. Chapman. Domain configurations of nanostructured permalloy elements. *Journal of Applied Physics*, 85(8):6163–6165, 1999. ISSN 00218979. doi: 10.1063/1.370030.
- [89] S. Felton, P. Warnicke, K. Gunnarsson, P. E. Roy, H. Lidbaum, and P. Svedlindh. Domain configuration of permalloy ellipses in a rotating magnetic field. *Journal of Physics D: Applied Physics*, 39(4):610, 2006. ISSN 00223727. doi: 10.1088/0022-3727/39/4/002.
- [90] T. Okuno, K. Shigeto, T. Ono, K. Mibu, and T. Shinjo. MFM study of magnetic vortex cores in circular permalloy dots: Behavior in external field. *Journal of Magnetism and Magnetic Materials*, 240(1-3):1–6, 2002. ISSN 03048853. doi: 10.1016/S0304-8853(01)00708-9.
- [91] T. Karabacak. Thin-film growth dynamics with shadowing and re-emission effects. *Journal of Nanomechanics and Micromechanics*, 5(1):052501, 2011. ISSN 21535434. doi: 10.1117/1.3543822.
- [92] R. Streubel, D. Makarov, F. Kronast, V. Kravchuk, M. Albrecht, and O. G. Schmidt. Magnetic vortices on closely packed spherically curved surfaces. *Physical Review B - Condensed Matter and Materials Physics*, 85(17):174429, 2012. ISSN 10980121. doi: 10.1103/PhysRevB.85.174429.
- [93] S. T. Bramwell and M. J. P. Gingras. Spin ice state in frustrated magnetic pyrochlore materials. *Science*, 294(5546):1495–1501, 2001. ISSN 00368075. doi: 10.1126/science.1064761.
- [94] R. Moriya, L. Thomas, M. Hayashi, Y. B. Bazaliy, C. Rettner, and S. S. P. Parkin. Probing vortex-core dynamics using current-induced resonant excitation of a trapped domain wall. *Nature Physics*, 4(5):368–372, 2008. ISSN 17452481. doi: 10.1038/nphys936.
- [95] H. F. Ding, S. Pütter, H. P. Oepen, and J. Kirschner. Experimental method for separating longitudinal and polar Kerr signals. *Journal of Magnetism and Magnetic Materials*, 212(1-2):5–11, 2000. ISSN 03048853. doi: 10.1016/S0304-8853(99)00790-8.

- [96] J. A. Arregi, P. Riego, and A. Berger. What is the longitudinal magneto-optical Kerr effect? *Journal of Physics D: Applied Physics*, 50(3):03LT01, 2017. ISSN 13616463. doi: 10.1088/1361-6463/aa4ea6.
- [97] K. Ounadjela, H. Lefakis, V. S. Speriosu, C. Hwang, and P. S. Alexopoulos. Thickness dependence of magnetization and magnetostriction of NiFe and NiFeRh films. *Le Journal de Physique Colloques*, 49(C8):C8–1709, 1988. ISSN 0449-1947. doi: 10.1051/jphyscol:19888776.
- [98] K. Zeissler, M. Chadha, E. Lovell, L. F. Cohen, and W. R. Branford. Low temperature and high field regimes of connected kagome artificial spin ice: The role of domain wall topology. *Scientific Reports*, 6(1):1–9, 2016. ISSN 20452322. doi: 10.1038/srep30218.
- [99] S. Ladak, D. Read, T. Tylizczak, W. R. Branford, and L. F. Cohen. Monopole defects and magnetic coulomb blockade. *New Journal of Physics*, 13(2):023023, 2011. ISSN 13672630. doi: 10.1088/1367-2630/13/2/023023.
- [100] L. K. Bogart, D. Atkinson, K. O’Shea, D. McGrouther, and S. McVitie. Dependence of domain wall pinning potential landscapes on domain wall chirality and pinning site geometry in planar nanowires. *Physical Review B - Condensed Matter and Materials Physics*, 79(5):054414, 2009. ISSN 10980121. doi: 10.1103/PhysRevB.79.054414.
- [101] MATLAB. *version 7.10.0 (R2010a)*. The MathWorks Inc., Natick, Massachusetts, 2010.
- [102] M. Barthelmess, C. Pels, A. Thieme, and G. Meier. Stray fields of domains in permalloy microstructures - Measurements and simulations. *Journal of Applied Physics*, 95(10):5641–5645, 2004. ISSN 00218979. doi: 10.1063/1.1697642.
- [103] M. E. Brooks-Bartlett, S. T. Banks, L. D. C. Jaubert, A. Harman-Clarke, and P. C. W. Holdsworth. Magnetic-moment fragmentation and monopole crystallization. *Physical Review X*, 4(1):011007, 2014. ISSN 21603308. doi: 10.1103/PhysRevX.4.011007.
- [104] Vassilios Kapaklis, Unnar B. Arnalds, Alan Farhan, Rajesh V. Chopdekar, Ana Balan, Andreas Scholl, Laura J. Heyderman, and Björgvin Hjörvarsson. Thermal fluctuations in artificial spin ice. *Nature Nanotechnology*, 2014. ISSN 17483395. doi: 10.1038/nnano.2014.104.